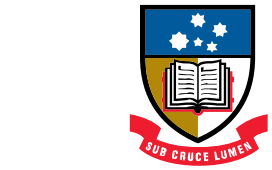

THE UNIVERSITY of ADELAIDE

Understanding the flow behaviour in human maxillary sinuses for drug delivery applications

Oveis Pourmehran

School of Mechanical Engineering

The University of Adelaide

Adelaide, Australia

A thesis submitted in fulfilment of the requirements
for the degree of PhD in Mechanical Engineering

2021

Thesis summary

The sinus infection, chronic rhinosinusitis (CRS), has a prevalence ranging from 4.9% to 10.9% worldwide. When a nasal cavity (NC) is exposed to pathogens carried by inhaled aerosols, the attached sinuses, especially the maxillary sinus (MS), are highly prone to infection. The MS, a hollow organ attached to the NC, plays the role of thermal insulation in a human skull and affects the quality of the human voice. The only opening, which connects the NC to the MS, is a circular slit-like opening called the ostium, with a channel of <5 mm in diameter. The narrowness of the ostium is a significant challenge for drug delivery to the MS for the treatment of CRS. Various non-invasive devices, including nasal sprays and jet nebulizers, are available for drug delivery to the MS; however, due to the poor accessibility of the MS and the narrowness of the ostium, the efficiency of drug delivery to the MS is very low.

Acoustic drug delivery (ADD) is a modern pathway for topical drug delivery to the MS, demonstrated to enhance drug delivery. This technology, using a fixed acoustic frequency, is currently available as a pre/post-surgical therapy but has not been able to demonstrate the full potential of delivering sufficient drug particles to the sinuses in most CRS cases. Several researchers investigated the effects of fixed acoustic frequencies, 45 Hz and 100 Hz, and reported an increase of 2 to 3-fold in the aerosol deposition in the MS when compared with conventional drug delivery. However, it has recently been hypothesised that the underlying mechanism of ADD is based on the Helmholtz resonator principle, where the air plug in the ostium oscillates when an external acoustic field is applied to the nostril. Oscillation of the air plug in the ostium leads to the delivery of the aerosols (nebulised drugs) from the NC to the MS. Accordingly, the maximum delivery of aerosols into the MS occurs when the amplitude of the oscillation of the air plug in the ostium is maximized. The

maximum amplitude of the oscillation of the air plug in the ostium occurs at the resonance frequency of the NC-MS combination. In a limited number of the studies, the equation for a Helmholtz resonator (derived for a combination of a spherical cavity and a cylindrical neck), was used for predicting the resonance frequency of the NC-MS combination, which was superimposed onto the nebulised medication entering the nostril. Under this method, the efficiency of drug delivery to the MS increased 5-fold at most, when compared with non-acoustic drug delivery. In a more recent study, an acoustic frequency sweep was applied to the nostril, which showed a 10-fold increase in the aerosol deposition in the MS compared with conventional drug delivery. Such an increase in drug delivery efficiency is still insufficient for the treatment of CRS. Hence, it is important to predict the resonance frequency of the NC-MS combination accurately to increase the ADD efficiency significantly.

The main aim of this thesis is to improve the efficiency of ADD to the MS by application of targeted excitation frequencies of the NC-MS combination to the nostril. Initially, the resonance frequency of an NC-MS combination was predicted as accurately as possible, and then the effect of various acoustic frequencies on ADD efficiency was investigated. In this thesis, several numerical models were explored, along with experimental testing. The numerical models include finite element analysis (FEA), computational fluid dynamics (CFD), and the Helmholtz resonator equation. The resonance frequencies of several simplified NC-MS combinations were predicted by this numerical model and compared with the experimental data to determine the most accurate numerical model. It was found that the Helmholtz resonator equation and FEA overpredict the resonance frequency of the NC-MS combination by 41% (depending on the size of the ostium and MS) compared with the experimental data. The CFD approach underpredicted the resonance frequency of the NC-MS combination by 8% compared with in-house experimental data, which proved to be the most accurate amongst the explored numerical models. The application of the Helmholtz resonator

equation and FEA were shown not to provide an accurate prediction of the resonance frequency of the NC-MS combination because the equations of the Helmholtz resonator and the linearised Eulerian equation used in FEA do not account for the effect of the shape of the MS and the presence of the NC, while the Navier-Stokes equation used in CFD does. Using the CFD model, the effect of geometrical parameters such as the ostium length/diameter, MS shape/volume, and the NC width on the resonance frequency of an NC-MS combination were also studied.

To examine the importance of the resonance frequency of the NC-MS combination on the ADD efficiency, a CFD model was developed to investigate the effect of various input frequencies, including the resonance and off-resonance frequencies, on the transport of particles from NC to the MS using an Eulerian-Lagrangian particle tracking scheme. Moreover, the effect of amplitude of the acoustic source and the inlet flow rate (at the nostril) on the transport of particles from the NC to the MS were investigated using a CFD model in a simplified NC-MS combination. The results showed that the highest transport of particles from the NC to the MS occurred when the inlet frequency was identical to the resonance frequency. It has been shown that the amplitude of the acoustic source has a monotonic relationship with the transport of particles from the NC to the MS; however, the airflow rate has an inverse relationship with it. Moreover, the effect of particle diameters and density on the penetration of particles in the MS were investigated using CFD modelling. It was found that increasing the particle diameter and density decreases the penetration of particles into the MS; the reason is that, in the presence of an acoustic field, increasing the particle diameter/density decreases the particle entrainment coefficient, which increases the acoustic Stokes number. An increase in the Stokes number reduces the ability of the particles to follow the oscillation of the air plug in the ostium with an amplitude identical to that of fluid.

To explore the feasibility of ADD in practice, a 3D printed model of a realistic NC-MS combination was used to conduct the experiments to investigate the effect of resonance frequency on particle deposition in the MS, where a 2.5% sodium fluoride (NaF) was used to as the drug tracer. A loudspeaker was used to generate the acoustic field of interest, which was then applied to the nostril. The results show that when an acoustic field at a frequency equal to the resonance frequency of the NC-MS (obtained experimentally) is applied to the nostril, the particle deposition in the MS increases by 75-fold when compared with conventional drug delivery. The effect of input acoustic amplitude on particle deposition was also studied using a 3D printed model. The experimental data shows that increasing the input acoustic amplitude increases the particle deposition in the MS; however, increasing the amplitude above 120dB does not have a significant effect on the deposition. This might imply that at certain acoustic amplitudes a saturation point for aerosol deposition is reached.

In the CFD simulation for a realistic NC-MS model, it was found that in the presence of an external acoustic field, not only does the air plug in the ostium oscillate but also a portion of the air plug in the middle meatus oscillates. Hence, to increase the ADD efficiency, it is important to transport particles to the middle meatus as much as possible. To do so, the effect of inlet flow parameters, as well as the impact of the diameter of the nozzle that injects the particles at the nostril, on the drug delivery to MM-Ostium regions was investigated. The term MM-Ostium refers to a region in the middle meatus (MM) where the ostium connects the MM to the MS. An increase in particle retention criterion in the MM-Ostium region was calculated to quantify the increase in the drug delivery to the MS region. The results have shown that the effect of turbulence at the inlet of the NC on drug delivery to the MM-Ostium region is negligible. It was also demonstrated that increasing the flow swirl at the inlet improves the total particle deposition due to the generation of centrifugal force, which acts on the particles in the nostril and vestibule. The results also suggest that drug delivery

efficiency to the MS can be increased by using a swirling flow with a moderate swirl number of 0.6. Finally, it was found that decreasing the nozzle diameter can increase drug delivery to the MM-Ostium region, which subsequently increases the drug delivery to the MS.

Thesis declaration

I certify that this work contains no material which has been accepted for the award of any other degree or diploma in my name, in any university or other tertiary institution and, to the best of my knowledge and belief, contains no material previously published or written by another person, except where due reference has been made in the text. In addition, I certify that no part of this work will, in the future, be used in a submission in my name, for any other degree or diploma in any university or other tertiary institution without the prior approval of the University of Adelaide and where applicable, any partner institution responsible for the joint-award of this degree.

I acknowledge that copyright of published works contained within this thesis resides with the copyright holder(s) of those works.

I also give permission for the digital version of my thesis to be made available on the web, via the University's digital research repository, the Library Search and also through web search engines, unless permission has been granted by the University to restrict access for a period of time.

I acknowledge the support I have received for my research through the provision of an Australian Government Research Training Program Scholarship.

Oveis Pourmehran

Acknowledgments

I would like to extend my appreciation to the many people who helped to bring this research project to fruition. First, and foremost, I would like to express my most sincere gratitude to my principal supervisor Prof. Maziar Arjomandi, who guided the process with great expertise, commitment and empathy. His insight, instruction, and approachable personality were invaluable, and I cannot thank him enough. Secondly, I wish to acknowledge my co-supervisor Prof. Ben Cazzolato for his continuous help and concern. I have been extremely lucky to have a supervisor who cared so much about my work, and who responded to my questions and queries so promptly. My special thanks go to my co-supervisor Dr Zhao Tian, for providing much appreciated guidance and direction, as well as for his consideration. My heartfelt gratitude goes to my loving wife Fatemeh for her unconditional love, patience, and for putting up with my late nights and stressful outbursts, and for having made so many sacrifices for me throughout this long journey. Many thanks also go to my parents and my beautiful sister for their everlasting support and encouragement. I also thank Prof. Peter-John Wormald, A/Prof Sarah Vreugde, Prof Alkis Psaltis, and Dr Shari Javadiyan for their productive collaboration in establishing the experimental setup at the Basil Hetzel Institute for Translational Health Research. A special thank goes to Dr Fabian Voisin, a research computing specialist, for his invaluable assistance in running complicated computational models in Phoenix HPC. I would also thank Dr Alison-Jane Hunter for editing the English of the manuscript. Last but not least, I am grateful to Prof. Jérémie Pourchez and Dr Lara Leclerc from the Université de Lyon, France, for their constructive comments in establishing the experimental setup for ADD.

Contents

List of figures

List of tables

Abbreviations

ADD	Acoustic drug delivery
3D	Three-dimensional
ATDD	Active targeting drug delivery
CAA	Computational aero-acoustics
CFD	Computational fluid dynamics
CRS	Chronic rhinosinusitis
CT	Computed tomography
DDS	Drug delivery system
DE	Deposition efficiency
DE	Deposition efficiency
DNS	Direct numerical simulation
DPM	Discrete phase model
DSCG	Disodium chromoglycate
ECDD	Electrically charged particle (drug) delivery
EPW	Elements per wavelength
ES	Ethmoid sinus
FEA	Finite element analysis
FEM	Finite element method
FESS	Functional endoscopic sinus surgery
FL	Frontal sinus: left
FR	Frontal sinus: right
FS	Frontal sinus
FVM	Finite volume method
HIFU	High-intensity focused ultrasound
IP	Inertial parameter
LES	Large eddy simulation
MAD	Median aerodynamic diameter
MDCs	Magnetic drug carriers
MDT	Magnetic drug targeting
Mic	Microphone

ML	Maxillary sinus: left
MP	Main passage
MR	Maxillary sinus: right
MRI	Magnetic resonance imaging
MS	Maxillary sinus
NC	Nasal cavity
NO	Nitric oxide
Non-ADD	Non-acoustic drug delivery
OMC	Ostiomeatal complex
OS	Ostium
PIV	Particle image velocimetry
PSD	Power spectral density
PTDD	Passive targeted drug delivery
RANS	Reynolds-Averaged Navier–Stokes
RMSE	Root mean square error
SBES	Stress-blended eddy simulation
SM	Superior meatus
SS	Sphenoid sinus
SST	Shear stress transport
STL	Stereolithography
TDD	Targeted drug delivery
TF	Transfer function
WALE	Wall-adapting local eddy-viscosity
WSS	Wall shear stress

Chapter 1

Introduction

1.1 Background and motivation

The term "nasal cavity (NC)" refers to one of the two separate parallel sides of the nose, or to a combination of both sides, which play an important role in the operation of the respiratory system for different physiological functions. Anatomical misalignments, such as septum deviation, explain why infections carried by aerosols during inhalation can cause the NC to malfunction, which can then lead to diseases emerging in the NC. One of the most common diseases in human upper airways is Chronic Rhinosinusitis (CRS), having a prevalence ranging from 4.9% to 10.9% worldwide (Bhattacharyya, 2012; Cho et al., 2010; Laube, 2007; Liu et al., 2018; Pilan et al., 2012). For example, statistics show that in the United States around 30 million CRS cases are diagnosed annually and about 0.6 million CRS patients undergo surgery (Lam et al., 2014).

CRS patients endure obstructed airways due to infections in the sinuses (Huang et al., 2005). The sinuses are hollow organs in the human skull and are categorised into four types: frontal, sphenoid, ethmoid, and maxillary sinuses (see Figure 1.1 (a-b)). The maxillary sinuses (MS) are the largest of all the sinuses and are located below the cheek and closer to the nostril than the other sinuses. Given their location, the MS are exposed to a wider range of diseases compared with the other sinuses, including bacterial colonisation and viral infection. In addition, MS infections can spread to the ethmoid sinuses (ES), frontal sinuses (FS), and maxillary teeth due to the proximity of the MS to these regions (Harbo et al., 1997).

Topical therapy with anti-inflammatory drugs (antibiotics) forms the mainstay of treatments of CRS. Various drug delivery methods are used, including nasal douching (Taccariello et al., 1999), nasal pump sprays and nebulisation (Moffa et al., 2019). In the nasal douching technique, the NC is irrigated with a drug solution to remove the infections from the sinuses and nose (Taccariello et al., 1999). Nasal douching is beneficial in reducing congestion of the NC, removing bacteria and viruses from the sinuses, and reducing the need for functional endoscopic sinus surgeries; however, washing the nose also flushes out the good mucus containing antimicrobial agents, which can lead to an increase in the frequency of acute infections (Moidee, 2019). Also, nasal douching is not a cost-efficient method for sinus drug delivery due to the large amount of drug waste (Snidvongs et al., 2008). To overcome the significant drug waste, pump sprays and nebulisers are potential candidates for new forms of sinus drug delivery.

Nasal pump sprays are usually used to deliver the drug solution locally in the NC for conditions such as nasal congestion and allergic rhinitis. Nasal pump sprays produce particles/droplets with a median aerodynamic diameter (MAD) of 50-100 μm. The majority of the droplets produced by sprays are deposited on the nasal valve and anterior regions of

the NC and cannot reach the posterior NC regions and poorly-ventilated areas, such as sinuses (Möller et al., 2014), where the efficiency of drug delivery is near zero (Suman et al., 1999).

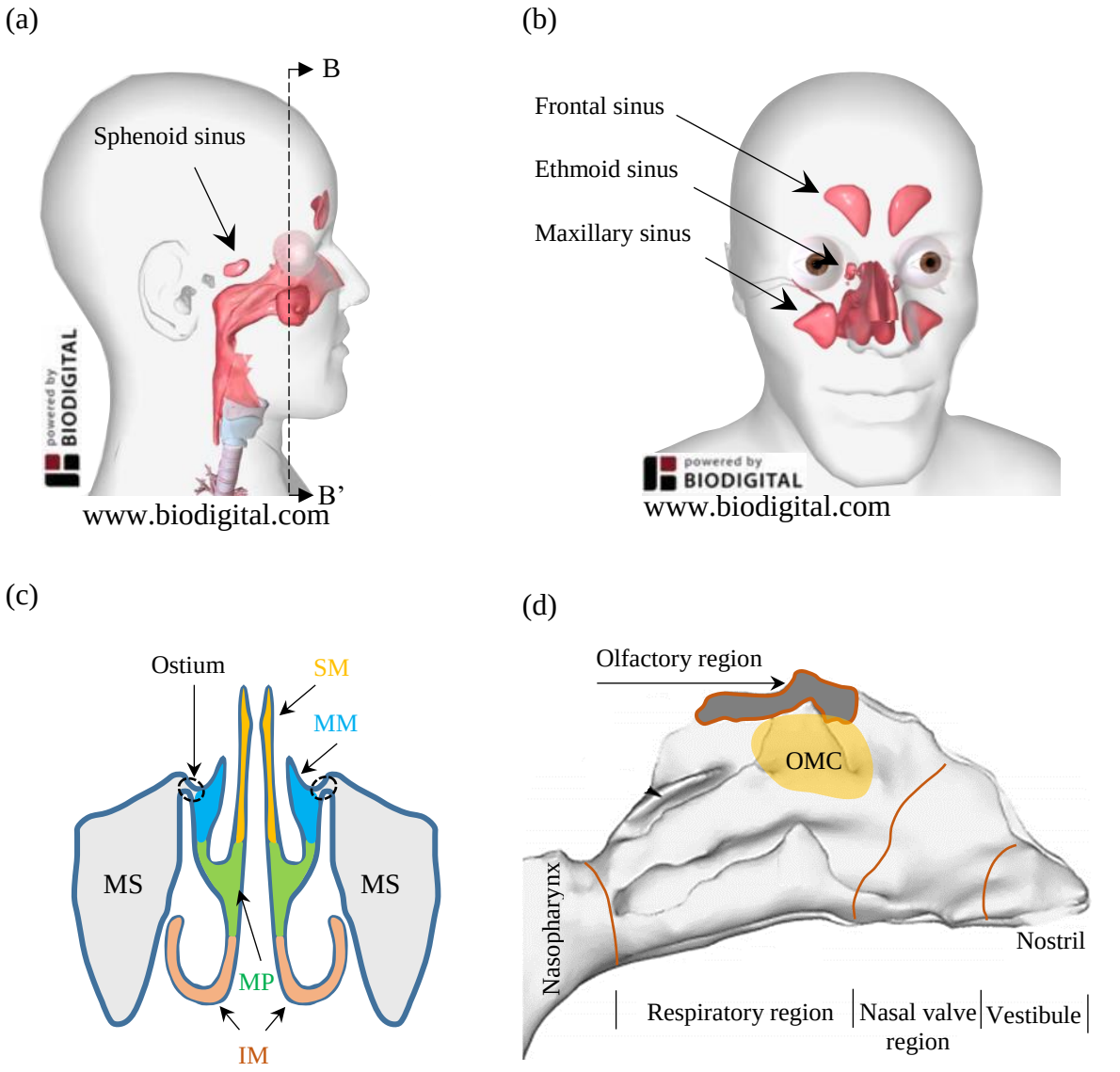

Figure 1.1: A schematic of the paranasal sinuses: (a) sagittal view; (b) front view; (c) section B-B' representing the maxillary sinuses (MS), ostium, superior meatus (SM), middle meatus (MM), main passage, (MP), and inferior meatus (IM), reproduced from Xi et al. (2017) with permission from Elsevier; (d) an overview of the NC representing the nasal vestibule, nostril, nasal valve region, the respiratory region, olfactory region, ostiomeatal complex (OMC) and nasopharynx, reprinted from Shi et al. (2007) with permission from Elsevier.

On the other hand, nebulisers produce finer particles/droplets in a range of 1-30 μm, which can be transported beyond the nasal valve and reach the posterior regions of the NC, ostiomeatal complex (OMC) and the sinuses (Hilton et al., 2008; Wofford et al., 2015).

Conventional nebulisers have proven advantageous for drug delivery to the superior meatus (SM), middle meatus (MM), and inferior meatus (IM), as well as the olfactory region (Hilton et al., 2008; Wofford et al., 2015). However, for topical drug delivery to the sinuses, particularly the MS, conventional nebulisers are likely to be an inefficient method due to the poor accessibility of the MS (Hyo et al., 1989; Möller et al., 2014; Wofford et al., 2015). The MS is connected to the NC through a narrow opening called the ostium. The diameter and length of the ostium are usually in the range 2-6 mm and 4-12 mm, respectively (Cannon et al., 2013). The small size of the ostium limits drug delivery to the MS (see Figure 1.1(c)) (Frank et al., 2013).

A novel technique called acoustic drug delivery (ADD) has recently been employed to overcome the low efficiency of conventional nebulisers for drug delivery to the MS (Leclerc et al., 2014). In ADD, the MS behaves like a Helmholtz resonator, an acoustic device composed of a cavity attached to a neck. In an NC-MS combination, the MS and the ostium play the role of the cavity and the neck of the Helmholtz resonator, respectively. When an external acoustic wave is applied to an NC-MS combination (Helmholtz resonator), the air plug in the ostium oscillates at a frequency equal to the frequency of the external acoustic waves (von Helmholtz et al., 1875). Based on the theory of the Helmholtz resonator, the amplitude of the oscillation of the air plug in the ostium becomes maximal when the frequency of the external acoustic wave is identical to the resonance frequency. Accordingly, when the combination of the NC and MS is at resonance, it is expected that the air exchange between the NC and the MS is increased, which leads to the highest penetration of nebulised medications to the MS.

Limited studies have investigated the efficacy of ADD for drug delivery to the MS, in which a fixed acoustic frequency (i.e. 45 Hz & 100 Hz) was applied at the nostril (Granqvist et al., 2006; Laube, 2007; Möller et al., 2011; Si et al., 2013; Xi et al., 2017). These studies,

using ADD with fixed frequencies, demonstrated an insignificant (2- to 3-fold) increase in the penetration of nebulised medications into the MS when compared with non-acoustic drug delivery (non-ADD) (Leclerc et al., 2014); however, the penetration of the drug into the MS varies for different sizes of the ostium and MS (Xi et al., 2017). The reason for the low efficiency of ADD with fixed frequencies of 45 Hz and 100 Hz might be due to the fact that the oscillation of the air plug in the ostium is not at resonance at these fixed frequencies.

In several studies, a classic Helmholtz resonator equation was used to predict the resonance frequency of the combination of the NC and MS in order to apply the obtained resonance frequency to the nostril (Durand et al., 2012; Maniscalco et al., 2006; Möller et al., 2010; Möller et al., 2014; Möller et al., 2008; Xi et al., 2017). *In-vitro* studies in the literature demonstrate that the penetration of the nebulised medication to the MS was not increased significantly compared with a non-ADD, even with the application of an acoustic wave at the resonance frequency of the NC-MS combination predicted by the Helmholtz resonator equation (Moghadam et al., 2018). The classic equation for the resonance frequency of a Helmholtz resonator is based on the volume of a spherical cavity and the length and diameter of a cylindrical neck, while the geometry of the MS and ostium are irregular. Therefore, the classic Helmholtz resonator equation will not accurately predict the resonance frequency of a specific geometry, leading to reduced efficiency of ADD.

An alternative to fixed-frequency is to apply a frequency sweep to the nostril. The frequency sweep covers a broader frequency range, so there should be an input frequency that either matches or is close to the resonance frequency of the NC-MS combination. In a recent ADD study by Moghadam et al. (2018), using a 3D printed model of a realistic nose-sinus model, the application of a frequency sweep (100-850 Hz) to the MS demonstrated an increase in the deposition of nebulised medications in the MS when compared with non-ADD. Although the frequency sweep technique increased the overall deposition of the nebulised

drugs in the MS, the total amount of the injected nebulised medications increased, and the treatment time was significantly extended in comparison with the application of a fixed frequency, which can lead to an increased risk of adverse side effects in the respiratory system.

Single fixed acoustic frequency (i.e., 45 Hz & 100 Hz) ADD technology is currently available as a topical therapy but has not yet been shown to enable the delivery of a sufficient amount of nebulised medications to the MS in most of the CRS cases. The primary motivation of this thesis is to develop a well-resolved model to understand the mechanisms underlying the ADD technique. The goals of the research are not only to develop a model to better understand the ADD technique but also to determine the potential geometric and aero-acoustic parameters influencing the efficiency of ADD in drug delivery to the MS.

All previous studies considered a uniform airflow entering the nostril for drug delivery applications. However, Ari et al. (2015) showed experimentally that different inhalation mask shapes affect the performance of drug delivery to the lung, which implies that the inlet flow parameters and distribution of the injected particles at the nostril can have an impact on the deposition and transport of the particles in different regions of the NC. Previous studies showed that the ventilation of both MM is much lower than the ventilation of the main nasal passage and IM, which contributes to a low drug delivery to the MS. The secondary aim of this project is to develop an understanding of the effect of the inlet flow parameters, such as a turbulent or swirling inlet flow, as well as the effect of the nozzle diameter (the diameter of the particles' injection at the nostril) on the flow structure and the particle transport/deposition patterns in the NC.

1.2 Objectives of the research

The main aim of this study is to develop a deep understanding of the mechanisms underlying ADD to the MS in order to increase the efficiency of this delivery technique, as well as to investigate the effect of inlet airflow patterns on flow features in the NC and sinuses. To achieve this aim, the following objectives are defined:

- *To develop a well-resolved numerical model to investigate the effect of different geometrical parameters on the resonance frequency of the NC-MS combination.*

  To maximise drug delivery efficiency in ADD, it is crucial to accurately predict the resonance frequency of the NC-MS combination. It has been demonstrated that the efficiency of ADD is not increased significantly when the input acoustic frequency is equal to the resonance frequency predicted by the Helmholtz resonator equation. Therefore, the classic Helmholtz resonator equation cannot predict an accurate resonance frequency of the NC-MS combination. Hence, a well-resolved model is required to accurately predict the resonance frequency of an NC-MS combination. Finite element analysis and computational aero-acoustics are potential candidates for this purpose. Once an accurate model is developed, the effect of different geometrical parameters on the resonance frequency of the nose-sinus model can be investigated to identify the important geometrical parameters in resonance frequency prediction.

- *To develop an understanding of airflow behaviour in a simplified NC-MS combination in the presence of an external acoustic field in order to investigate the effect of aero-acoustic parameters on the efficiency of ADD.*

  To do so, a well-developed numerical model is required to simulate the effect of aero-acoustic parameters, including the input acoustic frequency, input sound pressure level, and inlet mean flow rate on the particle dispersion and deposition patterns. The

particle dispersion and deposition patterns in the MS are representative of the efficiency of ADD.

- *To fabricate a well-designed experimental setup using a 3D printed model of a realistic NC-MS model to examine the efficacy of ADD in drug delivery to the MS.*

  Considering the vital aero-acoustic parameters identified in the second objective, the feasibility of ADD to the MS will be investigated and the optimal aero-acoustic parameters will be identified. The effect of the aero-acoustic parameters on the efficacy of ADD will be investigated and the deposition rates of nebulised drug particles/droplets will be compared with those obtained during non-ADD.

- *To develop a computational fluid dynamics (CFD) model to investigate the effect of the inlet flow parameters and the nozzle diameter on particle transport/deposition in a realistic NC-MS combination.*

  To increase ADD efficiency, not only it is necessary to predict the accurate resonance frequency of the NC-MS combination and to optimise the aero-acoustic parameters, but also important to attain sufficient nebulised medication (particles) dispersed in the middle meatus region where the ostium is located. The effect of different inlet flow parameters (i.e., turbulence and swirl), as well as the effect of the diameter of the nozzle used for injecting the particles into the nostril, on the particle transport/deposition patterns in the middle meatus region will be studied.

1.3 Structure of the thesis

The thesis is formatted as a collection of manuscripts that have been published in or submitted to high-quality journals and peer-reviewed conference proceedings.

In Chapter 2, a comprehensive literature review is carried out to establish a detailed framework for this research. The anatomy of the human respiratory system is initially discussed to understand the functions and important anatomical parameters of the NC and sinuses. The diseases related to the NC and sinuses are then introduced with a focus on chronic nose-sinus diseases such as CRS. The existing targeted drug delivery (TDD) methods are reviewed in detail to determine the most efficient, non-invasive, and feasible method of drug delivery to the NC and sinuses for the treatment of CRS. The airflow features, and aerosol transport pattern and deposition of aerosol in the NC and sinuses, are also discussed to understand the existing gaps and questions in nasal drug delivery in order to improve the efficiency of ADD.

In Chapter 3, as an initial step for improving drug delivery efficiency, a CFD model, cross-validated with experimental data, is presented to estimate the resonance frequency of the NC-MS combination. It is assumed that to achieve the highest ADD efficiency it is crucial to obtain an accurate resonance frequency of the NC-MS combination. Various numerical models, including FEA, CFD, and analytical, are used to determine the most accurate method for estimating the resonance frequency of the NC-MS combination. Then, a parametric study is conducted to investigate the effect of the geometrical parameters of the NC and MS on the resonance frequency of the NC-MS combination. Finally, the effect of the middle meatus on the estimation of resonance frequency is examined in a realistic NC-MS combination using a CFD model.

In Chapter 4, the aero-acoustic behaviour of a simplified NC-MS combination is studied using CFD modelling through the Eulerian-Lagrangian particle tracking approach. The CFD model is validated against experimental data, based on the estimation of the resonance frequency of the NC-MS combination. A parametric study is conducted to examine

the effect of various parameters such as input acoustic frequency, amplitude, and airflow rate on the efficiency of ADD for drug delivery to the MS. The effect of those parameters on the flow features in the NC, ostium, and MS is investigated. Furthermore, the effect of the particles and density on the efficiency of ADD is examined using assessment of the acoustic Stokes number.

In Chapter 5, a realistic NC-MS model is used to conduct a set of *in-vitro* experiments to investigate the application of acoustic excitation in drug delivery to the MS. The resonance frequency of the realistic NC-MS combination was measured experimentally. Then, the effects of input frequency (including the resonance and off-resonance frequencies), amplitude, and nebulisation flow rate on the deposition of aerosol in the MS are investigated. Nebulised 2.5wt% sodium fluoride (NaF) is used as the drug tracer. The deposited NaF in the MS is detected using a fluoride ion-selective electrode, together with an Ion-Selective Electrode (ISE) meter. Finally, an optimised acoustic wave and an optimum nebulisation flow rate are obtained to achieve the highest drug delivery efficiency for the NC-MS geometry of this study.

In addition to the aero-acoustic parameters, the efficiency of ADD is highly dependent on the number of particles dispersed in the MM region. In Chapter 6, the effect of inlet flow parameters on airflow structure and particle transport/deposition in a realistic NC-MS combination is investigated. A CFD model is developed to conduct a parametric study to assess the effect of a turbulent and swirling inlet flow, as well as the effect of nozzle diameter on drug delivery to the MS. The CFD model is validated against published experimental data, based on the pressure distribution in the NC.

Finally, the key conclusions and the main findings that have been documented throughout this thesis are presented in Chapter 7, along with suggestions for future research.

1.4 List of publications included as part of the thesis

The following publications have arisen from the research undertaken as part of this thesis.

Pourmehran, O., Arjomandi, M., Cazzolato, B., Ghanadi, F., & Tian, Z. (2020). The impact of geometrical parameters on acoustically driven drug delivery to maxillary sinuses. *Biomechanics and Modeling in Mechanobiology*, 19(2), 557-575.

Pourmehran, O., Cazzolato, B., Tian, Z., & Arjomandi, M. (2020). Acoustic behaviour of the human maxillary sinus: The importance of the middle meatus and the ostium on resonance frequency behaviour. *18th International Conference of Numerical Analysis and Applied Mathematics, Rhodes, Greece*. Oral presentation. Accepted to be published in AIP conference proceeding in winter 2021.

Pourmehran, O., Cazzolato, B., Tian, Z., & Arjomandi, M. (2020). Acoustically-driven drug delivery to maxillary sinuses: Aero-acoustic analysis. *European Journal of Pharmaceutical Sciences*, 151, No.105398.

Pourmehran, O., Arjomandi, M., Cazzolato, B., & Tian, Z. (2020). "Effect of particle diameter and density on acoustic drug delivery to maxillary sinus – A sensitivity study". *22nd Australasian Fluid Mechanics Conference (AFMC2020), Brisbane, Australia.* Oral presentation.

Pourmehran, O., Arjomandi, M., Cazzolato1, B., Tian, Z., Vreugde, S., Javadiyan, S., Psaltis, A., & Wormald, PJ. (2021), "Acoustic drug delivery to maxillary sinuses". *International Journal of Pharmaceutics, 120927 (In Press).*

Pourmehran, O., Arjomandi, M., Cazzolato, B., & Tian, Z. (2021). "Effect of the inlet flow profile and nozzle diameter on drug delivery to maxillary sinus". Submitted to *Biomechanics and Modeling in Mechanobiology*.

1.5 Thesis format

This thesis is based on the collection of the manuscripts produced during the PhD program and has been submitted according to the format approved by the University of Adelaide. The thesis is provided and available in both hard and soft copy, which are identical. The soft copy is available online at the University of Adelaide Library and can be viewed using Adobe Reader.

1.6 References

Ari, A., de Andrade, A. D., Sheard, M., AlHamad, B., & Fink, J. B. (2015). Performance comparisons of jet and mesh nebulizers using different interfaces in simulated spontaneously breathing adults and children. *Journal of Aerosol Medicine and Pulmonary Drug Delivery, 28*(4), 281-289.

Bhattacharyya, N. (2012). Functional limitations and workdays lost associated with chronic rhinosinusitis and allergic rhinitis. *American Journal of Rhinology & Allergy, 26*(2), 120-122.

Cannon, D. E., Frank, D. O., Kimbell, J. S., Poetker, D. M., & Rhee, J. S. (2013). Modeling nasal physiology changes due to septal perforations. *Otolaryngology—Head and Neck Surgery, 148*(3), 513-518.

Cho, Y. S., Choi, S. H., Park, K. H., Park, H. J., Kim, J. W., Moon, I. J., Rhee, C. S., Kim, K. S., Sun, D. I., Lee, S. H., Koo, J. W., Koh, Y. W., Lee, K. H., Lee, S. W., Oh, K. W., Pyo, E. Y., Lee, A., Kim, Y. T., & Lee, C. H. (2010). Prevalence of otolaryngologic diseases in South Korea: Data from the Korea national health and nutrition examination survey 2008. *Clinical and Experimental Otorhinolaryngology, 3*(4), 183-193.

Durand, M., Le Guellec, S., Pourchez, J., Dubois, F., Aubert, G., Chantrel, G., Vecellio, L., Hupin, C., De Gersem, R., & Reychler, G. (2012). Sonic aerosol therapy to target maxillary sinuses. *European Annals of Otorhinolaryngology, Head and Neck Diseases, 129*(5), 244-250.

Frank, D. O., Zanation, A. M., Dhandha, V. H., McKinney, K. A., Fleischman, G. M., Ebert Jr, C. S., Senior, B. A., & Kimbell, J. S. (2013). Quantification of airflow into the

maxillary sinuses before and after functional endoscopic sinus surgery. *International Forum of Allergy & Rhinology, 3*(10), 834-840.

Granqvist, S., Sundberg, J., Lundberg, J. O., & Weitzberg, E. (2006). Paranasal sinus ventilation by humming. *The Journal of the Acoustical Society of America, 119*(5), 2611-2617.

Harbo, G., Grau, C., Bundgaard, T., Overgaard, M., Elbrønd, O., Søgaard, H., & Overgaard, J. (1997). Cancer of the nasal cavity and paranasal sinuses: A clinico-pathological study of 277 patients. *Acta Oncologica, 36*(1), 45-50.

Hilton, C., Wiedmann, T., Martin, M. S., Humphrey, B., Schleiffarth, R., & Rimell, F. (2008). Differential deposition of aerosols in the maxillary sinus of human cadavers by particle size. *American Journal of Rhinology & Allergy, 22*(4), 395-398.

Huang, S. F., Lee, T. J., & Lin, K. L. (2005). Concomitant bilateral orbital and brain abscesses–unusual complications of pediatric rhinosinusitis. *Chang Gung Medical Journal, 28*(1), 51-55.

Hyo, N., Takano, H., & Hyo, Y. (1989). Particle deposition efficiency of therapeutic aerosols in the human maxillary sinus. *Rhinology, 27*(1), 17-26.

Lam, K., Hirsch, A. G., & Tan, B. K. (2014). The association of premorbid diseases with chronic rhinosinusitis with and without polyps. *Current Opinion in Otolaryngology & Head and Neck Surgery, 22*(3), 231-241.

Laube, B. L. (2007). Devices for aerosol delivery to treat sinusitis. *Journal of Aerosol Medicine, 20*(1), 5-18.

Leclerc, L., Pourchez, J., Aubert, G., Leguellec, S., Vecellio, L., Cottier, M., & Durand, M. (2014). Impact of airborne particle size, acoustic airflow and breathing pattern on delivery of nebulized antibiotic into the maxillary sinuses using a realistic human nasal replica. *Pharmaceutical Research, 31*(9), 2335-2343.

Liu, T., Cooper, T., Earnshaw, J., & Cervin, A. (2018). Disease burden and productivity cost of chronic rhinosinusitis patients referred to a tertiary centre in Australia. *Australian Journal of Otolaryngology, 1*(1), 1-9.

Maniscalco, M., Sofia, M., Weitzberg, E., & Lundberg, J. (2006). Sounding airflow enhances aerosol delivery into the paranasal sinuses. *European Journal of Clinical Investigation, 36*(7), 509-513.

Moffa, A., Costantino, A., Rinaldi, V., Sabatino, L., Trecca, E. M. C., Baptista, P., Campisi, P., Cassano, M., & Casale, M. (2019). Nasal delivery devices: A comparative study on cadaver model. *BioMed Research International, 2019*, 1-6.

Moghadam, S. J., Navarro, L., Leclerc, L., Hodin, S., & Pourchez, J. (2018). Toward smart nebulization: Engineering acoustic airflow to penetrate maxillary sinuses in chronic rhinosinusitis. *International Journal of Pharmaceutics, 546*(1-2), 188-193.

Moidee, S. P. (2019). Best practices for safe nasal irrigation. *Free Open Access Medical Education.* Retrieved from https://www.e4ent.com/articles/important-triangles-in-thyroid-surgery/

Möller, W., Lübbers, C., Münzing, W., & Canis, M. (2011). Pulsating airflow and drug delivery to paranasal sinuses. *Current Opinion in Otolaryngology & Head and Neck Surgery, 19*(1), 48-53.

Möller, W., Münzing, W., & Canis, M. (2010). Clinical potential of pulsating aerosol for sinus drug delivery. *Expert Opinion on Drug Delivery, 7*(11), 1239-1245.

Möller, W., Schuschnig, U., Bartenstein, P., Meyer, G., Häussinger, K., Schmid, O., & Becker, S. (2014). Drug delivery to paranasal sinuses using pulsating aerosols. *Journal of Aerosol Medicine and Pulmonary Drug Delivery, 27*(4), 255-263.

Möller, W., Schuschnig, U., Meyer, G., Mentzel, H., & Keller, M. (2008). Ventilation and drug delivery to the paranasal sinuses: Studies in a nasal cast using pulsating airflow. *Rhinology, 46*(3), 213-220.

Pilan, R. R., Pinna, F. d. R., Bezerra, T. F., Mori, R. L., Padua, F. G., Bento, R. F., Perez-Novo, C., Bachert, C., & Voegels, R. L. (2012). Prevalence of chronic rhinosinusitis in Sao Paulo. *Rhinology, 50*(2), 129-138.

Shi, H., Kleinstreuer, C., & Zhang, Z. (2007). Modeling of inertial particle transport and deposition in human nasal cavities with wall roughness. *Journal of Aerosol Science, 38*(4), 398-419.

Si, X. A., Xi, J., Kim, J., Zhou, Y., & Zhong, H. (2013). Modeling of release position and ventilation effects on olfactory aerosol drug delivery. *Respiratory Physiology & Neurobiology, 186*(1), 22-32.

Snidvongs, K., Chaowanapanja, P., Aeumjaturapat, S., Chusakul, S., & Praweswararat, P. (2008). Does nasal irrigation enter paranasal sinuses in chronic rhinosinusitis? *American Journal of Rhinology & Allergy, 22*(5), 483-486.

Suman, J. D., Laube, B. L., & Dalby, R. (1999). Comparison of nasal deposition and clearance of aerosol generated by a nebulizer and an aqueous spray pump. *Pharmaceutical Research, 16*(10), 1648-1652.

Taccariello, M., Parikh, A., Darby, Y., & Scadding, G. (1999). Nasal douching as a valuable adjunct in the management of chronic rhinosinusitis. *Rhinology, 37*(1), 29-32.

von Helmholtz, H., & Ellis, A. J. (1875). *On the Sensations of Tone as a Physiological Basis for the Theory of Music*. London: Longmans, Green and Company.

Wofford, M., Kimbell, J., Frank, D., Dhandha, V., McKinney, K., Fleischman, G., Ebert, C., Zanation, A., & Senior, B. (2015). A computational study of functional endoscopic sinus surgery and maxillary sinus drug delivery. *Rhinology, 53*(1), 41-48.

Xi, J., Si, X., Peters, S., Nevorski, D., Wen, T., & Lehman, M. (2017). Understanding the mechanisms underlying pulsating aerosol delivery to the maxillary sinus: In vitro tests and computational simulations. *International Journal of Pharmaceutics, 520*(1), 254-266.

Chapter 2

Literature review

2.1 Human respiratory system

The human respiratory system is categorised into two sections; the upper and lower airways. The upper airway, also known as the extra-thoracic zone, consists of the nasal cavity (NC), paranasal sinuses, the throat (or pharynx), and larynx (see Figure 2.1 (a)). The oral cavity is also partially related to the upper airway, as it can be used for respiration. The lower airway includes the trachea, bronchi, bronchioles, and alveoli (see Figure 2.1 (b-c)). Gas exchange is the main function of the human respiratory system, which takes place due to the differences in the air pressure between the alveolar spaces and the surrounding air.

The diaphragm is the main muscle of respiration located underneath the lungs, and its contraction enlarges the chest cavity leading to the air pressure in the lungs falling below the surrounding atmospheric pressure. This pressure difference causes the surrounding air to be pushed into the NC from outside, which forms the inhalation process. During inhalation, the

air moves through the main passage of the NC, pharynx, larynx, and trachea, and then enters the bronchi and bronchial tubes and finally reaches the alveoli. Then, the oxygen in the air diffuses into the blood through the walls of the alveoli ducts and the carbon dioxide is diffused from the blood to the alveoli ducts, completing the inhalation process.

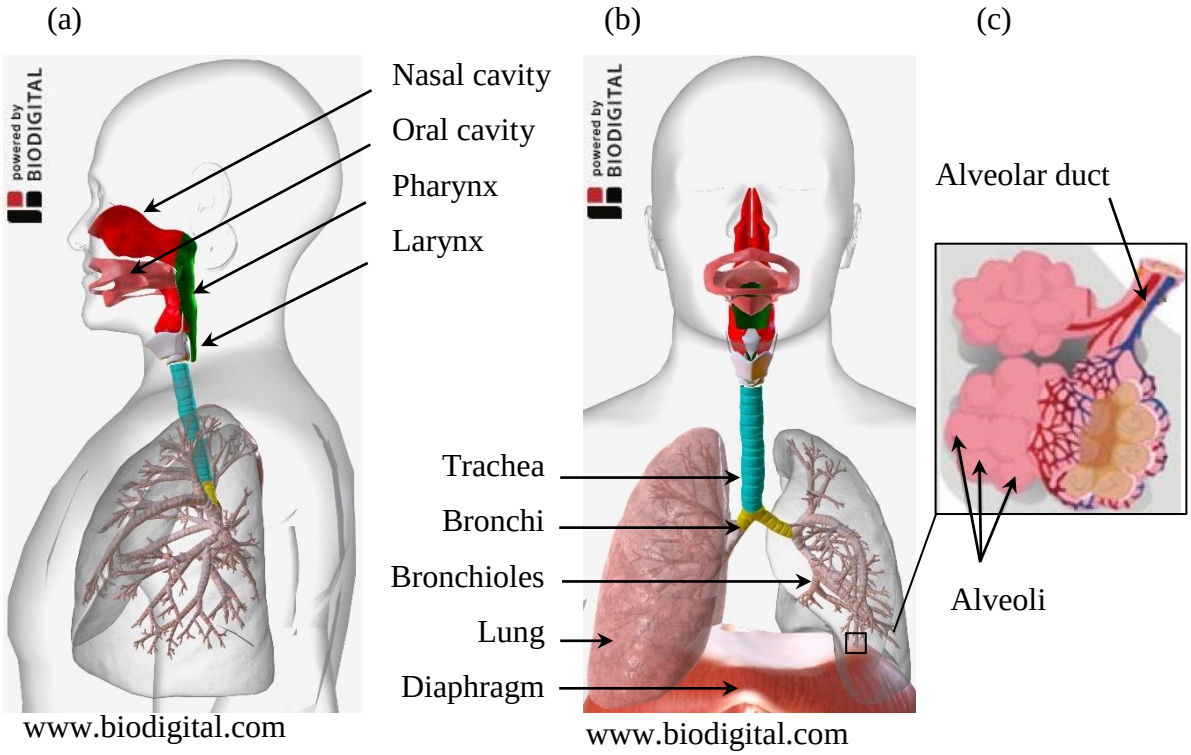

Figure 2.1: Schematic of a human respiratory system (a) sagittal view representing the upper airways including the nasal cavity, oral cavity, pharynx, and larynx; (b) frontal view representing the lower airways including the trachea, bronchi, and bronchioles, lung, and the diaphragm; (c) zoomed-in view of the alveoli and alveolar duct, reprinted from Tu et al. (2013), with permission from Springer Nature.

After completion of the inhalation process, the diaphragm relaxes and the volume of the lung is reduced, leading to higher air pressure in the lung than the atmospheric pressure in the surrounding air. The difference between the air pressure in the lung and the surrounding air causes the air to move from the lung into the NC and, finally, it is expelled through the nostrils, which forms the exhalation process (Stammberger, 1989). The airflow rate during respiration is high or low, depending on the magnitude of the pressure difference between the air in the lung and the surrounding medium (at the nostril).

2.1.1 Anatomy and function of the nasal cavity

The human nose consists of an external and internal sections. The external section is called the nose, which protrudes from the face (see Figure 2.2 (a)). The internal section of the nose is termed the nasal cavity. The nose is the sole part of the respiratory organs that is visible, and located above the upper lip. The nose is a pyramid-shaped structure, which is composed of cartilaginous and bony parts. The superior part of the nose is made of a bony structure and the inferior part is cartilaginous. There are two openings at the base of the nose called nostrils. The nostrils are the gateway of the respiratory system, where the air and aerosols enter the NC to be transported to the lungs. They are separated via cartilage, namely the nasal septum (see Figure 2.2 (b)).

The NC is divided into two parts via a septum forming left and right nasal cavities. These cavities are not symmetrical, although their volumes are approximately equal. The roof of the NC is composed of the frontal bone, nasal cartilages, nasal bones, and the cribriform plate of the sphenoid and ethmoid bones. The cribriform plate is a sieve-like structure that is located between the NC and anterior cranial cavity. The cribriform plate is perforated by several small holes that allow the olfactory nerves to pass from the brain to the roof of the NC. The olfactory nerves are responsible for sending olfactory sensory information to the brain. The floor of the NC includes the horizontal parts of the palatine bones and the palate of the maxilla (Wong et al., 2021). Figure 2.2 represents the different sections of the NC.

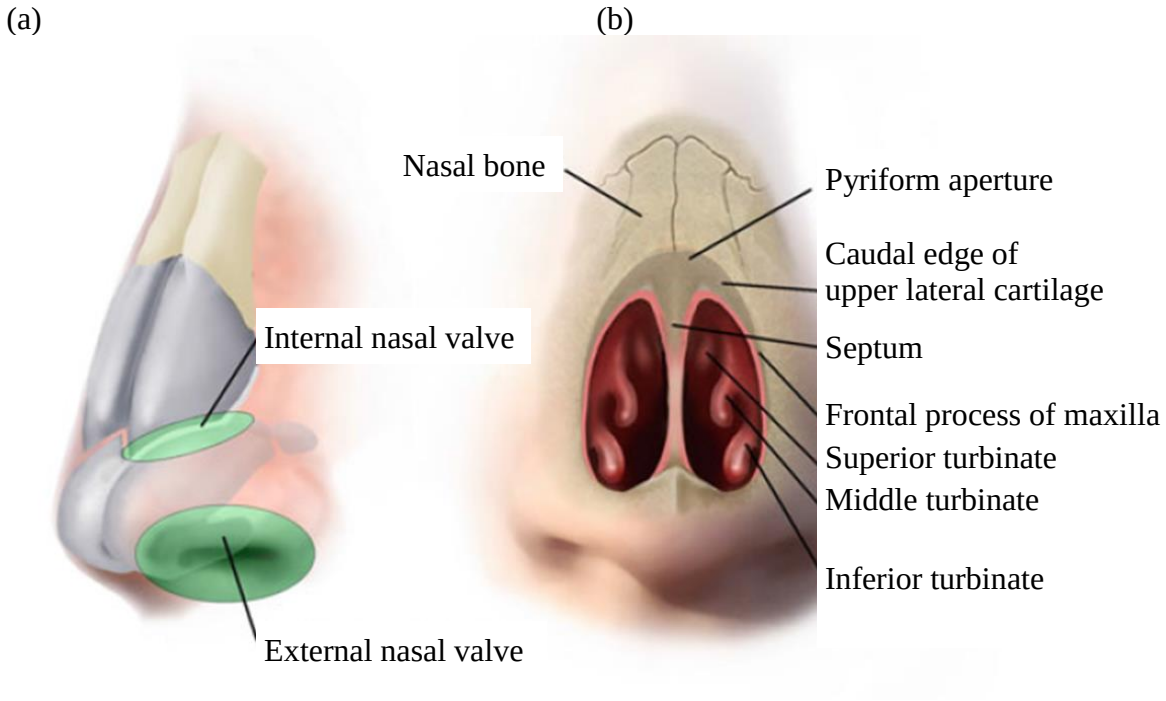

Figure 2.2: (a) Oblique view of the nose; and (b) frontal view of the NC at a frontal cross-section of the internal nasal valve, reprinted from Wong et al. (2021), with permission from Springer Nature.

The schematic diagrams of different regions of the NC are presented in Figure 2.3 (a-f). In each NC, the main airway consists of the vestibule, olfactory, and respiratory regions. The vestibule begins from the nostril opening, extending to the nasal valve, which is the narrowest part of the NC. The region between the nasal valve and the nasopharynx is called the respiratory region, which includes the superior meatus (SM), middle meatus (MM), and inferior meatus (IM), where the paranasal sinuses are attached. The olfactory region, which is located at the roof of the NC, is covered by the olfactory epithelium. The main functions of the NC are temperature adjustment and humidification of the inhaled air, filtering the inhaled air to clean it from foreign particulates and accommodate the olfactory nerve for sensing smells.

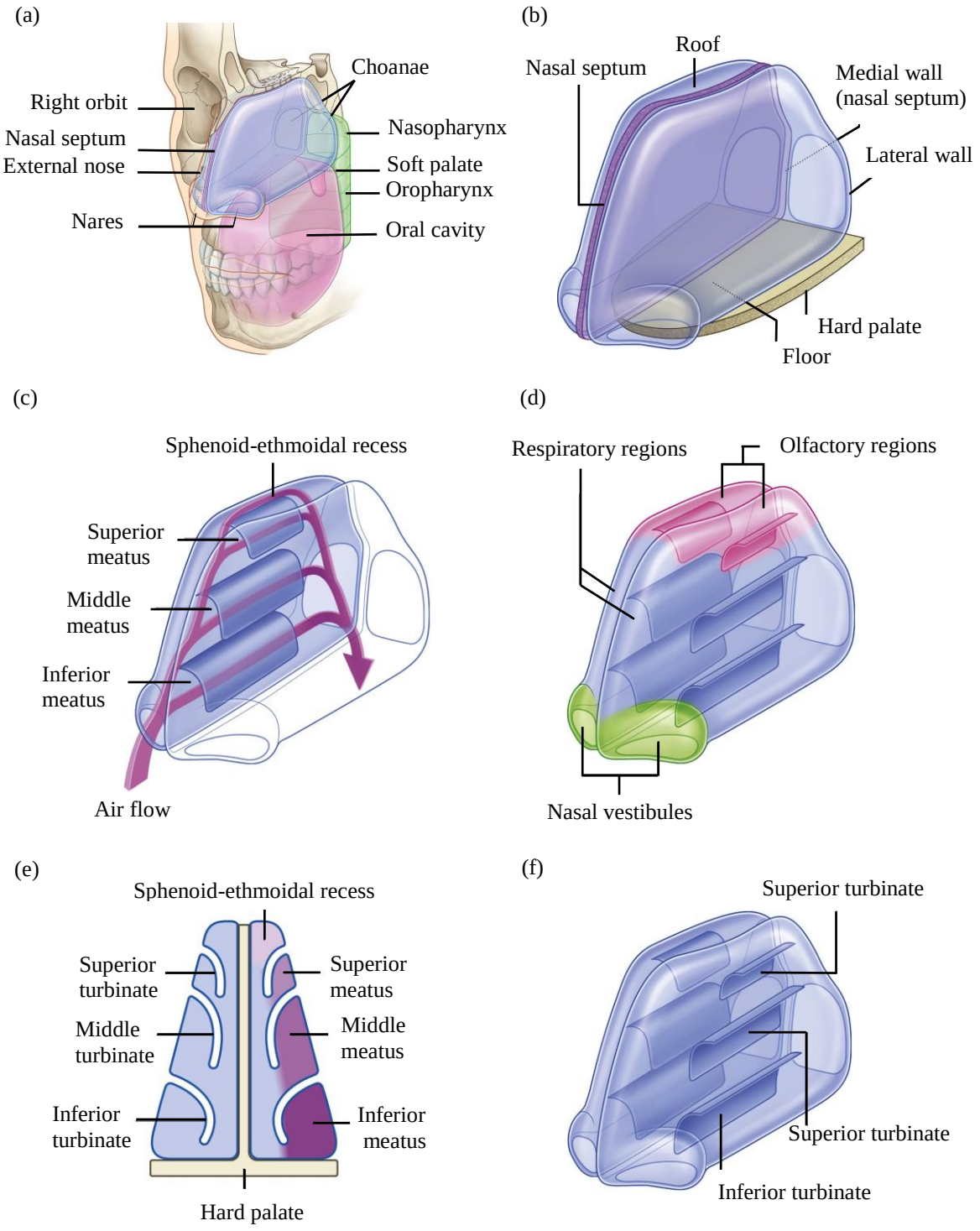

Figure 2.3: A schematic diagram of (a) nasal and oral cavities (isometric view) and their location in the skull; (b) roof, floor, and lateral walls of the nasal cavity; (c) airflow in the right nasal cavity ; (d) nasal vestibule, olfactory and respiratory regions; (e) coronal section of the nasal cavity; (f) turbinates on lateral walls, reprinted from Drake et al. (2020), with permission from Elsevier.

In terms of filtration, the nasal hairs are the initial organs that trap foreign particulates, which enter the NC through inhalation. The subsequent filtration occurs due to the convoluted passage of the airflow through the complicated anatomy of the NC. To be more specific, the direction of the airflow turns from vertical at the vestibule to horizontal at the nasal valve, then the airflow passes through the complicated anatomy of the meatuses, where the deposition of particulates is increased on the wall of the NC (see Figure 2.3 (c-d)). The deposited particulates are transported to the nasopharynx via mucociliary transport, to be swallowed and enter the stomach (Randell et al., 2006).

The surface of the main airway of the NC (i.e., the surfaces of SM, MM, and IM) is covered by a ciliated epithelium, which consists of different layers. The upper layer of the epithelium is lined by jelly mucus, located on the watery saline layer covering the cilia (see Figure 2.4), which beat 7-8 times per second (Zhou et al., 2009). The viscoelastic characteristic of the cilia enables the conversion of the energy from beating to transport of the mucus toward the nasopharynx (see Figure 2.4). About 125 mL of mucus is produced per day, which transports continuously towards the nasopharynx at a speed of 1-2 cm/h (Illum, 2003; Mistry et al., 2009; Ugwoke et al., 2005).

Although mucociliary transport is a vital mechanism in the filtration process, it negatively impacts the efficiency of nasal drug delivery, since it transports the deposited medication to the gastrointestinal system. This reduces the time for the medication to be diffused into the blood (F. Fry et al., 1973; Schmidt et al., 1998). Recently, the use of medications employing polymer-coated nanoparticles has demonstrated an increase in the efficiency of the diffusion of the drug particles into the blood after deposition on the wall of the NC and sinuses (Illum, 2012).

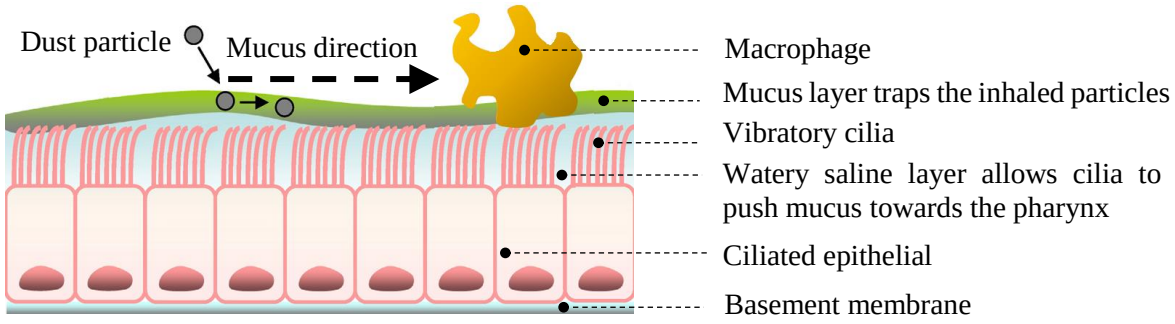

Figure 2.4: An overview of the structure of the nasal mucosa and the mechanism of mucociliary transport, reprinted from Zhang et al. (2011), with permission from Elsevier: a minor modification has been applied to the original figure in terms of labelling and particle trajectories.

2.1.2 Paranasal sinuses

An NC is surrounded by sphenoid sinuses (SS), ethmoid sinuses (ES), frontal sinuses (FS), and maxillary sinuses (MS). Figure 2.5 (a-b) shows the paranasal sinuses and their location in the skull. The sinuses are hollow cavities that are filled with air and are named after their surrounding bones. The sinuses are coated with mucus to protect the NC from drying out. SS are developed after adolescence. SS are two hollow cavities contained in the sphenoid bone, which is located between the eyes and behind the nose. ES, which are present at birth and develop with the body's growth, are a collection of small cavities surrounded by spongy ethmoid bone, located in the superior portion of the nose and between the eyes. FS, which are developed after the age of seven, are situated above the eye sockets (orbit) and behind the brow ridges. MS are the most voluminous of the paranasal sinuses and are situated on either side of the nose, above the teeth and underneath the cheeks. MS, which are not equal in size, exist at birth and develop throughout childhood to reach their final size at around the age of seventeen or eighteen. The MS are connected to the NC through a narrow channel called the ostium.

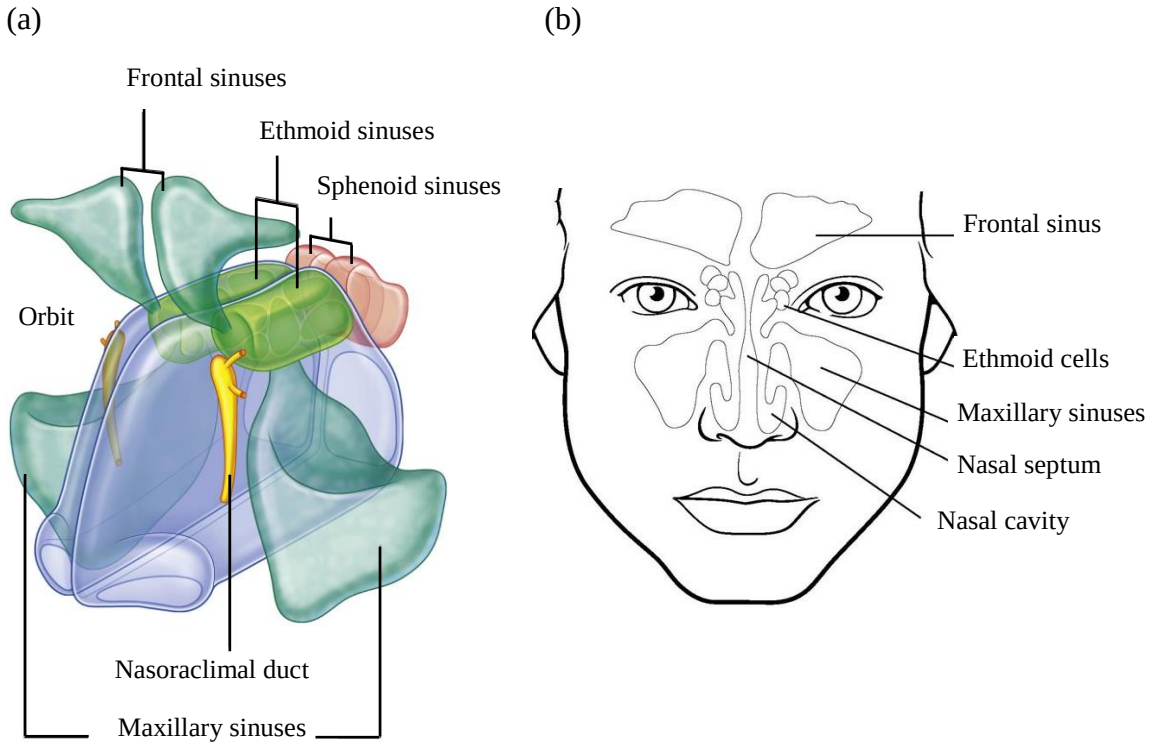

Figure 2.5: (a) A schematic diagram of the nasal cavity and paranasal sinuses (isometric view), reprinted from Drake et al. (2020), with permission from Elsevier; (b) coronal section represents the paranasal sinuses (frontal view), reprinted from Singh et al. (2017) with permission from Medscape Drugs & Diseases.

The main functions of the paranasal sinuses are as follows: lightening the skull, resonating speech sounds, and producing lysozyme, which protects the nasal mucus from bacterial infections (Boysen, 1982; Tu et al., 2012). One of the first reliable figures of the paranasal sinuses was drawn by Leonardo da Vinci in 1489. His drawing had good agreement with a contemporary figure of the paranasal sinuses (Crowe, 2005). Later on, in 1651, an accurate illustration of the MS was introduced by Highmore, called the antrum (hollow) of Highmore (Blanton et al., 1969). In ancient times, the secretions coming from the nose were suspected to stem from the brain, then flow into the NC; however, Schneider found that the secretions coming out from the nostril are produced by the sinuses' mucosa, which could be due to chronic rhinosinusitis (CRS) (Stammberger, 1989).

2.1.3 Chronic Rhinosinusitis

Chronic Rhinosinusitis (CRS) is a prevalent disease related to the human nose, originating from inflammation of the mucosa in the sinuses and the NC. According to the American Academy of Otolaryngology-Head and Neck Surgery, CRS refers to a condition where the symptoms of the inflammation exist for more than 12 weeks in a year, while persistence of symptoms for durations of 4 weeks and 4-12 weeks are defined as acute and subacute rhinosinusitis, respectively (Rosenfeld et al., 2007). To diagnose CRS, at least two of the following symptoms should be observed: facial fullness (70-85%), hyposmia (61-69%), nasal secretions (51-83%), and obstruction of the NC (81-95%) (Meltzer et al., 2004; Rosenfeld et al., 2007).

Historically, it was believed that CRS originated from bacterial infection as a result of obstruction of the sinus ostium. However, it is currently understood that CRS occurs due to different predisposing factors, such as local host factors (e.g., polyps, obstruction of the nasal anatomy, and tumours), environmental factors, (e.g., bacteria, pollution, fungi, and allergens), general host factors (e.g., immune deficiency, cystic fibrosis, defects, and genetics) (Marple et al., 2009; Rosenfeld et al., 2007). In fact, CRS, rather than being a single disease, is a group of symptoms stemming from different reasons, which has a prevalence ranging from 4.9-10.9% of the world population (Bhattacharyya, 2012; Cho et al., 2010; T. Liu et al., 2018; Pilan et al., 2012).

The available methods for the treatment of CRS are topical drug delivery, systemic drug delivery, and sinus surgery (Moghadam et al., 2018). The choice of a treatment method depends on several factors, such as the severity of the disease and nasal anatomy, as well as the patient’s compliance. Corticosteroids, saline nasal douching (nasal irrigation), and antibiotics form the primary treatments associated with the medical management of CRS

(Benninger et al., 1997; Lund, 2005). However, for drastic cases where the CRS-related disorder affects the quality of life of the patients, functional endoscopic sinus surgery (FESS), with a success rate of 70-90% is exercised (Iro et al., 2004; Stammberger et al., 1990). Figure 2.6 (a-b) illustrates computed tomography (CT) images of CRS before and after surgery. This Figure shows that the infections in the MS (see Figure 2.6 (a)) were removed completely after FESS (see Figure 2.6 (b)).

Post-surgical treatment is crucial for FESS. Insufficient post-surgical treatment may lead to an additional surgery or more and the entire treatment may be unsuccessful (Moghadam et al., 2018). Using a topical steroid spray for long-term treatment, a reduction in the inflammation of the sinuses and NC and an improvement of the symptoms of the CRS have been achieved (Grzincich et al., 2004; Lund, 2005). Using topical daily nasal steroids results in reducing the side-effects; however, long-term use of this medication leads to significant adverse side-effects (Gillespie et al., 2004; Grzincich et al., 2004). Therefore, it is crucial to develop a targeted drug delivery (TDD) technique to increase the efficiency of the drug delivery to the NC and sinuses and obtain the minimum number of adverse side effects. In the following sections, the available TDD techniques were reviewed in detail and the most efficient and promising technique for increasing the drug delivery to the MS was identified.

(a) (b)

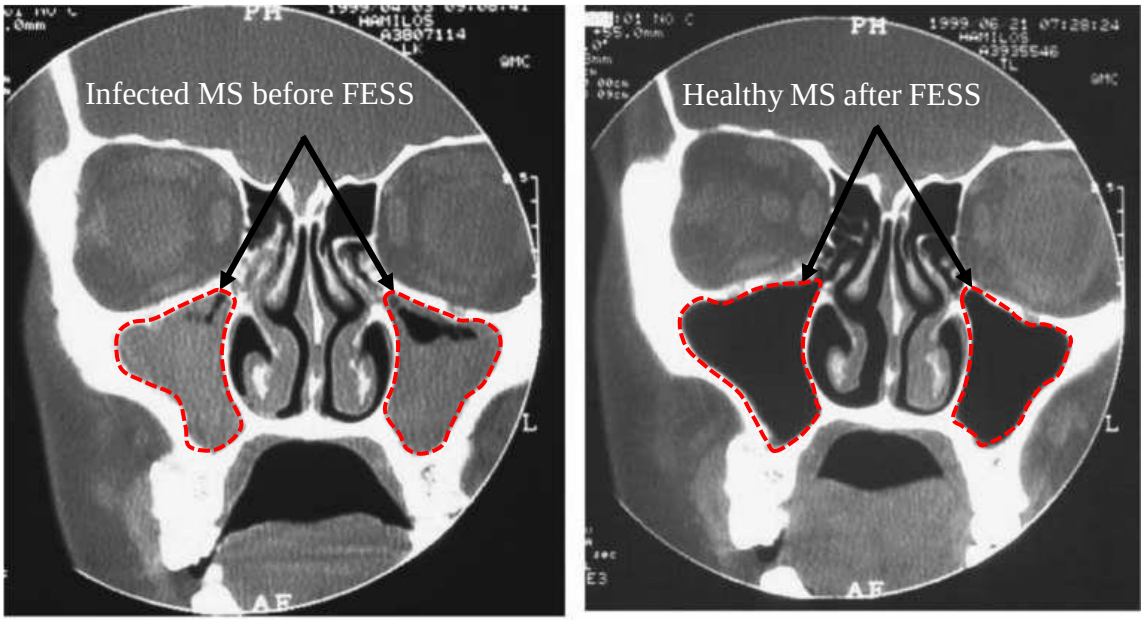

Figure 2.6: Frontal view of the NC of a CRS patient (a) before; and (b) after functional endoscopic sinus surgery (FESS), reprinted from Hamilos (2011), with permission from Elsevier.

2.2 Targeted drug delivery

In the conventional drug delivery method, medications are usually either injected into the blood circulation system or taken orally, known as systemic drug delivery. In this method, the drugs are not distributed topically but are distributed throughout the entire body. Such a drug distribution can damage healthy tissue and cells, which counts as an adverse side-effect. To avoid some side-effects, targeted drug delivery (TDD) provides an alternative smart technique for delivering medications to the human body, in which the concentration of the medications in a target site is greater than for other locations within the body.

In TDD, the medications are guided to the diseased tissue/cells and the healthy tissue/cells are less-likely to be affected, leading to a significant reduction in adverse side-effects. Reducing the adverse side-effects is crucial in many diseases such as in cancer therapy

and is advantageous in the treatment of diverse illnesses, such as nervous system disorders, sudden hearing loss and so on (YaLi Liu et al., 2019; Rosenblum et al., 2018; Shapiro et al., 2014; Venugopal et al., 2017). The main drawbacks of TDD are its cost and sometimes the complexity of instruments and the discomfort of patients.

The main aim of the TDD is to provide a safe, longer, localised and targeted interaction between the drug and diseased cells or tissues. In TDD, the medications are released at or delivered to a target site in the form of dosage, but in conventional drug delivery, the medications are absorbed through the biological membranes (Tan et al., 2015). For example, in chemotherapy, about 1% of the medications administered reach the tumour location, while 99% of the therapeutic agents are distributed to other locations in the body, which can damage healthy organs (Trafton, 2009). Hence, it is important to develop and use an efficient TDD for the treatment of such localised diseases (Bertrand et al., 2012).

The NC possesses a large vascularized surface area, which makes it an excellent choice for administration of pharmaceutical drug particles for treatment purposes (Suman, 2013). The NC is also the best route for the topical delivery of aerosolised medications in the treatment of local ailments related to the paranasal sinuses and the nose, such as CRS and allergic rhinitis. Moreover, the NC is an attractive pathway for systemic drug delivery and needle-free vaccination, especially when rapid effectiveness and quick absorption are required (Djupesland, 2013). For most drug delivery purposes, in which the medications are used for vaccines, local action, and systemic absorption, a broad drug distribution on the surfaces of the mucosal NC appears suitable (M. Vidgren et al., 1998). However, for some diseases, such as nasal polyposis and chronic rhinosinusitis, TDD to the SM and MM is more desirable because the nasal polyps originate from the SM and the ostium of the MS is located

in the MM (Laube, 2007). For cases where nose-to-brain delivery is required, TDD to the olfactory region is believed to be necessary (Aggarwal et al., 2004).

To perform TDD, it is important to account for the following criteria: the disease, the pathway considered for the delivery of the medication, the characteristics of the drug, the potential adverse side-effects, and the targeted organ. TDD is usually classified into two categories: passive targeting and active targeting (Hadilou et al., 2018; Lewis Jr et al., 2007; Sengupta et al., 2018). These TDD approaches are explained and reviewed in the following sections.

2.2.1 Passive targeting

In nasal drug delivery using the passive targeting approach, the medications are directed to a target site in the airways (such as the lung, nasal cavity, MS, olfactory regions, etc.) by modification of the dosage of the medication, size of the droplets (e.g., aerosol), the timing of the injection of the aerosolized medications, inhalation flow rate (breathing pattern), and the inhaled gas density (Dolovich et al., 2011). Several different methods/devices are available that exploit the passive targeted drug delivery (PTDD) approach for drug delivery to different parts of the NC, sinuses, and olfactory regions. These methods/devices are briefly described in the following sections and the most efficient PTDD method for drug delivery to the NC and MS is identified.

2.2.1.1 Drop delivery with a pipette

Delivery of drops and vapour to the nose is one of the oldest nasal drug delivery techniques that use the PTDD approach. Historically, drops of breast milk were dripped in an infant's nose to treat nasal congestion, and methanol vapour was used to awaken fainted people (Djupesland, 2013). Although the drops have mostly been switched to metered-dose spray

pumps, inexpensive and over-the-counter saline and decongestants are still produced in the form of blow-fill-seal pipettes. Drop delivery is an efficient method for treating polyps, since the drug liquids need to be delivered to the MM where the polyps usually appear (Keith et al., 2000; Penttilä et al., 2000). Although drop delivery is an efficient PTDD technique for the treatment of some diseases such as polyps, it results in discomfort since the patient must locate themselves in a head-down body position to assist with the deposition of drops driven by gravity (Aggarwal et al., 2004). Using this method of drug delivery is not prescribed for patients suffering from CRS because the head-down position causes increased headaches and inconvenience (Merkus et al., 2006).

2.2.1.2 Liquid delivery with a rhinyle catheter

Liquid delivery to the NC using a rhinyle catheter and squirt tube is a simple drug delivery method such that the medications (in the form of a liquid) are deposited at the target site by inserting the tip of a micropipette or a catheter into the target site and squirting the drug liquid into that region. This method is usually employed in animal studies, when they are sedated. It can also be used for drug delivery in the human NC, even without sedation, but care should be taken to avoid direct contact with the vulnerable mucosal layer (Bakke et al., 2006). However, this drug delivery technique is not convenient for patients if self-administration is required.

Using 200 µl of liquid desmopressin, Harris et al. (1986) investigated the effect of a pipette and rhinyle catheter on drug absorption in the NC for the treatment of diabetes insipidus. For the rhinyle catheter, the liquid medication was placed into a thin plastic tube. A dropper was designed and located at one end of the tube and the other end of the tube was designed such that it fitted the mouth for blowing. The tube with the dropper was placed into the nostril where the medication was injected into the NC in forms of the drops or liquid-jet

driven by blowing into the other end of the tube (Harris et al., 1986). Using gamma scintigraphy, they found that the drug absorption in the target site after using the rhinyle catheter was greater than that after using the pipette (Harris et al., 1986). Nonetheless, given the considerable low accuracy of this method in terms of dosing and due to its cumbersome process, it is neither an attractive nor a popular method of nasal drug delivery.

2.2.1.3 Squeeze bottles

Squeeze bottles are simple devices composed of a plastic bottle that is partly filled with the drug and air, and a nozzle for expelling the liquid drug. The nozzle is located in the nostril and, when the plastic bottle is squeezed, the liquid is injected into the nose. The dose of the liquid injected to the nose changes with the force applied to squeeze the bottle. Then, releasing the pressure used for squeezing the bottle creates suction to draw the nasal discharges into the bottle, where dried nasal mucus and infections in the nose can be suctioned into the bottle and infect the liquid medication in the bottle (M. Vidgren et al., 1998). The squeeze bottle is a convenient, efficient, and simple device for the treatment of typical nasal congestions using over-the-counter decongestants. However, because 90% of the atomised medication deposits on the anterior region of the NC, such as the nasal valve, and due to the inconsistent doses of injected medications, it is not an efficient method for the treatment of severe nasal diseases such as CRS (Newman et al., 1987, 1988). For efficient treatment of CRS, a considerable amount of the administered drug should be transported beyond the anterior region.

2.2.1.4 Multi-dose spray pumps

Multi-dose spray pumps dominate the market for nasal drug delivery. They were first introduced about 40 years ago. They usually generate small particles (fine droplets) at a size of 50-100 μm and sprinkle 0.25-2 ml of the medication per spray (Moffa et al., 2019). In this

method, the geometry of the spray plume and the size of the particles can alter depending on factors such as the characteristics of the actuator orifice, the force implemented on the pump, and the viscosity of the medication (M. Vidgren et al., 1998).

The multi-dose spray pump has been demonstrated to be an efficient method for the delivery of corticosteroids for the treatment of seasonal allergic rhinitis and nasal polyps (Berger et al., 2007; Newman et al., 1987). To keep the conformity of the required dose, multi-dose spray pumps should be slightly overfilled and require some degree of priming. Hence, they are not well-suited for expensive vaccines and medications, which require careful control of the dose and single-administration. For such applications, single-dose or dual-dose spray pumps are recommended (Mutsch et al., 2004; Nichol et al., 1999).

In general, conventional devices, including pipettes, rhinyle catheters, squeeze bottles and spray pumps, are not efficient PTDD methods for delivering drugs to a target site, especially to the sinuses, since most of the drug deposits in the anterior region (i.e., the nasal valve), septum and the nasopharynx (Suman, 2013). Using multi-dose spray pumps, several *in-vivo* studies examined the efficiency of these devices for drug delivery to the NC. By using gamma scintigraphy technology, they demonstrated that a very small portion (<10%) of the injected aerosols reaches the posterior region of the NC, middle and superior meatuses, and the paranasal sinuses, since a significant portion of the aerosols is deposited in the anterior part of the NC (Hardy et al., 1985; Harris et al., 1988; Newman et al., 1987, 1988; Thorsson et al., 1993; P. Vidgren et al., 1991).

The deposition of the most aerosols in the anterior part of the NC when using spray pumps is not only due to the large particle size (50-100 µm) but also because of the mismatch between the spray plume geometry and the geometry of the anterior part of the NC, such as the nasal valve. When the spray pump is actuated by an external force acting on it, the

medication (in the form of liquid) flows into the swirl chamber, then comes out through the nozzle located at the tip of the spray pump (Inthavong et al., 2008). Due to the radial and axial velocities of the egressed liquid, a swirling cone-shaped sheet is formed at the proximity of the nozzle, which breaks up into ligaments after a short distance (known as the break-up length) and then the particles are generated (see Figure 2.7 (a-b)) (Shrestha et al., 2020). It should be noted that the particles are mainly generated at the margin of the cone-shaped geometry (known as the spray plume).

The performance of the spray plume, which affects the particle deposition pattern in the NC, is highly influenced by the following key factors: the swirl intensity, the break-up length, nozzle diameter, and the cone angle of the spray. Using CFD simulation, Inthavong et al. (2008) estimated the diameter of the cone-shaped plume of a nasal spray at the break-up point. For a spray with a cone angle of 30°, nozzle diameter of 0.5 mm, and a break-up length of 3.5 mm, they estimated the diameter of the spray cone as 4 mm (Inthavong et al., 2008). In an *in-vitro* study, Suman et al. (2006) measured the smallest diameter of the spray cone of a spray pump with a spray angle of 54.6° at a specific distance from the nozzle. They reported that the spray cone diameter at a distance of 25 mm from the nozzle was obtained as 30.8 mm and at a distance of 10 mm from the nozzle it is 19.2 mm (Suman et al., 2006). Hence, even though the tip of the nasal pump is inserted in the nose at a distance of 10-15 mm from the nostril, the spray plume size (with diameter≈20 mm) and shape are mismatched with the narrow nasal valve, which has a triangular shape and a hydraulic diameter of 4-10 mm (Hosseini et al., 2020). Therefore, because most of the particles are at the margin of the cone-shaped plume, a significant number of particles deposit in the anterior region, especially in the nasal valve, resulting in a low deposition in the posterior region, such as the middle meatus and sinuses.

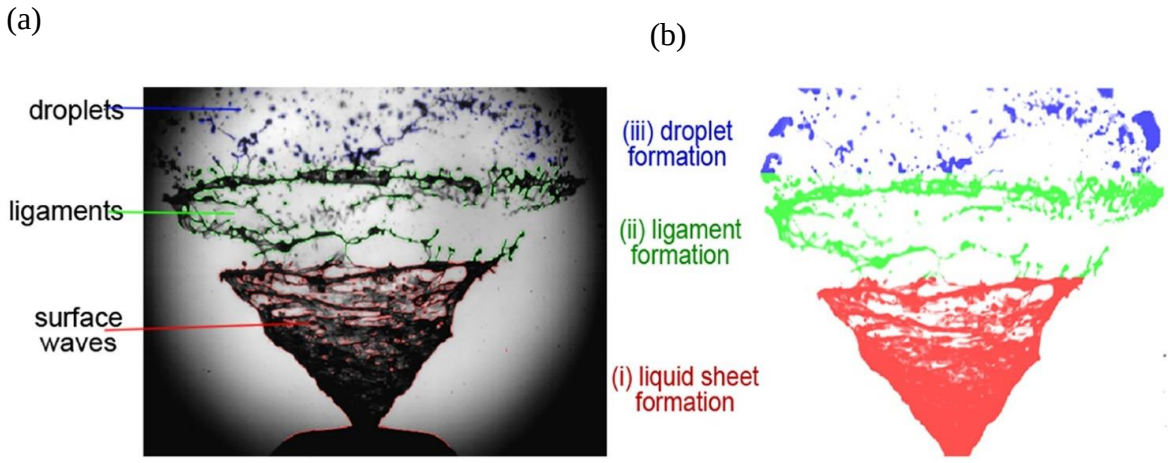

Figure 2.7: (a) Raw image of the formation of spray; (b) post-processed image of the formation of spray, adapted from Spray plume development during pre-stable phase by Shrestha et al. (2020), licensed under CC BY 4.0.

2.2.1.5 Nebulizers

To overcome the issue of the large particles (50-100 µm) associated with nasal spray pumps, nebulisers are used. Nebulisers generate fine aerosol particles within a range of 1-30 µm using mechanical power or compressed gasses (Wofford et al., 2015). Nebulisers have been demonstrated to have a higher efficiency of drug delivery to the superior meatus, middle meatus, and paranasal sinuses when compared with spray pumps, which is primarily due to the smaller particle size and slower speed of the aerosols (Hilton et al., 2008; Laube, 2007). Given the very small size of the nebulised particles, more than 60% of the administered medications are transported to the posterior region, which implies that nebulisers are the most efficient PTDD devices for drug delivery to the paranasal sinuses and olfactory regions (Suman et al., 1999).

2.2.2 Active targeting

Using an active targeting drug delivery (ATDD) approach, the efficiency of drug delivery can be significantly increased when compared with the PTDD approach. Several different methods can be adopted to accomplish active targeting. One way is to identify the features of

the receptor on the targeted cancer/tumour cell to be able to use the cell-specific ligands that can be conjugated to the drug-loaded nanoparticles. Then, the nanoparticles will be able to attach to cancer/tumour cells having the complementary receptor (Galvin et al., 2012). As a result, the amount of medications delivered to the target site increases significantly when compared with the passive method where non-ligands-conjugated nanoparticles are used.

Furthermore, a triggering mechanism that is specifically associated with the target region can be utilised to accomplish active targeting. For example, pH-responsive materials can be used as the drug-carrier nanoparticles. More specifically, the pH level is almost neutral in most of the body; however, in some regions of the body, the pH level is more acidic. Hence, using pH-responsive materials enables the drug-loaded nanoparticles to release the medications when they reach a region with a specific pH level (Galvin et al., 2012). In addition to the abovementioned methods for implementation of active targeting, which are mostly associated with chemical and biological factors, some physical and environmental resources, such as magnetic, electric, and acoustic fields, can also be used as the triggering mechanism to deliver medication to a targeted site actively (Vasir et al., 2005). The available ATDD methods are briefly described in the following sections.

2.2.2.1 Magnetic drug delivery

The first use of magnetic fields in disease treatment goes back to 1941, when Gilchrist et al. (1957) designed an *in-vitro* experiment to investigate the thermal effects of small magnetic particles (Fe_2O_3) on lymph nodes for cancer and tumour therapy. They injected magnetic microparticles into the body and then applied an electromagnetic field to increase the temperature of the particles, using hysteresis loss, to destroy the tumour/cancer (Häfeli, 2004). Later on, in the 1970s, when microparticles coated with polymer were first developed, magnetic drug targeting (MDT) using drug-loaded microparticles attracted great attention

from many researchers seeking to elaborate on drug delivery options to targeted sites. MDT is an active targeting approach, in which an external magnetic field manipulates the magnetic drug carriers (MDCs) to deliver a drug to targeted locations in the body and retains them there (see Figure 2.8). The MDCs contain the magnetic substances that react to magnetic fields, such as ferric oxide nano/microparticles. Transmission of the magnetic fields through the body is safe, which enables the manipulation of MDCs to target locations at deep tissue level (YaLi Liu et al., 2019).

The first clinical trial of MDT was carried out in 1996 for the treatment of tumours, when a magnetic field with a density of 0.8 T was located at the vicinity of the skin surface to concentrate drug-loaded magnetic nanoparticles (Lübbe et al., 1996). Since then, over the past two decades, many researchers have focused on MDT for the treatment of cancer/tumours and other diseases (Bose et al., 2013; Hedayati et al., 2018; Larimi et al., 2016; Lübbe et al., 1996; Mathieu et al., 2006; Riegler et al., 2011; Riegler et al., 2010; Shapiro et al., 2014).

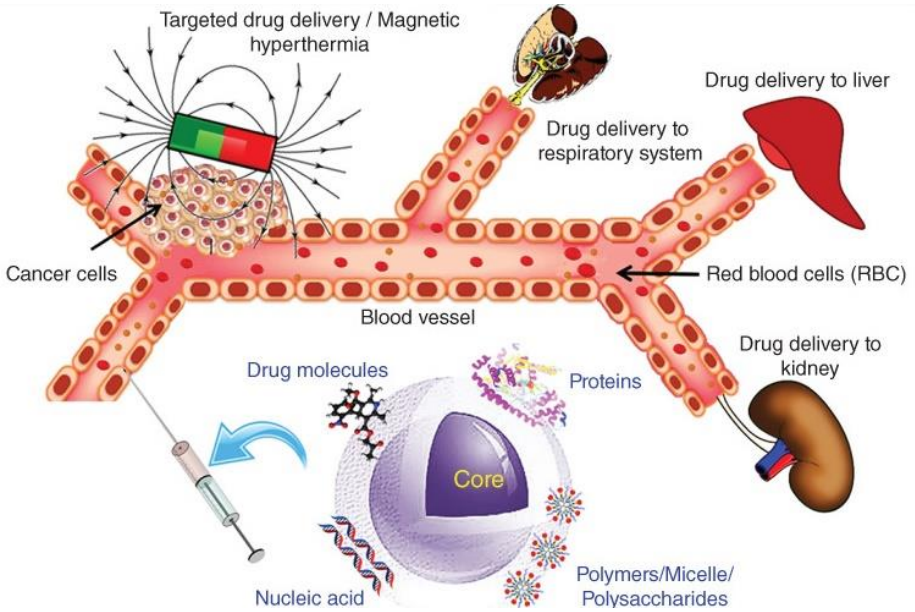

Figure 2.8: Magnetic drug targeting in the recirculation system for killing cancer cells, reprinted from Mondal et al. (2018), with permission from John Wiley and Sons.

Most previous studies of MDT have involved drug delivery to diseased sites associated with the blood circulation system, where the drug-loaded particles are injected into the artery or vein and are transported in the blood flow (see Figure 2.8). For MDT through the blood circulation system, the viscous drag force implemented by the blood flow must be overcome by the magnetic force acting on the particles under the effect of the external magnetic field so that the drug-loaded particles are not passed away from the target location (Ally, 2010).

Given that the only fluid surrounding the particles in the blood circulation system is the blood, the mechanisms of both the deposition and the retention of the particles at the target location are similar. However, MDT is more complicated for drug delivery through the airways (from the mouth/nostril to the lung) because of the drug-loaded magnetic particles that are suspended in the airflow (gas phase) deposit on the walls of the airways, which are lined by a mucus layer (liquid phase). When a drug particle deposits on a mucus-lined wall, it moves towards the nasopharynx under the effect of the mucociliary transport mechanism; however, in the blood circulation system, the walls of the arteries are not lined with a mucus layer where the deposited particles do not move. Therefore, in practice, the deposition and retention of particles in the airways should be considered separately when MDT is used, which makes MDT in the respiratory system more complicated than MDT in the blood circulation system.

Ally (2010) investigated the effect of magnetic fields on the deposition and retention of polymer-coated magnetic microparticles on the wall of a pipe, to emulate the trachea. In their study, a thin layer of agar was coated on the wall of the target site to simulate the mucus layer; also, a very thin layer of water was caused to flow above the agar bed with a very slow velocity (0.1 mm/s) to simulate the transportation of mucus. They demonstrated that a high-

gradient magnetic field is needed for the deposition of particles in the lung. They reported a negligible particle deposition using a uniform magnetic field. Pourmehran et al. (2016) used a realistic lung model consisting of the oral cavity, larynx, pharynx, trachea, and six generations of the lungs to investigate the deposition pattern in human tracheobronchial airways under the effect of an external magnetic field using computational fluid dynamics (CFD) modelling. They developed the optimal magnetic drug characteristics and magnetic source coordinates for efficient magnetic drug delivery in human airways, where the efficiency of drug delivery to the second bifurcation of the left lung (the targeted site) was increase more than 80% when compared with conventional drug delivery without the application of the MDT.

Xi, Zhang, et al. (2015) used numerical modelling to investigate the effect of a magnetic field on drug delivery to the olfactory region, where the medications can directly enter the brain, for treatment of diseases associated with the brain and spinal cord. They demonstrated that by using a well-designed MDT system (see Figure 2.9), the efficiency of drug delivery to the olfactory region increased 64-fold compared with conventional drug delivery that did not have a magnetic field. However, due to the complexity of the NC anatomy and the secluded location of the sinuses, the implementation of MDT for drug delivery to the sinuses is likely to be more complicated, for which no previous study has been conducted.

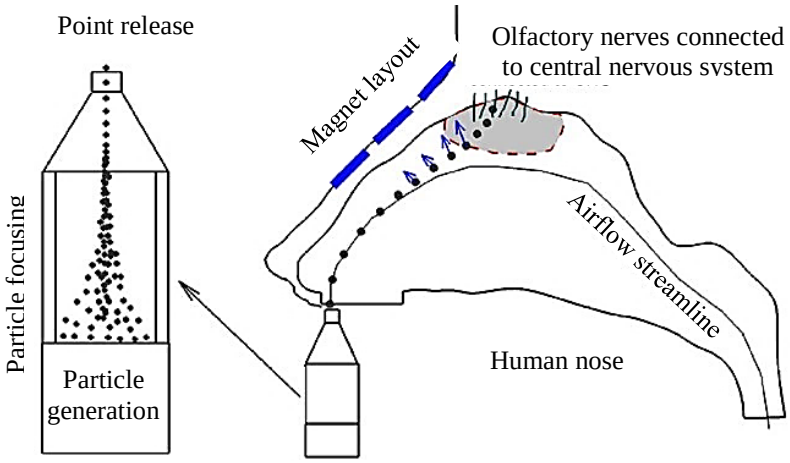

Figure 2.9: Schematic of magnetic drug targeting to the olfactory region, reprinted from Xi, Zhang, et al. (2015), with permission from Dove Medical Press.

2.2.2.2 Electrically-charged particle (drug) delivery

Electrically charged particle (drug) delivery (ECDD) is an ATDD approach, which can only be implemented in the respiratory system. In ECDD, a set of electrodes are located in a specific region outside the body with a well-designed configuration. The drug particles are charged electrically, then released into the NC through the nostril. The charged particles are directed to a target region using the electrostatic forces acting on them through the external electric fields. In the process of the generation of aerosol, electrical charges can be induced through conduction or induction. An atomizer usually produces aerosol droplets that are highly charged (Bologa et al., 2001). Also, for inhaled pharmaceutical powders, the fine particles are in contact with the wall of the device and with each other. Due to the different potentials of the surfaces, such contacts cause the particles to become charged through electron exchange (Karner et al., 2011). ECDD cannot be applied to the circulation system because the blood discharges the particles. The transport and deposition patterns of the inhaled aerosols highly depend on the electric charges carried by the particles. Since humidity dissipates the electric charges of individual particles, the electrostatic effects of the charges carried by particles are likely to be significant in the upper airways, where the humidity is less than in the lower airways.

The concept of using electrically charged particles to increase particle deposition in human airways was first proposed by Wilson (1947). Later on, Vincent et al. (1981) used mechanical dispersion to charge fibrous asbestos up to a relatively moderate level. Then they exposed rats to these charged particles to investigate the particle deposition in the rats' lungs. They reported an enhancement in particle deposition in rats' lungs after inhaling the fibrous asbestos dust. Ferin et al. (1983) showed that the retention of the particles in the rats' lungs could be enhanced significantly when they inhaled charged polymetric particles. Using an ECDD in clinical studies, Melandri et al. (1983) and Prodi et al. (1985) reported an enhancement in the aerosol deposition in the airways of humans after inhaling charged pharmaceutical particles.

In addition to ECDD to the lung and upper airways, the system has also been considered for nasal drug delivery (F. Fry, 1970; Xi et al., 2014). Using numerical modelling, Xi et al. (2014) conducted a feasibility study to investigate the effect of external electric fields on drug delivery to the olfactory region. They injected particles (500 nm in diameter) with a point-released injection pattern at the nostril, where the particles were directed to the olfactory region using external electrodes located at specific locations on the nose skin. By implementing appropriate electrophoretic guidance, they demonstrated a significant increase in the deposition of particles in the olfactory region, in which 90% of the injected particles were deposited in the olfactory region, while the deposition fraction for uncharged particles was less than 1% (Xi et al., 2014).

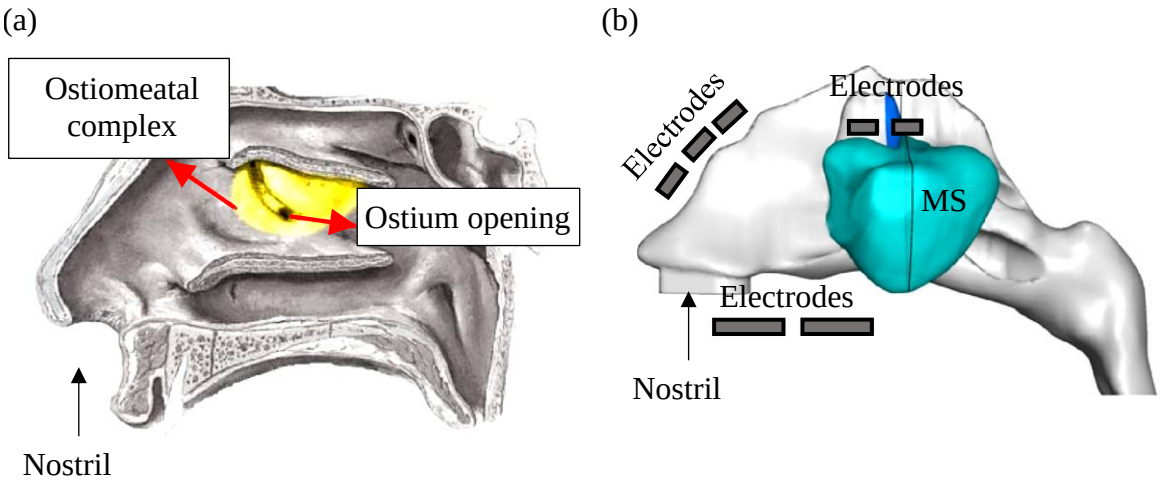

Figure 2.10: (a) The location of OMC and ostium opening in an NC; (b) schematic of electrode layouts for drug delivery to the ostiomeatal complex (OMC) using ECDD, reprinted from Xi, Yuan, et al. (2015), with permission from Dove Medical Press.

In another study, Xi, Yuan, et al. (2015) examined the effect of external electric fields on drug delivery to the ostiomeatal complex (OMC), which is important for drug delivery to the MS (see Figure 2.10 (a-b). Since the MS is connected to the NC through the ostium, which is located in the OMC, an increase in drug delivery to the OMC can contribute to increasing the efficiency of drug delivery to the MS. Using an optimised design of the electrodes generating the desired electric field (see Figure 2.10 (b)), they demonstrated that the deposition of electrically charged particles in the OMC can be increased up to 10-fold when compared with conventional nasal drug delivery methods. To summarise, although electrically charged particle delivery is an effective ATDD method for increasing the particle deposition in the OMC, it cannot deliver drug particles into the MS (Xi, Yuan, et al., 2015).

2.2.2.3 Acoustically-driven drug delivery

The use of acoustics in biomedical practices has been expanded from diagnostic applications to non-invasive drug delivery. The use of acoustics in drug delivery procedures can be divided into two categories: ultrasonic-enhanced drug delivery (known as high-intensity focused ultrasound (HIFU)) and low-frequency acoustic drug delivery (ADD). In the former, the

acoustic frequency (f) that is used for the drug delivery falls in the spectrum of $f > 20$ kHz, which is beyond the threshold of human hearing. In the latter drug delivery method (i.e., ADD), the low frequencies refer to frequencies below 2 kHz, which can be sensed by the human ear.

The utilisation of HIFU for treatment purposes was first suggested by Lynn et al. (1942); however, it was first applied for the treatment of subcutaneous neuroma in a clinical trial in 1960 (Ballantine et al., 1960; W. Fry et al., 1960). Nevertheless, this technique was unable to obtain broad acceptance from clinicians until the 1990s (ter Haar et al., 2007). A schematic of the mechanism of HIFU for the treatment of a tumour is presented in Figure 2.11. Recently, researchers have demonstrated several advantageous bioeffects of the propagation of ultrasound fields through tissues using focused, non-focused, low-amplitude, and high-amplitude ultrasound fields at frequencies ranging from 100 kHz to 9 MHz. Some therapeutic scenarios resulting from such bioeffects are as follows:

- Prompt and topical heating of the tissue for ablation of small masses (Kennedy, 2005; Leslie et al., 2007; ter Haar et al., 2007).
- Transcutaneous ablations of small renal masses using nonthermal mechanical effects of ultrasound fields (Roberts et al., 2006).
- Enhancement of thrombolysis using pulsed ultrasound fields. Thrombolysis is a therapy for resolving blood clots in blood vessels (Datta et al., 2006; Everbach et al., 2000; Trübestein et al., 1976).
- Stopping bleeding from damaged blood vessels at the depth of parenchymal tissues using HIFU (Vaezy et al., 2007). This method is called acoustic haemostasis. A parenchyma is the lump of functional parts of a structure in the body such as a tumour.

- Enhancement of TDD and controlling the release time of drugs, known as Sonodynamic therapy (Jeffers et al., 1991; Kinoshita et al., 2006). In this method, medications that are cytotoxic in the presence of ultrasound waves are used for TDD in cancer therapy. When the cytotoxic drugs arrive at the cancer cells, the ultrasound beam is focused on the target site and activates the cytotoxic drugs to kill the cancer cells. These drugs are not toxic when they are not exposed to the ultrasound field. Hence, any adverse side-effects are reduced, and the drug delivery efficiency is enhanced. The underlying mechanism of Sonodynamic therapy is still not fully understood; however, some researchers have demonstrated that the associated luminescence, thermal, and chemical processes, as well as acoustic cavitation, might be involved (McHale et al., 2016; Rosenthal et al., 2004).

The use of transcutaneous ultrasound for therapeutic purposes (the above-mentioned therapeutic scenarios) has been shown to be a promising active targeting approach when used in the blood circulation system. However, transcutaneous ultrasound cannot be utilised for therapeutic purposes in the respiratory system. This is because the lungs and airways are filled with gas, by which the ultrasound is scattered and reflected. Hence, it is not possible to focus an ultrasound beam at a target site in the respiratory airways (Pitt et al., 2004).

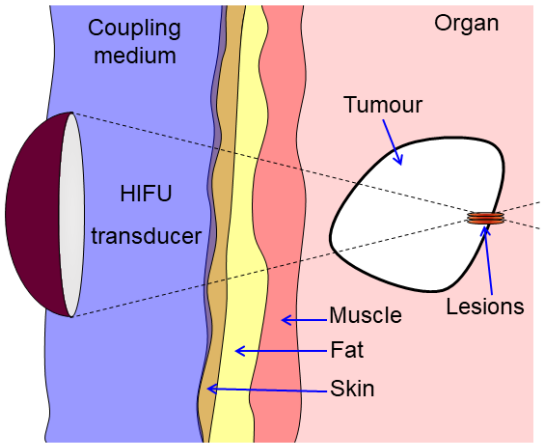

Figure 2.11: Schematic illustration of the HIFU principle. An HIFU transducer is used to generate ultrasound signals outside the body to concentrate on a target site deep within the tissue. The heating induced by HIFU leads the nanoparticles to kill the cells in the target region, adopted from An investigation into the use of cavitation for the optimisation of high intensity focused ultrasound (HIFU) treatments by James Ross McLaughlan, licenced under CC BY-SA 4.0.

On the other hand, a low-frequency acoustic field has recently been demonstrated to be advantageous in nasal drug delivery, especially for drug delivery to the MS. Previous studies have reported that low frequency ADD to the MS can enhance drug deposition in the MS significantly (El-Merhie et al., 2016; Farnoud et al., 2020; Leclerc et al., 2015; Moghadam et al., 2018; Möller, Münzing, et al., 2010; Möller et al., 2014; Navarro et al., 2019; Xi et al., 2017). In this method, the medications are produced in the form of aerosols, which are injected into the NC through the nostril, then an external acoustic field is applied to the nostril, affecting the aerosol's transport and deposition pattern.

Over the last few years, adding acoustics to a nebuliser (i.e., ibrENT PARI Pharma GmbH) has demonstrated a higher drug deposition in the sinuses when compared with a nebuliser without acoustics (Möller, Schuschnig, et al., 2010). Given that the sinuses are non-ventilated areas, the oscillating airflow generated by the acoustic field increases the gas exchange between the sinuses and the NC (Suman, 2013).

Using an *in-vivo* study, Möller et al. (2011) investigated the efficacy of drug delivery to the sinuses of five healthy human volunteers using a nebuliser coupled with an acoustic field (ADD). The median aerodynamic diameter (MAD) of the particles generated by the nebuliser was 3 μm, administered to the nostril at a rate of 300 μL/min for 20 s. Utilising dynamic gamma camera imaging, they reported that 2.8% of the administered aerosols deposited in all sinuses, 27% were trapped by the exit filter representing the exhaled aerosols, 60.2% deposited in the NC, and 10% of the administered aerosols were deposited in the lungs (Möller et al., 2011). On the other hand, 100% of the aerosol administered to the NC via spray pumps, which generated particles with MAD of 50 μm, was deposited in the NC, while no particles were deposited in the lungs and the MS. Therefore, a combination of a nebuliser with an acoustic wave is an efficient and promising method for drug delivery to the MS. Although the drug delivery to the MS is increased through the application of ADD, the efficiency of the drug delivery is still insufficient for successful treatment of CRS (Leclerc et al., 2015). To enhance the efficiency of ADD for drug delivery to the MS, it is crucial to develop an understanding of the mechanism underlying this technique, which is the main aim of the current study. A comprehensive literature review on ADD is presented in the following sections.

2.3 Acoustic drug delivery to maxillary sinuses

Several experimental and a limited number of numerical studies have focused on acoustic drug delivery to the sinuses, which are presented in detail in the following sections.

2.3.1 Experimental studies in ADD

The history of ADD for drug delivery to the sinuses goes back to 1959, when Guillerm et al. (1959) showed the feasibility of aerosol penetration into the non-ventilated sinus-like cavity

by superimposing a sound wave at a frequency of 100 Hz to a jet nebuliser (Durand et al., 2001). They used a blown glass as a model of the sinus and also conducted an *in-vivo* study on a canine's FS (Durand et al., 2001). Later, several studies further confirmed the benefits of a sound wave for aerosol penetration to the sinuses, as presented below.

Durand et al. (2001) investigated the penetration of aerosols into the MS using two plastinated models of the NC and the sinuses of two adult males. To check the accuracy of the model, they compared the CT images of the plastinated models with those of adult males. For the nebulisation process, they utilised the ATOMISOR NL11S® "sonic nebulizer" to nebulise 5 mL of technetium 99-labelled sterile water. The nebuliser produced small particles with MAD of 4.7 µm and they superimposed a 100 Hz sound wave onto the nebulised aerosols entering the nostril. Using scintigraphy, they measured the aerosol deposition in the sinuses qualitatively and reported a 1.3-fold increase in the penetration of aerosols into the MS under the effect of the 100 Hz sound wave when compared with non-acoustic drug delivery (non-ADD) (see Figure 2.12).

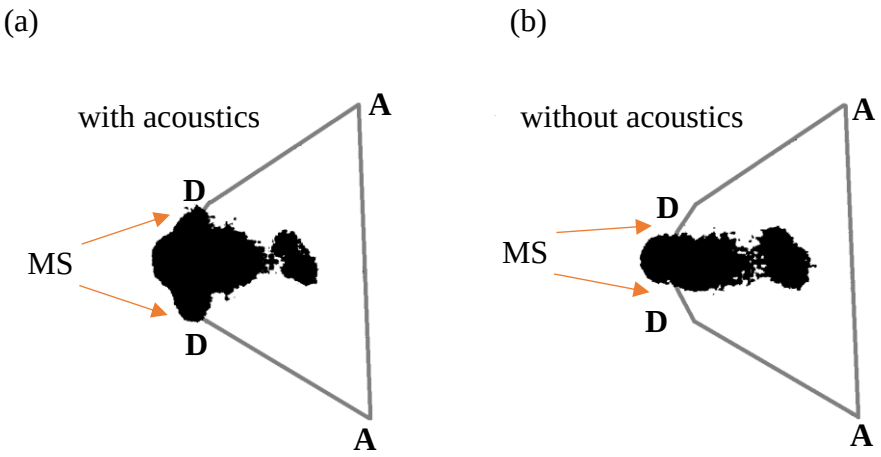

Figure 2.12: Scintigraphic image of the top view of the plastinated nose-sinus model (a) with acoustics; (b) without acoustics, reprinted from Durand et al. (2001), with permission from Mary Ann Liebert, Inc. , publishers; a minor modification has been applied to the original figure in the labelling and the line colour to improve the quality of the images. **A**: top of the ears, **B**: middle of the MS.

To determine the impact of acoustic waves on the air exchange rate between the NC and MS, Weitzberg et al. (2002) investigated the amount of nitric oxide (NO) in exhaled air during "humming". The respiratory system releases nitric oxide (NO) in exhaled air, which is largely produced by the paranasal sinuses (Lundberg et al., 1995). Using a clinical study, Weitzberg et al. (2002) showed that the humming action significantly increases the NO level exhaled from the nose. To be more specific, they measured the NO level of ten healthy adult males after a single-exhalation using a chemiluminescence system (NIOX, Aerocrine AB, Stockholm, Sweden). The subjects were asked to exhale for 5 seconds with or without humming (nasally) or phonation (orally). The subjects wore a nasal mask for the nasal exhalation and a mouthpiece for the oral exhalation measurements. The exhalation flow rate was adjusted at 0.2 L/s by connecting a dynamic flow restrictor to the nasal mask and mouthpiece. Weitzberg et al. (2002) reported that the NO level during nasal humming was increased 15-fold when compared with a quiet exhalation (2818$\pm$671 nL/minute vs. 189$\pm$30 nL/minute); however, the level of NO in the exhaled air under the effect of the oral phonation was not different from that of quiet exhalation (103$\pm$43 vs. 104$\pm$48 nL/minute). The results of their study showed qualitatively that the gas exchange between the NC and the sinuses increases when an acoustic wave (such as humming) is implemented to the nose during exhalation, which was confirmed by Maniscalco et al. (2003).

Using a measurement method similar to that of Weitzberg et al. (2002), in a clinical and an *in-vitro* study, Maniscalco et al. (2003) demonstrated that the increase in the concentration of exhaled NO is primarily sensitive to the frequency of both the humming and the diameter of the maxillary ostium. They applied three different humming frequencies of 120, 200, and 450 Hz and they found that a frequency of 200 Hz results in the greatest NO exchange for 295 nL/min. They also reported an increase in the NO exchange by increasing the ostium diameter, in which 100% NO exchange for an ostium diameter of 4 mm was

observed. They used a two-compartment model, including a syringe and a cylinder resembling the sinus and NC, respectively, which is shown in Figure 2.13. In a later work by Maniscalco et al. (2006), a 2- to 4-fold increase in sinus deposition was reported using acoustic airflows produced by human nasal humming at a frequency of 200 Hz, compared with non-ADD.

To demonstrated the effect of ADD on all paranasal sinuses, Möller et al. (2008) examined the effect of pulsating airflow on the gas exchange between the NC and all paranasal sinuses in a nasal cast, produced using Polyoxymethylene (see Figure 2.14 (a)). The sinuses and ostia were made using cylindrical glass vials. They reported that the gas exchange between the NC and all sinuses with pulsation was increased 6-fold when compared with gas flow without pulsation. The result was then quantitively confirmed in a clinical study on healthy volunteers conducted by Möller, Münzing, et al. (2010).

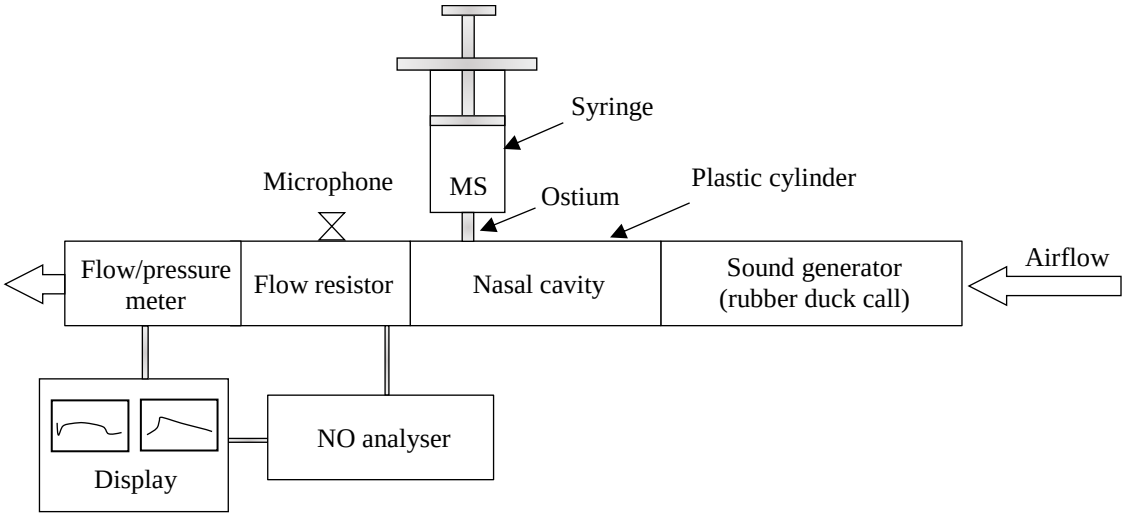

Figure 2.13: Schematic diagram of the simplified nose-sinus model. The syringe tip resembles the sinus and the plastic cylinder resembles the NC, reproduced from Maniscalco et al. (2003), with permission from the European Respiratory Society.

In a study by Möller et al. (2008), a dynamic ^{81m}Kr-gas imaging technique was used for the measurement of the gas exchange between the NC and MS in a nasal replica (see

Figure 2.14 (a)). The nasal replica was ventilated with ^{81m}Kr-gas through a jet nebuliser (PARI PRONEB Ultra II Compressor Nebulizer System) and a gamma camera (DIACAM, Siemens, Erlangen, Germany) was placed in front of the nasal replica to record serial images of the gas flow. The experiments were conducted with and without pulsation (pressure wave) for 30 seconds. A pressure wave at a frequency of 45 Hz with an amplitude of 25 mbar was generated through a pressure wave generator, which was driven by the motor of the compressor nebuliser (Möller et al., 2008). They demonstrated that pulsation (frequency of 45 Hz and amplitude of 25 mbar) could increase the gas exchange in all sinuses more than 20-fold (see Figure 2.14 (b-c)).

Möller et al. (2008) also investigated the effect of pulsation on aerosol delivery to the sinuses using the same nose-sinus replica, nebuliser, and experimental setup as was used for the gas exchange measurement. This time, they used air instead of ^{81m}Kr-gas as the gas supply of the nebuliser but used a solution composed of "99mTc-DTPA mixed 1:1 with 10 mg/mL disodium chromoglycate (DSCG) isotonic solution" for the nebulisation process. Using the gamma camera imaging technique, ^{99m}Tc-activity was detected during the experiments (2 minutes' running time). To investigate the effect of the geometric parameter on the sinuses, they examined the effect of the ostium diameter (1mm, 2mm, 3mm, and 5 mm) and sinus volume (5 mL, 10 mL, and 20 mL) on the aerosol deposition in the sinuses. They showed that the aerosol deposition in the sinuses relative to the total nebulised aerosol with pulsation (frequency of 45 Hz and amplitude of 25 mbar) could be decreased by increasing the ostium diameter for a sinus volume of 5 mL. However, this behaviour did not occur in larger sinuses with volumes of 10 mL and 20 mL, where the particle deposition in the sinus was at its maximum with an ostium diameter of 2 mm. Such behaviour of aerosol deposition in the sinuses due to the ostium and sinus geometry variation may imply a resonance effect between the geometry of the sinus, ostium and NC.

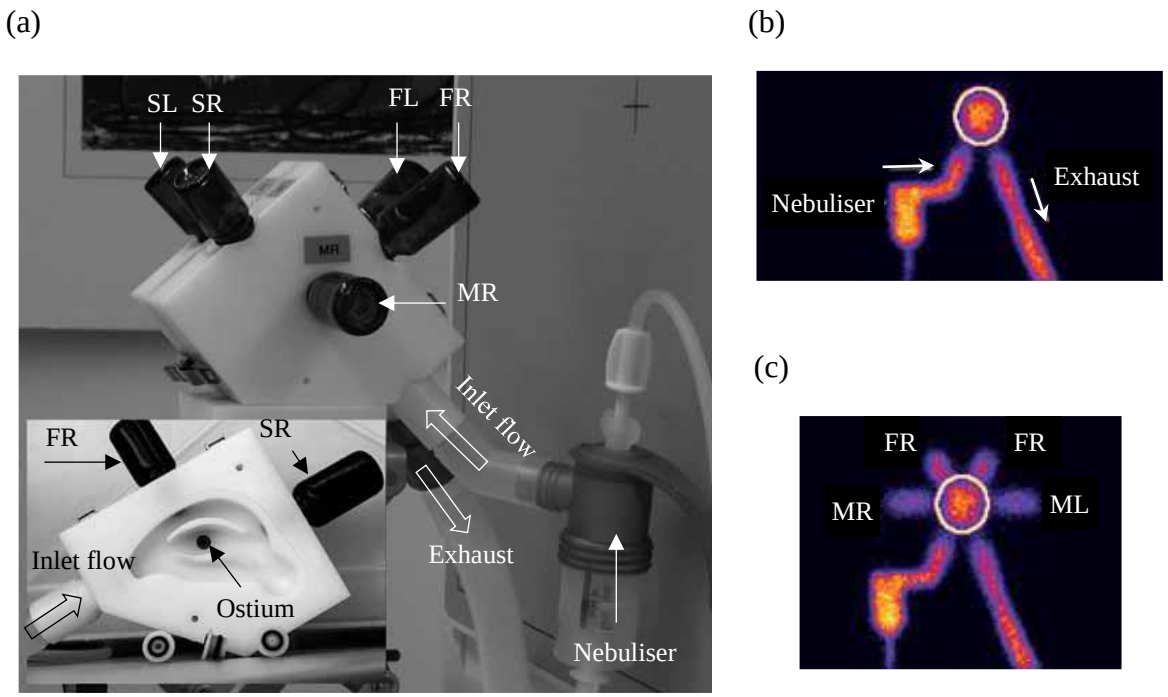

Figure 2.14: (a) The nasal replica with the bottles resembling the sinuses; (b) the frontal view of the gamma camera image of Kr-gas ventilation of the nasal cast without an acoustic wave; and (c) with an acoustic wave. FR: right frontal sinus; FL: left frontal sinus; MR: right maxillary sinus; ML: left maxillary sinus, reprinted from Möller et al. (2008), with permission from Rhinology; modification has been applied to the labelling.

The effect of a 100 Hz acoustic wave, superimposed on the airflow carrying the nebulised aerosol, on the aerosol deposition in the MS using a human plastinated nasal cast was investigated by Durand et al. (2011). They reported a 3-fold increase in the deposition of gentamicin in the MS under the effect of the acoustic wave (frequency of 100 Hz and sound pressure level of 107 dB) when compared with non-ADD (Durand et al., 2011). They used gentamicin as the drug tracer, which was nebulised by a jet nebuliser injected into the nose through the nostril. Each experiment was tested across 10 minutes and then the gentamicin deposited in the MS was collected by flushing the MS through a physiological serum, using a syringe. The collected gentamicin from each sinus was quantified using a fluorescence polarization immunoassay with a TDxFLx® analyzer (Durand et al., 2011).

Using a clinical trial, Möller et al. (2013) explored the effect of a nasal spray pump and an acoustic nebuliser (with an acoustic frequency of 25 Hz, the amplitude was not stated in the publication) on the deposition of aerosols (^{99m}Tc-DTPA) in the SS and the MS using a gamma camera imaging technique. They demonstrated 100% of the aerosol generated by a spray pump deposited in the NC, with insignificant aerosol deposition in the sinuses and lungs in healthy volunteers. However, using the acoustic nebuliser, about 55.3% of the nebulised aerosols deposited in the NC and around 6% deposited in the SS and MS in healthy subjects (Möller et al., 2013). In CRS patients, the aerosol deposition in the NC and SS, and MS before surgery were 54% and 2.7% of all nebulised aerosols, and after the surgery become 42.9% and 3.8% of all nebulised aerosols (see Figure 2.15).

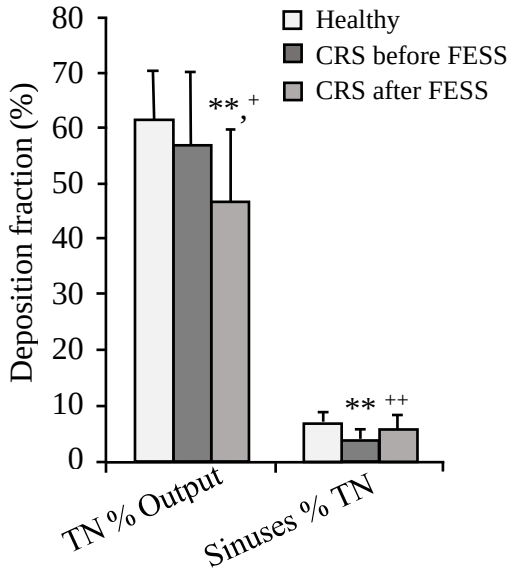

Figure 2.15: Aerosol deposition fraction in total nose (TN % output) and in maxillary sinuses (Sinuses % TN) before and after FESS in healthy volunteers and CRS patients. **: p <0.01 compared to healthy; +: p<0.05 ++: p < 0.01 lateral versus anterior imaging, reprinted from Topical drug delivery in chronic rhinosinusitis patients before and after sinus surgery using pulsating aerosols by Möller et al. (2013), licenced under CC BY 4.0; a part of the original figure has been removed.

The effect of particle size, inhalation pattern (non-nasal breathing and normal nasal breathing), and a 100 Hz acoustic wave (the amplitude was not stated in the publication) on aerosol deposition in the MS was explored by Leclerc et al. (2014). They used a realistic nose-

sinus model using a transparent, water-resistant, nonporous resin, manufactured using a stereolithography technique. In each experimental test, they used 4 mL of gentamicin antibiotic as the marker to generate aerosol, using a jet nebuliser for 10 minutes. They reported that using the ADD (at a frequency of 100 Hz), the non-nasal breathing condition increased the aerosol deposition in the MS by 2- to 3-fold when compared with a normal breathing condition (Leclerc et al., 2014). Under the effect of a 100 Hz acoustic wave, Leclerc et al. (2014) demonstrated a weak deposition of 9.9 μm particles but a significant deposition of 2.8 μm particles (up by 2- to 3-fold) in the MS. This difference may be due to the orthokinetic motion of the particles in an acoustic field. When an acoustic wave is applied to an aerosol, the particles oscillate at the frequency of the acoustic wave but with a different phase and amplitude. The oscillating particle velocity is given by (Marshall et al., 2014):

$$u_{\mathrm{p}} = \eta_{\mathrm{p}} A_{\mathrm{u}} \sin\left(2\pi f t - \phi_{\mathrm{p}}\right), \tag{2-1}$$

where A_{u} is the maximum particle velocity amplitude, η_{p} is the particle entrainment coefficient, and ϕ_{p} is the phase factor. The η_{p} is the ratio of the amplitude of particle velocity to the amplitude of the fluid velocity. The phase factor and the particle entrainment coefficient are given by (Marshall et al., 2014):

$$\eta_{\mathrm{p}} = \frac{1}{\sqrt{1 + (St_{\mathrm{ac}})^2}}, \tag{2-2}$$

$$\phi_{\mathrm{p}} = \tan^{-1}(St_{\mathrm{ac}}), \tag{2-3}$$

where St_{ac} is the acoustic Stokes number (Marshall et al., 2014) given by:

$$St_{\mathrm{ac}} = \frac{2\pi f \rho_{\mathrm{p}} d_{\mathrm{p}}^2}{18\mu}, \tag{2-4}$$

where f, ρ_{p}, d_{p}, and μ are the frequency of the acoustic wave, density of the particle, diameter of the particle, and the dynamic viscosity of the fluid. Accordingly, an increase in particle diameter, d_{p}, increases the acoustic Stokes number, which decreases the particle entrainment coefficient (Equation (2-2)); subsequently, the amplitude of the particle velocity (Equation (2-1)) decreases. Therefore, for a larger particle diameter, fewer particles can penetrate into the MS.

For a long time, acoustic frequencies of 50 Hz and 100 Hz were used in the ADD for drug delivery to sinuses. Historically, these acoustic frequency values were discovered accidentally when researchers found dust deposition in the sinuses of workers who worked with electrical rotating machines, generating sinusoidal waves at frequencies of 50 Hz and 100 Hz (Navarro et al., 2019). However, in several recent studies, it was hypothesised that the underlying rationale of increased aerosol deposition in the sinuses is based on the principle of the Helmholtz resonator (Möller et al., 2014).

A Helmholtz resonator is an acoustical device, which is composed of a cavity attached to a narrow straight tube (known as the neck). When a Helmholtz resonator is in the presence of an external acoustic field, the air plug inside the neck fluctuates at a frequency equal to that of the acoustic field. Using a mechanical analogy, the flow behaviour in a Helmholtz resonator can be described as a mass-spring system (Ghanadi, 2015). The mass of air plug in the neck ($m = \rho L_n S_0$) and the compressibility of the air (with stiffness of $K = \rho c^2 S_0^2 / V_c$) in the cavity are assumed as the mass and spring of the mass-spring system, respectively. The term ρ is the air density, L_n is the length of the neck, c is the sound speed, S_0 is the cross-section area of the neck, and V_c is the cavity (Hemon et al., 2004). Using a lumped element analysis, the displacement of the air plug in the neck (Meissner, 2002) is given by:

$$m\frac{d^2\sigma}{dt^2} + R\frac{d\sigma}{dt} + K\sigma = F_{act} \tag{2-5}$$

where t, m, σ, R, and F_{act} are the time, mass of air plug in the neck, displacement of the air plug in the neck, damping constant, and the force acting on the air plug in the neck, respectively. The airflow in the neck and cavity acts as a mass-spring-damper, where the system is damped with a damping constant of R due to the energy loss by the radiation and the viscous effect of the air flow in the neck (Meissner, 2002). The damping constant is given by:

$$R = \frac{\rho c}{S_0}\left(0.288k\delta\log\left(\frac{4S_0}{\pi S_0^2}\right) + \frac{S_0 k^2}{4\pi} + Ma\right), \tag{2-6}$$

where k, δ, c, and Ma are the wavenumber, thickness of the boundary layer, speed of the sound, and the Mach number of the flow. Assuming a harmonic motion of air in the Helmholtz resonator, the displacement of the air plug in the neck is given by:

$$\sigma(f) = \frac{F_{act}(f)}{-4m\pi^2 f^2 + 2if\pi R + K}\ , \tag{2-7}$$

where f is the applied acoustic frequency and $i = \sqrt{-1}$ is the imaginary number (Ghanadi, 2015). Therefore, the amplitude of the air plug oscillation in the neck changes according to the variation of the frequency of the external acoustic field. The amplitude of the air plug oscillation reaches its maximum at a specific frequency called the "resonance frequency" (Leclerc et al., 2015; von Helmholtz et al., 1875). To be more specific, when f approaches the resonance frequency of the system, $f_r = f_n\sqrt{1-\zeta^2}$ (where $f_n = \sqrt{K/4m\pi^2}$ is the natural frequency and ζ is the damping ratio), the denominator in Equation (2-7) approaches zero, which implies that the amplitude of the displacement of the air plug in the neck becomes very large (Ghanadi, 2015). For a Helmholtz resonator with a spherical cavity and a cylindrical neck, the resonance frequency is estimated by (Leclerc et al., 2015):

$$f_r = \frac{c}{2\pi}\sqrt{\frac{S_0}{V_c L_n}}, \tag{2-8}$$

where c is the sound speed, $S_0 = \pi {D_n}^2/4$ is the cross-section area of the neck (where D_n is the diameter of the neck), V_c is the volume of the cavity, and L is the length of the neck. More accurate expressions, depending on the shape of the cavity and neck, are derived and reported by Alster (1972) and Howard et al. (2000).

Exploiting this analogy, a nose-sinus combination is similar to a Helmholtz resonator, where the sinus and ostium behave like the cavity and neck of the Helmholtz resonator. Hence, drawing on the principle of the Helmholtz resonator, if an external acoustic field is applied to the nostril at a frequency equal to the resonance frequency of the nose-sinus combination, the air exchange between the NC and the sinus should be maximised. The gas exchange between the NC and sinuses is the main factor affecting the transport of particles from the NC to the sinuses.

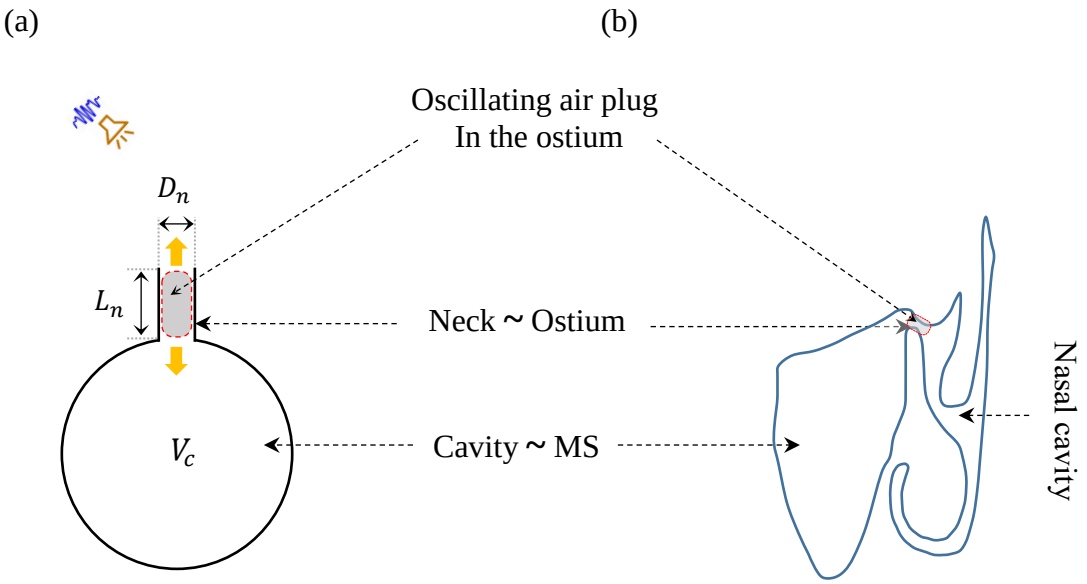

Figure 2.16: (a) Schematic of a Helmholtz resonator; (b) schematic of a cross-section view of an NC-MS combination, reproduced from Pourmehran et al. (2021) with permission from Elsevier. The neck and cavity of the Helmholtz resonator resemble the ostium and MS.

Considering the Helmholtz resonator principle, limited studies have investigated the effect of an acoustic wave superimposed on nebulisation during drug delivery to the sinuses. Leclerc et al. (2015) investigated the effect of two acoustic frequencies (45 Hz and 200 Hz) superimposed on nebulised aerosols, on the aerosol deposition in the MS using a nasal replica manufactured using a stereolithography technique and the experimental setup described in Leclerc et al. (2014). Using the CT images of the nasal replica, Leclerc et al. (2014) measured the volume of the left and right MS as 14 cm^3 and 10 cm^3, respectively. They also estimated the geometric features of the broad and short ostium of the left MS (diameter of 4–5 mm and length of 4–5 mm, respectively) and the long and narrow ostium of the right MS (diameter of 3–4 mm and length of 7–8 mm, respectively) (Leclerc et al., 2015). Referring to the classic Helmholtz resonator equation (Equation (2-8)) the resonance frequency of the left and right MS were estimated to be 300-400 Hz and 150-200 Hz, respectively. Two different types of jet nebulisers, driven by a compressor, were used for nebulisation. In that study (Leclerc et al., 2015), one nebuliser (DTF Medical, Saint-Etienne, France) generated aerosols with the superposition of an acoustic wave at 200 Hz (termed high frequency), while in the other nebuliser (Pari GmbH, Starnberg, Germany) the acoustic frequency was 45 Hz (termed low frequency). Leclerc et al. (2015) reported that in comparison with non-acoustic nebulisation, the aerosol depositions in the left and right MS were increased by 4-fold and at least 2-fold, respectively, under the effect of 200 Hz acoustic wave. When 45 Hz (the amplitude was not stated in the publication) was applied, the aerosol depositions in the left and right MS were increased by 2-fold and 4-fold, respectively, when compared with the non-acoustic condition (Leclerc et al., 2015). They reported that, according to the Helmholtz resonator equation, a broad and short ostium resulted in a higher resonance frequency than a long and narrow ostium; hence, the aerosol deposition in the left MS, with a broad and short ostium, under the

effect of high frequency was more than that of the right MS, with a long and narrow ostium (Leclerc et al., 2015).

In summary, the efficacy of the ADD using a fixed acoustic frequency (i.e., 45 Hz, 100 Hz, and 200 Hz) superimposed on the aerosols' flow entering the nostril has been investigated in several previous studies. Given that the Helmholtz resonator equation was derived for a spherical cavity attached to a cylindrical neck, the resonance frequency of the realistic nose-sinus combination estimated in the previous studies does not have acceptable accuracy. Hence, it was not guaranteed that the air plug in the ostium was activating efficiently under the effect of the fixed acoustic frequency obtained by the Helmholtz resonator equation. Accordingly, the highest efficiency of drug delivery could not be achieved.

The use of an acoustic frequency sweep, instead of a fixed frequency, for an optimised ADD technique was proposed by El-Merhie et al. (2016). It was proposed that by superimposing a frequency sweep at a specific range of frequency on the airflow (including the aerosol) entering the nostril, there must be an input frequency that falls in the proximity of the resonance frequency of the NC-MS combination. El-Merhie et al. (2016), in an *in-vitro* study, investigated the effect of the acoustic frequency sweep on aerosol deposition in the MS. They used 2.5% sodium fluoride (NaF) as the drug tracer and employed a jet nebuliser to generate droplets (particles) with a MAD of 2.75µm (El-Merhie et al., 2016). Three frequency spans were superimposed on the inlet airflow (carrying aerosols) ranging from 45-500 Hz, 45-800 Hz, and 100-500 Hz, with three sweep cycles of duration 0.3 s, 3 s, and 30 s. A realistic model of the NC with all paranasal sinuses was manufactured using 3D printing technology. El-Merhie et al. (2016) demonstrated that the acoustic sweep frequency can increase the aerosol deposition by 2-fold in the right MS and by 2.5-fold in the left MS when

compared with a fixed input frequency of 300 Hz, (see Figure 2.17 (a)). They also reported that the shorter the sweep cycle duration, the greater the NaF deposition in the MS, which is in contrast with the findings of a recent study by Moghadam et al. (2018).

Using an experimental setup and procedure similar to that of El-Merhie et al. (2016) but with a different nose geometry, Moghadam et al. (2018) investigated the effect of an extended range of acoustic frequency sweeps of 100-500 Hz and 100-850 Hz, as well as a sweep cycle duration of 0.1 s, 0.3 s, 1 s, 1.5 s, and 2 s on the aerosol (NaF) deposition in the MS. They demonstrated that, by expanding the frequency span from 100-500 Hz to 100-850 Hz, the aerosol deposition increased by 3-fold in the left MS but had no significant effect on the right MS (Moghadam et al., 2018). The increase in aerosol deposition in the left MS might be due to the fact that the resonance frequency of the left MS falls in a frequency range between 500-800 Hz. In respect to the sweep cycle duration, Moghadam et al. (2018) showed that the aerosol deposition in the MS has a nonlinear relationship with the sweep cycle duration, where the maximum aerosol deposition in the MS occurs at a sweep cycle duration of 1 s (see Figure 2.17 (b)) .

(a)

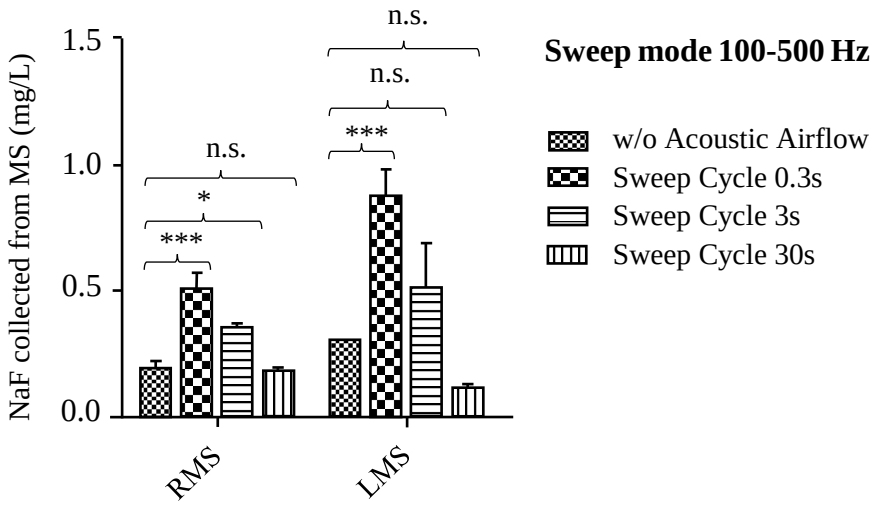

(b)

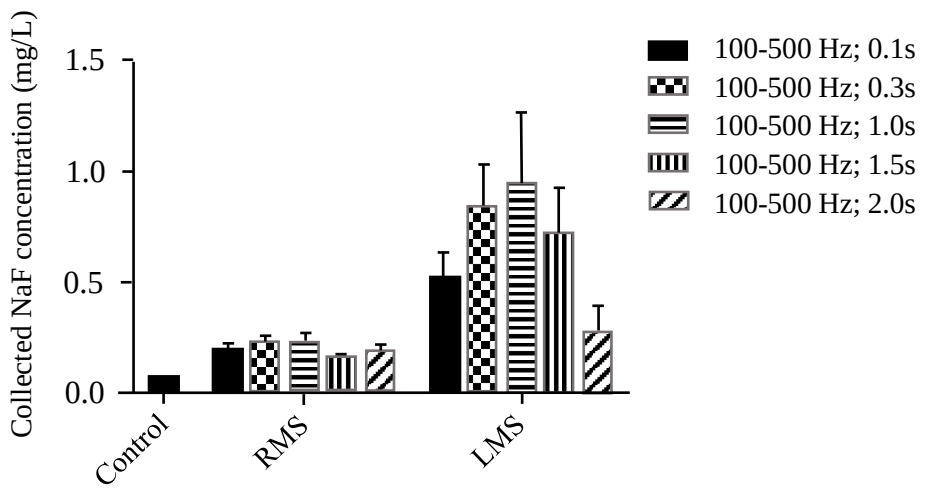

Figure 2.17: (a) Effect of the acoustic sweep cycle duration on NaF deposition in the MS reported in El-Merhie et al. (2016).**: p<0.01), ***: p<0.001, reprinted from El-Merhie et al. (2016), Copyright (2016), with permission from Springer Nature ; (b) effect of the sweep cycle duration (with an amplitude of 120 dB) on NaF deposition in the MS reported by Moghadam et al. (2018), control: without acoustic, reprinted from Moghadam et al. (2018), with permission from Elsevier.

Although the acoustic frequency sweep technique can slightly increase the aerosol deposition in the MS, more time is required for injecting the nebulised drug into the nose to cover an extended range of frequency. Therefore, the total dosage of the drug injected into the nose in the form of aerosols is increased due to an increased injection duration. Accordingly, the risk of adverse side effects on the respiratory system is increased.

2.3.2 Numerical studies in ADD

Despite several experimental studies, there are limited numerical studies investigating the effect of acoustics/pulsation on aerosol deposition in the NC and MS. In the literature, computational fluid dynamics (CFD) modelling was employed to simulate the ADD in drug delivery to the maxillary sinus. Two different discretisation and solution schemes were used to establish the CFD models: a finite elements method (FEM) through COMSOL software, and a finite volume method (FVM) via OpenFOAM.

In a recent study, using a modified Helmholtz resonator equation, Xi et al. (2017) estimated the resonance frequency of a two-bottle model resembling the nose-sinus combination. The modified Helmholtz resonator equation is similar to Equation (2-8) but the term L_n should be replaced by L_{eq}, the equivalent length of the neck, which can be obtained by $L_{eq}=L_n+0.6D_n$ (Xi et al., 2017). They also employed numerical modelling to predict the resonance frequency of the model through the finite element method (FEM) using COMSOL Multiphysics software. In that study, Xi et al. (2017) showed a good agreement between the value of the resonance frequency of the two-bottle model (neck diameter=7 μm, neck length=10 μm, small bottle (sinus) volume: 250 mL) obtained by the modified Helmholtz resonator equation (169 Hz) and that obtained by FEM (168 Hz). They also predicted the resonance frequency of a realistic NC-MS model using both the equation and FEM, in which the FEM underpredicted the resonance frequency when compared with the modified Helmholtz resonator equation.

The resonance frequency of the realistic NC-MS model, with an ostium diameter and length of 3 mm and sinus volume of 10.314 mL, was predicted by the modified Helmholtz equation and FEM at 652 Hz and 545 Hz, respectively (Xi et al., 2017). The discrepancy between the results of the Helmholtz equation and FEM might be due to the oversimplification of the realistic nose-sinus model. Hence, further studies are required to investigate the effect of geometric features on the NC and the MS in terms of prediction of the resonance frequency. In the two-bottle model, Xi et al. (2017) showed that the highest aerosol (MAD of 3μm) deposition in the small bottle (as the MS) occurred at an input frequency equal to the resonance frequency of the NC-MS combination (see Figure 2.18). The airflow features in the NC and MS were not discussed in that study.

(a)

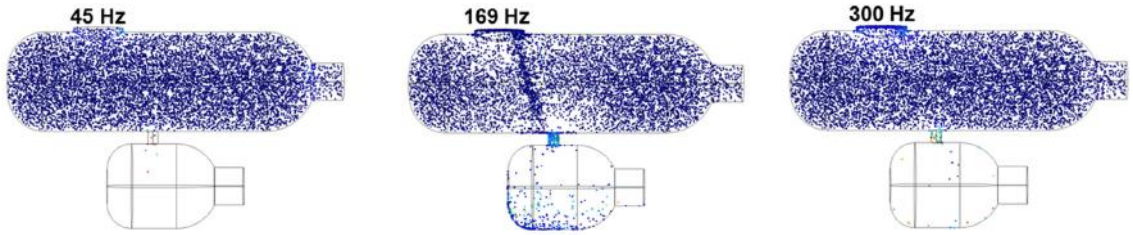

(b)

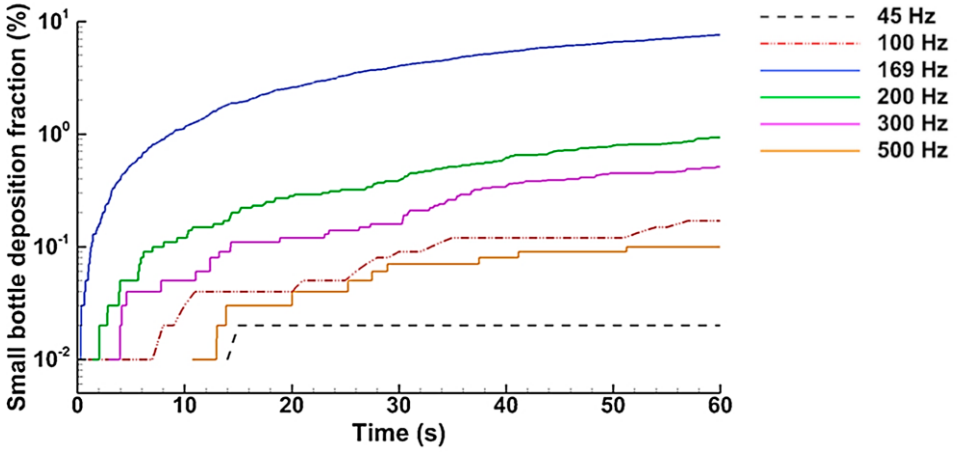

Figure 2.18: Numerical simulation of acoustic aerosol delivery at different input acoustic frequencies, carried out using COMSOL software, in a two-bottle model resembling the combination of the NC and the MS. (a) The aerosol transport pattern after 60 s at frequencies of 45Hz, 169Hz, and 300 Hz; (b) the effect of various acoustic frequencies, 45Hz, 169Hz, 200 Hz, 300 Hz, and 500 Hz on the aerosol deposition fraction in the small bottle, reprinted from Xi et al. (2017), with permission from Elsevier.

Using CFD modelling with the OpenFOAM software package, Farnoud et al. (2017) investigated the effect of a pulsating airflow on the deposition of particles in the nasal passages, excluding all the paranasal sinuses. They implemented a pulsating airflow to the inlet boundary (nostril) using the following velocity profile:

$$U = U_0|\sin(2\pi f^* t)| \tag{2-9}$$

where $\omega^* = \omega/2$ and ω=45 Hz, U_0 is the maximum airflow velocity (1.48 m/s), and t is time. They injected 10,000 mono-dispersed inert particles (with a diameter of 2.4 μm) into the nostril over the first time-step at 10^{-5} s.

Farnoud et al. (2017) reported that the deposition of particles in the NC under the effect of a pulsating airflow increased by 1.5-fold when compared with a uniform inlet airflow. They found that the uniform inlet airflow led to the deposition of particles in the nasal valve, nasopharynx, and septum; however, the pulsating airflow increased the ventilation and particle deposition in the olfactory regions, as well as the SM and MM. They proposed that an increased deposition in the MM can lead to increased particle delivery and deposition in the MS.

In a recent numerical study, Farnoud et al. (2020) examined the effect of a clockwise inclination of 45° and 90° of the nose on particle deposition in paranasal sinuses of a realistic nose-sinus model, under the effect of an oscillating airflow (45 Hz) entering the nostril. They used the following velocity profile as the velocity inlet boundary condition (Farnoud et al., 2020):

$$U = U_0(1 + |\sin(2\pi\omega^* t)|). \quad (2\text{-}10)$$

Farnoud et al. (2020) demonstrated that the oscillating airflow increased the overall particle deposition in the sinuses by 1.5-fold and 2.5-fold for the cases with a nosepiece inclination of 90° and 45°, respectively, when compared with a uniform airflow (non-oscillating). It should be noted that in the numerical studies conducted by Farnoud et al. (2017) and Farnoud et al. (2020), the pulsating/oscillating airflow was not considered to be an acoustic wave because they assumed the air to be an incompressible fluid and also did not apply a non-reflecting boundary condition to the inlet and outlet. Hence, the ADD was not simulated accurately, given the reflection of an acoustic wave affects the oscillation of the air plug inside the ostium.

When an acoustic wave is emitted, it travels toward the boundaries and reflects when it hits a reflective boundary, such as a solid wall. The reflection of the acoustic wave affects the pressure at the boundary due to interference between the reflected and incident pressure waves. However, when an acoustic wave travels towards a non-reflecting boundary, it does not reflect and passes through the boundary. In practice, the inlet (nostril) and outlet (nasopharynx) in an NC-MS combination are almost non-reflecting boundaries. However, they represent a minor impedance change and there will be minor reflections, which should be considered in any numerical modelling. When a reflecting boundary condition is applied to the inlet and outlet in a CFD model, these boundaries are treated as a solid wall. Therefore, the acoustic pressure at the inlet and outlet boundaries reaches higher/lower values compared with a realistic boundary condition. Consequently, the acoustic pressure within the entire NC-MS is changed, which affects the oscillation of the air plug in the ostium. In the current study, a high-fidelity CFD model considering the non-reflecting inlet/outlet boundary conditions using a compressible airflow was developed to predict the resonance frequency of an NC-MS combination as well as to simulate ADD for drug delivery to the MS, which are later presented in Chapter 3 and Chapter 4, respectively.

Although several previous studies investigated the feasibility of ADD in enhancing drug deposition in MS, the underlying mechanism of ADD is still controversial. A fundamental study on understanding the important parameters in the prediction of the resonance frequency of the NC and MS combination is also missing in the literature. Moreover, the underlying mechanism of particle deposition and transport patterns in the NC, ostium, and MS due to the application of an external acoustic field is still not well-understood.

2.3.3 Limitations in nasal drug delivery

The complex structure of the NC leads to some limitations in drug delivery to the NC and MS. The initial flow-limiting part of the NC is the nasal valve, which has a narrow triangular shape located near the nostril opening (Cole, 2003). The nasal valve changes the direction and velocity of the airflow during inhalation (Cole, 1992; Fodil et al., 2005). During quiet breathing, the air velocity at the nasal valve comes close to 18 m/s (gale force) and approaches 32 m/s during sniffing (Cole, 1992). During quiet breathing (15 L/min), the flow regimen throughout the NC is mostly laminar; however, downstream of the nasal valve, it becomes locally-turbulent when the flow rate increases to 25 L/min (Cole, 1992; Fodil et al., 2005).

During inhalation, the nasal valve is narrowed progressively when the inhaled flow rate increases, which takes place due to the Bernoulli effect acting on the orifice-like structure of the nasal valve (Cole, 1993). During exhalation, the nasal valve helps the pharynx, trachea, and lower airways to stay open by preserving a positive pressure at the expiratory airways due to its narrow structure (Hairfield et al., 1987). The braking behaviour of the nasal valve also provides the alveoli with more time for the gas exchange. The narrowed structure of the nasal valve and its braking behaviour can be seen as advantageous factors for patients with obstructive sleep apnoea disorder (Djupesland et al., 2001). However, in terms of nasal drug delivery, the triangular shape of the nasal valve and its small dimensions represent critical hurdles to achieving efficient drug delivery, especially when it becomes narrowed during inhalation. In addition to the anatomical limitations due to the small dimensions of the nasal valve, the vulnerability of the mucosa in the nasal valve and the vestibule region represents another limitation to nasal drug delivery. The concentrated local-deposition of the drug on the wall of the septum, as well as the possible direct touch of the spray nasal tip during aerosol injection, may cause damage and irritation to the mucosa, potentially leading to perforation,

crusting, and bleeding of the nose (Waddell et al., 2003). However, in the context of the potential for nasal drug delivery, the vulnerability of the nasal mucosa is usually neglected, particularly in the evaluation of the results from CFD and *in-vitro* studies using a cast or 3D printing technology.

2.4 Airflow behaviour and particle motion in the nose

Understanding the airflow behaviour in the NC and MS is crucial for improving drug delivery efficiency. Several numerical and experimental studies have investigated the airflow features in the NC and MS. The main goal of these studies is to evaluate the characteristics of the flow pattern in the NC and consequently assess the efficiency of particle deposition. Generally, the particle transport/deposition behaviour in a fluid flow is quantified by the dimensionless Stokes number (*St*), which is the ratio of the particles' momentum response time to the flow-field time scale (Krstić, 2006) given by:

$$St = \frac{\rho_{\mathrm{p}} d_{\mathrm{p}}^2 U}{18 \mu L} \tag{2-11}$$

where U and L are the characteristic velocity and characteristic length, normally taken as the mean flow velocity and hydraulic diameter of the inlet, respectively. The Stokes number implies an imperative criterion for understanding the particle transport behaviour in the fluid flow. It indicates whether the particles are in kinetic equilibrium with the fluid phase (Tian et al., 2005). In other words, St presents a measure of the effect of the inertial impact of the particles within the fluid flow. Nevertheless, the application of the St depends highly on the characteristic length of the domain of interest, which alters between different geometries of the NC. To overcome this limitation of the St, the inertial parameter (*IP*) is widely used for the assessment of particle deposition in the NC and respiratory airways because the

characteristic length and the characteristic velocity associated with the St is normalised out by using a constant flow rate. The inertial parameter is given by (Inthavong et al., 2011):

$$IP = Q\, d_{\mathrm{ae}}^{2} \tag{2-12}$$

where Q is the airflow rate and d_{ae} is the equivalent aerodynamic diameter given by:

$$d_{\mathrm{ae}} = d_{\mathrm{e}}\sqrt{\frac{\rho_{\mathrm{p}}}{1000\mathrm{X}}} \tag{2-13}$$

where d_{ae} is the aerodynamic diameter is defined as "the diameter of the spherical particle with a density of 1000 kg/m^3 that has the same settling velocity as the particle under study" (Yang et al., 2012). The d_{e} and X are the equivalent volume diameter and the shape factor of the particle, respectively (Yang et al., 2012). For a spherical particle, the d_{e} equals to the particle diameter and X is unity (Yang et al., 2012). The inertial parameter is a convenient parameter that is normally used for comparing the effects of particle diameters and airflow rates on the deposition efficiency. However, the use of a constant flow rate is a limitation of the inertial parameter given that it does not take into account the complicated shape of the geometry of the NC. Despite this limitation, the inertial parameter is normally used for the demonstration of deposition efficiency of particles, particularly where the determination of characteristic length is limited due to the geometry variation.

2.4.1 Experimental studies

Since the 1950s, a handful of *in-vivo* and *in-vitro* studies were established to develop an understanding of the airflow in the NC and the sinuses. The deposition of monodisperse polystyrene particles was measured by Hounam et al. (1971), with diameters from 1 to 7 μm for airflow rates ranging from 5 to 40 L/min. They conducted the experiments on three healthy subjects for 20 seconds. They found a direct relationship between the pressure drop along the

NC and particle deposition in the NC. Using laser Doppler anemometry, Girardin et al. (1983) investigated the airflow pattern and aerosol deposition in the NC using a cadaver model. They showed that the velocity of the airflow in the inferior region of the NC is greater than the air flow velocity in the superior region of the NC.

The aerosol deposition pattern in the NC was investigated experimentally by Suman et al. (1999), where the particles were administered to the nostril using a nebuliser and spray pump, separately. They demonstrated that the particles can be transported beyond the nasal valve and anterior region of the NC when a nebuliser is used for administration of the drug particles; however, using the nasal spray pump, the penetration of particles to the posterior region is negligible. They showed that the ratio of particle deposition in the posterior region to the particle deposition in the anterior region is 0.211 and 0.073 when the nebuliser and the nasal spray pump are used, respectively. The low penetration of the particles to the posterior region of the NC originates from the inertial impaction (Yu et al., 1998). The inertial impaction takes place when the direction of the flow changes abruptly, wherein the particles are pushed to deviate their streamline while the particles' inertia pushes them to move on their initial trajectories (Darquenne, 2020). Using particle image velocimetry (PIV), Kelly et al. (2000) examined the deposition pattern of pollutants in the NC by applying a solution of water and glycerol to the nostril at a flow rate of 7.5 L/min. They found that the highest airflow velocity occurs in the nasal valve and inferior region of the airways of the NC. Kelly et al. (2000) demonstrated that a very low airflow rate was observed in the olfactory and superior region, which implies a negligible deposition of pollutants in the olfactory region.

Using an MRI-based reconstructed model of NC and nasal spray pumps, Cheng et al. (2001) investigated the deposition pattern of particles in different regions of the NC. They reported that a large number of the particles deposited in the anterior region and the turbinates;

however, a small fraction of the particles could reach the nasopharynx. Using high-speed photography and laser diffraction technology, they measured the particle deposition on the inner wall of the nasal replica and reported that the particle deposition pattern varies with the size of the particles and the spray angle, in which a higher particle size and spray angle increase the particle deposition in the anterior region of the NC. Using mathematical modelling, they demonstrated that the diffusion mechanism is dominant in particle deposition in the NC for particles smaller than 0.5 μm; however, the inertial impaction is the dominant mechanism of deposition for particles greater than 0.5 μm.

To account for the effect of the geometry of the NC on airflow and deposition patterns, Kim et al. (2004) used a silicon-made nasal replica of two healthy persons to investigate the airflow pattern in the NC by applying an airflow rate of 7.5 L/min to the nostril. They found that the number of flow recirculation zones in the NC varies with the shape of the NC geometry. Chung et al. (2008) reported that the differences in the airflow patterns in various NC models stem from the variation of the geometry of the inferior, middle, and superior turbinates. Doorly et al. (2008) examined the flow pattern in the NC using PIV measurements and a CFD simulation. They found a recirculation zone at the end of the nasal valve in both the experiments and the CFD simulation. This recirculation zone was created because the section area of the end point of the nasal valve expands suddenly. Doorly et al. (2008) showed that a jet flow and a sheer layer between the jet flow and the recirculation zone is seen immediately after the nasal valve.

The effect of particle size on the deposition of the particles in the sinuses after FESS was assessed by Hilton et al. (2008). They reported that the deposition of particles in the NC with a particle diameter smaller than 5 μm is lower than the deposition of particles with a diameter greater than 5 μm. Yuan Liu et al. (2009) reconstructed a standardised NC model (known as the Carleton-Civic model) based on CT images of 30 different healthy persons.

Using this model, Yuan Liu et al. (2010) examined the particle deposition patterns of particles with diameters of 1.71 μm to 9.14 μm under the effect of airflow rates of 30 to 90 L/min. They demonstrated that inertia was the dominant mechanism for particle deposition in their study. Using computational and experimental studies, Rennie et al. (2011) investigated the air exchange between the NC and MS using ^{81m}Kr gas as a working fluid. They demonstrated that the gas exchange between the NC and MS could increase 50-fold by adding an additional ostium (see Figure 2.19 (a-c)). Moreover, they reported a direct relationship between the gas exchange and the ostium diameter.

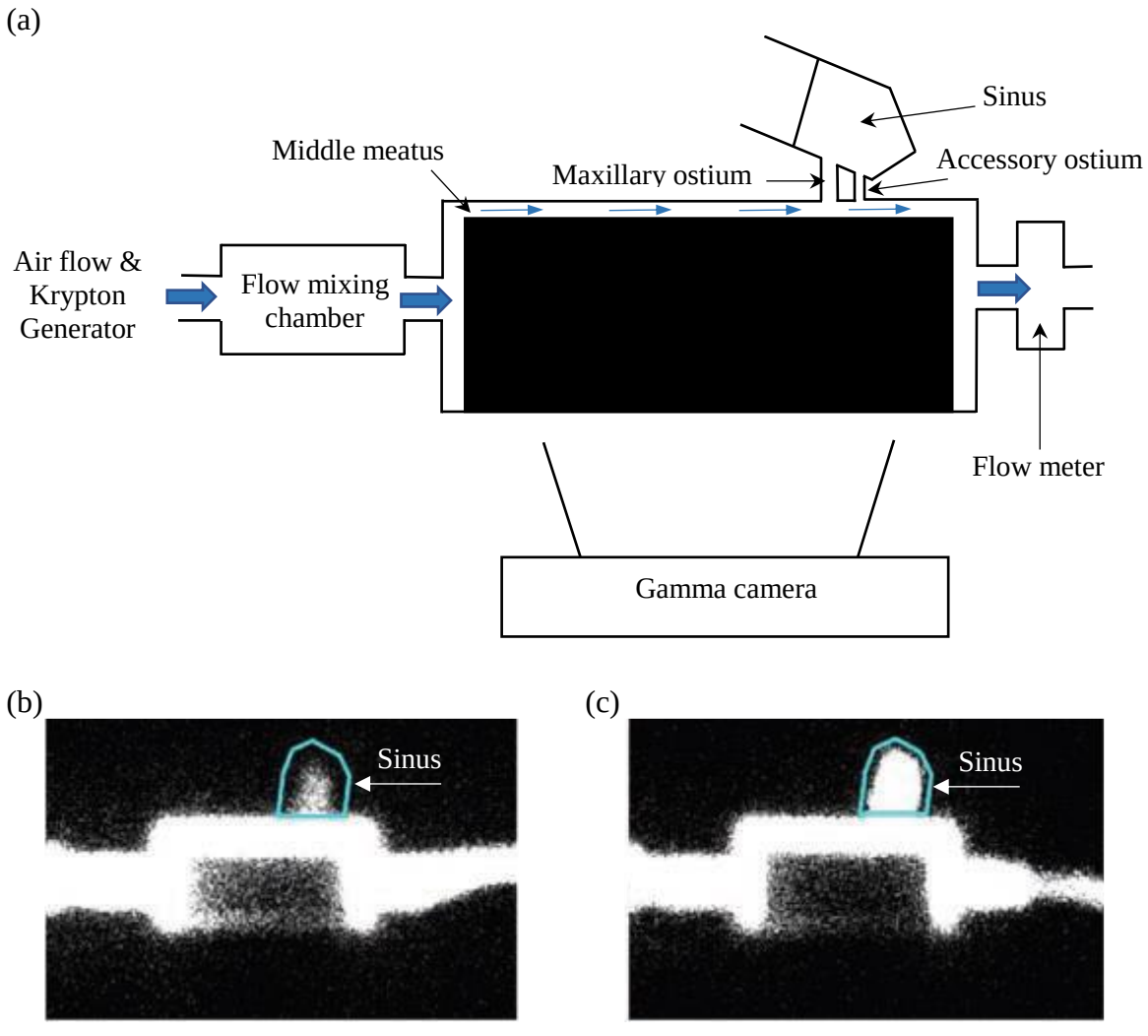

Figure 2.19: (a) Schematic diagram of an experimental setup used in the study by Rennie et al. (2011). Raw g-camera images for (b) single ostium and (c) double-ostium configurations, for a 10 mL sinus and an inlet flow rate 5 L/min, reproduced from Rennie et al. (2011), with permission from SAGE Publications.

2.4.2 Numerical studies

Advances in tomography imaging techniques have resulted in a large number of numerical studies using image-based geometries to develop a better understating of the airflow behaviour in the NC and MS. Accordingly, several studies have employed CFD to model the airflow in an NC, mostly without considering the MS.

The earliest numerical study investigating the flow structure in an NC dates back to 1995 when Keyhani et al. (1995) simulated the laminar flow patterns in a realistic geometry of the NC at quiet breathing flow rates using a CFD model (steady-state and laminar flow) through the finite element software package FIDAP (Fluid Dynamics International). They demonstrated that about 30% of the inhaled volumetric flow passed through the floor of the inferior turbinate and nearly 10% passed through the superior meatus (olfactory region). Using FIDAP, Subramaniam et al. (1998) investigated the effect of inlet flow rates of 15 L/min and 26 L/min on the flow structure in an anatomically accurate NC model, reconstructed from MRI images. They demonstrated a recirculation and swirling flow occurs in the vestibule and nasopharynx (see Figure 2.20). Subramaniam et al. (1998) also showed that the flow in the NC was laminar for both flow rates of 15 L/min and 26 L/min, which is in agreement with the results of a study by (Hahn et al., 1993), while it is in contrast with (Swift et al., 1977) who demonstrated the flow in the NC is turbulent for a flow rate of 25 L/min.

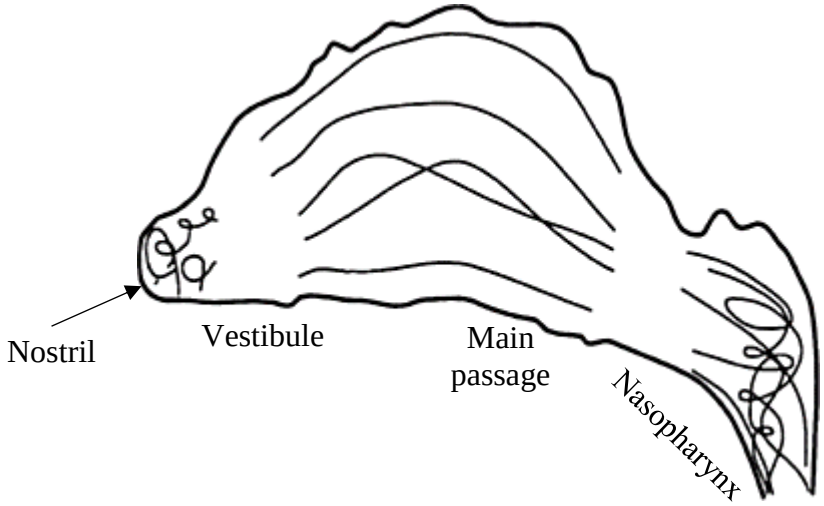

Figure 2.20: Illustration of streamlines in the vestibule, main passage, and nasopharynx for a steady flow, adapted from Subramaniam et al. (1998), with permission from Taylor & Francis.

The studies in the literature have demonstrated that the anatomy of the NC influences the flow structure in the NC. Zhao et al. (2004) investigated the effect of various shapes of the nasal valve and olfactory airway on the sense of smell and the flow structure in the NC. They found that the flow patterns in the olfactory region vary in different anatomies of the nasal cavity and olfactory airways, which can describe the sensitivity of each person to the odorant. They also demonstrated that the majority of the volumetric inlet flow passes through the inferior meatus. Hörschler et al. (2006) simulated the laminar flow (Re=400-500) in an NC with and without turbinates to investigate the sensitivity of the inhalation/exhalation flow pattern to the anatomy of the NC using commercial software, FLUENT/UNS 4.2 and experiments. They found that the effect of the sensitivity of the flow pattern to the NC geometry (with and without turbinates) during the inhalation period is much more than that during the exhalation phase. Using a large eddy simulation (LES) turbulent model, Lee et al. (2010) investigated the flow behaviour in a realistic geometry of an NC, reconstructed by CT images, using an unsteady-state CFD model. They demonstrated that the highest wall shear stress (WSS) occurs in the nasopharynx; however, the peak WSS varies during the inhalation

and exhalation phases. They also reported that a secondary flow was observed in the nasopharynx, and the flow circulation zone occurred in the olfactory airway. Hood et al. (2009) computationally modelled the air exchange in two different simplified models of the human MS (see Figure 2.21). They examined the effect of ostium size and the addition of an accessory ostium on the air exchange between the MS and NC (see Figure 2.21 (b)). They also simulated mucociliary transport and found no effect on the gas exchange between the MS and the NC. Hood et al. (2009) demonstrated that the dominant transport mechanism for the small ostium (diameter ≤ 2 mm) was diffusion; however, convection was the dominant transport mechanism for the large ostium (diameter > 2 mm). They also observed an increase in MS ventilation by adding one more accessory ostium, which is in agreement with the study by Zhu et al. (2012).

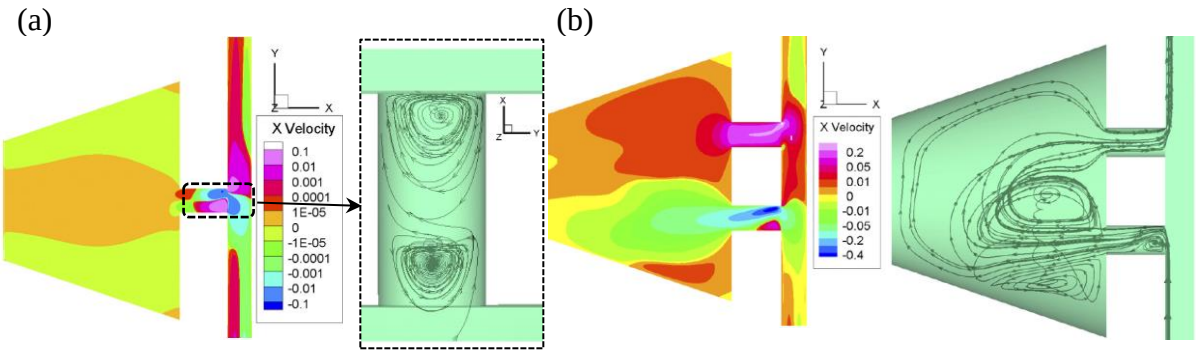

Figure 2.21: (a) x-Velocity contours and sinus streamlines for (a) a single ostium; and (b) the addition of an accessory ostium, reprinted from Hood et al. (2009), with permission from the American Physiological Society.

Gabory et al. (2017) conducted a numerical simulation of a CT image-based reconstructed model of a nasal passage, together with the sinuses, using consecutive nasal respiratory cycles. They considered the airflow and assessed the flow velocity, wall shear stress, pressure, and particle residence time using a low Reynolds number k-ω turbulence model in two consecutive respiratory cycles within the nasal passage. They found that the pressure within the sinus cavities depends on the distance to the NC airstream. For instance, the pressure in the MS, ES, and SS was lower than that in the FS for expiration, in comparison with inspiration (see Figure 2.22).

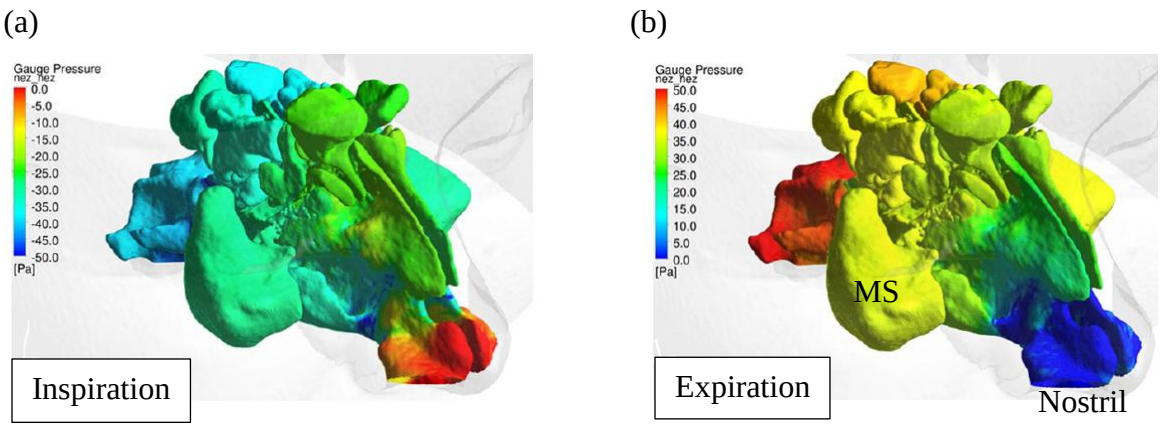

Figure 2.22: Pressure contours for the maximum flow rate for; (a) inspiration and; (b) expiration, reprinted from Gabory et al. (2017), with permission from Elsevier.

The anatomy of the NC changes after nasal surgery. Several numerical studies have demonstrated the effectiveness of the surgery on the flow structure and particle deposition pattern in the NC and MS. Frank et al. (2013) used the realistic geometries of NC before and after nasal surgery, to investigate the deposition of particles in the NC using CFD modelling. They employed a Eulerian-Lagrangian particle tracking scheme using ANSYS® Fluent to simulate the trajectories of particles injected into the nostril simulating sprays with particle sizes ranging from 10 μm to 110 μm in aerodynamic diameter. They demonstrated that the transport of particles to the unventilated regions (before the surgery) was increased after the removal of the obstructions in the NC. They also showed that the particle deposition in the

anterior region and posterior region decreased by 13% and increased by 118%, respectively (see Figure 2.23).

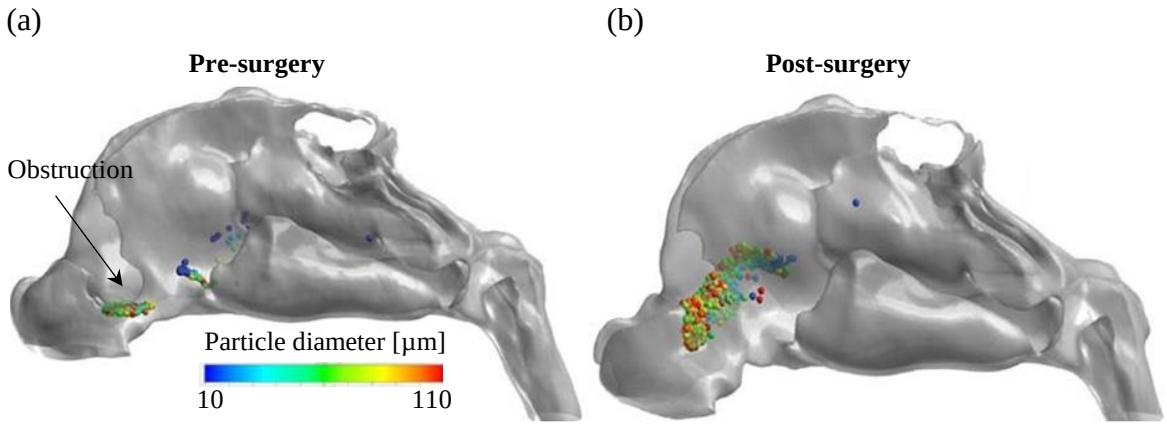

Figure 2.23: Particle deposition patterns for (a) pre-surgery; and (b) post-surgery geometries of NC, reprinted from Frank et al. (2013) with permission from Elsevier.

The effect of nasal surgery on airflow behaviour and particle deposition in the NC was investigated by Moghadas et al. (2011) using CFD modelling. They demonstrated that flow behaviour and particle deposition depends highly on the anatomy of the main passage of the NC. They found that the particle deposition in the main passage of an NC with a septal deviation was higher than that of a healthy subject. They also reported that any obstruction in the NC decreased the airflow rate and caused problems with breathing; however, a normal breathing condition was observed after the NC surgery.

In addition to the nasal surgery, where the obstruction on the NC is removed, sinus surgery is carried out when the maxillary ostium is obstructed. This type of surgery takes place for the treatment of CRS. Abouali et al. (2012) investigated the penetration of particles to the MS before and after functional endoscopic sinus surgery (FESS). They used a realistic geometry of the nose-sinus combination of a healthy subject and removed the uncinate process to simulate the FESS (marked in red in Figure 2.24 (a)). They used a Eulerian-Lagrangian particle tracking scheme and considered one-way coupling between the particle and flow phases for predicting the particles' transport/deposition patterns in the NC and MS

using ANSYS® Fluent. They explored the fact that no ventilation occurred in the MS before the FESS; however, the airflow could enter the MS after FESS (see Figure 2.24 (b-c)). They demonstrated that the deposition of particles in the MS in a post-FESS subject increased10-fold when compared with a pre-FESS subject.

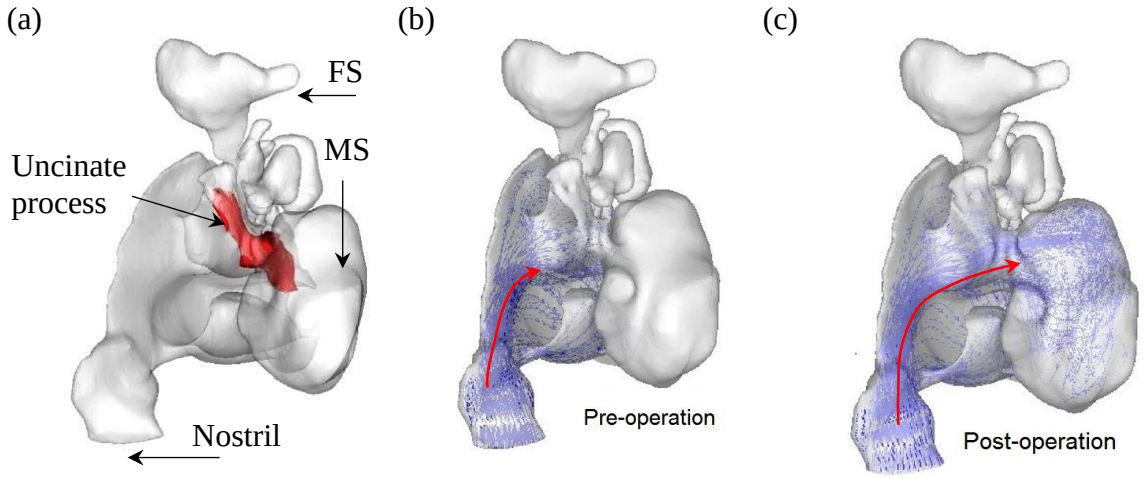

Figure 2.24: (a) An illustration of the nasal cavity and paranasal sinuses; the red part represents the removed area in the surgery; the streamlines of airflow: (b) before; and (c) after the operation for Q = 4 L/min, reprinted from Abouali et al. (2012), with permission from Elsevier.

Using the Eulerian-Lagrangian method, Shanley et al. (2008) investigated numerically the effect of particle diameter on particle deposition in the NC using a steady and laminar inlet flow. They used a realistic geometry of NC reconstructed from MRI images. They injected monodispersed particles with a diameter in the range of 1 µm and 10 µm. They showed that an increase in the diameter of the particles increases the overall deposition of particles in the NC. They also found that the deposition of particles in the nasal valve and anterior region increases with an increase in the inlet flow rate and particle size. The effect of the weight of the particles on particle deposition in the NC was investigated by Inthavong et al. (2010) using a CFD model. They used a realistic geometry of an NC, reconstructed by CT images of a human NC, to simulate the airflow behaviour at a flow rate of 7.5 L/min, as well as to predict the transport/deposition of particles with different densities and diameters. They demonstrated the size of the particle affects the particle inertia more than its density. An

increase in the particle inertia increases the deposition fraction. They also reported that the dominant mechanism of the deposition of nanoparticles is diffusion. Using a CFD model, Shi et al. (2007) examined the effect of particle diameters ranging from 1 μm to 50 μm on the particle deposition patterns in the NC for inlet flow rates of 7.5 to 20 L/min. They used a realistic geometry of an NC reconstructed by MRI scans to develop a CFD model employing a Lagrangian particle tracking scheme via the commercial CFX software package. They demonstrated that the small particles (e.g., 2 μm) could reach the posterior region of the NC and then enter the pharynx. Moreover, they investigated the effect of the roughness of the NC wall on the deposition particles and reported that particle deposition increases when the roughness of the surface is increased. Schroeter et al. (2011) investigated the effect of surface roughness on the deposition of particles in the NC by modifying the smoothness of the wall of a realistic geometry of an NC in the Mimics software package. They employed ANSYS® Fluent to simulate the particle deposition patterns in the NC using a Lagrangian particle tracking scheme and one-way coupling between the particles and the fluid phase. They reported that even a slight variation in the smoothness of the surface of the NC has a significant effect on the deposition of the particles in the NC, which implies that this information should be taken into account when the results of CFD modelling are compared with the experimental data using a 3D printed or cast nasal replica. The effect of different factors of a spray on the particle deposition in the NC was studied by Inthavong et al. (2006) using CFD modelling. Monodispersed microparticles were injected into the nostril and the deposition patterns under different insertion angles of a nasal spray were examined. The insertion angle is the angle between the nasal spray and the horizontal plane (Inthavong et al., 2006). They demonstrated that the maximum particle deposition occurred when the diameter of the particles is in the range of 10 μm to 15 μm and the insertion angle is 100°; however, the minimum deposition occurred when the insertion angle was 70°.

As reviewed above, several studies have investigated airflow features and particle depositions in the NC and sinuses in various scenarios, including different nose-sinus models, different particle sizes, different airflow rates, etc. Nevertheless, the effect of variation of the inlet airflow precondition such as inlet swirling and turbulent flow, as well as the particles' release patterns on the airflow features and particle deposition in the NC and sinuses, has not yet been studied.

2.5 Concluding Remarks and perspectives

This chapter reviewed the broad research areas associated with this thesis, in particular, an overview of TDD systems for the treatment of CRS, their advantages and related challenges, and the main factors that affect their performance in drug delivery to the NC and sinuses.

The NC is an important organ of the human body with crucial functionalities such as warming and humidification of inhaled air, filtering inhaled air to clean it of foreign particulates and accommodate the olfactory region for sensing smells. The sinuses are also responsible for critical functionalities such as lightening the skull, resonating speech sounds and producing lysozyme, which protects the nasal mucus against bacterial infections. Some diseases, such as viral infections and CRS, highly affect the functionalities of the NC and sinuses. CRS has a prevalence of 4.9% to 10.9% worldwide. CRS patients endure excessive mucus secretion, swollen mucosa, and obstructed airways due to infections in the sinuses. Hence, it is important to develop an efficient treatment for this chronic disease. Efficient medicine for the treatment of CRS is available through phage therapy; however, an efficient method of delivery of the medication (bacteriophage) is yet to be developed. TDD systems are potential candidates for delivering the drug to the sinuses.

Various existing methods of TDD were reviewed in this chapter: MDT, ECDD, and acoustically-driven therapy. MDT, as a method of active drug targeting, enhances drug delivery efficiency using an increase in the temperature of a target point to release the drugs (hyperthermia) or by guiding the particles to a target site (magnetically-guided drug delivery). The former approach, hyperthermia, should take place in a fluid medium (i.e., via blood in the human body), which cannot be used for drug delivery in human airways such as the NC or sinuses. MDT and ECDD can be used for drug delivery in a gas medium, such as human airways, and demonstrate a significant increase in drug delivery to the olfactory and OMC regions, respectively. However, due to the complexity of the NC anatomy and the poor accessibility of the sinuses, the implementation of these methods for drug delivery to the sinuses is likely to be more complicated, for which no previous study has been conducted.

Acoustically-driven therapy is divided into two categories: ultrasonic-enhanced drug delivery and low-frequency ADD. Based on the literature, the use of ultrasonic-enhanced drug delivery for therapeutic purposes is a promising active targeting approach when used in the circulation system. However, it cannot be utilised for therapeutic purposes in the respiratory system. This is because the lung and airway tissues are filled with gas, whereby the ultrasound is scattered and reflected. Hence, it is not possible to focus an ultrasound beam at a target site in the NC and sinuses. On the other hand, low-frequency acoustic fields have recently been demonstrated to be advantageous in nasal drug delivery, especially for drug delivery to the MS.

The feasibility of ADD has been demonstrated in several *in-vitro* and *in-vivo* studies. The main components of ADD are the nebulisation of the medication and the superposition of an acoustic wave on the aerosols entering the nostril. Several studies have examined the effect of fixed frequencies of 45 Hz and 100 Hz on the efficacy of ADD in drug delivery to

the MS, which demonstrated an increase in the drug deposition in the MS of at most 3-fold; however, in some cases, a negligible increase was reported. Due to the similarity of the NC-MC combination and a Helmholtz resonator, and to explain the inconsistency of the observed results, researchers have recently hypothesised that the highest drug delivery to the MS takes place at the resonance frequency of the NC-MS combination. Accordingly, they exploited the equation of a Helmholtz resonator to estimate the resonance frequency of the NC-MS and applied this to the nostril for the assessment of ADD, after which a 5-fold increase in drug delivery to the MS was reported, when compared with non-ADD approaches.

The classic equation of a Helmholtz resonator estimates the resonance frequency of a spherical cavity attached to a cylindrical neck, which differs significantly from the complex geometry of an NC-MS. Therefore, it is critical to develop a model to estimate the accurate resonance frequency of the NC-MS combination and assess it for the variations in geometrical parameters, which will be discussed in Chapter 3. To improve ADD efficiency, developing an understanding of the flow features in the NC-MS combination under the effect of an external acoustic wave is necessary, and will be investigated in Chapter 4 using CFD modelling. The effect of the application of an accurate resonance frequency in the ADD technique for the assessment of the drug deposition in a realistic model of NC-MS should be investigated using *in-vitro* experiments to verify the hypothesis that the highest ADD efficiency occurs at the resonance frequency, and this is considered in Chapter 5. In addition to the acoustic component of the ADD technique, the characteristics of the drug nebulisation and inlet airflow are crucial in drug delivery efficacy. The effect of various inlet airflow rates on drug delivery to the NC and MS were examined in several studies, where no significant increase in the efficiency of drug delivery to the NC and MS were reported. However, Ari et al. (2015) experimentally showed that different nasal mask configurations affect the performance of drug delivery to the lungs. This implies that the inlet airflow preconditioning,

and particle distribution pattern at the inlet, can have an impact on aerosol deposition and transport in different regions of the NC. Accordingly, the effect of different inlet flow preconditionings, such as turbulent and swirling flows, as well as the effect of the nozzle diameter, will be presented in Chapter 6. The thesis is concluded in Chapter 7, which also provides recommendations for future work.

2.6 References

Abouali, O., Keshavarzian, E., Ghalati, P. F., Faramarzi, A., Ahmadi, G., & Bagheri, M. H. (2012). Micro and nanoparticle deposition in human nasal passage pre and post virtual maxillary sinus endoscopic surgery. *Respiratory Physiology & Neurobiology, 181*(3), 335-345.

Aggarwal, R., Cardozo, A., & Homer, J. J. (2004). The assessment of topical nasal drug distribution. *Clinical Otolaryngology and Allied Sciences, 29*(3), 201-205.

Ally, J. M. (2010). *Magnetically targeted deposition and retention of particles in the airways for drug delivery.* (PhD thesis), University of Alberta, Canada.

Alster, M. (1972). Improved calculation of resonant frequencies of Helmholtz resonators. *Journal of Sound and Vibration, 24*(1), 63-85.

Ari, A., de Andrade, A. D., Sheard, M., AlHamad, B., & Fink, J. B. (2015). Performance comparisons of jet and mesh nebulizers using different interfaces in simulated spontaneously breathing adults and children. *Journal of Aerosol Medicine and Pulmonary Drug Delivery, 28*(4), 281-289.

Bakke, H., Samdal, H. H., Holst, J., Oftung, F., Haugen, I. L., Kristoffersen, A. C., Haugan, A., Janakova, L., Korsvold, G. E., Krogh, G., Andersen, E. A., Djupesland, P., Holand, T., Rappuoli, R., & Haneberg, B. (2006). Oral spray immunization may be an alternative to intranasal vaccine delivery to induce systemic antibodies but not nasal mucosal or cellular immunity. *Scandinavian Journal of Immunology, 63*(3), 223-231.

Ballantine, H., Bell, E., & Manlapaz, J. (1960). Progress and problems in the neurological applications of focused ultrasound. *Journal of Neurosurgery, 17*(5), 858-876.

Benninger, M. S., Anon, J., & Mabry, R. L. (1997). The medical management of rhinosinusitis. *Otolaryngology—Head and Neck Surgery, 117*(3), 41-49.

Berger, W. E., Godfrey, J. W., & Slater, A. L. (2007). Intranasal corticosteroids: The development of a drug delivery device for fluticasone furoate as a potential step toward improved compliance. *Expert Opinion on Drug Delivery, 4*(6), 689-701.

Bertrand, N., & Leroux, J. C. (2012). The journey of a drug-carrier in the body: An anatomo-physiological perspective. *Journal of Controlled Release, 161*(2), 152-163.

Bhattacharyya, N. (2012). Functional limitations and workdays lost associated with chronic rhinosinusitis and allergic rhinitis. *American Journal of Rhinology & Allergy, 26*(2), 120-122.

Blanton, P. L., & Biggs, N. L. (1969). Eighteen hundred years of controversy: The paranasal sinuses. *American Journal of Anatomy, 124*(2), 135-147.

Bologa, A., & Bologa, A. (2001). Electrohydrodynamic instability of droplets as an influencing factor for aerosol space charge generation. *Journal of Electrostatics, 51*, 470-475.

Bose, S., Datta, A., Ganguly, R., & Banerjee, M. (2013). Lagrangian magnetic particle tracking through stenosed artery under pulsatile flow condition. *Journal of Nanotechnology in Engineering and Medicine, 4*(3), 1-10.

Boysen, M. (1982). The surface structure of the human nasal mucosa. I. Ciliated and metaplastic epithelium in normal individuals. A correlated study by scanning/transmission electron and light microscopy. *Virchows Archiv. B, Cell Pathology Including Molecular Pathology, 40*(3), 279-294.

Cheng, Y., Holmes, T., Gao, J., Guilmette, R., Li, S., Surakitbanharn, Y., & Rowlings, C. (2001). Characterization of nasal spray pumps and deposition pattern in a replica of the human nasal airway. *Journal of Aerosol Medicine, 14*(2), 267-280.

Cho, Y. S., Choi, S. H., Park, K. H., Park, H. J., Kim, J. W., Moon, I. J., Rhee, C. S., Kim, K. S., Sun, D. I., Lee, S. H., Koo, J. W., Koh, Y. W., Lee, K. H., Lee, S. W., Oh, K. W., Pyo, E. Y., Lee, A., Kim, Y. T., & Lee, C. H. (2010). Prevalence of otolaryngologic diseases in South Korea: Data from the Korea national health and nutrition examination survey 2008. *Clinical and Experimental Otorhinolaryngology, 3*(4), 183-193.

Chung, S.-K., & Kim, S. K. (2008). Digital particle image velocimetry studies of nasal airflow. *Respiratory Physiology & Neurobiology, 163*(1-3), 111-120.

Cole, P. (1992). Nasal and oral airflow resistors: Site, function, and assessment. *Archives of Otolaryngology--Head & Neck Surgery, 118*(8), 790-793.

Cole, P. (1993). *Nasal respiratory function*. St Louis: Mosby-Year Book Inc.

Cole, P. (2003). The four components of the nasal valve. *American Journal of Rhinology, 17*(2), 107-110.

Crowe, C. T. (2005). *Multiphase flow handbook*. United States: CRC press.

Darquenne, C. (2020). Deposition mechanisms. *Journal of Aerosol Medicine and Pulmonary Drug Delivery, 33*(4), 181-185.

Datta, S., Coussios, C.-C., McAdory, L. E., Tan, J., Porter, T., De Courten-Myers, G., & Holland, C. K. (2006). Correlation of cavitation with ultrasound enhancement of thrombolysis. *Ultrasound in Medicine & Biology, 32*(8), 1257-1267.

Djupesland, P. G. (2013). Nasal drug delivery devices: Characteristics and performance in a clinical perspective-a review. *Drug Delivery and Translational Research, 3*(1), 42-62.

Djupesland, P. G., Skatvedt, O., & Borgersen, A. K. (2001). Dichotomous physiological effects of nocturnal external nasal dilation in heavy snorers: The answer to a rhinologic controversy? *American Journal of Rhinology, 15*(2), 95-104.

Dolovich, M. B., & Dhand, R. (2011). Aerosol drug delivery: Developments in device design and clinical use. *The Lancet, 377*(9770), 1032-1045.

Doorly, D., Taylor, D., Franke, P., & Schroter, R. (2008). Experimental investigation of nasal airflow. *Proceedings of the Institution of Mechanical Engineers, Part H: Journal of Engineering in Medicine, 222*(4), 439-453.

Drake, R., Vogl, A. W., Mitchell, A. W., Tibbitts, R., & Richardson, P. (2020). *Gray's Atlas of Anatomy E-Book*: Elsevier Health Sciences.

Durand, M., Pourchez, J., Aubert, G., Le Guellec, S., Navarro, L., Forest, V., Rusch, P., & Cottier, M. (2011). Impact of acoustic airflow nebulization on intrasinus drug deposition of a human plastinated nasal cast: New insights into the mechanisms involved. *International Journal of Pharmaceutics, 421*(1), 63-71.

Durand, M., Rusch, P., Granjon, D., Chantrel, G., Prades, J. M., Dubois, F., Esteve, D., Pouget, J. F., & Martin, C. (2001). Preliminary study of the deposition of aerosol in the maxillary sinuses using a plastinated model. *Journal of Aerosol Medicine, 14*(1), 83-93.

El-Merhie, A., Navarro, L., Delavenne, X., Leclerc, L., & Pourchez, J. (2016). A new strategy to improve drug delivery to the maxillary sinuses: The frequency sweep acoustic airflow. *Pharmaceutical Research, 33*(5), 1074-1084.

Everbach, E. C., & Francis, C. W. (2000). Cavitational mechanisms in ultrasound-accelerated thrombolysis at 1 MHz. *Ultrasound in Medicine & Biology, 26*(7), 1153-1160.

Farnoud, A., Baumann, I., Rashidi, M. M., Schmid, O., & Gutheil, E. (2020). Simulation of patient-specific bidirectional pulsating nasal aerosol dispersion and deposition with clockwise 45° and 90° nosepieces. *Computers in Biology and Medicine, 123*, 1-15.

Farnoud, A., Cui, X., Baumann, I., & Gutheil, E. (2017). *Numerical simulation of the dispersion and deposition of a spray carried by a pulsating airflow in a patient-specific human nasal cavity.* Paper presented at the 28th Conference on Liquid Atomization and Spray Systems, Valencia, Spain.

Ferin, J., Mercer, T., & Leach, L. (1983). The effect of aerosol charge on the deposition and clearance of TiO2 particles in rats. *Environmental Research, 31*(1), 148-151.

Fodil, R., Brugel-Ribere, L., Croce, C., Sbirlea-Apiou, G., Larger, C., Papon, J. F., Delclaux, C., Coste, A., Isabey, D., & Louis, B. (2005). Inspiratory flow in the nose: A model coupling flow and vasoerectile tissue distensibility. *Journal of Applied Physiology, 98*(1), 288-295.

Frank, D. O., Kimbell, J. S., Cannon, D., & Rhee, J. S. (2013). Computed intranasal spray penetration: Comparisons before and after nasal surgery. *International Forum of Allergy & Rhinology, 3*(1), 48-55.

Fry, F. (1970). Charge distribution on polystyrene aerosols and deposition in the human nose. *Journal of Aerosol Science, 1*(2), 135-146.

Fry, F., & Black, A. (1973). Regional deposition and clearance of particles in the human nose. *Journal of Aerosol Science, 4*(2), 113-124.

Fry, W., & Fry, F. (1960). Fundamental neurological research and human neurosurgery using intense ultrasound. *IRE Transactions on Medical Electronics, 7*(3), 166-181.

Gabory, L., Reville, N., Baux, Y., Boisson, N., & Bordenave, L. (2017). Numerical simulation of two consecutive nasal respiratory cycles: Toward a better understanding of nasal physiology. *International Forum of Allergy & Rhinology, 8*(6), 676-685.

Galvin, P., Thompson, D., Ryan, K. B., McCarthy, A., Moore, A. C., Burke, C. S., Dyson, M., MacCraith, B. D., Gun'ko, Y. K., & Byrne, M. T. (2012). Nanoparticle-based drug delivery: Case studies for cancer and cardiovascular applications. *Cellular and Molecular Life Sciences, 69*(3), 389-404.

Ghanadi, F. (2015). *Application of a Helmholtz resonator excited by grazing flow for manipulation of a turbulent boundary layer*. (PhD thesis), The University of Adelaide, Australia.

Gilchrist, R. K., Medal, R., Shorey, W. D., Hanselman, R. C., Parrott, J. C., & Taylor, C. B. (1957). Selective inductive heating of lymph nodes. *Annals of Surgery, 146*(4), 596-606.

Gillespie, M. B., & Osguthorpe, J. D. (2004). Pharmacologic management of chronic rhinosinusitis, alone or with nasal polyposis. *Current Allergy and Asthma Reports, 4*(6), 478-485.

Girardin, M., Bilgen, E., & Arbour, P. (1983). Experimental study of velocity fields in a human nasal fossa by laser anemometry. *Annals of Otology, Rhinology & Laryngology, 92*(3), 231-236.

Grzincich, G., Capra, L., Cammarata, M. G., Spaggiari, C., & Pisi, G. (2004). Effectiveness of intranasal corticosteroids. *Acta Bio Medica Atenei Parmensis, 75*(1), 22-25.

Guillerm, R., Badre, R., Flottes, L., Riu, R., & Rey, A. (1959). A new method of aerosol penetration into the sinuses. *La Presse Medicale, 67*(27), 1097-1098.

Hadilou, N., Khoshgenab, A. N., Amoli-Diva, M., & Sadighi-Bonabi, R. (2018). Remote trice light, temperature, and ph-actuation of switchable magneto-plasmonic nanocarriers for combinational photothermal and controlled/targeted chemotherapies. *Journal of Pharmaceutical Sciences, 107*(12), 3123-3133.

Häfeli, U. O. (2004). Magnetically modulated therapeutic systems. *International Journal of Pharmaceutics, 277*(1), 19-24.

Hahn, I., Scherer, P. W., & Mozell, M. M. (1993). Velocity profiles measured for airflow through a large-scale model of the human nasal cavity. *Journal of Applied Physiology, 75*(5), 2273-2287.

Hairfield, W. M., Warren, D. W., Hinton, V. A., & Seaton, D. L. (1987). Inspiratory and expiratory effects of nasal breathing. *The Cleft Palate Journal, 24*(3), 183-189.

Hamilos, D. L. (2011). Chronic rhinosinusitis: Epidemiology and medical management. *Journal of Allergy and Clinical Immunology, 128*(4), 693-707.

Hardy, J., Lee, S., & Wilson, C. (1985). Intranasal drug delivery by spray and drops. *Journal of Pharmacy and Pharmacology, 37*(5), 294-297.

Harris, A. S., Nilsson, I. M., Wagner, Z. G., & Alkner, U. (1986). Intranasal administration of peptides: Nasal deposition, biological response, and absorption of desmopressin. *Journal of Pharmaceutical Sciences, 75*(11), 1085-1088.

Harris, A. S., Svensson, E., Wagner, Z. G., Lethagen, S., & Nilsson, I. M. (1988). Effect of viscosity on particle size, deposition, and clearance of nasal delivery systems containing desmopressin. *Journal of Pharmaceutical Sciences, 77*(5), 405-408.

Hedayati, N., Ramiar, A., & Larimi, M. (2018). Investigating the effect of external uniform magnetic field and temperature gradient on the uniformity of nanoparticles in drug delivery applications. *Journal of Molecular Liquids, 272*, 301-312.

Hemon, P., Santi, F., & Amandolèse. (2004). On the pressure oscillations inside a deep cavity excited by a grazing airflow. *European Journal of Mechanics-B/Fluids, 23*(4), 617-632.

Hilton, C., Wiedmann, T., Martin, M. S., Humphrey, B., Schleiffarth, R., & Rimell, F. (2008). Differential deposition of aerosols in the maxillary sinus of human cadavers by particle size. *American Journal of Rhinology & Allergy, 22*(4), 395-398.

Hood, C. M., Schroter, R. C., Doorly, D. J., Blenke, E. J., & Tolley, N. S. (2009). Computational modeling of flow and gas exchange in models of the human maxillary sinus. *Journal of Applied Physiology, 107*(4), 1195-1203.

Hörschler, I., Brücker, C., Schröder, W., & Meinke, M. (2006). Investigation of the impact of the geometry on the nose flow. *European Journal of Mechanics-B/Fluids, 25*(4), 471-490.

Hosseini, S., Schuman, T. A., Walenga, R., Wilkins Jr, J. V., Babiskin, A., & Golshahi, L. (2020). Use of anatomically-accurate 3-dimensional nasal airway models of adult human subjects in a novel methodology to identify and evaluate the internal nasal valve. *Computers in Biology and Medicine, 123*, 1-10.

Hounam, R., Black, A., & Walsh, M. (1971). The deposition of aerosol particles in the nasopharyngeal region of the human respiratory tract. *Journal of Aerosol Science, 2*(1), 47-61.

Howard, C. Q., Cazzolato, B. S., & Hansen, C. H. (2000). Exhaust stack silencer design using finite element analysis. *Noise Control Engineering Journal, 48*(4), 113-120.

Illum, L. (2003). Nasal drug delivery—possibilities, problems and solutions. *Journal of Controlled Release, 87*(1-3), 187-198.

Illum, L. (2012). Nasal drug delivery—recent developments and future prospects. *Journal of Controlled Release, 161*(2), 254-263.

Inthavong, K., Tian, Z., Li, H., Tu, J., Yang, W., Xue, C., & Li, C. G. (2006). A numerical study of spray particle deposition in a human nasal cavity. *Aerosol Science and Technology, 40*(11), 1034-1045.

Inthavong, K., Tian, Z. F., Tu, J. Y., Yang, W., & Xue, C. (2008). Optimising nasal spray parameters for efficient drug delivery using computational fluid dynamics. *Computers in Biology and Medicine, 38*(6), 713-726.

Inthavong, K., Tu, J., & Heschl, C. (2011). Micron particle deposition in the nasal cavity using the v2–f model. *Computers & Fluids, 51*(1), 184-188.

Inthavong, K., Wen, J., & Tu, J.-Y. (2010). Modelling the inhalation of drug aerosols in a human nasal cavity. *Journal of Biomedical Science and Engineering, 3*(1), 52-58.

Iro, H., Mayr, S., Wällisch, C., Schick, B., & Wigand, M. E. (2004). Endoscopic sinus surgery: Its subjective medium-term outcome in chronic rhinosinusitis. *Rhinology, 42*(4), 200-206.

Jeffers, J., Feng, R., Fowlkes, J., Brenner, D., & Cain, C. (1991). *Sonodynamic therapy: Activation of anticancer agents with ultrasound.* Paper presented at the IEEE 1991 Ultrasonics Symposium, Orlando, FL, USA.

Karner, S., & Urbanetz, N. A. (2011). The impact of electrostatic charge in pharmaceutical powders with specific focus on inhalation-powders. *Journal of Aerosol Science, 42*(6), 428-445.

Keith, P., Nieminen, J., Hollingworth, K., & Dolovich, J. (2000). Efficacy and tolerability of fluticasone propionate nasal drops 400 microgram once daily compared with placebo for the treatment of bilateral polyposis in adults. *Clinical & Experimental Allergy: Journal of the British Society for Allergy & Clinical Immunology, 30*(10), 1460-1468.

Kelly, J., Prasad, A., & Wexler, A. (2000). Detailed flow patterns in the nasal cavity. *Journal of Applied Physiology, 89*(1), 323-337.

Kennedy, J. E. (2005). High-intensity focused ultrasound in the treatment of solid tumours. *Nature Reviews Cancer, 5*(4), 321-327.

Keyhani, K., Scherer, P., & Mozell, M. (1995). Numerical simulation of airflow in the human nasal cavity. *Journal of Biomechanical Engineering, 117*(4), 429-441.

Kim, S., & Chung, S. (2004). An investigation on airflow in disordered nasal cavity and its corrected models by tomographic PIV. *Measurement Science and Technology, 15*(6), 1090-1096.

Kinoshita, M., & Hynynen, K. (2006). Mechanism of porphyrin-induced sonodynamic effect: Possible role of hyperthermia. *Radiation Research, 165*(3), 299-306.

Krstić, M. (2006). Mixing control for jet flows. In G. D. Roy (Ed.), *Combustion Processes in Propulsion* (pp. 87-96). Burlington: Butterworth-Heinemann.

Larimi, M., Ramiar, A., & Ranjbar, A. (2016). Numerical simulation of magnetic drug targeting with Eulerian-Lagrangian model and effect of viscosity modification due to diabetics. *Applied Mathematics and Mechanics, 37*(12), 1631-1646.

Laube, B. L. (2007). Devices for aerosol delivery to treat sinusitis. *Journal of Aerosol Medicine, 20*(1), 5-18.

Leclerc, L., El-Merhie, A., Navarro, L., Prévôt, N., Durand, M., & Pourchez, J. (2015). Impact of acoustic airflow on intrasinus drug deposition: New insights into the vibrating mode and the optimal acoustic frequency to enhance the delivery of nebulized antibiotic. *International Journal of Pharmaceutics, 494*(1), 227-234.

Leclerc, L., Pourchez, J., Aubert, G., Leguellec, S., Vecellio, L., Cottier, M., & Durand, M. (2014). Impact of airborne particle size, acoustic airflow and breathing pattern on delivery of nebulized antibiotic into the maxillary sinuses using a realistic human nasal replica. *Pharmaceutical Research, 31*(9), 2335-2343.

Lee, J.-H., Na, Y., Kim, S.-K., & Chung, S.-K. (2010). Unsteady flow characteristics through a human nasal airway. *Respiratory Physiology & Neurobiology, 172*(3), 136-146.

Leslie, T., & Kennedy, J. (2007). High intensity focused ultrasound in the treatment of abdominal and gynaecological diseases. *International Journal of Hyperthermia, 23*(2), 173-182.

Lewis Jr, G., Olbricht, W., & Lewis Sr, G. (2007). Acoustic targeted drug delivery in neurological tissue. *The Journal of the Acoustical Society of America, 122*(5), 3007-3007.

Liu, T., Cooper, T., Earnshaw, J., & Cervin, A. (2018). Disease burden and productivity cost of chronic rhinosinusitis patients referred to a tertiary centre in Australia. *Australian Journal of Otolaryngology, 1*(1), 1-9.

Liu, Y., Chen, D., Shang, P., & Yin, D.-C. (2019). A review of magnet systems for targeted drug delivery. *Journal of Controlled Release, 302*, 90-104.

Liu, Y., Johnson, M. R., Matida, E. A., Kherani, S., & Marsan, J. (2009). Creation of a standardized geometry of the human nasal cavity. *Journal of Applied Physiology, 106*(3), 784-795.

Liu, Y., Matida, E. A., & Johnson, M. R. (2010). Experimental measurements and computational modeling of aerosol deposition in the Carleton-Civic standardized human nasal cavity. *Journal of Aerosol Science, 41*(6), 569-586.

Lübbe, A. S., Bergemann, C., Riess, H., Schriever, F., Reichardt, P., Possinger, K., Matthias, M., Dörken, B., Herrmann, F., Gürtler, R., Hohenberger, P., Haas, N., Sohr, R., Sander, B., Lemke, A. J., Ohlendorf, D., Huhnt, W., & Huhn, D. (1996). Clinical experiences with magnetic drug targeting: A phase I study with 4'-epidoxorubicin in 14 patients with advanced solid tumors. *Cancer Research, 56*(20), 4686-4693.

Lund, V. J. (2005). Maximal medical therapy for chronic rhinosinusitis. *Otolaryngologic Clinics of North America, 38*(6), 1301-1310.

Lundberg, J., Farkas-Szallasi, T., Weitzberg, E., Rinder, J., Lidholm, J., Änggård, A., Hökfelt, T., Lundberg, J., & Alving, K. (1995). High nitric oxide production in human paranasal sinuses. *Nature Medicine, 1*(4), 370-373.

Lynn, J. G., Zwemer, R. L., Chick, A. J., & Miller, A. E. (1942). A new method for the generation and use of focused ultrasound in experimental biology. *The Journal of General Physiology, 26*(2), 179.

Maniscalco, M., Sofia, M., Weitzberg, E., & Lundberg, J. (2006). Sounding airflow enhances aerosol delivery into the paranasal sinuses. *European Journal of Clinical Investigation, 36*(7), 509-513.

Maniscalco, M., Weitzberg, E., Sundberg, J., Sofia, M., & Lundberg, J. (2003). Assessment of nasal and sinus nitric oxide output using single-breath humming exhalations. *European Respiratory Journal, 22*(2), 323-329.

Marple, B. F., Stankiewicz, J. A., Baroody, F. M., Chow, J. M., Conley, D. B., Corey, J. P., Ferguson, B. J., Kern, R. C., Lusk, R. P., & Naclerio, R. M. (2009). Diagnosis and management of chronic rhinosinusitis in adults. *Postgraduate Medicine, 121*(6), 121-139.

Marshall, J. S., & Li, S. (2014). *Adhesive particle flow*: Cambridge University Press.

Mathieu, J.-B., Beaudoin, G., & Martel, S. (2006). Method of propulsion of a ferromagnetic core in the cardiovascular system through magnetic gradients generated by an MRI system. *IEEE Transactions on Biomedical Engineering, 53*(2), 292-299.

McHale, A. P., Callan, J. F., Nomikou, N., Fowley, C., & Callan, B. (2016). Sonodynamic therapy: Concept, mechanism and application to cancer treatment. *Advances in Experimental Medicine and Biology, 880*, 429-450.

Meissner, M. (2002). Excitation of Helmholtz resonator by grazing air flow. *Journal of Sound and Vibration, 256*(2), 382-388.

Melandri, C., Tarroni, G., Prodi, V., De Zaiacomo, T., Formignani, M., & Lombardi, C. C. (1983). Deposition of charged particles in the human airways. *Journal of Aerosol Science, 14*(5), 657-669.

Meltzer, E. O., Hamilos, D. L., Hadley, J. A., Lanza, D. C., Marple, B. F., Nicklas, R. A., Bachert, C., Baraniuk, J., Baroody, F. M., & Benninger, M. S. (2004). Rhinosinusitis: Establishing definitions for clinical research and patient care. *Journal of Allergy and Clinical Immunology, 114*(6), 155-212.

Merkus, P., Ebbens, F. A., Muller, B., & Fokkens, W. J. (2006). Influence of anatomy and head position on intranasal drug deposition. *European Archives of Otorhinolaryngology, 263*(9), 827-832.

Mistry, A., Stolnik, S., & Illum, L. (2009). Nanoparticles for direct nose-to-brain delivery of drugs. *International Journal of Pharmaceutics, 379*(1), 146-157.

Moffa, A., Costantino, A., Rinaldi, V., Sabatino, L., Trecca, E. M. C., Baptista, P., Campisi, P., Cassano, M., & Casale, M. (2019). Nasal delivery devices: A comparative study on cadaver model. *BioMed Research International, 2019*, 1-6.

Moghadam, S. J., Navarro, L., Leclerc, L., Hodin, S., & Pourchez, J. (2018). Toward smart nebulization: Engineering acoustic airflow to penetrate maxillary sinuses in chronic rhinosinusitis. *International Journal of Pharmaceutics, 546*(1-2), 188-193.

Moghadas, H., Abouali, O., Faramarzi, A., & Ahmadi, G. (2011). Numerical investigation of septal deviation effect on deposition of nano/microparticles in human nasal passage. *Respiratory Physiology & Neurobiology, 177*(1), 9-18.

Möller, W., Münzing, W., & Canis, M. (2010). Clinical potential of pulsating aerosol for sinus drug delivery. *Expert Opinion on Drug Delivery, 7*(11), 1239-1245.

Möller, W., Saba, G. K., Haussinger, K., Becker, S., Keller, M., & Schuschnig, U. (2011). Nasally inhaled pulsating aerosols: Lung, sinus and nose deposition. *Rhinology, 49*(3), 286-291.

Möller, W., Schuschnig, U., Bartenstein, P., Meyer, G., Häussinger, K., Schmid, O., & Becker, S. (2014). Drug delivery to paranasal sinuses using pulsating aerosols. *Journal of Aerosol Medicine and Pulmonary Drug Delivery, 27*(4), 255-263.

Möller, W., Schuschnig, U., Celik, G., Münzing, W., Bartenstein, P., Häussinger, K., Kreyling, W. G., Knoch, M., Canis, M., & Becker, S. (2013). Topical drug delivery in chronic rhinosinusitis patients before and after sinus surgery using pulsating aerosols. *PloS One, 8*(9), 1-10.

Möller, W., Schuschnig, U., Khadem Saba, G., Meyer, G., Junge-Hülsing, B., Keller, M., & Häussinger, K. (2010). Pulsating aerosols for drug delivery to the sinuses in healthy volunteers. *Otolaryngology—Head and Neck Surgery, 142*(3), 382-388.

Möller, W., Schuschnig, U., Meyer, G., Mentzel, H., & Keller, M. (2008). Ventilation and drug delivery to the paranasal sinuses: Studies in a nasal cast using pulsating airflow. *Rhinology, 46*(3), 213-220.

Mondal, S., Dorozhkin, S. V., & Pal, U. (2018). Recent progress on fabrication and drug delivery applications of nanostructured hydroxyapatite. *Wiley Interdisciplinary Reviews Nanomedicine Nanobiotechnology, 10*(4), 1-32.

Mutsch, M., Zhou, W., Rhodes, P., Bopp, M., Chen, R. T., Linder, T., Spyr, C., & Steffen, R. (2004). Use of the inactivated intranasal influenza vaccine and the risk of Bell's palsy in Switzerland. *The New England Journal of Medicine, 350*(9), 896-903.

Navarro, L., Leclerc, L., & Pourchez, J. (2019). Does acoustic overlay of music improve aerosol penetration into maxillary sinuses? *Online Journal of Otolaryngology and Rhinology, 1*(4), 1-3.

Newman, S. P., Morén, F., & Clarke, S. W. (1987). The nasal distribution of metered does inhalers. *The Journal of Laryngology & Otology, 101*(2), 127-132.

Newman, S. P., Morén, F., & Clarke, S. W. (1988). Deposition pattern of nasal sprays in man. *Rhinology, 26*(2), 111-120.

Nichol, K. L., Mendelman, P. M., Mallon, K. P., Jackson, L. A., Gorse, G. J., Belshe, R. B., Glezen, W. P., & Wittes, J. (1999). Effectiveness of live, attenuated intranasal influenza virus vaccine in healthy, working adults: A randomized controlled trial. *Journal of the American Medical Association (JAMA), 282*(2), 137-144.

Penttilä, M., Poulsen, P., Hollingworth, K., & Holmström, M. (2000). Dose-related efficacy and tolerability of fluticasone propionate nasal drops 400 microg once daily and twice daily in the treatment of bilateral nasal polyposis: A placebo-controlled randomized study in adult patients. *Clinical and Experimental Allergy: Journal of the British Society for Allergy and Clinical Immunology, 30*(1), 94-102.

Pilan, R. R., Pinna, F. d. R., Bezerra, T. F., Mori, R. L., Padua, F. G., Bento, R. F., Perez-Novo, C., Bachert, C., & Voegels, R. L. (2012). Prevalence of chronic rhinosinusitis in Sao Paulo. *Rhinology, 50*(2), 129-138.

Pitt, W. G., Husseini, G. A., & Staples, B. J. (2004). Ultrasonic drug delivery–a general review. *Expert Opinion on Drug Delivery, 1*(1), 37-56.

Pourmehran, O., Arjomandi, M., Cazzolato, B., Tian, Z., Vreugde, S., Javadiyan, S., Psaltis, A. J., & Wormald, P.-J. (2021). Acoustic drug delivery to the maxillary sinus. *International Journal of Pharmaceutics,* (In Press), 120927.

Pourmehran, O., Gorji, T. B., & Gorji-Bandpy, M. (2016). Magnetic drug targeting through a realistic model of human tracheobronchial airways using computational fluid and particle dynamics. *Biomechanics and Modeling in Mechanobiology, 15*(5), 1355-1374.

Prodi, V., & Mularoni, A. (1985). Electrostatic lung deposition experiments with humans and animals. *Annals of Occupational Hygiene, 29*(2), 229-240.

Randell, S. H., & Boucher, R. C. (2006). Effective mucus clearance is essential for respiratory health. *American Journal of Respiratory Cell and Molecular Biology, 35*(1), 20-28.

Rennie, C. E., Hood, C. M., Blenke, E. J., Schroter, R. S., Doorly, D. J., Jones, H., Towey, D., & Tolley, N. S. (2011). Physical and computational modeling of ventilation of the maxillary sinus. *Otolaryngology--Head and Neck Surgery, 145*(1), 165-170.

Riegler, J., Lau, K. D., Garcia-Prieto, A., Price, A. N., Richards, T., Pankhurst, Q. A., & Lythgoe, M. F. (2011). Magnetic cell delivery for peripheral arterial disease: A theoretical framework. *Medical Physics, 38*(7), 3932-3943.

Riegler, J., Wells, J. A., Kyrtatos, P. G., Price, A. N., Pankhurst, Q. A., & Lythgoe, M. F. (2010). Targeted magnetic delivery and tracking of cells using a magnetic resonance imaging system. *Biomaterials, 31*(20), 5366-5371.

Roberts, W. W., Hall, T. L., Ives, K., Wolf, J. S., Fowlkes, J. B., & Cain, C. A. (2006). Pulsed cavitational ultrasound: A noninvasive technology for controlled tissue ablation (histotripsy) in the rabbit kidney. *The Journal of Urology, 175*(2), 734-738.

Rosenblum, D., Joshi, N., Tao, W., Karp, J. M., & Peer, D. (2018). Progress and challenges towards targeted delivery of cancer therapeutics. *Nature Communications, 9*(1), 1-12.

Rosenfeld, R. M., Andes, D., Bhattacharyya, N., Cheung, D., Eisenberg, S., Ganiats, T. G., Gelzer, A., Hamilos, D., Haydon III, R. C., & Hudgins, P. A. (2007). Clinical practice guideline: Adult sinusitis. *Otolaryngology—Head and Neck Surgery, 137*(3), S1-S31.

Rosenthal, I., Sostaric, J. Z., & Riesz, P. (2004). Sonodynamic therapy—a review of the synergistic effects of drugs and ultrasound. *Ultrasonics Sonochemistry, 11*(6), 349-363.

Schmidt, M. C., Peter, H., Lang, S. R., Ditzinger, G., & Merkle, H. P. (1998). In vitro cell models to study nasal mucosal permeability and metabolism. *Advanced Drug Delivery Reviews, 29*(1-2), 51-79.

Schroeter, J. D., Garcia, G. J., & Kimbell, J. S. (2011). Effects of surface smoothness on inertial particle deposition in human nasal models. *Journal of Aerosol Science, 42*(1), 52-63.

Sengupta, S., & Balla, V. K. (2018). A review on the use of magnetic fields and ultrasound for non-invasive cancer treatment. *Journal of Advanced Research, 14*, 97-111.

Shanley, K. T., Zamankhan, P., Ahmadi, G., Hopke, P. K., & Cheng, Y.-S. (2008). Numerical simulations investigating the regional and overall deposition efficiency of the human nasal cavity. *Inhalation Toxicology, 20*(12), 1093-1100.

Shapiro, B., Kulkarni, S., Nacev, A., Sarwar, A., Preciado, D., & Depireux, D. A. (2014). Shaping magnetic fields to direct therapy to ears and eyes. *Annual Review of Biomedical Engineering, 16*(1), 455-481.

Shi, H., Kleinstreuer, C., & Zhang, Z. (2007). Modeling of inertial particle transport and deposition in human nasal cavities with wall roughness. *Journal of Aerosol Science, 38*(4), 398-419.

Shrestha, K., Van Strien, J., Singh, N., & Inthavong, K. (2020). Primary break-up and atomization characteristics of a nasal spray. *PloS One, 15*(8), e0236063.

Singh, A., & Massey, C. J. (2017). Paranasal sinus anatomy. *Drugs & Diseases: Anatomy*. Retrieved from https://emedicine.medscape.com/article/1899145-overview

Stammberger, H. (1989). History of rhinology: Anatomy of the paranasal sinuses. *Rhinology, 27*(3), 197-210.

Stammberger, H., & Posawetz, W. (1990). Functional endoscopic sinus surgery. *European Archives of Otorhinolaryngology, 247*(2), 63-76.

Subramaniam, R. P., Richardson, R. B., Morgan, K. T., Kimbell, J. S., & Guilmette, R. A. (1998). Computational fluid dynamics simulations of inspiratory airflow in the human nose and nasopharynx. *Inhalation Toxicology, 10*(2), 91-120.

Suman, J. D. (2013). Current understanding of nasal morphology and physiology as a drug delivery target. *Drug Delivery and Translational Research, 3*(1), 4-15.

Suman, J. D., Laube, B. L., & Dalby, R. (1999). Comparison of nasal deposition and clearance of aerosol generated by a nebulizer and an aqueous spray pump. *Pharmaceutical Research, 16*(10), 1648-1652.

Suman, J. D., Laube, B. L., & Dalby, R. (2006). Validity of in vitro tests on aqueous spray pumps as surrogates for nasal deposition, absorption, and biologic response. *Journal*

of Aerosol Medicine : The Official Journal of The International Society for Aerosols in Medicine, 19(4), 510-521.

Swift, D. L., & Proctor, D. F. (1977). Access of air to the respiratory tract. In J. D. Brain, D. F. Proctor, & L. M. Reid (Eds.), *Respiratory Defense Mechanisms* (pp. 63-93). New York: Marcel Dekker.

Tan, S., Wu, T., Zhang, D., & Zhang, Z. (2015). Cell or cell membrane-based drug delivery systems. *Theranostics, 5*(8), 863-881.

ter Haar, G., & Coussios, C. (2007). High intensity focused ultrasound: Physical principles and devices. *International Journal of Hyperthermia, 23*(2), 89-104.

Thorsson, L., Newman, S. P., Weisz, A., Trofast, E., & Morén, F. (1993). Nasal distribution of budesonide inhaled via a powder inhaler. *Rhinology, 31*(1), 7-10.

Tian, Z., Tu, J., & Yeoh, G. (2005). Numerical simulation and validation of dilute gas-particle flow over a backward-facing step. *Aerosol Science and Technology, 39*(4), 319-332.

Trafton, A. (2009). Targeting tumors using tiny gold particles. *MIT News Office,* pp. 4-4.

Trübestein, G., Engel, C., Etzel, F., Sobbe, A., Cremer, H., & Stumpff, U. (1976). Thrombolysis by ultrasound. *Clinical Science and Molecular Medicine, 51*(3), 697-698.

Tu, J., Inthavong, K., & Ahmadi, G. (2012). *Computational Fluid and Particle Dynamics in The Human Respiratory System*: Springer Science & Business Media.

Tu, J., Inthavong, K., & Ahmadi, G. (2013). The human respiratory system. In *Computational Fluid and Particle Dynamics in the Human Respiratory System* (pp. 19-44). Dordrecht: Springer Netherlands.

Ugwoke, M. I., Agu, R. U., Verbeke, N., & Kinget, R. (2005). Nasal mucoadhesive drug delivery: Background, applications, trends and future perspectives. *Advanced Drug Delivery Reviews, 57*(11), 1640-1665.

Vaezy, S., & Zderic, V. (2007). Hemorrhage control using high intensity focused ultrasound. *International Journal of Hyperthermia, 23*(2), 203-211.

Vasir, J. K., Reddy, M. K., & Labhasetwar, V. D. (2005). Nanosystems in drug targeting: Opportunities and challenges. *Current Nanoscience, 1*(1), 47-64.

Venugopal, I., Habib, N., & Linninger, A. (2017). Intrathecal magnetic drug targeting for localized delivery of therapeutics in the CNS. *Nanomedicine, 12*(8), 865-877.

Vidgren, M., & Kublik, H. (1998). Nasal delivery systems and their effect on deposition and absorption. *Advanced Drug Delivery Reviews, 29*(1-2), 157-177.

Vidgren, P., Vidgren, M., Paronen, P., Vainio, P., & Nuutinen, J. (1991). Nasal distribution of radioactive drug administered using two dosage forms. *European Journal of Drug Metabolism and Pharmacokinetics, 3*, 426-432.

Vincent, J., Johnston, W., Jones, A., & Johnston, A. (1981). Static electrification of airborne asbestos: A study of its causes, assessment and effects on deposition in the lungs of rats. *American Industrial Hygiene Association Journal, 42*(10), 711-721.

von Helmholtz, H., & Ellis, A. J. (1875). *On the Sensations of Tone as a Physiological Basis for the Theory of Music*. London: Longmans, Green and Company.

Waddell, A. N., Patel, S. K., Toma, A. G., & Maw, A. R. (2003). Intranasal steroid sprays in the treatment of rhinitis: Is one better than another? *The Journal of Laryngology & Otology, 117*(11), 843-845.

Weitzberg, E., & Lundberg, J. O. (2002). Humming greatly increases nasal nitric oxide. *American Journal of Respiratory and Critical Care Medicine, 166*(2), 144-145.

Wilson, I. B. (1947). The deposition of charged particles in tubes, with reference to the retention of therapeutic aerosols in the human lung. *Journal of Colloid Science, 2*(2), 271-276.

Wofford, M., Kimbell, J., Frank, D., Dhandha, V., McKinney, K., Fleischman, G., Ebert, C., Zanation, A., & Senior, B. (2015). A computational study of functional endoscopic sinus surgery and maxillary sinus drug delivery. *Rhinology, 53*(1), 41-48.

Wong, E., Siu, J., Douglas, R., & Singh, N. (2021). Anatomy and physiology of the human nose. In K. Inthavong, N. Singh, E. Wong, & J. Tu (Eds.), *Clinical and Biomedical Engineering in the Human Nose: A Computational Fluid Dynamics Approach* (pp. 9-29). Singapore: Springer Singapore.

Xi, J., Si, X., & Gaide, R. (2014). Electrophoretic particle guidance significantly enhances olfactory drug delivery: A feasibility study. *PloS One, 9*(1), e86593.

Xi, J., Si, X., Peters, S., Nevorski, D., Wen, T., & Lehman, M. (2017). Understanding the mechanisms underlying pulsating aerosol delivery to the maxillary sinus: In vitro tests and computational simulations. *International Journal of Pharmaceutics, 520*(1), 254-266.

Xi, J., Yuan, J. E., Si, X., & Hasbany, J. (2015). Numerical optimization of targeted delivery of charged nanoparticles to the ostiomeatal complex for treatment of rhinosinusitis. *International Journal of Nanomedicine, 10*, 4847-4861.

Xi, J., Zhang, Z., & Si, X. (2015). Improving intranasal delivery of neurological nanomedicine to the olfactory region using magnetophoretic guidance of microsphere carriers. *International Journal of Nanomedicine, 10*(1), 1211-1222.

Yang, Y., Sze To, G. N., & Chao, C. Y. (2012). Estimation of the aerodynamic sizes of single bacterium-laden expiratory aerosols using stochastic modeling with experimental validation. *Journal of Aerosol Science and Technology, 46*(1), 1-12.

Yu, G., Zhang, Z., & Lessmann, R. (1998). Fluid flow and particle diffusion in the human upper respiratory system. *Aerosol Science and Technology, 28*(2), 146-158.

Zhang, J., Wu, L., Chan, H.-K., & Watanabe, W. (2011). Formation, characterization, and fate of inhaled drug nanoparticles. *Advanced Drug Delivery Reviews, 63*(6), 441-455.

Zhao, K., Scherer, P. W., Hajiloo, S. A., & Dalton, P. (2004). Effect of anatomy on human nasal air flow and odorant transport patterns: Implications for olfaction. *Chemical Senses, 29*(5), 365-379.

Zhou, H., Wang, X., Brighton, L., Hazucha, M., Jaspers, I., & Carson, J. L. (2009). Increased nasal epithelial ciliary beat frequency associated with lifestyle tobacco smoke exposure. *Inhalation Toxicology, 21*(10), 875-881.

Zhu, J. H., Lee, H. P., Lim, K. M., Gordon, B. R., & Wang, D. Y. (2012). Effect of accessory ostia on maxillary sinus ventilation: A computational fluid dynamics (CFD) study. *Respiratory Physiology & Neurobiology, 183*(2), 91-99.

Chapter 3

Resonance frequency of the combination of the nasal cavity and maxillary sinuses

In this chapter, a computational fluid dynamics (CFD) model, a finite element analysis (FEA) model, and an analytical equation of the classic Helmholtz resonator were used to predict the resonance frequency of the NC-MS combination. A simplified model of NC-MS, with dimensions close to a realistic model of NC-MS, was used to conduct a broad range of parametric studies. The results of these numerical models were compared with the results of in-house experiments to assess the accuracy of the models. Using the most accurate model (i.e., CFD), the effect of geometric parameters such as the ostium length, ostium diameter, NC width, MS volume, and MS shape on the resonance frequency was investigated. Then, the geometric parameters with the highest effect on the resonance frequency of the NC-MS were determined. Aero-acoustic analysis was also carried out to develop the relationship between the damping ratio of the air plug oscillation in the ostium and the drug delivery

efficiency, and the resonance frequency. Finally, the effect of the middle meatus on the estimation of the resonance frequency of a realistic model of NC-MS was investigated using the CFD model. Accordingly, a correction to the equation of the Helmholtz resonator was developed, which accounts for the effect of the middle meatus for estimation of the resonance frequency of the realistic NC-MS model. Overall, the models developed, and the discussions made in this chapter, address the first objective of this work, that is, *"to develop a well-resolved numerical model to investigate the effect of different geometrical parameters on the resonance frequency of the NC-MS combination"*.

3.1 Published articles

This chapter consists of a published journal article and a conference paper. In the journal article, the effect of geometrical parameters on the resonance frequency of an NC-MS combination was investigated. In the conference paper, the effect of the middle meatus on the prediction of the resonance frequency of the NC-MS model was examined.

Pourmehran, O., Arjomandi, M., Cazzolato, B., Ghanadi, F., & Tian, Z. (2020). The impact of geometrical parameters on acoustically driven drug delivery to maxillary sinuses. *Biomechanics and Modeling in Mechanobiology*, 19(2), 557-575.

Pourmehran, O., Cazzolato, B., Tian, Z., & Arjomandi, M. (2020). Acoustic behaviour of the human maxillary sinus: The importance of the middle meatus and the ostium on resonance frequency behaviour. Presented in *18th International Conference of Numerical Analysis and Applied Mathematics, Rhodes, Greece*. Accepted to be published in AIP conference proceeding in winter 2021.

Statement of Authorship

Title of Paper	The impact of geometrical parameters on acoustically driven drug delivery to maxillary sinuses
Publication status	☑ Published ☐ Accepted for Publication ☐ Submitted for Publication ☐ Unpublished and Unsubmitted work written in manuscript style
Publication Details	Pourmehran, O., Arjomandi, M., Cazzolato, B., Ghanadi, F., & Tian, Z. (2020). The impact of geometrical parameters on acoustically driven drug delivery to maxillary sinuses. Biomechanics and Modeling in Mechanobiology, 19(2), 557-575.

Principal Author

Name of Principal Author (Candidate)	Oveis Pourmehran
Contribution to the Paper	Ideas and Concepts • Conducted a comprehensive literature review to find the gaps in the knowledge • Developed the ideas and concepts based on the gaps Experiments and Modelling • Developed the simplified and realistic NC-MS models using ANSYS® DesignModeler and Autodesk® Inventor • Designed and fabricated an experimental setup and conducted the experiments • Developed FEA and CFD models using ANSYS® Workbench for estimating the resonance frequency of the NC-MS models • Developed a CFD model to simulate the acoustic wave propagation in a 1D model • Developed a user-defined function (UDF) code to apply an acoustic wave to the inlet Interpretation of Results • Extracted raw data from the experiments and simulation • Post-processed the simulation results using ANSYS® CFD-Post • Developed a MATLAB code to conduct signal processing for experimental data as well as to extract the figures • Interpreted the simulation results and compared them with the experimental data Manuscript • Developed the first full draft of the manuscript • Applied comments given by co-authors • Revised the manuscript after review and produced a rejoinder • Acted as the corresponding author
Overall percentage (%)	80%
Certification:	This paper reports on original research I conducted during the period of my Higher Degree by Research candidature and is not subject to any obligations or contractual agreements with a third party that would constrain its inclusion in this thesis. I am the primary author of this paper.
Signature	Date: 28/04/2021

Co-Author Contributions

By signing the Statement of Authorship, each author certifies that:

I. the candidate's stated contribution to the publication is accurate (as detailed above);
II. permission is granted for the candidate in include the publication in the thesis; and
III. the sum of all co-author contributions is equal to 100% less the candidate's stated contribution.

Name of Co-Author	Maziar Arjomandi
Contribution to the Paper	Supervised the development of the research, participated in developing ideas, helped in interpretation of results and evaluation of the manuscript.
Signature	Date: 28/04/2021

Name of Co-Author	Benjamin Cazzolato		
Contribution to the Paper	Supervised the research and contributed in academic discussion and manuscript review.		
Signature		Date	28/04/2021

Name of Co-Author	Farzin Ghanadi		
Contribution to the Paper	Helped in designing the experimental setup and contributed in academic discussion and manuscript review.		
Signature		Date	03/05/2021

Name of Co-Author	Zhao Tian		
Contribution to the Paper	Supervised the research and contributed in academic discussion and manuscript review.		
Signature		Date	29/04/2021

Biomechanics and Modeling in Mechanobiology (2020) 19:557–575
https://doi.org/10.1007/s10237-019-01230-5

ORIGINAL PAPER

The impact of geometrical parameters on acoustically driven drug delivery to maxillary sinuses

Oveis Pourmehran[1] · Maziar Arjomandi[1] · Benjamin Cazzolato[1] · Farzin Ghanadi[1] · Zhao Tian[1]

Received: 26 May 2019 / Accepted: 21 September 2019 / Published online: 1 October 2019

Abstract
Acoustically driven nebulized drug delivery (acoustic aerosol delivery) is the most efficient noninvasive technique for drug delivery to maxillary sinuses (MS). This method is based on the oscillation of the air plug inside the ostium to transport drug particles from the nasal cavity (NC) to the MS. The larger the wavelength of the air plug oscillation in the ostium, the greater the penetration of drug particles to the MS. However, using this technique, the maximum drug delivery efficiency achieved to date is 5%, which means 95% of the aerosolized drugs do not enter the MS and are wasted. Since the largest amplitude of the air plug oscillation occurs at its resonance frequency, to achieve an improved MS drug delivery efficiency, it is important to determine the resonance frequency of the nose–sinus combination accurately. This paper aims to investigate the impact of geometrical parameters on the resonance frequency of the nose–sinus model. Both experimental and computational acoustic models, along with the theoretical analysis, were conducted to determine the resonance frequency of an idealized nose–sinus model. The computational modeling was carried out using computational fluid dynamics (CFD) and finite element analysis (FEA), whereas in the analytical solution, the mathematical relationships developed for a conventional Helmholtz resonator were employed. A series of experiments were also conducted to measure the resonance frequency of a realistic NC–MS combination. The results demonstrated a good agreement between the experimental and CFD modeling, while the FEA and theoretical analysis showed a significant deviation from the experimental data. Also, it was shown that the resonance frequency of the idealized nose–sinus model increases by up to twofold with increasing the ostium diameter from 3 to 9 mm; however, it has an inverse relationship with the ostium length and sinus volume. It was also reported that the resonance frequency of the nose–sinus model is independent of the NC width and MS shape.

Keywords Nebulized drug delivery · Helmholtz effect · Drug delivery · Resonance frequency · Computational fluid dynamics · Finite element analysis · Maxillary sinuses

Abbreviations

cyl	Cylindrical
CFD	Computational fluid dynamics
CRS	Chronic rhinosinusitis
DE	Deposition efficiency
EPW	Elements per wavelength
FS	Frontal sinus
FEA	Finite element analysis
MS	Maxillary sinus
Mic	Microphone
NC	Nasal cavity
NC–MS	NC and MS combination
PSD	Power spectral density
sph	Spherical
rec	Rectangular
SS	Sphenoid sinus
TF	Transfer function

List of symbols

α	Acoustic attenuation coefficient
c	Speed of sound (m/s)
C_{xy}	Coherence function between x and y
c_p	Specific heat for constant pressure (J/mol K)
c_v	Specific heat for constant volume (J/mol K)
$D_{H,os}$	Hydraulic diameter of the ostium (m)
D_{os}	Ostium diameter (m)
f	Frequency (Hz)
F_r	Resonance frequency (Hz)
γ	Specific heats ratio

✉ Oveis Pourmehran
oveis.pourmehran@adelaide.edu.au

[1] Present Address: School of Mechanical Engineering, The University of Adelaide, North Terrace, Adelaide, SA 5005, Australia

G_{xy}	Cross-power spectral density between input and response (Pa^2/Hz)
G_{xx}	Power spectral density of input (Pa^2/Hz)
G_{yy}	Power spectral density of response (Pa^2/Hz)
κ	Thermal conductivity (W/m K)
λ	Wavelength (m)
λ_i	Characteristic velocity (m/s)
L_s	Ostium length (m)
L_{eq}	Equivalent length of the ostium (m)
μ	Dynamic viscosity (kg/m s)
μ_0	The reference value of density (kg/m s)
ν	Kinetic viscosity (m^2/s)
ω	Angular frequency (Hz)
P	Pressure (Pa)
p_0	Gauge pressure (Pa)
p_i	Pressure amplitude (Pa)
Q	Quality factor
ρ	Fluid density (kg/m^3)
S	Effective temperature (K)
S_0	Ostium cross-sectional area (m^2)
T	Temperature (K)
T_{xy}	Transfer function estimate
U	Velocity (m/s)
V_{MS}	Maxillary sinus volume (mL)
w_{in}	Incident sound power at inlet
w_t	Transmitted sound power at outlet
W_{NC}	Nasal cavity width (mm)
ζ	Damping ratio

1 Introduction

Rhinosinusitis (sinus infection) is one of the most common diseases associated with rhinology, which affects up to 15% of the population throughout the world (Laube 2007). Since the nasal cavity (NC) is exposed to the infections carried by the inhaled aerosols, the attached sinuses such as the maxillary sinus (MS) are highly prone to infection. For example, in the USA, every year a total of approximately 30 million people are diagnosed with chronic sinusitis, leading to about 0.6 million NC surgeries, which results in US $5.8 billion in health care expenses per year (Lam et al. 2014). In some cases, brain infection and other serious side effects are likely to occur with acute sinusitis of the MS (Huang et al. 2005). The MS is the most voluminous of all paranasal sinuses. Due to its location, it is prone to a broader range of diseases such as viral infection, bacterial colonization, and anatomical obstruction (Harbo et al. 1997). Accordingly, given the narrowness of the ostium, which is a channel that connects the MS to the NC, the MS is not ventilated well, which results in poor drug delivery to the MS. It is also worth noting that, although paranasal sinus cancer is rare, it is most usually detected in the MS (Harbo et al. 1997).

Several treatment techniques, such as aerosolized inhalation therapy, surgery intervention, saline irrigation, and oral therapy, are employed for rhinosinusitis treatments (Rau 2005). Nevertheless, due to the low therapeutic efficiency of inhalation drug delivery, and the surgical side effects of operational treatment, many patients prefer an alternative and more efficient noninvasive drug delivery technique. In this regard, the nebulizer is a potential device that forms a swirling cloud of small particles close to the outlet of the mouthpiece of the device (Hallberg et al. 2014). In this study, this type of nebulizer is called a non-acoustic nebulizer. Although a non-acoustic nebulizer can significantly improve the aerosol delivery beyond the nasal valve region, its efficiency of aerosol delivery to the MS is less than 1% (Xi et al. 2015). Recently, an active drug delivery technique using acoustically driven aerosols (or humming flow) has gained increasing attention because of its higher efficacy than non-acoustic nebulized delivery (Durand et al. 2011; Leclerc et al. 2014; Maniscalco et al. 2006; Möller et al. 2013, 2014). In this technique, the MS is excited similar to a Helmholtz resonator, in which the air plug within the ostium is activated if the frequency of the flow pulsation at the nostril is equal to the resonance frequency of the nose–sinus combination (Möller et al. 2014). When the air plug within the ostium is activated at the resonance frequency, the highest penetration of the drug particles to the MS occurs, which results in an enhanced air exchange between the NC and MS.

Several in vitro studies have been conducted on acoustic aerosol delivery to the MS. Hyo et al. (1989) examined the acoustically driven drug delivery to an MS by applying a positive pressure of 10–15 mbar between the MS and NC and an observed deposition efficiency (DE) of 2.3% and 1.3% for a maxillary ostium with the diameters of 5 mm and 1 mm, respectively. By measuring the nitric oxide (NO) exhaled by healthy person, Weitzberg and Lundberg (2002) determined that the concentration of the exhaled NO was enhanced 15-fold through humming exhalation in comparison with quiet exhalation. Moreover, they showed that the increase in the concentration of exhaled NO is very sensitive to the frequency of the humming and the size of the ostium (Maniscalco et al. 2003). In the later finding of Maniscalco et al. (2006), a twofold to fourfold increase in drug deposition on the MS wall was reported when an acoustic airflow was produced by human nasal humming. These results revealed that the humming in nasal exhalation dramatically increases the air exchange between the MS and the NC. Furthermore, an experimental study on drug delivery to the paranasal sinuses by means of an acoustically driven aerosol injection showed that using acoustic waves increases the deposition of aerosol in the maxillary sinuses and enhances the ventilation of sinuses (Durand et al. 2012). In this study, the authors used a nasal sonic nebulizer (ATOMISOR® NL11SN) to produce a nebulized pulsating aerosol with a

frequency of 100 Hz. These nebulizers can produce finer particles than sprays (i.e., 4 vs. 30 μm), so the medical particles can reach the target sites beyond the NC. Durand et al. (2011) reported a positive effect of 100 Hz sinusoidal airflow on the nebulized aerosols' deposition on the MS wall. It was revealed that airflow pulsation at about 100 Hz can improve the DE 2 to threefold, depending on the concentration of drugs used.

The diameter and length of an ostium are two major parameters that affect the particle deposition on the MS wall (Xi et al. 2017). It has been demonstrated that the number of delivered particles to the MS decreases when the ostium length increases (Xi et al. 2017). For example, the DE for an ostium diameter of 9.6 mm is 40% lower than that for the smaller length of 6.5 mm, which is similar to the finding reported by Maniscalco et al. (2003). Maniscalco et al. (2006) also noted that the delivery efficiency increases with increased ostium diameter. The underlying mechanism of this variation may not be the ostium diameter, but the resonance frequency (Xi et al. 2017).

Overall, using the acoustically driven aerosol delivery technique, many previous studies considered a fixed frequency (i.e., 45 Hz) for inlet pulsating aerosols, which were tested in vitro and through clinical experiments (Granqvist et al. 2006; Laube 2007; Möller et al. 2011; Si et al. 2013; Xi et al. 2017). Since the resonance frequency of the nose–sinus model was not measured accurately, it was not guaranteed that the fixed acoustic frequency applied to the nostril-injected aerosols was activating the air plug inside the ostium efficiently, thus the highest drug delivery efficiency could not occur. To cover an extended range of frequency, Moghadam et al. (2018) conducted an in vitro experiment in which they applied a frequency sweep to the aerosol injected from the nostril, whereby there must be one input frequency that comes close to the resonance frequency of the nose–sinus realistic model. The model was constructed using a mold made by an image reconstruction technique and 3D printing and cast using a translucent, waterproof, nonporous resin. They reported that expanding the frequency range from 100–500 Hz to 100–850 Hz, applied at the nostril, resulted in increasing the DE in the MS up to twofold.

In the frequency sweep technique, although the application of an extended range of frequencies, for example, from 100–500 Hz to 100–850 Hz, slightly increases the overall deposition efficiency (DE) on the MS wall, it requires more time to inject particles to cover the extended frequency range. Hence, the total dosage of the injected particles, which depends on the injection time and consequently the frequency range, is increased. Therefore, for a large frequency range, the total dosage of the injected particles increases, which may contribute to increasing the risk of adverse side effects on the pulmonary system. To sum up, both of the acoustically driven drug delivery schemes, including the fixed and sweep frequency techniques, can only increase the MS drug delivery efficiency up to a mere 5% (Xi et al. 2017). The reason for this low rate of delivery is mostly due to the fact that the frequency of acoustically driven airflow cannot activate the air plug in the ostium and MS (Xi et al. 2017).

2 Problem description

Several studies have shown the benefits of acoustically superimposed airflow for enhancing MS drug delivery efficiency (Xi et al. 2017). Based on this finding, several medical companies have produced a sonic nebulizer device, which superimposes an acoustic wave with a fixed frequency (i.e., 45 Hz and 100 Hz) on the nostril-injected aerosol for the purpose of aerosolized drug delivery to the MS. The drug delivery efficiency using this technique depends greatly on the amplitude of the oscillation of the air plug inside the ostium. Since the human NC–MS combination is similar to a Helmholtz resonator system (El Merhie et al. 2016; Maniscalco et al. 2006; Moghadam et al. 2018; Möller et al. 2010, 2011; Xi et al. 2017), it is inferred that its resonance frequency is determined by the geometrical size of the ostium and MS. However, the presence of the nasal cavity attached to the ostium, as well as the non-spherical shape of the MS causes the NC–MS combination to deviate from that of a Helmholtz resonator. Hence, in addition to the ostium length and diameter and MS volume, the MS shape and NC width can affect the NC–MS resonance frequency. Since the shape and size of the NC–MS combination differ for individuals, i.e., ostium diameter, ostium length, and MS volume range from approximately 1–7 mm, 7–15 mm, and 4–30 mL, respectively (Cankurtaran et al. 2007; Moghadam et al. 2018; Sharma et al. 2014; Tarhan et al. 2005; Xi et al. 2017), using a sonic nebulizer with a fixed frequency for every chronic rhinosinusitis (CRS) patient does not maximize the efficiency of drug delivery to the MS, unless the applied frequency happens to be close to the resonance frequency. Therefore, it is crucial to determine the resonance frequency of every individual NC–MS combination accurately.

The aim of this paper is; (1) to develop a validated numerical model for calculating the resonance frequency of the NC–MS combination and (2) to identify the parameters affecting the resonance frequency of the NC–MS combination. In doing so, a parametric study has been conducted using an idealized NC–MS model. The reason for using an idealized geometry stems from the complexity of the realistic nose–sinus model, in which the feasibility of changing the geometry for using parametric studies is limited. For the development of an idealized model, a range of geometrical sizes identical to those of a realistic human nose–sinus combination was selected. Figure 1 shows the schematic of the

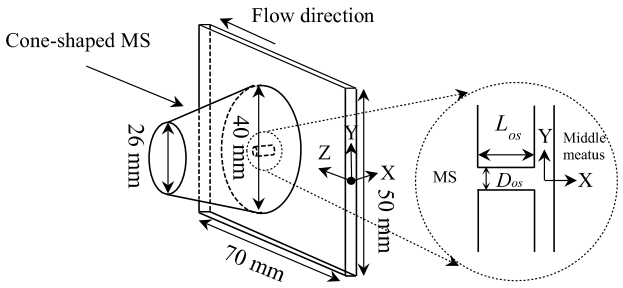

Fig. 1 Details of the idealized NC–MS model with a cone-shaped MS

idealized NC–MS model, in which the MS is replaced by a cone-shaped cavity, the ostium by a circular channel, and the nasal cavity by a rectangular channel. This geometry was selected based on the previous work by Hood et al. (2009), in which they examined the air exchange between the MC and MS with a constant pressure difference between the inlet and outlet numerically. The selected geometric parameters are detailed in Table 1.

In addition to the idealized model shown in Fig. 1, a realistic NC–MS model has been developed to measure the resonance frequency of a real human nose–sinus combination. To develop this model, the three-dimensional (3D) geometry of a nasal cavity of a healthy person, based on computed tomographic (CT) imaging of a human head adopted from Kumar et al. (2016) was used. For simplicity, only one side of a human nose–sinus was 3D printed. This model contains a nostril, frontal sinus, maxillary sinus, maxillary ostia, and sphenoid sinus (Fig. 2a, b). The inlet of the realistic model is the nostril and the outlet connects the nasal cavity to the trachea. Figure 2c illustrates a section view of the left side of the realistic NC–MS model. The volume of the realistic MS is 15.18 mL, the ostium hydraulic diameter is about 3 mm (cross-section perimeter = 10.75 mm, area = 8.10 mm^2), and the ostium length is 6 mm.

3 Methods

To investigate the effects of the ostium diameter, ostium length, MS volume, and NC width on the resonance frequency of the proposed model, a total number of 21 different idealized NC–MS models were considered (Table 1). Moreover, to investigate the effect of MS shape on the resonance frequency, four different MS shapes, including cone-shaped, rectangular, cylindrical, and spherical, were considered with a constant volume of $V_{MS} = 30$ mL (Figs. 1, 3). Four different techniques including analytical, CFD, FEA, and experimental tests were employed to investigate the resonance frequency of the NC–MS combination.

Table 1 Dimensions of different parts of the idealized nose–sinus model

Case	D_{os} (mm)	L_{os} (mm)	W_{NC} (mm)	V_{MS} (mL)	MS shape
1–7	3, 4, 5, 6, 7, 8, 9	6	3	30	Cone
8–14	3	6, 7, 8, 9, 10, 11, 12	3	30	Cone
15–18	3	6	5, 7, 9, 11	30	Cone
19–22	3	6	3	10, 15, 20, 30, 40	Cone
23–25	3	6	3	30	rec, cyl, sph

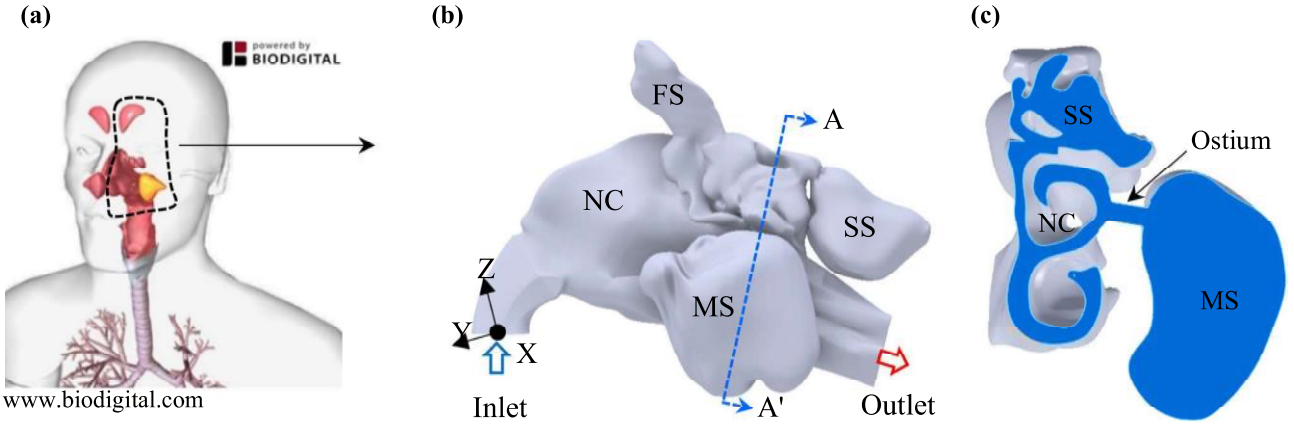

Fig. 2 Schematic of **a** the computational domain (BioDigital 2019); **b** the CT-image-based reconstruction of a realistic nose–sinus model (Kumar et al. 2016); **c** section A–A′

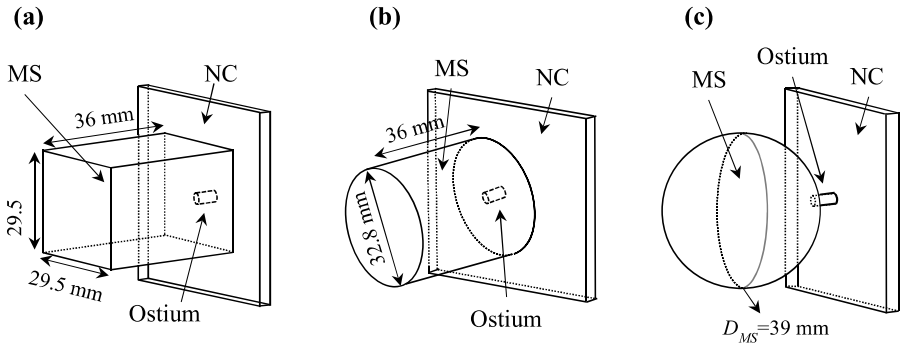

Fig. 3 Schematic of the idealized nose–sinus model. **a** Rectangular MS; **b** cylindrical MS; **c** spherical MS for $D_{os}=3$ mm, $L_{os}=6$ mm, $V_{MS}=30$ mL and $W_{NC}=3$ mm

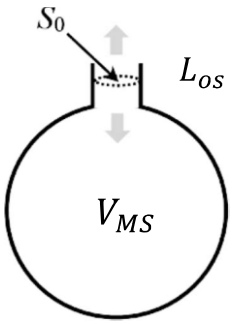

Fig. 4 Schematic of a Helmholtz resonator

3.1 Application of the Helmholtz resonator theory

The first method of investigation is based on the classical formulation of the Helmholtz resonator given by (Xi et al. 2017).

$$F_r = \frac{c}{2\pi}\sqrt{\frac{S_0}{V_{MS}L_{eq}}}, \tag{1}$$

where c is the sound speed, V_{MS} is the volume of MS, S_0 denotes the cross-sectional area of the ostium, and L_{eq} is the equivalent length of the ostium, which can be obtained by $L_{eq} = L_{os} + 0.6D_{H,os}$, with L_{os} as the length of the ostium and $D_{H,os}$ as the hydraulic diameter of the ostium (Fig. 4). Depending on the exact shape of ostium and the MS, a more sophisticated formula can be derived (Alster 1972).

3.2 Experimental design

Figure 5a presents a schematic of the experimental test rig used in this study. Based on Table 1, a total number of 14 different idealized nose–sinus models (case 1–14) were 3D printed at the University of Adelaide. In this work, a white broadband noise signal was applied, as it was a fast and convenient method to characterize the plant. For the most part, the coherence exceeds 90% in the frequency range of interest, and hence the frequency response provides an accurate estimate given the number of spectral averaged used (Bendat and Piersol 2011). A white noise broadband signal with a frequency range of 10–800 Hz was applied at the inlet of the nasal cavity (nostril) using a loudspeaker. Figure 5b shows the white noise pressure oscillation versus time, as well as the Welch power spectral density (PSD) estimate in the frequency domain. As shown in Fig. 5c–e, two $^1/_{4''}$ pressure-field unshielded microphones were used to measure the sound pressure. One microphone was installed at the inlet of the channel to detect the excitation sound pressure at the nostril, and another microphone was attached to the interior wall of the MS to detect the response sound pressure.

The magnitude-squared coherence function was used for quantifying the degree of linearity between the input pressure signal (x) and the response pressure signal (y), measured by Mics 1 & 2 at the nostril and MS, respectively. The magnitude-squared coherence estimate is a function of frequency with values between 0 and 1. These values indicate how well x corresponds to y at each frequency, which is defined by:

$$C_{xy}(f) = \frac{\left|G_{xy}(f)\right|^2}{G_{xx}(f)G_{yy}(f)}, \tag{2}$$

where f is the sound wave frequency, G_{xy} is the cross-power spectral density between the input and response signals, and G_{xx} and G_{yy} are the power spectral densities of the input and response pressure signals, respectively. A unit value of C_{xy} implies that the sound detected by the microphones is only coherent with the loudspeaker and the incoherent sound from external sources is 'screened out' and not considered, whereas a zero value for C_{xy} indicates that the input and response sounds are unrelated.

The relationship between the input (x) and response (y) is modeled by the linear, time-invariant transfer function T. The peak values of the T_{xy} indicate the resonance frequencies of the system. In the frequency domain, $Y(f) = T_{xy}(f)X(f)$, where $T_{xy}(f)$ is the ratio of the Fourier transform of the input, $X(f) = F\{x(t)\}$, to the Fourier transform of the response,

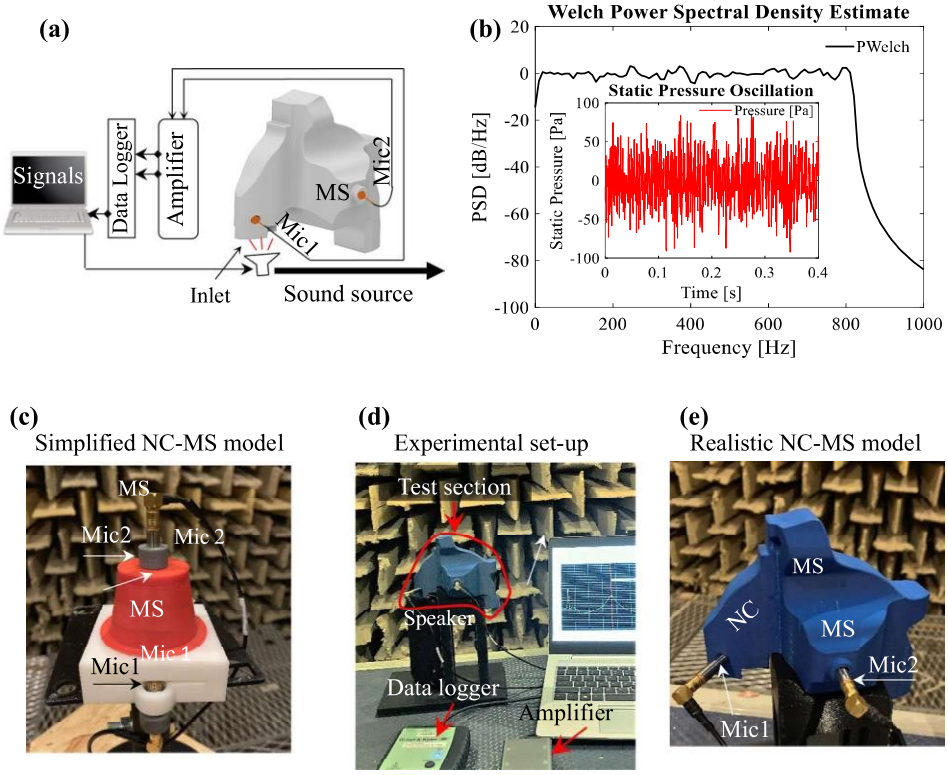

Fig. 5 **a** Schematic diagram of the experimental setup for measurement of the resonance frequency, **b** input sound wave and the PSD in the frequency domain, **c** microphones attached to the simplified model; **d** photograph of the experimental setup; **e** microphones attached to the realistic model

$Y(f) = F\{y(t)\}$. For a single-input/single-response system, which is applicable for the current research, the $T_{xy}(f)$ estimate of the transfer function is given by:

$$T_{xy}(f) = \frac{G_{xy}(f)}{G_{xx}(f)}, \tag{3}$$

The PSD values were obtained using a Hanning window with 2^{10} FFT points and a 75% overlap for averaging. All experiments were conducted five times for each case to ensure the repeatability and predictability of the obtained results. The overall uncertainty associated with the microphone measurements comprises both systematic and measurement errors. The systematic errors arise from geometric uncertainty, manufacturing tolerances, and measurement uncertainties. The measurement uncertainties from the Mics were measured to be $\pm 2\%$ of the desired frequency range.

3.3 Finite element analysis (FEA)

The FEA was used to simulate the sound propagation using ANSYS Mechanical (Harmonic Response module). In this method, the linearized Euler equations (LEE) are solved via finite element discretization (ANSYS 2015). The ACT Acoustic extension is used for solving these types of simulations (ANSYS 2015), which was implemented in ANSYS® Workbench to apply the acoustic boundary conditions. An acoustic radiation boundary condition was set for the inlet and outlet to create a non-reflecting condition. An acoustic normal surface velocity with an amplitude of 10^{-3} m/s was set at the inlet of the model to simulate the excitation. The speed of sound, viscosity, specific heat ratio, thermal conductivity, and heat capacity were considered at a temperature of 300 K and 1 atmospheric pressure and are tabulated in Table 2.

Regarding the mesh generation of an acoustic body, according to Howard and Cazzolato (2014), at least 6–12 elements per wavelength (EPW) are required for resolving the acoustic wave propagation accurately. The wavelength can be quantified as follows (Bies et al. 2017):

$$\lambda = \frac{c}{f}, \tag{4}$$

where λ is the wavelength, c is the speed of sound, and f is the frequency of interest. In this study, a frequency range 10–800 Hz was set in ANSYS Harmonic Response, hence based on Eq. (4) and Table 2 the minimum wavelength becomes $\lambda = 0.344$ m. The model was meshed using quadratic FLUID221 tetrahedral elements with a minimum and maximum element size of 5×10^{-4} m and 1×10^{-3} m, respectively (Fig. 6). Therefore, in the FEA simulation, a minimum mesh density of 343 EPW was used for the entire computational domain, except in the areas of high-pressure gradients where a mesh density of as high as 686 EPW was used, which was found to be sufficient to provide mesh independence (Howard and Cazzolato 2014). The resulting

Table 2 Parameters used for FEA for the simplified nose–sinus model and numerical setup

Parameter	Symbol	Value	Units
Acoustic body			
Density	ρ	1.225	kg/m^3
Sound speed	c	344	m/s
Dynamic viscosity	μ	1.7894×10^{-5}	kg/m s
Thermal conductivity	κ	0.0242	W/m K
Specific heat capacity at constant pressure	c_p	1012	J/kg K
Specific heat capacity at constant volume (per unit mass)	c_v	722.9	J/kg K

Element type	EPW at the highest frequency	Acoustic radiation boundary	Frequency range (Hz)	Excitation
Numerical setup				
FLUID221	343–686	Inlet and Outlet	10–800	At the inlet: acoustic normal surface velocity Amplitude: 0.001 m/s

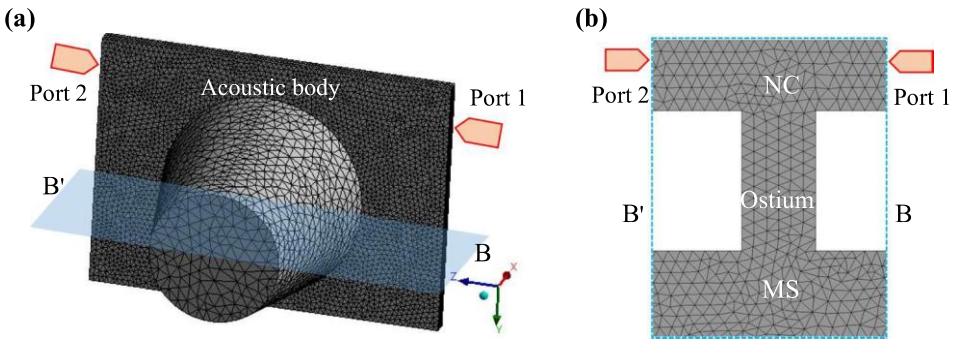

Fig. 6 **a** 3D FEA mesh using ANSYS® Harmonic. **b** Mesh between Port 1 and Port 2

acoustic element count is 155,975 and the node count is 268,819.

The transmission loss between Port 1 (inlet) and Port 2 (outlet) estimates the resonance frequency of the idealized NC–MS models. The transmission loss is defined as (ANSYS 2015):

$$\mathrm{TL} = 10 \cdot \log_{10}\left(\frac{w_{\mathrm{in}}}{w_{\mathrm{t}}}\right) \tag{5}$$

where TL is the transmission loss in dB, w_{in} is the incident sound power at the inlet (Port 1), and w_{t} is the transmitted sound power at the outlet (Port 2). Using this method, the maximum value of the transmission loss indicates the resonance frequency of the computational domain.

3.4 Computational fluid dynamics (CFD)

Given acoustical fields intrinsically propagate within the fluidic media, the current paper focuses on the simulation of an idealized NC–MS model using CFD, in addition to the FEA presented in the previous section. In the CFD method, a pressure-based solver for the nonlinear Navier–Stokes equations is performed using finite volume discretization. A pressure-based solver was used for solving the Navier–Stokes equations. This method enables investigation of the flow behavior in a computational domain to better understand the flow features in the presence of an acoustic wave. ANSYS® FLUENT was used to conduct the CFD simulations. The fluid medium for this analysis is air. To mimic the experimental conditions discussed in Sect. 3.2, and to consider the Helmholtz effect on the ostium and MS, the air density for the simulation was resolved using the ideal gas law for compressible analysis. The viscosity of the model was measured using Sutherland's law with three coefficients, defined as (Sutherland 1893):

$$\mu = \mu_0 \left(\frac{T}{T_0}\right)^{3/2} \frac{T_0 + S}{T + S}, \tag{6}$$

where μ is the viscosity, T is the static temperature, and μ_0 is the reference viscosity 1.7894×10^{-5} kg/ms, which is the air viscosity at a reference temperature $T_0 = 273.11$ K, and S is the effective temperature (Sutherland constant), which is 110.56 K for air.

It must be noted that, if an acoustic field is applied, the acoustic wave traveling toward the boundaries is reflected, which artificially doubles the pressure at the boundary because of the superposition of the reflected and incident pressure

waves. To avoid such artificial superposition, a general non-reflecting boundary condition (NRBC) should be applied on the inlet and outlet boundaries. In this method, the modified Euler equations are solved on the boundary of the model in an algorithm identical to the flow equations applied to the interior part of the domain (Fluent 2009; Thompson 1990). According to NRBC theory (Thompson 1990), for an entering flow to a boundary, four waves (λ_1, λ_2, λ_3, and λ_4) enter the domain and one wave (λ_5) leaves the domain (Fig. 7a), while, when a flow leaves a boundary, four waves (λ_2, λ_3, λ_4, and λ_5) leave the domain and one wave (λ_1) enters the domain (Fig. 7b).

The inlet boundary condition is also defined as a pressure inlet with a zero-gauge pressure; however, the Transparent Flow Forcing Boundary Condition was used for simulating the acoustic source at the inlet. A quasi-white noise input signal was applied as a user-defined function (UDF). The UDF was defined based on the input used in experiments given by Eq. (7):

$$P = p_0 + \sum_{i=1}^{n} \left(p_i \times \sin\left(2\pi F_i t + 2\pi\varphi_i\right)\right) \tag{7}$$

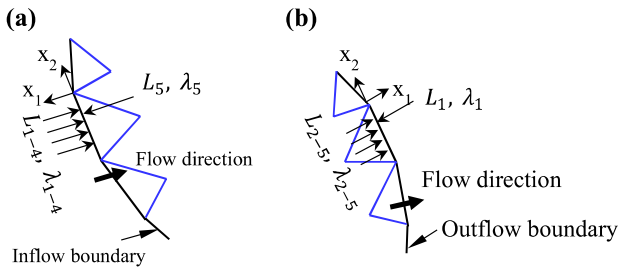

Fig. 7 **a** Waves leaving and **b** Entering face on inflow and outflow boundaries (Fluent 2009)

where P is the inlet pressure, p_0 is the gauge pressure, p_i is the signal amplitude for the phasor, F_i is the frequency of the phasor, φ_i is the signal phase, which is a random number in the range $[0, 1)$, and n is the total number of input frequencies. For human MS with a volume range of $V_{MS} \cong 10–40$ mL, ostium length of $L_{os} \cong 6–12$ mm, and ostium diameter of $D_{os} \cong 3–9$ mm, using Eq. (1), the resonance frequency varies between $F_r \cong 190–520$ Hz. However, to cover more ranges of the frequency, a frequency range of $F_i \cong 10–800$ Hz was applied to the inlet in this study. Moreover, a *no-slip* boundary condition was used on the walls and due to the low magnitude of the Reynolds number (< 500 in this study), the laminar flow solver was employed.

The use of non-reflecting boundary conditions requires a very small time step to achieve a more stable and converged solution. The effect of a time step on the acoustic analysis using CFD is discussed in Sect. 3.5. To keep the simulation runtime as short as possible, a non-iterative time advancement (NITA) algorithm using a PISO pressure–velocity coupling scheme is used. However, using NITA, which decreased the simulation runtime by more than 20-fold in comparison with the iterative time advancement (ITA), the University of Adelaide's Phoenix high-performance computer was utilized for 150 h to simulate a flow time of $t = 0.4$ s, with a time step $\Delta t = 10^{-6}$ s. The convergence criterion of the scaled residuals was set at 10^{-5} for the continuity equation and velocity fields, and 10^{-6} for the energy equation. More details regarding the CFD specifications can be found in Table 3 (in the Appendix). A total number of 25 case studies for the idealized NC–MS model (Table 1) were considered for the acoustics simulation using CFD. Depending on the geometry size and shape, 25 different meshes were generated with the total element numbers between

Table 3 Numerical setup and material properties for CFD study

Parameter	Symbol	Value	Units
Material (air)			
Density	ρ	Ideal gas	kg/m^3
Sound speed	c	344	m/s
Dynamic viscosity	μ	Sutherland' law	kg/m s
Thermal conductivity	κ	0.0242	W/m K
Specific heat capacity at constant pressure	c_p	1012	J/kg K
Molecular weight	M	28.966	g/mol

Element type	Inlet boundary	Outlet boundary	Wall	Solver/Algorithm
Numerical setup				
Tetrahedral 428–4280 EPW	Flow: Pressure inlet; Acoustic wave: Transparent Flow Forcing (using UDF); Frequency range: 10–800 Hz; Temperature: 300 K	Pressure outlet Acoustic: Non-reflecting	No-slip condition, Adiabatic	Pressure-based/ NITA (PISO)

580,000 and 1,600,000 hexahedral elements, with a mesh density between 428 and 4280 EPW. An overview of the mesh generated for Case 1 (Table 1) is illustrated in Fig. 8.

3.5 Evaluation of numerical dissipation for CFD simulation

The dissipation of the numerical solution is unavoidable in the iterative numerical simulations due to the truncation errors and numerical damping used for CFD stability. Dispersive error terms cause oscillations in the solution. One fix to this is through the addition of artificial dissipation to decrease the size of the dispersive errors which, in turn, cause a smoothing of the gradients. However, a level of dissipation comparable to the actual physical viscosity may contaminate the solution. For example, simulated boundary layers may be thicker than the real boundary layers. The truncation error is the error made by truncating an infinite sum and approximating it by a finite sum. Given an acoustic field produces pressure perturbations, dissipation error terms can artificially increase the attenuation of the wave propagation within the computational domain. Using ANSYS FLUENT, the time step size and element density (number of EPW) are two controllable parameters in CFD simulation, which can control the numerical dissipation. In fact, decreasing the time step and element sizes can decrease the numerical dissipation to minimize the artificial dissipation of the simulated pressure fluctuation representing the sound field. To fundamentally investigate and quantify the effect of the time step and element density on the numerical dissipation of the direct computation acoustics CFD simulation, one-dimensional (1D) wave propagation along a duct was considered. A 3D rectangular duct is taken as the computational domain, in which the walls are considered as a free slip condition to provide an equivalent to a 1D simulation (Fig. 9). The material properties and solver specifications are tabulated in Table 3 in "Appendix".

In this section, the criterion is the sound pressure level (SPL), which is measured by the root mean square of static pressure at the inlet and outlet of the duct. The difference between the SPL of the inlet and the outlet boundaries is

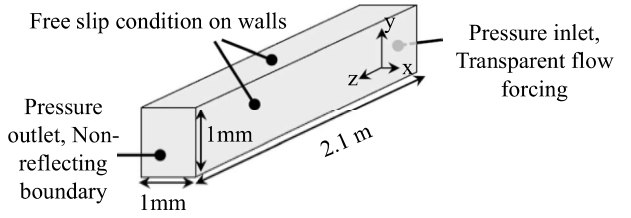

Fig. 9 Schematic of the 3D duct used to quantify acoustic energy dissipation (Howard and Cazzolato 2014)

the attenuation. The attenuation of the sound pressure level in dB per meter considering viscothermal losses is given by Howard and Cazzolato (2014),

$$-20\log_{10} e^{-\alpha} = 8.69\alpha \text{ dB/m} \tag{8}$$

where α is the attenuation coefficient, which for low frequencies can be approximated by Howard and Cazzolato (2014),

$$\alpha \approx \frac{\omega^2 \delta_{\text{cl}}}{c^3} \tag{9}$$

$$\delta_{\text{cl}} = \frac{\nu}{2}\left(\frac{4}{3} + 0.6\right) + \frac{\gamma - 1}{\text{Pr}} \tag{10}$$

where ω is angular frequency, and c is the speed of sound and the subscript cl indicates classical (absorption). Also, $\nu = \mu/\rho_0$ is the kinetic viscosity, $\gamma = c_p/c_v$ is the specific heat ratio, $\text{Pr} = \mu c_p/\kappa$ is the Prandtl number, and κ is the thermal conductivity. Using the parameters in Table 2 and Eqs. (8)–(10) the sound pressure level attenuation per meter for classical absorption is 4.39×10^{-6} dB/m for a plane wave with a frequency of $f = 500$ Hz. For the CFD simulation of plane wave propagation, the inlet boundary condition was defined as a pressure inlet with zero-gauge pressure. A sinusoidal wave with a frequency of $f = 500$ Hz was implemented as "Transparent Flow Forcing Boundary Condition" for the acoustic model at the inlet boundary condition.

As shown in Fig. 10a, the SPL attenuation (dB/m) is almost proportional to the time step size, in which the smaller the time step size that is applied, the lower the SPL attenuation that is achieved. The time step size for a direct

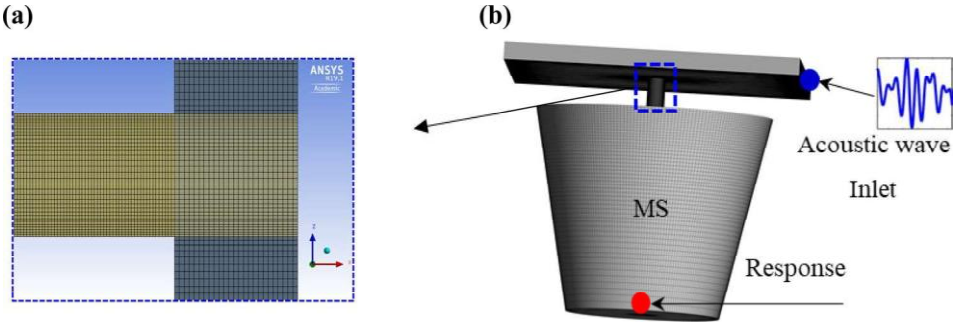

Fig. 8 **a** Section view of the generated CFD mesh for the idealized NC–MS model; **b** 3D view of the generated mesh and illustration of the acoustic inlet and response points

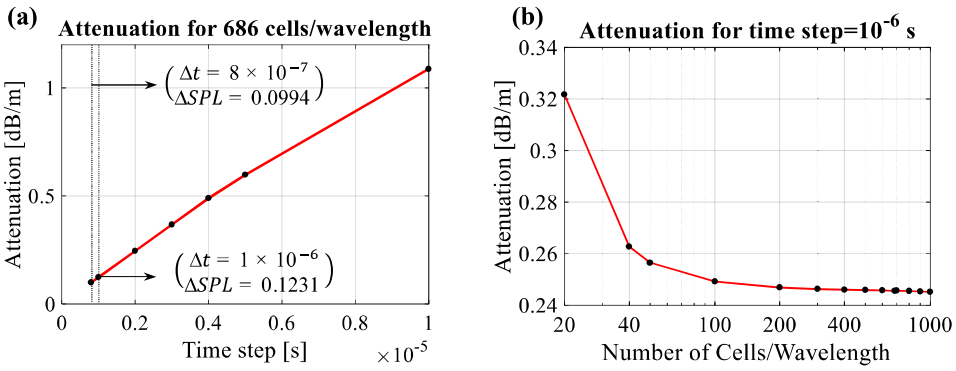

Fig. 10 The effects of **a** the time step and **b** the number of EPW on the attenuation of sound pressure level along a 1D duct using CFD

computational acoustics simulation should satisfy Eq. (11) given by (FLUENT 2008),

$$\Delta t \leq \frac{1}{10 \times f_{\max}} \tag{11}$$

where Δt is the time step size, and $f_{\max}$ is the maximum acoustic frequency. The maximum acoustic frequency for the simplified NC–MS models in this study is $f_{\max} = 800\,\text{Hz}$. The maximum time step size that could be used in this study was $\Delta t = 1.25 \times 10^{-4}$s. Different time step sizes ($\Delta t \leq 1.25 \times 10^{-4}$s) were examined for acoustic simulation of the simplified NC–MS models. The numerical solution converged at $\Delta t \leq 10^{-6}$s. The simulation runtime for each case study at $\Delta t_1 = 1 \times 10^{-6}$s was about 150 h with 64 CPU cores. However, for a smaller time step size, for example at $\Delta t_2 = 8 \times 10^{-7}$s, the simulation runtime was about 190 h with 64 CPU cores. In this work, 25 different case studies were investigated, thus an overall runtime for Δt_2 was about 1000 h (41 days) more than for Δt_1. On the other hand, as can be seen in Fig. 10a, the difference in SPL attenuation between the results obtained for Δt_1 and Δt_2 can be calculated by $\Delta\text{SPL}_{\text{attenuation}} = 0.1231 - 0.0994 = 0.0237\,\text{dB/m}$. For the length of the duct (2.1 m) this represents an error of 0.05 dB, which is much less than the accuracy of an experiment, which is typically 0.1 dB. Given the minimal change in the SPL attenuation, but the dramatic increase in runtime (1000 h) between Δt_1 and Δt_2, a time step size of $\Delta t = 1 \times 10^{-6}$s was used for the direct computational acoustic CFD simulation of simplified NC–MS models in this study.

Moreover, as can be seen in Fig. 10b, the SPL attenuation decreases with increasing the number of elements. However, the change in SPL attenuation, for an element density of more than 100 EPW, is negligible in comparison with the change in SPL attenuation obtained by an element density in a range of 20–100 EPW. While the recommended minimum element density for estimating the resonance frequency of a Helmholtz resonator using an FEA simulation is 6–12 EPW (Howard and Cazzolato 2014), a direct computational acoustics (DCA) simulation using CFD requires a higher numbers of EPW, which depends on the order of solver (Beck and Munz 2018; Tam 1995). For the solver used in the current CFD study, a minimum number of 100 EPW is required to achieve an acceptable accuracy and stability. In this CFD simulation, a minimum mesh density of 428 EPW was used for the entire computational domain, however, in areas of high-pressure gradients, a mesh density as high as 4280 EPW was used.

4 Results and discussion

The outcome of this study reveals two main points. Firstly, it shows how well the numerical methods including the CFD, FEA, and the classical Helmholtz resonator formula calculate the resonance frequency of the idealized NC–MS model in comparison with the experimental data. Secondly, using the pre-determined most accurate numerical method, what the effect of geometrical parameters on the idealized NC–MS model.

Moreover, an acoustic analysis for a 3D printed model of a realistic NC–MS combination was carried out to examine whether a CFD simulation of an identical simplified model can predict the resonance frequency of a realistic model.

4.1 Numerical validation study

Experiments have been carried out to determine the most accurate numerical model for measuring the resonance frequency of an idealized NC–MS model, which is used in the acoustic drug delivery technique. In doing so, a total of 14 idealized NC–MS 3D printed models were considered, based on Case Numbers 1–14 presented in Table 1. Experiments were conducted for 10 min for each model. Every experiment was repeated five times for each case and the average of the obtained resonance frequencies is reported as the resonance frequency of the model. As an illustration, Fig. 11 shows the transfer function (TF) and coherence (Coh) estimates for two different cases (Case Numbers 2 and 10). As can be seen in Fig. 11a, c there are two peaks in

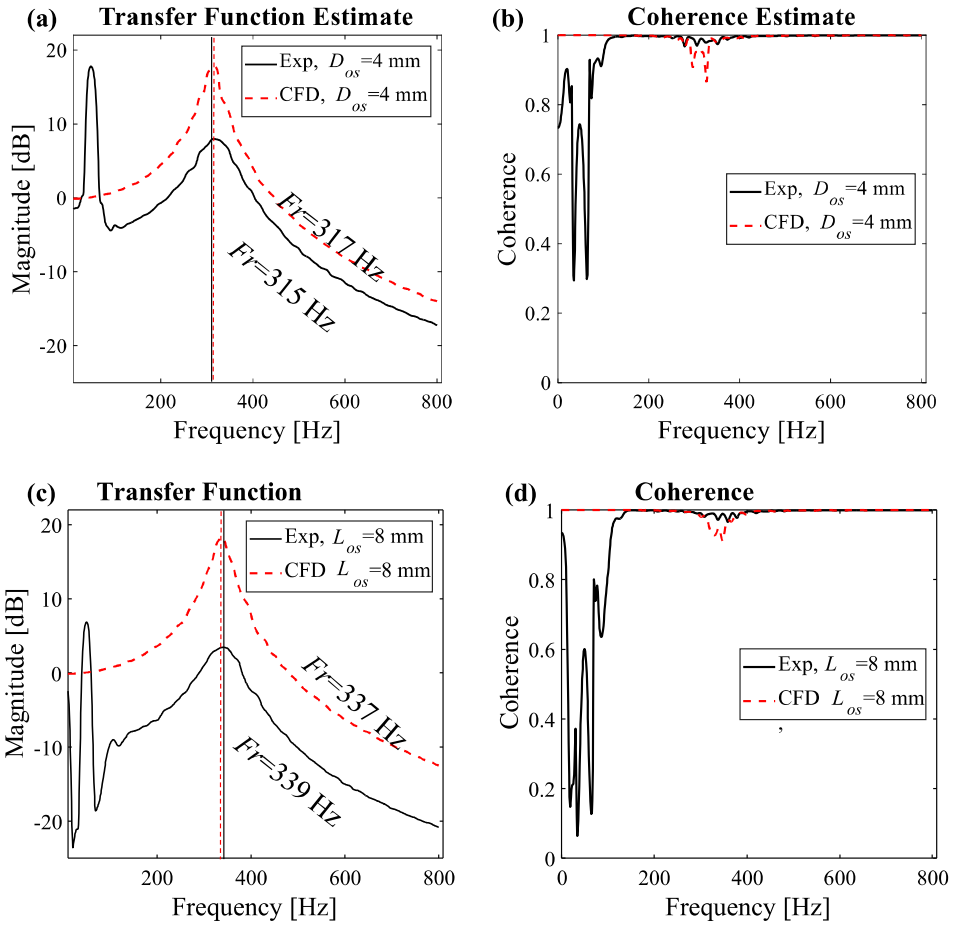

Fig. 11 Comparison of the experimental data with CFD results for TF-estimate and Coh-estimate for the idealized nose–sinus model for **a**, **b** Case Number 2; **c**, **d** Case Number 10

the TF-estimate for each case. The first peak at 50 Hz stems from the electrical noise. This claim is confirmed by the Coh-estimates presented in Fig. 11b, d, which show that the signals obtained by microphones at the inlet and response points are not coherent for the range of frequencies below 100 Hz, where the first peak in the TF-estimate occurs. The second peak represents the resonance frequency of the 3D printed models. Moreover, the Coh-estimate for frequencies above 100 Hz shows a value greater than 0.9, which confirms the coherence and reliability of the pressure oscillation signals obtained by the microphones.

Figure 11 also shows the TF and Coh-estimates for Case Numbers 2 and 10 obtained by CFD. As can be seen, unlike for the experimental results, there is only one peak for the TF-estimate in the frequency range 10–800 Hz. This peak is associated with the resonance frequency of the aforementioned models. To ensure the reliability of the pressure signals detected in CFD, Fig. 11b, d shows that the Coh-estimates for Cases 2 and 10 are between 0.9 and unity, which indicates an acceptable coherence between the input and response signals obtained by CFD.

Accompanying the experimental and CFD results in Fig. 11, it can be seen that the magnitude of the TF-estimate obtained by experiments is fractionally lower than that obtained by CFD. The difference in the TF-estimate magnitude stems from the difference between the amplitude of the sound waves applied at the inlet in the CFD and the experiments.

The experiments showed that the difference in the maximum amplitude of the input pressure wave does not affect the resonance frequency (Fig. 12). It is worth mentioning that the experiments also showed that the thickness and material of the tested model do not affect the acoustic resonance frequency. To investigate the effect of the thickness of the test section, plasticine was also attached to the outer wall of the model with different uniform thicknesses. The results reveal that the resonance frequency of the model remains almost unaltered with a negligible change within the experimental error margin (± 2 Hz).

Figure 13a shows the resonance frequency of several different idealized NC–MS models (Case Numbers 1–7) obtained from the classical Helmholtz resonator formula, FEA, CFD, and the experimental tests. As shown in Fig. 13a, the results of the resonance frequencies obtained by the classical Helmholtz resonator formula, given by Eq. (1), and FEA do not have good agreement with the experimental

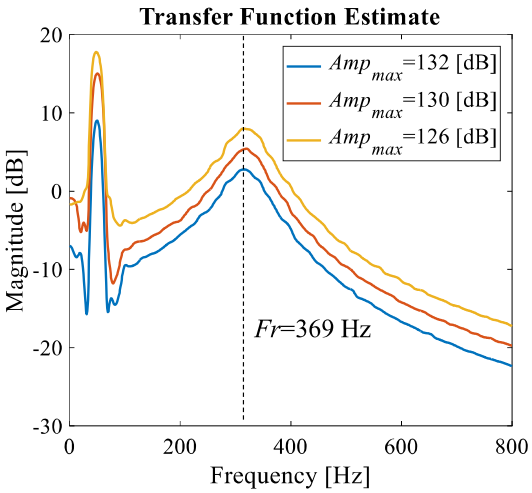

Fig. 12 Comparison of experimental data for a TF-estimate of Case Number 3 for three different amplitudes of the inlet pressure wave

results, while the CFD modeling is in good agreement with the experimental data. Figure 13b demonstrates the deviation of the resonance frequencies obtained by the numerical models (Theory, FEA, and CFD) from those obtained by the experimental tests.

It can be seen that the errors of CFD results are smaller than the errors of the FEA and theoretical modeling. The error is defined as the deviation of the CFD results from the experimental data. The errors for CFD are between 0.6 and 8%, while the errors for FEA and theoretical modeling are between 16 and 41%, depending on the ostium diameter. Moreover, it can be seen that the results diverge with increasing D_{os}. The divergence observed when the ostium diameter increases may not be due to the ostium diameter variation, but because of the increase in resonance frequency.

Figure 14a shows that the same phenomenon occurs when the ostium length increases. This Figure represents the comparison of the resonance frequencies for a range of ostium lengths from 6 to 12 mm. The results show that there is a converging trend between the data obtained by numerical modeling including the FEA and Theory, and those obtained by the experiments when the resonance frequency decreases by increasing the ostium length.

Figure 14b also quantitatively shows the deviation of the numerical results with the experimental data for the variation of L_{os}. According to this figure, the errors dominantly decrease with the increasing L_{os} (which results in decreasing the resonance frequency). Therefore, it is inferred that the accuracy of the FEA and Theory inversely depends on the resonance frequency of the system.

The current study found that the classical Helmholtz resonator formula and the FEA overestimate the resonance frequency with an unacceptable deviation (more than 20%) from the experiments, whereas the CFD mostly estimates the resonance frequency in good agreement (between 0.6 and 8%) with the experiments. The difference between the results obtained by CFD and FEA is due to the underlying governing equations for each method. While it is known that the estimate of the resonance frequency of the Helmholtz resonator provided by Eq. (1) deviates from non-idealized geometries (Howard et al. 2000), FEA can usually account for such effects. However, the differences in resonance frequencies observed in Figs. 13 and 14 indicate flow behavior not captured from the acoustic field itself. As discussed in Sect. 3, ANSYS® FLUENT solves the nonlinear Navier–Stokes equations for the flow simulations, while the ANSYS® Mechanical (Harmonic Response) solves the linearized Euler equations for the acoustic problem.

According to Fig. 15, three different domains are defined around a solid body for an acoustic problem. This solid body can be considered as the wall boundaries in this study. In a domain close to the solid body nonlinear phenomena occur, which can be numerically simulated using the full nonlinear

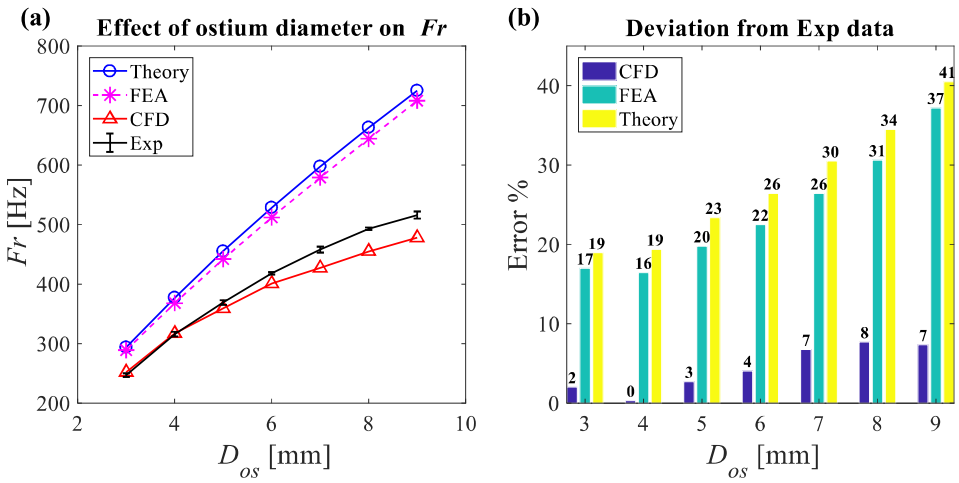

Fig. 13 Comparison of the theoretical, FEA, CFD, and experimental results for cases 1–7: **a** the effect of D_{os} on resonance frequency; **b** error with respect to the experiments

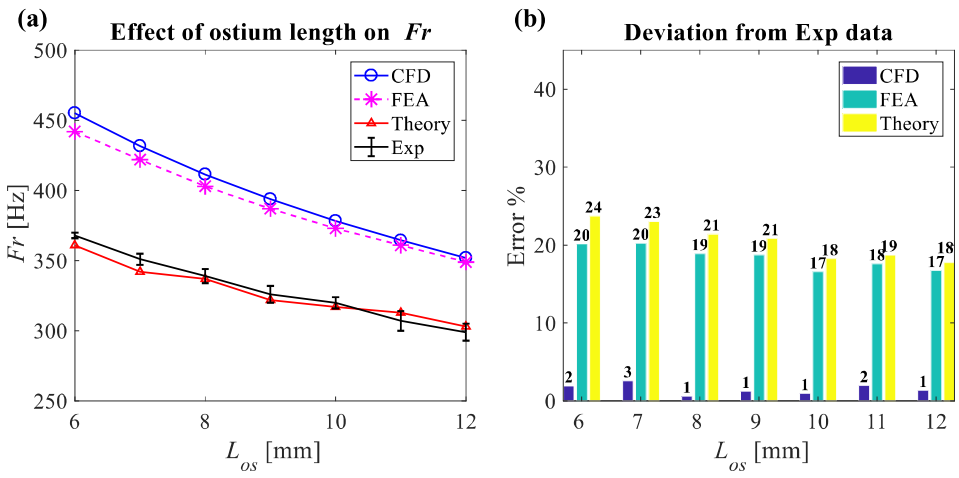

Fig. 14 Comparison of the Theory, FEA, CFD, and experimental data for Case Numbers 8–14: **a** the effect of L_{os} on resonance frequency; **b** error with respect to the experiments

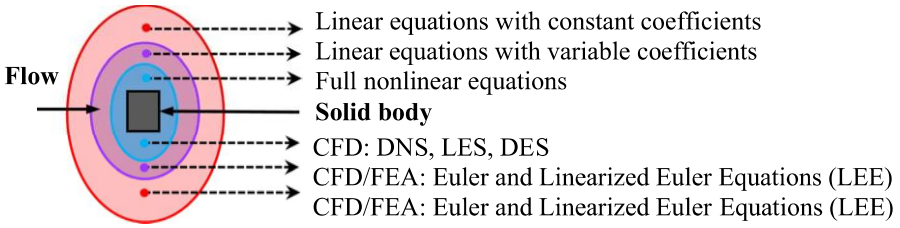

Fig. 15 Aero-acoustic domain around a solid body (Grace 2004)

Navier–Stokes equations. In the other two domains, the phenomena are predominantly linear and simulated using linear equations with variable/constant coefficients such as Euler and linearized Euler equations (LEEs). CFD is able to simulate all three domains numerically, while the FEA is unable to simulate the nonlinear phenomena that occur in the first domain because it uses the linearized Euler equations (LEEs). Therefore, it can be concluded that ANSYS® Mechanical (Harmonic Response) is not able to predict the vortices generated near the wall and sharp edges.

Figure 16a shows the instantaneous velocity vectors within and around the ostium obtained by CFD. As can be seen, there are vortices within the ostium and near the wall attached to the ostium. These vortices are generated due to the oscillation of the air plug within the ostium. However, Fig. 16c shows the velocity vector in the same area, in which no vortex has been generated either in the ostium or in the area around the ostium. The weakness of FEA to predict such phenomena in an acoustic problem results in an overestimation of the resonance frequency.

This combination of findings provides some support for the conceptual premise that the CFD is able to predict the acoustical phenomena better than the theoretical formula and the FEA. An accurate resonance frequency of the NC–MS model can be calculated using CFD, however, it is accurate within the error margin of CFD. Using the error margin, an optimized frequency range for the use of acoustically driven aerosol delivery using the frequency sweep technique can be estimated. As an illustration, assume Case 10, in which the maximum CFD error occurs (Error = 8%). The resonance frequency obtained for this case using CFD is 339 Hz. In this case, a frequency range between 271 and 402 Hz (339 ± 8%) can be applied at the nostril for the use of acoustically driven aerosol delivery using a sweep frequency instead of the frequency range of 100–850 Hz that was used in Moghadam et al. (2018). Therefore, using this shortened range of frequencies, the drug injection period and the drug dosage decreases thereby increases the drug delivery efficiency. Nevertheless, a more accurate resonance frequency is achievable by decreasing the time step size; however, it is not cost-effective because it requires a huge computational resource.

4.2 The effect of nose–sinus geometry size on the resonance frequency

Direct computational acoustics using CFD simulation has been identified as a reliable method for acoustics modeling and has been cross-validated in the previous section; hereafter further parametric studies have been conducted using CFD. Figure 17 demonstrates the effect of the geometrical parameters, including the ostium diameter, ostium length, nasal cavity width, MS volume, and the MS shape, on the resonance frequency of all 25 models (Table 1). Figure 17 indicates that the sinus resonance frequency is relatively independent of the MS shape variations. This figure also

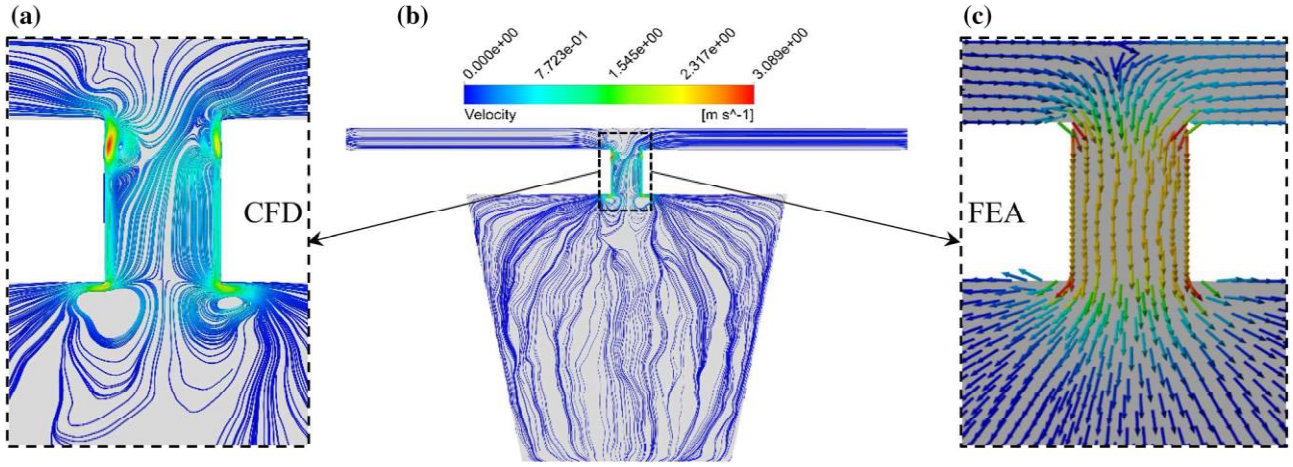

Fig. 16 Instantaneous velocity streamlines for Case 2 where the inlet frequency equals the resonance frequency $F_r = 317$ Hz: **a**, **b** obtained by CFD; **c** obtained by FEA

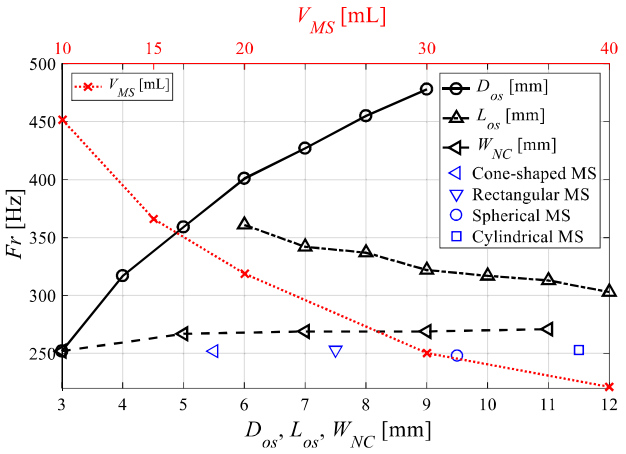

Fig. 17 Effect of geometry on resonance frequency of an idealized NC–MS model for variation of D_{os} with $L_{os} = 6$ mm, $W_{NC} = 3$ mm, $V_{MS} = 30$ mL, and cone-shaped MS; L_{os} with $D_{os} = 5$ mm, $W_{NC} = 3$ mm, $V_{MS} = 30$ mL, and cone-shaped MS; W_{NC} with $D_{os} = 3$ mm, $L_{os} = 6$ mm, $V_{MS} = 30$ mL, and cone-shaped MS; V_{MS} with $D_{os} = 3$ mm, $L_{os} = 6$ mm, $W_{NC} = 3$ mm, and cone-shaped MS; and the MS shape with $D_{os} = 3$ mm, $L_{os} = 6$ mm, $W_{NC} = 3$ mm

shows that for the cases investigated, the nasal cavity width does not significantly affect the resonance frequency of the NC–MS. According to Fig. 17, although the resonance frequency has an increasing trend from 252 to 271 Hz depending on the NC width, a 20 Hz difference of resonance frequencies between the $W_{NC} = 3$ mm and $W_{NC} = 11$ mm is not significant in comparison with 252 Hz. This difference falls in the error margin (± 8%), as discussed in the previous section. Therefore, it can be inferred that the NC–MS resonance frequency is mostly independent of the nasal cavity and MS geometrical variations, which is consistent with Eq. (1).

This finding may help us to understand the parameters that significantly affect the NC–MS resonance frequency and are related to the ostium and MS size. This reveals that the efficiency of the acoustically driven aerosol delivery is not sensitive to the human nasal cavity and MS shape. According to Fig. 17, it is clear that the MS volume and the ostium diameter have a significant impact on the resonance frequency of the NC–MS. Also, the effect of the ostium length on the resonance frequency is not negligible. This figure shows that the sinus resonance frequency is approximately proportional to the ostium diameter. To support this, Table 4 (in Appendix) indicates that the resonance frequency varies from 247 Hz to 520 Hz for the ostium diameter from 3 to 9 mm, which quantitatively confirms the significant effect of the ostium diameter on the resonance frequency.

Figure 17 also illustrates an inverse proportion of the resonance frequency to the MS volume and the ostium length. More details regarding the value of the NC–MS resonance frequency for different geometrical parameters can be found in Table 4. Overall, the quantitative results represented in Fig. 17 indicate that the resonance frequency of the NC–MS cannot be classified by human age. This is due to the fact that human growth results in increasing the MS volume, ostium length, and ostium diameter, which separately affect the resonance frequency, followed by affecting the drug delivery efficiency.

4.3 Damping ratio

To investigate the decay rate of the oscillation of the air plug in the ostium, the damping ratio is measured for each case. The damping ratio, ζ, is a dimensionless measurement describing how oscillations in a system decay after a disturbance

Table 4 Resonance frequency for entire cases obtained by Exp, CFD, FEA, and Theory

	Exp	CFD		FEA		Theory	
	Fr	Fr	Error%	Fr	Error%	Fr	Error%
Cone-shaped $L_{os} = 6$ mm $W_{NC} = 3$ mm $V_{MS} = 30$ mL							
Ostium diameter							
3 mm	247	252	*2.02*	289	*17.00*	294	*18.93*
4 mm	315	317	*0.63*	368	*16.83*	377	*19.76*
5 mm	369	359	*2.71*	442	*19.78*	455	*23.37*
6 mm	418	401	*4.07*	512	*22.49*	529	*26.44*
7 mm	458	427	*6.77*	579	*26.42*	598	*30.48*
8 mm	493	455	*7.71*	644	*30.63*	663	*34.48*
9 mm	520	478	*8.08*	708	*36.15*	725	*39.43*
Cone-shaped $D_{os} = 3$ mm $W_{NC} = 3$ mm $V_{MS} = 30$ mL							
Ostium length							
6 mm	369	359	*2.71*	442	*19.78*	455	*23.37*
7 mm	351	342	*2.56*	422	*20.23*	432	*23.01*
8 mm	339	337	*0.59*	403	*18.88*	412	*21.4*
9 mm	326	322	*1.23*	387	*18.71*	394	*20.82*
10 mm	320	317	*0.94*	373	*16.56*	378	*18.22*
11 mm	310	308	*0.65*	361	*16.45*	364	*17.56*
12 mm	307	303	*1.3*	349	*13.68*	352	*14.65*
Cone-shaped $D_{os} = 3$ mm $L_{os} = 6$ mm $V_{MS} = 30$ mL							
NC width							
3 mm		252		289		294	
5 mm		267		292		294	
7 mm		269		292		294	
9 mm		269		292		294	
11 mm		271		292		294	
Cone-shaped $D_{os} = 3$ mm $W_{NC} = 3$ mm $L_{os} = 6$ mm							
MS volume							
10 mL		452		512		519	
15 mL		367		418		524	
20 mL		320		362		367	
30 mL		252		289		294	
40 mL		223		255		260	
$D_{os} = 3$ mm $W_{NC} = 3$ mm $V_{MS} = 30$ mL $L_{os} = 6$ mm							
MS shape							
Cone		252				294	
rec		253				294	
cyl		248				294	
sph		253				294	

The italics show the deviation of obtained resonance frquency by each categoty i.e. CFD, FEA, Theory from the resonance frequency obtained experimentally

(Alciatore 2007), which is given by $\zeta = 1/2Q$, where Q is the quality factor obtained by 3 dB bandwidth given by:

$$Q = \frac{F_r}{\Delta F}, \quad \Delta F = F_2 - F_1, \tag{12}$$

where F_r is the resonance frequency, ΔF is the bandwidth, and F_1, F_2 are the lower and higher frequency of the 3 dB bandwidth, respectively, which are defined in Fig. 18a. The lower the damping ratio, the lower the rate of decay of oscillations. Figure 18a–j demonstrates the TF-estimate and the related damping ratio for all cases mentioned in Table 1. The damping ratios in these figures were calculated from the TF-estimates obtained experimentally. It should be noted that the sharper peak in the TF-estimate curve indicates a lower damping ratio.

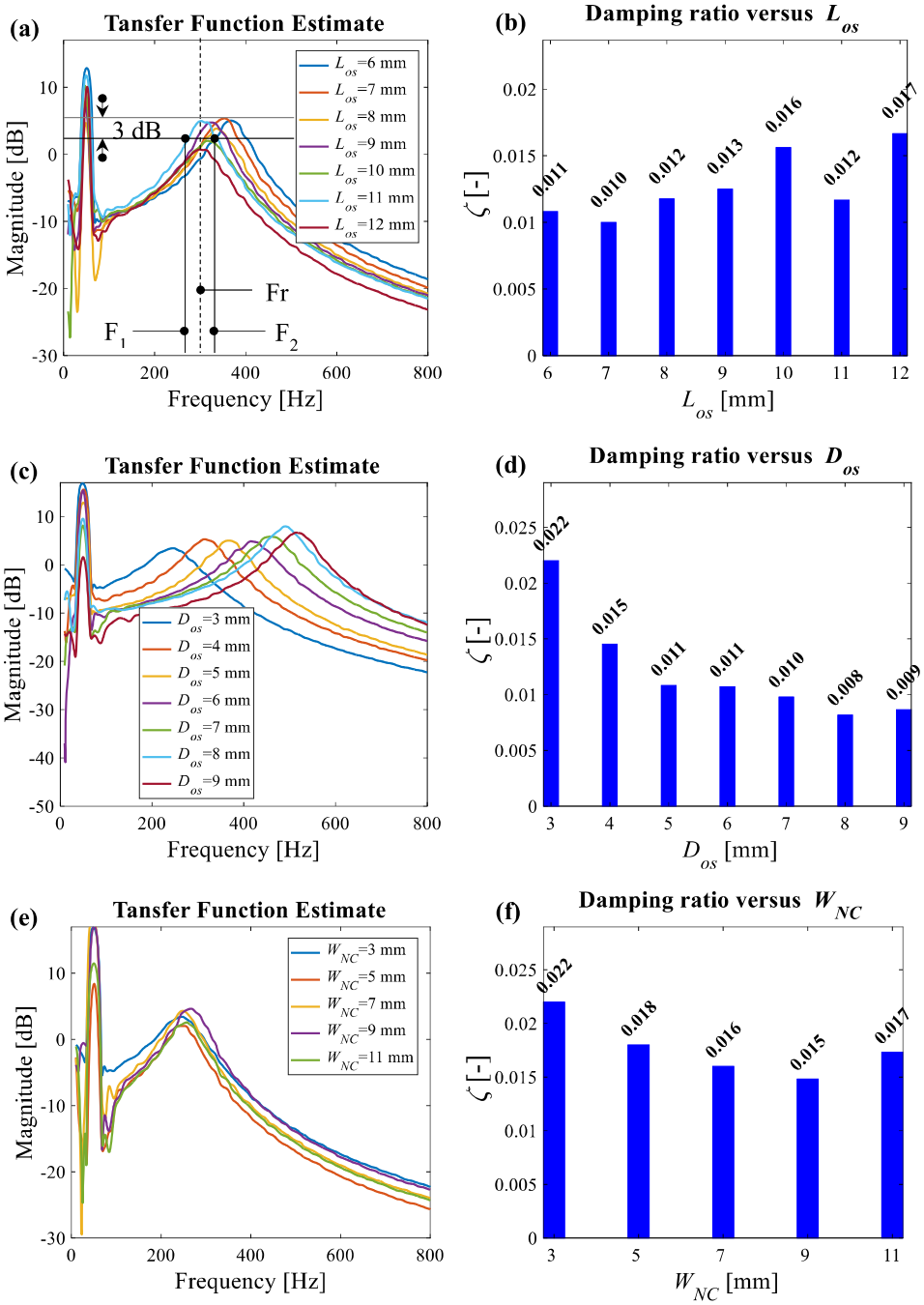

Fig. 18 TF estimates and damping ratios obtained by experiments for variations of **a**, **b** ostium length; **c**, **d** ostium diameter; **e**, **f** NC width

Since the oscillation decay rate increases with the increasing damping ratio, the pressure amplitude of the acoustic source (applied at the nostril) should be enhanced to rectify the reduced pressure amplitude at the resonance frequency of the air plug in the ostium. Therefore, the calculation of the damping ratio of the ostium air plug oscillation enables us to estimate an optimized inlet acoustic wave amplitude to achieve better drug delivery efficiency.

Figure 18a, b represents a direct relationship between the ostium length and damping ratio. For example, according to Fig. 18a, b, a comparison of the values of the damping ratio between $L_{os} = 7$ mm (Case 9) and $L_{os} = 12$ mm (Case 14) reveals that the damping ratio for Case 9 is lower than that of Case 14. Figure 18c–f illustrates an inverse relationship between the damping ratio and the ostium diameter and NC width. The results of the damping ratio in this study reveal a qualitative implication. It implies that the required amplitude of the acoustic pressure (applied at the nostril) for Case 14 should be higher than that required for Case 9. In other words, assume the geometrical sizes of the nose–sinus

combination of two persons are identical except for the volume of their MSs. In this case, for the use of acoustically driven aerosol delivery with sweep frequency, not only the range of input frequencies (applied at the nostril), but also the amplitude of the acoustic wave for each these two persons should be different. Further work is required to establish a better knowledge of the relationship between the damping ratio and the input acoustic pressure amplitude for improving the design of an acoustically driven aerosol delivery device.

4.4 Acoustic analysis for a realistic NC–MS combination

An experimental investigation was conducted to calculate the resonance frequency of a realistic NC–MS combination. The left side of the nose is considered for the experiment (Fig. 5a). In this experiment, a realistic NC–MS model was 3D printed in two separate parts, including a nasal cavity (part 1) and an MS with an ostium attached (part 2). One Mic was attached to the interior wall of the MS and another Mic was attached to the nostril to detect the response and input pressure signals, respectively. Attaching part 2 to part 1 forms a complete one-sided realistic NC–MS combination. Using a quasi-white noise at the nostril, the resonance frequency of the realistic NC–MS is obtained via a TF-estimate, as presented in Fig. 19. In this figure, the black line shows the TF-estimate for the realistic NC–MS combination obtained by the experimental test. In a frequency range of 10–800 Hz, except for the first peak at 50 Hz which is due to the electrical noise, two main peaks are seen in this plot, indicating two resonance frequencies.

To determine which peak value is associated with the resonance frequency of the MS, a different experiment was conducted. In this experiment, a thin acoustically absorptive screen (a tissue filter) was placed across the ostium opening and then part 1 and part 2 were attached. Afterward, the experiment was run identically to the previous experiments to obtain the TF-estimate to see which peak associates with the resonance frequency of the MS. In Fig. 19 the red dash-line demonstrates the TF-estimate of this ostium-filtered experiment. According to this line plot, it is obvious that the first main peak obtained in the non-filtered model (black line) disappeared in the ostium-filtered model (red dash-line), which indicates that the resonance frequency of the MS occurs at the first peak, which is 348 Hz for the realistic NC–MS geometry of this study.

As discussed in Sect. 4.2, the effect of the nasal cavity width (W_{NC}) and the shape of the MS have a negligible effect on the resonance frequency of the NC–MS combination. Therefore, the resonance frequency of a simplified model (obtained by CFD), with the closest ostium length/diameter and MS volume to the realistic one, is compared with the resonance frequency of the realistic model obtained by the experimental tests. The simplified model Case 20 (Table 1) with $L_{os} = 6$ mm, $D_{os} = 3$ mm, $V_{MS} = 15$ mL is the closest CFD case to the realistic NC–MS geometry of this study with $L_{os} \approx 6$ mm, $D_{os} \approx 3$ mm, $V_{MS} = 15.18$ mL. The blue dash-line in Fig. 19 represents the TF-estimate of Case 20, which is close to the first main peak of the TF-estimate of the non-filtered realistic model (black line plot in Fig. 19). According to Fig. 19, the experimentally obtained resonance frequency of the realistic NC–MS model is $Fr = 348$ Hz, while the CFD-obtained resonance frequency of Case 20 is Fr = 367 Hz, with an Error at 5.5%. Therefore, a CFD simulation of a simplified NC–MS model with the ostium diameter/length and MS volume identical to a realistic NC–MS model could predict the resonance frequency of the MS of the realistic model of the current study with an Error of less than 6%.

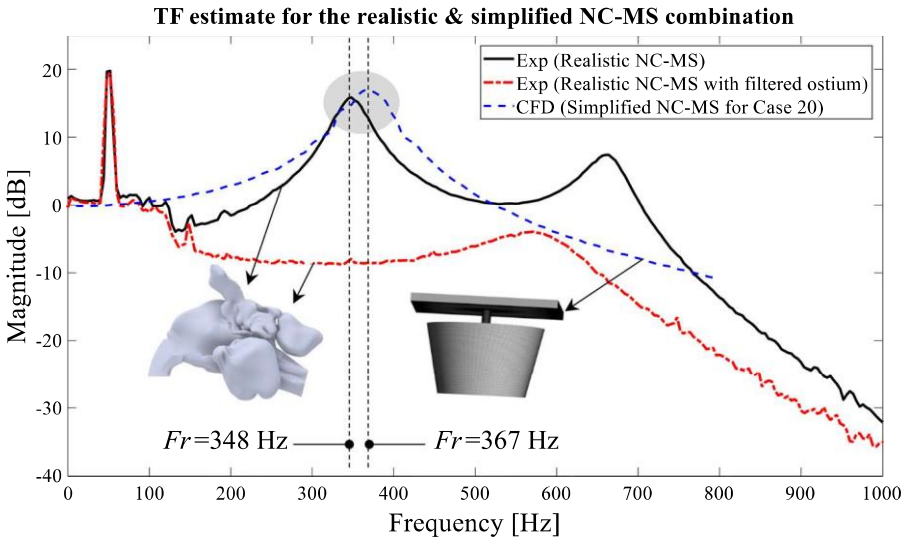

Fig. 19 Comparison of the resonance frequency of realistic/simplified NC–MS models

5 Conclusion

This study has focused on the calculation of the resonance frequency of the human nose–sinus (NC–MS) combination for improvement in the efficiency of acoustical aerosol delivery to the maxillary sinus. A total of 25 different idealized models were considered for acoustic modeling. Three different numerical models, including the classical Helmholtz resonator formula, finite element analysis (FEA), and the computational fluid dynamics (CFD), were conducted for a validation study in comparison with experiments for 14 different idealized NC–MS models. Moreover, a geometrical parametric study was investigated to understand the effect of the ostium diameter/length, MS volume/shape, and nasal cavity width on the resonance frequency of the NC–MS combination. In summary, the following remarks can be drawn from the present work:

- The geometrical shape of the MS does not significantly affect its resonance frequency. Also, the nasal cavity width has a negligible effect (±2%) on the resonance frequency of the NC–MS combination. Thus, the efficiency of the acoustic aerosol delivery is independent of the nasal cavity size and MS shape.
- The resonance frequency of the NC–MS combination has an inverse relationship with the square root of the ostium length and with the MS volume, while it has a direct relationship with the ostium diameter. For example, doubling the ostium diameter (from 3 to 6 mm) results in significantly increasing the resonance frequency from 250 to 400 Hz. However, doubling the ostium length (from 6 to 12 mm) and the MS volume (from 10 to 20 mL) leads the resonance frequency to decrease by about 27% and 16%, respectively. Hence, the drug delivery efficiency is highly dependent on these parameters.
- To achieve improved drug delivery efficiency, the amplitude of the input acoustic wave applied at the nostril should be adjusted with the damping ratio. The results showed that the damping ratio has a direct relationship with the ostium length, and has an inverse relationship with the ostium diameter and nasal cavity width.
- The Direct Computational Acoustics (DCA) using CFD simulation is more accurate than FEA and the classical Helmholtz resonator formula for the calculation of the resonance frequency of a nose–sinus combination. This is due to the governing equations underlying these methods. The CFD can capture an acoustical problem better than an FEA since it can simulate the nonlinear phenomena which occur near the walls of a solid body, while the FEA (ANSYS Harmonic Response) only solves the linearized Euler equations.
- The size of the time step used in CFD simulation greatly affects the absorption of the sound, which is due to the discretization error in the numerical solution. This can influence the accuracy of the acoustical CFD simulations. Thus, the smaller the time step, the more accurate the acoustical CFD simulation.
- The mesh density is an important parameter in the simulation of an acoustical problem. For an acoustical CFD simulation, to achieve an acceptable accuracy in pressure signal detection, at least 100 elements per wavelength are required.
- The resonance frequency of the MS of the realistic NC–MS combination of this study could be predicted by a DCA simulation of a simplified NC–MS model with ostium diameter/length and MS volume identical to the realistic one with an Error of less than 6%.

Acknowledgements Financial support for the project has been provided by the Australian Government Research Training Program (RTP), and the Beacon of Enlightenment PhD Scholarship provided by the University of Adelaide. The authors would like to acknowledge the support of the School of Mechanical Engineering, Phoenix High Performance Computing (HPC), and the workshop at the University of Adelaide.

Compliance with ethical standards

Conflict of interest The authors declare that they have no conflicts of interest.

Appendix

Table 3 shows the numerical setup and material properties for the CFD study. Table 4 presents the values of resonance frequency for all idealized cases obtained by Exp, CFD, FEA, and Theory.

References

Alciatore DG (2007) Introduction to mechatronics and measurement systems. Tata McGraw-Hill Education, New York

Alster M (1972) Improved calculation of resonant frequencies of Helmholtz resonators. J Sound Vib 24:63–85. https://doi.org/10.1016/0022-460X(72)90123-X

ANSYS (2015) ANSYS mechanical, 16.1st edn. Canonsburg, Pennsylvania

Beck A, Munz C-D (2018) Direct aeroacoustic simulations based on high order discontinuous Galerkin schemes. In: Kaltenbacher M (ed) Computational acoustics. Springer, Cham, pp 159–204. https://doi.org/10.1007/978-3-319-59038-7_4

Bendat JS, Piersol AG (2011) Random data: analysis and measurement procedures, vol 729. Wiley, Hoboken

Bies DA, Hansen C, Howard C (2017) Engineering noise control. CRC Press, New York

BioDigital (2019) Human complete anatomy. https://human.biodigital.com/index.html

Cankurtaran M, Çelik H, Coşkun M, Hizal E, Cakmak O (2007) Acoustic rhinometry in healthy humans: accuracy of area estimates and ability to quantify certain anatomic structures in the nasal cavity. Ann Otol Rhinol Laryngol 116:906–916

Durand M et al (2011) Impact of acoustic airflow nebulization on intrasinus drug deposition of a human plastinated nasal cast: new insights into the mechanisms involved. Int J Pharm 421:63–71

Durand M et al (2012) Sonic aerosol therapy to target maxillary sinuses. Eur Ann Otorhinolaryngol Head Neck Dis 129:244–250

El Merhie A, Navarro L, Delavenne X, Leclerc L, Pourchez J (2016) A new strategy to improve drug delivery to the maxillary sinuses: the frequency sweep acoustic airflow. Pharm Res 33:1074–1084

FLUENT (2008) Tutorial: modeling aeroacoustics for a Helmholtz resonator using the direct method (CAA), 6.3rd edn. Centerra, USA

FLUENT A (2009) User Guide (Release 12.0) Chapter, vol 24, pp 1315–1434

Grace SM Tutorial (2004) Computational methods in aeroacoustics. In: ASME IMECE

Granqvist S, Sundberg J, Lundberg JO, Weitzberg E (2006) Paranasal sinus ventilation by humming. J Acoust Soc Am 119:2611–2617

Hallberg CJ, Lysaught MT, Zmudka CE, Kopesky WK, Olson LE (2014) Characterization of a human powered nebulizer compressor for resource poor settings. Biomed Eng 13:77

Harbo G, Grau C, Bundgaard T, Overgaard M, Elbrønd O, Søgaard H, Overgaard J (1997) Cancer of the nasal cavity and paranasal sinuses: a clinico-pathological study of 277 patients. Acta Oncol 36:45–50

Hood CM, Schroter RC, Doorly DJ, Blenke EJ, Tolley NS (2009) Computational modeling of flow and gas exchange in models of the human maxillary sinus. J Appl Physiol 107:1195–1203

Howard CQ, Cazzolato BS (2014) Acoustic analyses using Matlab® and Ansys®. CRC Press, New York

Howard CQ, Cazzolato BS, Hansen CH (2000) Exhaust stack silencer design using finite element analysis. Noise Control Eng J 48:113–120

Huang S-F, Lee T-J, Lin K-L (2005) Concomitant bilateral orbital and brain abscesses–unusual complications of pediatric rhinosinusitis. Chang Gung Med J 28:51–55

Hyo N, Takano H, Hyo Y (1989) Particle deposition efficiency of therapeutic aerosols in the human maxillary sinus. Rhinology 27:17–26

Kumar H, Jain R, Douglas RG, Tawhai MH (2016) Airflow in the human nasal passage and sinuses of chronic rhinosinusitis subjects. PloS One 11:e0156379. https://doi.org/10.1371/journal.pone.0156379

Lam K, Hirsch AG, Tan BK (2014) The association of premorbid diseases with chronic rhinosinusitis with and without polyps. Curr Opin Otolaryngol Head Neck Surg 22:231–241

Laube BL (2007) Devices for aerosol delivery to treat sinusitis. J Aerosol Med 20:S5–S18

Leclerc L, Pourchez J, Aubert G, Leguellec S, Vecellio L, Cottier M, Durand M (2014) Impact of airborne particle size, acoustic airflow and breathing pattern on delivery of nebulized antibiotic into the maxillary sinuses using a realistic human nasal replica. Pharm Res 31:2335–2343

Maniscalco M, Weitzberg E, Sundberg J, Sofia M, Lundberg J (2003) Assessment of nasal and sinus nitric oxide output using single-breath humming exhalations. Eur Respir J 22:323–329

Maniscalco M, Sofia M, Weitzberg E, Lundberg J (2006) Sounding airflow enhances aerosol delivery into the paranasal sinuses. Eur J Clin Invest 36:509–513

Moghadam SJ, Navarro L, Leclerc L, Hodin S, Pourchez J (2018) Toward smart Nebulization: engineering acoustic airflow to penetrate maxillary sinuses in chronic rhinosinusitis. Int J Pharm 546:188–193

Möller W, Münzing W, Canis M (2010) Clinical potential of pulsating aerosol for sinus drug delivery. Expert Opin Drug Deliv 7:1239–1245

Möller W, Lübbers C, Münzing W, Canis M (2011) Pulsating airflow and drug delivery to paranasal sinuses. Curr Opin Otolaryngol Head Neck Surg 19:48–53

Möller W et al (2013) Topical drug delivery in chronic rhinosinusitis patients before and after sinus surgery using pulsating aerosols. PloS One 8:e74991. https://doi.org/10.1371/journal.pone.0074991

Möller W, Schuschnig U, Bartenstein P, Meyer G, Häussinger K, Schmid O, Becker S (2014) Drug delivery to paranasal sinuses using pulsating aerosols. J Aerosol Med Pulm Drug Deliv 27:255–263

Rau JL (2005) The inhalation of drugs: advantages and problems. Respir Care 50:367–382

Si XA, Xi J, Kim J, Zhou Y, Zhong H (2013) Modeling of release position and ventilation effects on olfactory aerosol drug delivery. Resp Physiol Neurobiol 186:22–32

Sharma SK, Jehan M, Kumar A (2014) Measurements of maxillary sinus volume and dimensions by computed tomography scan for gender determination. J Anat Soc India 63:36–42

Sutherland W (1893) The viscosity of gases and molecular force. Lond Edinb Dublin Philos Mag J Sci 36:507–531

Tam CK (1995) Computational aeroacoustics-Issues and methods. AIAA J 33:1788–1796

Tarhan E, Coskun M, Cakmak O, Celik H, Cankurtaran M (2005) Acoustic rhinometry in humans: accuracy of nasal passage area estimates, and ability to quantify paranasal sinus volume and ostium size. J Appl Physiol 99:616–623

Thompson KW (1990) Time-dependent boundary conditions for hyperbolic systems II. J Comput Phys 89:439–461

Weitzberg E, Lundberg JO (2002) Humming greatly increases nasal nitric oxide. Am J Respir Crit Care Med 166:144–145

Xi J, Yuan JE, Si XA, Hasbany J (2015) Numerical optimization of targeted delivery of charged nanoparticles to the ostiomeatal complex for treatment of rhinosinusitis. Int J Nanomed 10:4847–4861

Xi J, Si XA, Peters S, Nevorski D, Wen T, Lehman M (2017) Understanding the mechanisms underlying pulsating aerosol delivery to the maxillary sinus: in vitro tests and computational simulations. Int J Pharm 520:254–266

Statement of Authorship

Title of Paper	Acoustic Behaviour of the Human Maxillary Sinus: The Importance of the Middle Meatus and the Ostium on Resonance Frequency Behaviour
Publication status	☐ Published ☑ Accepted for Publication ☐ Submitted for Publication ☐ Unpublished and Unsubmitted work written in manuscript style
Publication Details	Pourmehran, O., Cazzolato, B., Tian, Z., & Arjomandi, M. (2020). Acoustic behaviour of the human maxillary sinus: The importance of the middle meatus and the ostium on resonance frequency behaviour. Presented in 18th International Conference of Numerical Analysis and Applied Mathematics, Rhodes, Greece. Accepted to be published in AIP conference proceeding in winter 2021.

Principal Author

Name of Principal Author (Candidate)	Oveis Pourmehran		
Contribution to the Paper	Ideas and Concepts • Conducted a comprehensive literature review to find the gaps in the knowledge • Developed the ideas and concepts based on the gaps Experiments and Modelling • Developed a realistic NC-MS model using ANSYS® SpaceClaim and Autodesk® Inventor • Designed and fabricated an experimental setup and conducted the experiments • Developed a CFD model using ANSYS® Fluent for estimating the resonance frequency of the NC-MS combination • Validated the CFD model against the experimental data Interpretation of Results • Extracted raw data from the experiments and simulation • Post-processed the simulation results using ANSYS® CFD-Post • Developed a MATLAB code to conduct signal processing for experimental data as well as to extract the figures • Interpreted the simulation results and compared them with the experimental data Manuscript • Developed the first full draft of the manuscript • Applied comments given by co-authors • Revised the manuscript after review and produced a rejoinder • Acted as the corresponding author		
Overall percentage (%)	80%		
Certification:	This paper reports on original research I conducted during the period of my Higher Degree by Research candidature and is not subject to any obligations or contractual agreements with a third party that would constrain its inclusion in this thesis. I am the primary author of this paper.		
Signature		Date	28/04/2021

Co-Author Contributions

By signing the Statement of Authorship, each author certifies that:

IV. the candidate's stated contribution to the publication is accurate (as detailed above);
V. permission is granted for the candidate in include the publication in the thesis; and
VI. the sum of all co-author contributions is equal to 100% less the candidate's stated contribution.

Name of Co-Author	Benjamin Cazzolato		
Contribution to the Paper	Supervised the research and contributed in academic discussion and manuscript review.		
Signature		Date	28/04/2021

Name of Co-Author	Zhao Tian		
Contribution to the Paper	Supervised the research and contributed in academic discussion and manuscript review.		
Signature		Date	29/04/2021

Name of Co-Author	Maziar Arjomandi		
Contribution to the Paper	Supervised the development of the research, participated in developing ideas, helped in interpretation of results and evaluation of the manuscript.		
Signature		Date	28/04/2021

Acoustic Behaviour of the Human Maxillary Sinus: The Importance of the Middle Meatus and the Ostium on Resonance Frequency Behaviour

Oveis Pourmehran[1, a)], Benjamin Cazzolato[1], Zhao Tian[1], Maziar Arjomandi[1]

[1]*School of Mechanical Engineering, the University of Adelaide, Adelaide, Australia.*

[a)]Corresponding author: oveis.pourmehran@adelaide.edu.au

Abstract. This study aims to investigate the resonance frequency of the human maxillary sinus for the application of acoustically-driven drug delivery. An improved model of the classic Helmholtz resonator formula has been developed to predict the resonance frequency of a nasal cavity and maxillary sinus combination, using computational fluid dynamics (CFD). To be more specific, a 3-D CFD model of the left side of a healthy human nose, composed of a nasal cavity connected to the maxillary sinus through an ostium, has been developed to undertake direct computational acoustics for predicting the resonance frequency. The simulations of the acoustic airflow in the nasal cavity, ostium, and maxillary sinus were carried out by solving the continuity and Navier-Stokes equations. A series of experiments were conducted for validation of CFD modelling using the resonance frequency of the nasal cavity and maxillary sinus combination as a criterion. The results showed that the classic Helmholtz resonator formula overpredicted the resonance frequency of the realistic nasal cavity and maxillary combination by 50% compared to measured experimental data. However, the results of the CFD simulation demonstrated a good agreement with the experimental data, showing a difference of 10%. Further, it is shown that by accounting for the fluid mass within both the maxillary sinus and the middle meatus the resonance frequency of the nasal cavity and maxillary sinus combination can be accurately predicted.

INTRODUCTION

Rhinosinusitis, known as a sinus infection, is one of the most widely-recognized ailments related to rhinology, which affects up to 15% of the global population [1]. The maxillary sinus (MS) is the most voluminous of the all paranasal sinuses and, due to its location, it is prone to a broader range of diseases, such as viral infection, bacterial colonization, and anatomical obstruction. The MS is located in a secluded place in the nasal cavity, which limits the drug delivery to this area [2]. Most drugs administered via the nostril, using conventional nebulizers, fail to reach the MS efficiently due to the specific geometry of the nasal cavity (NC) and MS combination [1]. However, the acoustically-driven drug delivery (ADD) technique, first proposed by Guillerm, Badre, Flottes, Riu and Rey [3], has gained considerable attention from many researchers due to its higher efficiency than the conventional nebulization drug delivery technique [4-8]. In this technique, an acoustic field is superimposed onto the nebulized drug particles (aerosols), which have been clinically used as a medicinal treatment to enhance the penetration of the drug particles into the MS, for several decades.

For a long time, a sinusoidal sound signal with a frequency of 50 Hz and 100 Hz was used by researchers and clinicians as the principle of the acoustically-driven nebulization process [9]. However, many recent studies have focused on the calculation of other frequencies to improve the efficiency of ADD to MS, exploiting the Helmholtz resonator principle and an external sound signal applied at the nostril [8, 10-12]. A Helmholtz resonator is a device composed of a cavity connected to a small tube (neck) [13]. In an NC-MS combination, the MS is assumed to be the cavity, and the ostium is considered to be the neck of a Helmholtz resonator. According to the theory, the air plug inside the neck oscillates along the length of the neck when an external sound signal is applied [13]. A frequency equal to the resonance frequency of the Helmholtz resonator device should be applied as an external sound at the nostril to

Sutherland's law [19] with three coefficients was used. The walls were set up to be adiabatic and acoustically reflective. For the inlet and outlet, pressure-inlet and pressure-outlet boundary conditions, both with zero-gauge-pressure, were defined. A zero-pressure and zero-velocity were used as the initial condition. It must be noted that the inlet and outlet must be acoustically non-reflective for the planned acoustic simulation. Therefore, a general non-reflecting boundary condition (NRBC) was applied to the outlet and Transparent Flow Forcing boundary condition was applied to the inlet, which simulates the NRBC, as well as superimposing the acoustic wave to the inlet zero-gauge-pressure. An acoustic sweep in a range of frequencies identical to those produced by white bandlimited noise signal in the experiments (from 150 Hz to 800 Hz), was used as the Transparent Flow Forcing via a User Defined Function (UDF) given by, $p(t) = A\sin(f_0 t + t^2(f_1 - f_0)/2T_s)$, where $p(t)$, A, f_0, and f_1 are the pressure as a function of time, the incident pressure amplitude, starting frequency, and final frequency, respectively. Also, T_s is the time it takes to sweep from f_0 to f_1. A non-iterative time-advancement (NITA) algorithm using a PISO pressure-velocity coupling scheme was used in this simulation. Second-order spatial discretization, Third-Order MUSCL, and QUICK methods were used for the pressure, density, and momentum and energy equations, respectively. Moreover, the second-order implicit method was performed for the transient formulation. A total of 1.28 million polyhedral elements with two boundary layers were generated for the flow simulation for a duration of t = 0.2 s, using a time-step size of $\Delta t = 0.4\mu s$. The use of polyhedral-elements in this study is due to their advantages, including better convergence, shorter computational time and high WSS accuracy [20]. An overview of the mesh generated for the realistic NC-MS model is illustrated in Fig. 1.

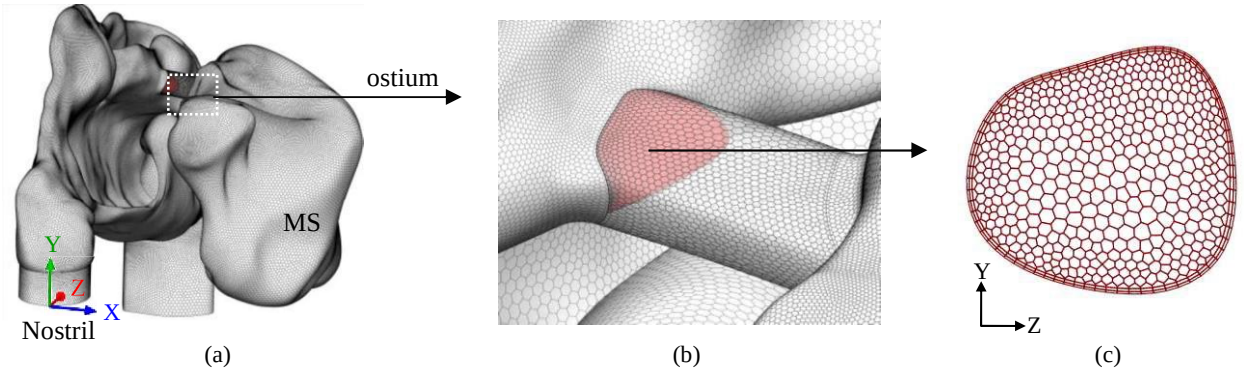

FIGURE 1. (a) frontal view of the polyhedral mesh generated for a 3-D NC-MS model, (b) zoomed view of the ostium (c) 2-D view of the polyhedral mesh on the interface between the ostium and the nasal cavity on the Z-Y plane.

RESULTS AND DISCUSSION

A series of experimental tests were conducted for the validation of the CFD simulation, focused on the resonance frequency of the realistic NC-MS combination. Figure 2 (a) shows the transfer function estimate between the input and response points obtained for two 3-D printed and one CFD NC-MC models. As can be seen in this Fig., the resonance frequency of the realistic NC-MS model created with low-resolution printing ($Exp_{low\text{-}res}$) is f_r = 410 Hz, which is 18 Hz more than that obtained from a model created with high-resolution printing ($Exp_{high\text{-}res}$). One can infer from Fig. 2 (a) and Equation (1) that the discrepancy between the resonance frequencies obtained through $Exp_{low\text{-}res}$ and $Exp_{high\text{-}res}$ stems from the high sensitivity of the resonance frequency to the ostium diameter and length. Accordingly, the data collected by $Exp_{high\text{-}res}$ is used for the evaluation of the results obtained using CFD and the classic Helmholtz resonator formula (Theory). Figure 2 (b) illustrates the deviation of the resonance frequency calculated using CFD and Theory from the experimental data, which are quantified by E_{CFD} and E_{Theory}, respectively. This Fig. reveals that the CFD simulation predicted the resonance frequency of the realistic NC-MS combination with an error of E_{CFD} = 10%, which is more accurate than that obtained by Equation (1) with E_{Theory} = 49%. Thus, the results demonstrated a good agreement between the experimental and CFD modelling. Figure 3 (a) shows the root mean squared error (RMSE) of static pressure, which quantifies the amplitude of the pressure fluctuations on different planar surfaces along the nasal cavity. According to this Fig., the RMSE static pressure on an X-Y plane coincided with the ostium centerline, demonstrates that the maximum pressure fluctuation occurs inside the MS, which implies a maximum transfer function between the inlet and MS, showing a similar behaviour of the MS and ostium to a Helmholtz resonator. Figure 3 (b) presents the RMSE X-Velocity on different planar surfaces, which confirms the oscillation of the air plug inside the ostium. This Fig. also shows that not only does the air plug inside the ostium

achieve the maximum amplitude of the air plug oscillation. The frequency can be calculated by the classic Helmholtz resonator formula, as follows [12]:

$$f_r = \frac{c}{2\pi}\sqrt{\frac{S_0}{V_{MS}L_{eff}}}, \quad (1)$$

where f_r, c, V_{MS}, and S_0, are the resonance frequency, the sound speed, the volume of the MS, and the area of the ostium cross-section, respectively. L_{eff} in Equation (1) is the effective length of the ostium, which is defined by $L_{eff} = L_{os} + 0.6\ D_{H,os}$ [12], where L_{os} and $D_{H,os}$ are the length and hydraulic diameter of the ostium, respectively. The term $0.6\ D_{H,os}$ represents an end-correction. Using this principle, several researchers have investigated the efficacy of ADD, considering different variables such as geometrical and acoustic parameters, particle sizes, and breathing patterns [4, 5, 7, 10, 14, 15]. Xi, Si, Peters, Nevorski, Wen and Lehman [12] investigated the particle deposition fraction on the MS wall using the ADD technique through both finite element analysis (FEA) and experiments. They reported that the resonance frequency of the NC-MC model in their study was $f_r = 652$Hz; however, the maximum deposition efficiency on the MS wall occurred at a different inlet frequency of $f_r = 545$Hz. Pourmehran, Arjomandi, Cazzolato, Ghanadi and Tian [16] investigated the effect of geometrical parameters on the resonance frequency of an idealized NC-MS combination using CFD, FEA, the Helmholtz resonator formula, and experimentation. The findings of their study revealed that the classic Helmholtz resonator formula overestimates the resonance frequency of the idealized NC-MS combination by more than 20% compared to the experimental data. Thus, it is essential to understand how accurately the Helmholtz resonator formula predicts the resonance frequency of a realistic NC-MS combination. This study aims to investigate the fluid features of the acoustic airflow in a realistic NC-MS combination at a fundamental level, as well as undertaking an acoustic analysis to predict the resonance frequency of the model.

METHODOLOGY

A numerical model of a real NC-MS combination was developed based on computer tomography images provided by Inthavong, Wen, Tian and Tu [17] and Kumar, Jain, Douglas and Tawhai [18]. This geometry is composed of the left side of the nasal cavity attached to the ostium and MS with $D_{H,os} \approx 4$ mm, $L_{os} \approx 6$ mm, and $V_{MS} \approx 15$ mL. The frontal, sphenoid, and ethmoid sinuses are excluded from the geometry. For validation purposes, the resonance frequency of the NC-MS combination was used. The resonance frequency of the realistic NC-MS model was calculated using the Helmholtz resonator theory (Equation (1)), experiments, and CFD simulation.

Experimental Design

The realistic model of the NC-MS combination was manufactured using 3-D printing techniques at the University of Adelaide. Two different materials were used for printing the models to evaluate the sensitivity of the accuracy of 3-D printed models. The plastic material resulted in a resolution of 0.2 mm (low-resolution), and the resin-based material created a model with a resolution of 0.09 mm (high-resolution). Using a similar experimental test rig and the procedure described in Pourmehran, Arjomandi, Cazzolato, Ghanadi and Tian [16], the resonance frequency of the 3-D printed NC-MS models were measured. To do so, a white bandlimited noise signal from 150 Hz to 800 Hz, was applied to the nostril using a loudspeaker. The transfer function between the input and response pressure signals was estimated in the frequency domain using a MATLAB code. A magnitude-squared coherence function (Coh) was used to verify the degree of linearity between the input and response signals. The Coh is a function of frequency and has a value between zero and unity, which exceeded 0.9 for the most part in this study, showing a high level of coherence and demonstrating an acceptable level of accuracy. The TF estimate and coherence function was obtained using a Hanning window with 1024 FFT points and a 75% overlap for a total of 17 averagings. To ensure that the results are predictable and repeatable, the experiments were conducted five times for each NC-MS 3-D printed model.

CFD Simulation

The airflow features in the real NC-MS combination were simulated using ANSYS® FLUENT. To resolve the flow features in the presence of an acoustic field, a pressure-based solver was used for solving the compressible transient nonlinear Navier-Stokes equations. To simulate the conditions of the experiment, the fluid medium in this study was dry air, and the ideal gas law was used to resolve the air density. Also, for calculating the viscosity,

oscillate in the presence of an external acoustic field, but also a portion of the air plug in the middle meatus fluctuates in the ostium length direction, which offers new insight into the correction of the Helmholtz resonator formula for ADD application.

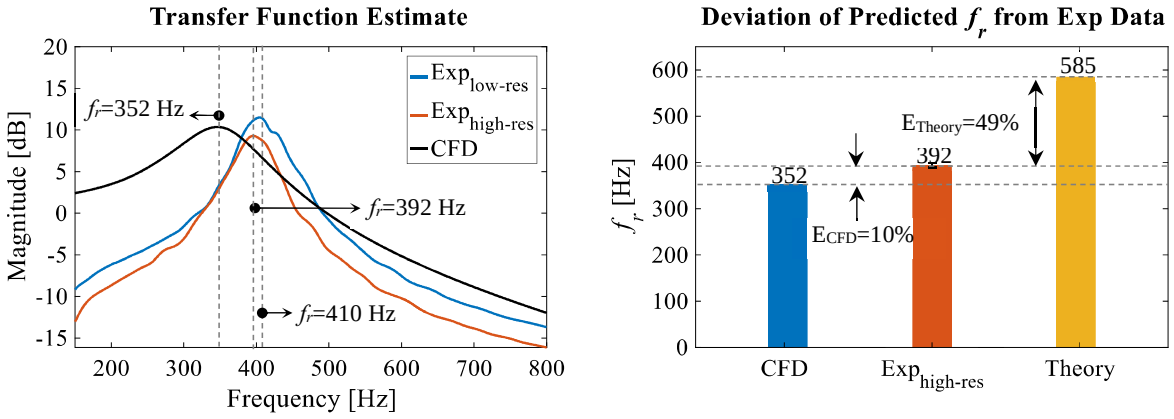

(a) (b)

FIGURE 2. (a) TF estimate obtained by experiments and CFD, (b) comparison of f_r obtained by different methods

According to the correction mentioned above, the effective length, L_{eff}, in Equation (1) is assumed to be $L_{eff} = L_{os} + \beta_{os} D_{H,os} + L_{MM} + \beta_{MM} D_{H,os}$, where L_{MM} is the length of the middle meatus (MM) as identified in Fig. 3 (b). The length of MM in this study is $L_{MM} = 7$ mm. Also, β_{os} and β_{MM} are the neck length correction factor related to the ostium and the MM. The ostium end is assumed to be flanged, in which the end-correction factor is $\beta_{os} = 0.5 \times 8 S_0^{0.5} / 3\pi^{1.5} = 0.425$ [21]. The end-correction for the MM is deduced from the resonance frequency obtained experimentally through substituting the known parameters in Equation (1), which gives $\beta_{MM} = 0.387$. Therefore, the corrected effective length of the neck in Equation (1) becomes $L_{eff} = L_{os} + 0.425 D_{H,os} + L_{MM} + 0.387 D_{H,os}$. Using this correction, Equation (1) gives an accurate resonance frequency of $f_r = 392$ Hz. However, this correction is only valid for the specific, realistic geometry used in this study. A series of realistic NC-MS models should be analyzed experimentally and numerically to generalise the correction of the classic Helmholtz resonator formula.

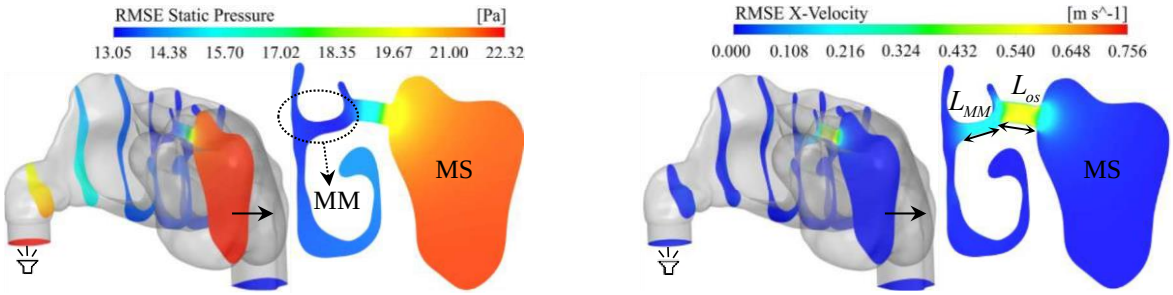

(a) (b)

FIGURE 3. (a) RMSE static pressure on different planes, (b) RMSE X-Velocity on different planes

CONCLUSION

In this study, the resonance frequency of a realistic human NC-MS model was investigated using experiments, CFD, and the Helmholtz resonator formula for the application of acoustically-driven drug delivery to the MS. The results showed that CFD was more accurate than the classic Helmholtz resonator formula. However, a correction was made to the neck effective length in the classic Helmholtz resonator formula to improve the resonance frequency prediction. Using that correction, the Helmholtz resonator formula could predict the resonance frequency of a specific, realistic NC-MS combination more accurately than the classic one. Nevertheless, for a generalization of the correction, more realistic NC-MS models will need to be investigated further.

ACKNOWLEDGMENTS

Financial support for the project has been provided by the Australian Government Research Training Program (RTP), the Beacon of Enlightenment PhD Scholarship offered by the University of Adelaide. The authors would like to acknowledge the support of the School of Mechanical Engineering, Phoenix High-Performance Computing (HPC), and the 3-D printing workshop at the University of Adelaide.

REFERENCES

1. B. L. Laube, Journal of Aerosol Medicine **20** (s1), S5-S18 (2007).
2. D. O. Frank, A. M. Zanation, V. H. Dhandha, K. A. McKinney, G. M. Fleischman, C. S. Ebert Jr, B. A. Senior and J. S. Kimbell, International Forum of Allergy & Rhinology **3** (10), 834-840 (2013).
3. R. Guillerm, R. Badre, L. Flottes, R. Riu and A. Rey, La Presse Medicale **67** (27), 1097-1098 (1959).
4. M. Maniscalco, M. Sofia, E. Weitzberg and J. Lundberg, European Journal of Clinical Investigation **36** (7), 509-513 (2006).
5. M. Durand, J. Pourchez, G. Aubert, S. Le Guellec, L. Navarro, V. Forest, P. Rusch and M. Cottier, International Journal of Pharmaceutics **421** (1), 63-71 (2011).
6. W. Möller, U. Schuschnig, G. Celik, W. Münzing, P. Bartenstein, K. Häussinger, W. G. Kreyling, M. Knoch, M. Canis and S. Becker, PloS One **8** (9), e74991 (2013).
7. L. Leclerc, J. Pourchez, G. Aubert, S. Leguellec, L. Vecellio, M. Cottier and M. Durand, Pharmaceutical Research **31** (9), 2335-2343 (2014).
8. W. Möller, U. Schuschnig, P. Bartenstein, G. Meyer, K. Häussinger, O. Schmid and S. Becker, Journal of Aerosol Medicine and Pulmonary Drug Delivery **27** (4), 255-263 (2014).
9. L. Navarro, L. Leclerc and J. Pourchez, Online Journal of Otolaryngology and Rhinology **1** (4), 1-3 (2019).
10. M. Durand, S. Le Guellec, J. Pourchez, F. Dubois, G. Aubert, G. Chantrel, L. Vecellio, C. Hupin, R. De Gersem and G. Reychler, European Annals of Otorhinolaryngology, Head and Neck Diseases **129** (5), 244-250 (2012).
11. A. El Merhie, L. Navarro, X. Delavenne, L. Leclerc and J. Pourchez, Pharmaceutical Research **33** (5), 1074-1084 (2016).
12. J. Xi, X. A. Si, S. Peters, D. Nevorski, T. Wen and M. Lehman, International Journal of Pharmaceutics **520** (1), 254-266 (2017).
13. H. Von Helmholtz and A. J. Ellis, *On the Sensations of Tone as a Physiological Basis for the Theory of Music*. (Longmans, Green and Company, London, 1875).
14. M. Maniscalco, E. Weitzberg, J. Sundberg, M. Sofia and J. Lundberg, European Respiratory Journal **22** (2), 323-329 (2003).
15. O. Pourmehran, B. Cazzolato, Z. Tian and M. J. E. J. o. P. S. Arjomandi, 105398 (2020).
16. O. Pourmehran, M. Arjomandi, B. Cazzolato, F. Ghanadi and Z. Tian, Biomechanics and Modeling in Mechanobiology **19** (2), 557-575 (2020).
17. K. Inthavong, J. Wen, Z. Tian and J. Tu, Journal of Aerosol Science **39** (3), 253-265 (2008).
18. H. Kumar, R. Jain, R. G. Douglas and M. H. Tawhai, PloS One **11** (6), e0156379 (2016).
19. W. Sutherland, The London, Edinburgh, and Dublin Philosophical Magazine and Journal of Science **36** (223), 507-531 (1893).
20. M. Spiegel, T. Redel, Y. J. Zhang, T. Struffert, J. Hornegger, R. G. Grossman, A. Doerfler, C. J. C. m. i. b. Karmonik and b. engineering, **14** (01), 9-22 (2011).
21. M. Monteiro, A. C. Marti, P. Vogt, L. Kasper and D. Quarthal, The Physics Teacher **53** (4), 247-249 (2015).

Chapter 4

Understanding of the underlying mechanism of acoustic drug delivery to the maxillary sinus

In the previous chapter (Chapter 3), the resonance frequency of the combination of the nasal cavity (NC) and maxillary sinus (MS) has been predicted using various numerical models, and the computational fluid dynamics (CFD) model has demonstrated an acceptable accuracy. To investigate the effect of the resonance frequency, obtained using the CFD model described in Chapter 3, as well as to understand the underlying mechanism of acoustic drug delivery (ADD) to the maxillary sinus (MS) on the transport and deposition patterns of particles (drugs) in an NC-MS combination, a CFD model was developed. A Eulerian-Lagrangian particle tracking scheme was used to understand the aerosol transport pattern and deposition of aerosols in the MS under the effect of an acoustic wave with different aero-acoustic

characteristics. A parametric study was conducted to investigate the effect of aero-acoustic parameters such as input frequency (including the resonance and off-resonance frequency), amplitude, and inlet airflow rate on the flow features within the NC, ostium and MS. Using the parametric study, the optimised value of the acoustic wave was determined to achieve the highest drug delivery efficiency. The effect of the acoustic radiation force on ADD was discussed through assessment of the acoustic Stokes number. The effect of particle density and diameter on the ADD efficiency were also investigated, considering their effects on the acoustic Stokes number. The models developed in this chapter address the second objective of this study that is "*to develop an understanding of airflow behaviour in a simplified NC-MS combination in the presence of an external acoustic field in order to investigate the effect of aero-acoustic parameters on the efficiency of ADD".*

4.1 Published articles

This chapter consists of a published journal article and a conference paper. In the journal article, the effect of aero-acoustic parameters on ADD efficiency, and in the conference article, the effect of particle diameter and density on ADD efficiency, are presented.

Pourmehran, O., Cazzolato, B., Tian, Z., & Arjomandi, M. (2020). Acoustically-driven drug delivery to maxillary sinuses: Aero-acoustic analysis. *European Journal of Pharmaceutical Sciences,* 151, No.105398.

Pourmehran, O., Arjomandi, M., Cazzolato, B., & Tian, Z. (2020). "Effect of particle diameter and density on acoustic drug delivery to maxillary sinus – A sensitivity study". *22nd Australasian Fluid Mechanics Conference (AFMC2020), Brisbane, Australia*. Oral presentation.

Statement of Authorship

Title of Paper	Acoustically-driven drug delivery to maxillary sinuses: Aero-acoustic analysis
Publication status	☑ Published ☐ Accepted for Publication ☐ Submitted for Publication ☐ Unpublished and Unsubmitted work written in manuscript style
Publication Details	Pourmehran, O., Cazzolato, B., Tian, Z., & Arjomandi, M. (2020). Acoustically-driven drug delivery to maxillary sinuses: Aero-acoustic analysis. European Journal of Pharmaceutical Sciences, 151, No.105398.

Principal Author

Name of Principal Author (Candidate)	Oveis Pourmehran
Contribution to the Paper	Ideas and Concepts • Conducted a comprehensive literature review to find the gaps in the knowledge • Developed the ideas and concepts based on the gaps Experiments and Modelling • Developed the simplified NC-MS models using ANSYS® DesignModeler • Conducted the experiments • Developed the CFD models using ANSYS® Fluent to estimate the resonance frequency of the NC-MS combination and to simulate the acoustic wave propagation and particle tracking and particle tracking • Validated the simulated model with the experimental data Interpretation of Results • Extracted raw data from the experiments and simulation • Post-processed the simulation results using ANSYS® CFD-Post • Developed a MATLAB code to conduct signal processing for experimental data and to extract the figures • Interpreted the simulation results and compared them with the experimental data Manuscript • Developed the first full draft of the manuscript • Applied comments given by co-authors • Acted as the corresponding author
Overall percentage (%)	80%
Certification:	This paper reports on original research I conducted during the period of my Higher Degree by Research candidature and is not subject to any obligations or contractual agreements with a third party that would constrain its inclusion in this thesis. I am the primary author of this paper.
Signature	Date: 28/04/2021

Co-Author Contributions

By signing the Statement of Authorship, each author certifies that:

VII. the candidate's stated contribution to the publication is accurate (as detailed above);
VIII. permission is granted for the candidate in include the publication in the thesis; and
IX. the sum of all co-author contributions is equal to 100% less the candidate's stated contribution.

Name of Co-Author	Benjamin Cazzolato
Contribution to the Paper	Supervised the research and contributed in academic discussion and manuscript review.
Signature	Date: 28/04/2021

Name of Co-Author	Zhao Tian
Contribution to the Paper	Supervised the research and contributed in academic discussion and manuscript review.

Signature		Date	29/04/2021

Name of Co-Author	Maziar Arjomandi		
Contribution to the Paper	Supervised the development of the research, participated in developing ideas, helped in interpretation of results and evaluation of the manuscript.		
Signature		Date	28/04/2021

European Journal of Pharmaceutical Sciences 151 (2020) 105398

Contents lists available at ScienceDirect

European Journal of Pharmaceutical Sciences

journal homepage: www.elsevier.com/locate/ejps

Acoustically-driven drug delivery to maxillary sinuses: Aero-acoustic analysis

Oveis Pourmehran*, Benjamin Cazzolato, Zhao Tian, Maziar Arjomandi

School of Mechanical Engineering, the University of Adelaide, Adelaide, Australia

ARTICLE INFO

Keywords:
Acoustically-driven drug delivery
Maxillary sinuses
Computational fluid dynamics
Aero-acoustics
Targeted drug delivery
Resonance frequency

ABSTRACT

This paper investigates the effect of aero-acoustic parameters on the efficiency of acoustically-driven drug delivery (ADD) to human maxillary sinus (MS). To be more specific, the effect of the frequency, amplitude at the acoustic excitation, and the inlet mean flow rate on the efficiency of ADD to the MS is studied. Direct computational aero-acoustics, using a validated computational fluid dynamics (CFD) model, has been utilised to carry out the parametric study. The transport pattern of the particles (drugs) in the presence of an external acoustic field has been investigated through the discrete phase model. Extensive computational simulations have revealed that the most important parameter in acoustically-driven drug delivery to the MS is the amplitude of the oscillation of the air plug in the ostium, which is largest when the combination of nasal cavity and MS is at resonance. Also, it has been found that the amplitude of the inlet acoustic wave has a direct correlation with the efficiency of the drug delivery to the MS. Moreover, the inlet mean airflow rate adversely affects the efficiency of the drug delivery to the MS. The results of this study suggest that applying an external acoustic field after distributing the drug particles with no mean flow results in a better drug delivery than in the presence of an inlet mean flow.

1. Introduction

Acoustically-driven drug delivery (ADD) to the maxillary sinus (MS) is a non-invasive technique for rhinosinusitis treatment that has recently gained great attention from many scientists in the field of targeted drug delivery (TDD) for the respiratory system. Early studies on TDD showed the potential of acoustic vibration in facilitating aerosolised drug penetration into the sinuses by adding sound waves to nasal aerosol therapy (Kauf, 1968; Sato et al., 1981). The efficacy of ADD was demonstrated experimentally by Weitzberg and Lundberg (2002), who measured the amount of nitric oxide (NO) during humming exhalation and found a 15-fold increase in drug delivery to the MS in comparison with non-humming expiration. They also showed that NO concentration during exhalation is highly dependent on the humming frequency. Similarly, Maniscalco et al. (2006) reported that human nasal humming produces a sound wave, which can enhance the efficiency of particle deposition on the MS wall by up to 4 times. Moreover, Durand et al. (2012) conducted an experimental investigation into the effect of ADD on MS drug delivery and reported an enhancement of the sinuses' ventilation, as well as an increase in the drug deposition efficiency on the MS wall (Durand et al., 2011).

The underlying mechanism of ADD is based on the Helmholtz resonator theory (Leclerc et al., 2014). A Helmholtz resonator is a device comprising a neck (a narrow straight tube) attached to a cavity (Von Helmholtz & Ellis, 1875). In a Helmholtz resonator, the air plug inside the neck oscillates in the presence of an external acoustic field. The amplitude of the air plug oscillation approaches its maximum at the resonance frequency of the Helmholtz resonator, where the maximum air-exchange between the neck and the cavity occurs (Von Helmholtz & Ellis, 1875). In a nose-sinus system, the ostium, which connects the nasal cavity (NC) to the MS, operates as the Helmholtz resonator's neck and the MS as the Helmholtz resonator's cavity. Drawing upon the Helmholtz resonator concept, drug delivery to the MS should be maximised if the acoustic field applied at the nostril has a frequency equal to the resonance frequency of the NC-MS combination. The resonance frequency of a Helmholtz resonator with a cylindrical neck and spherical cavity can be estimated by (Xi et al., 2017)

$$f_r = \frac{c}{2\pi}\sqrt{\frac{S_0}{V_{MS}L_{eq}}}, \quad (1)$$

where c, V_{MS}, and S_0 are the speed of sound, MS volume, and the area of the ostium cross-section, respectively. L_{eq} is the equivalent length of the ostium, which is obtained by $L_{eq} = L_{os} + 0.6D_{H,os}$, where L_{os} and $D_{H,\ os}$

* Corresponding author. School of Mechanical Engineering, the University of Adelaide, North Terrace, Adelaide, SA, 5005, Australia.
E-mail address: oveis.pourmehran@adelaide.edu.au (O. Pourmehran).

https://doi.org/10.1016/j.ejps.2020.105398
Received 27 April 2020; Accepted 26 May 2020
Available online 30 May 2020

Nomenclature

A_p	pressure wave amplitude [Pa]
A_u	velocity amplitude [m/s]
c	speed of sound [m/s]
C_{xy}	coherence function between input and response
C_d	drag coefficient
d_p	particle diameter [m]
D_{os}	ostium diameter [m]
D	hydraulic diameter of the inlet [m]
η_p	particle entrainment coefficient
ϕ_p	phase factor
f	frequency [Hz]
f_C	collision efficiency
f_0	starting frequency [Hz]
f_1	final frequency [Hz]
f_r	resonance frequency [Hz]
$\vec{F}$	body force [N]
$\vec{F}_B$	Brownian force [N]
$\vec{F}_{Basset}$	Basset force [N]
$\vec{F}_D$	drag force [N]
$\vec{F}_{Faxen}$	Faxen force [N]
$\vec{F}_g$	gravitational force [N]
$\vec{F}_m$	Magnus force [N]
$\vec{F}_p$	the total force on a particle [N]
$\vec{F}_{p.gradient}$	pressure-gradient force [N]
$\vec{F}_{rad}$	acoustic radiation force [N]
$\vec{F}_{Saffman}$	Saffman force [N]
$\vec{F}_T$	thermophoretic force [N]
$\vec{F}_v$	virtual mass force [N]
G_{xy}	cross power spectral density between input and response [Pa^2/Hz]
G_{xx}	power spectral density of input [Pa^2/Hz]
G_{yy}	power spectral density of response [Pa^2/Hz]
L_{os}	ostium length [m]
L_{eq}	the equivalent length of the ostium [m]
m_p	particle mass [kg]
M_w	molecular weight [g/mol]
μ	dynamic viscosity [kg/m.s]
μ_0	reference viscosity [kg/m.s]
p_{in}	inlet pressure [Pa]
p	local static pressure [Pa]
p_{op}	operating pressure [Pa]
p_0	initial pressure [Pa]
ρ	fluid density [kg/m^3]
ρ_p	particle density [kg/m^3]
R_g	global gas constant [J/mol.K]
R_{os}	ostium radius [m]
Re	Reynolds number
Re_p	particle Reynolds number ($\rho d_p \lvert u\text{-}u_p \rvert/\mu$)
S	Sutherland constant [K]
S_m	source term [kg/m^3.s]
S_0	ostium cross-sectional area [m^2]
St	Stokes number
St_{ac}	acoustic Stokes number
t	real-time [s]
T	period [s]
T_{local}	local temperature [K]
T_0	reference temperature [K]
T_{xy}	transfer function estimate
T_s	acoustic sweep cycle duration [s]
$\bar{\bar{\tau}}$	stress tensor
τ_r	particle relaxation time [s]
$\vec{u}$	fluid flow velocity [m/s]
$\vec{u}_p$	particle velocity [m/s]
U	fluid mean velocity [m/s]
V_{MS}	maxillary sinus volume [mL]
W_{NC}	nasal cavity width [mm]

Abbreviations

ADD	acoustically-driven drug delivery
CFD	computational fluid dynamics
DDE	drug delivery efficiency
MS	maxillary sinus
NC	nasal cavity
OS	ostium
PSD	power spectral density
RMSE	root mean square error
TDD	targeted drug delivery
TF	transfer function

are the ostium length and ostium hydraulic diameter, respectively. Depending on the shape of the MS and ostium, more accurate expressions can be derived (Alster, 1972; Howard et al., 2000). The effects of geometric parameters on the resonance frequency of an NC-MS combination were reported in a recent study by Pourmehran et al. (2020). They also demonstrated that the MS shape and NC width do not have a significant effect on the resonance frequency of an NC-MS combination.

A number of researchers have investigated the effect of the ostium diameter and length on the efficiency of ADD to the MS. Maniscalco et al. (2006) reported an increase in ostium diameter has an increasing effect on the efficiency of ADD to the MS, which is aligned with the results reported by Hyo et al. (1989). In that study, Hyo et al. (1989) showed an increase in the deposition efficiency from 1.3% to 2.3% by increasing the ostium diameter from 1 mm to 5 mm when a 10-15 mbar positive pressure is applied between the NC and MS. In terms of the ostium length, it was determined that the efficiency of drug delivery to the MS has an inverse relationship with the ostium length (Xi et al., 2017), which confirms the findings demonstrated by Maniscalco et al. (2003). It can be concluded that nasal humming and the application of an acoustic field at the nostril increases the exchange of air between the two sides of the ostium. In addition to the geometric parameters, aero-acoustic parameters, such as the sound pressure amplitude, frequency, and the inlet mean flow, also affect the efficiency of ADD to the MS.

The effect of sound frequency at the inlet on the particle deposition on the MS wall has rarely been reported in the literature (Moghadam et al., 2018). Although it was demonstrated in previous studies that the drug delivery efficiency (DDE) is maximal at the resonance frequency of the NC-MS complex, the details of the flow feature are not clear. This study seeks to examine the effect of inlet sound pressure amplitude, frequency, and mean flow rate on the flow features in the ostium and particle transport patterns. Moreover, CFD modelling will be used to investigate the flow features and underlying mechanism of the ADD.

2. Problem definition and case studies

Several experimental studies have investigated the ADD to the MS and have shown the benefit of this technique (El Merhie et al., 2016; Moghadam et al., 2018; Navarro et al., 2019). However, further investigations are required to understand the underlying mechanism of the ADD. This research will undertake a parametric study to

demonstrate the effect of aero-acoustic parameters on the efficiency of ADD, as well as to investigate the underlying mechanism of the ADD technique using CFD modelling. Because the shape of the MS and NC does not have a significant effect on the resonance frequency of the NC-MS combination (Pourmehran et al., 2020), a simplified NC-MS model (Figure 1), instead of a realistic one, was used for the sensitivity study, to enable straightforward manipulation of the geometry (Hood et al., 2009). The dimensions of the simplified NC-MS model were adapted from the dimension of a realistic NC-MS model as follows: the ostium diameter is $D_{os} = 4$ mm, ostium length is $L_{os} = 4$ mm, nasal cavity width is $W_{NC} = 3$ mm, and the MS volume is $V_{MS} = 15$ mL.

A total of 18 different cases were considered to investigate the effect of inlet sound frequency (6 cases), sound pressure amplitude (7 cases), and inlet mean flow rate (5 cases) on the flow features in the ostium and on the efficiency of ADD to the MS. The ADD efficiency in this study is defined as the ratio of the number of particles entering the MS to the particles that were injected at the inlet of the NC. The dimensions of the idealized geometry are depicted in Figure 2 and the details of the case studies for idealized geometry are tabulated in Table 1.

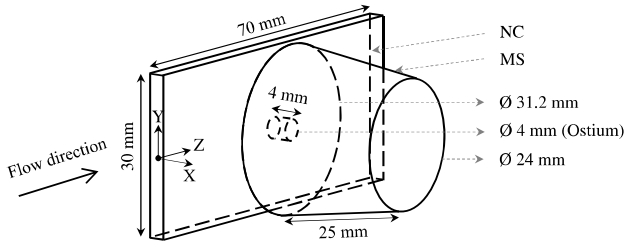

Figure 2. The dimensions of the idealized NC-MS model.

3. Governing equations and boundary conditions

3.1. Fluid phase

In this study, the 3-dimensional (3D) continuity, momentum, and energy equations are used as the governing equations of the unsteady-state acoustically-driven airflow. The airflow was assumed to be compressible and Newtonian. Direct computational aero-acoustics were used for the acoustic analysis. The governing equations of the continuum phase are given below.

The mass conservation equation is given by

$$\frac{\partial \rho}{\partial t} + \nabla\cdot(\rho\vec{u}) = S_m, \tag{2}$$

where t, ρ, $\vec{u}$ are the time, fluid density, and flow velocity, respectively. S_m is a source term representing the mass added to the continuum phase (e.g. because of the vaporization of the droplets), which is zero in this study.

The equation of momentum conservation is given by

$$\frac{\partial}{\partial t}(\rho\vec{u}) + \nabla\cdot(\rho\vec{u}\vec{u}) = -\nabla p + \nabla\cdot(\bar{\bar{\tau}}) + \rho\vec{g} + \vec{F}, \tag{3}$$

where p, $\bar{\bar{\tau}}$, $\rho\vec{g}$, and $\vec{F}$ are the local static pressure, stress tensor, gravitational body force, and external body force, respectively. The external body force is zero in this study. The stress tensor, $\bar{\bar{\tau}}$,is given by (Fluent Theory Guide, 2019):

$$\bar{\bar{\tau}} = \mu\left[(\nabla\vec{u} + \nabla\vec{u}^{T}) - \frac{2}{3}\nabla\cdot\vec{u}I\right] \tag{4}$$

where I is the unit tensor. Given the compressibility of the flow and the presence of the external acoustic field, air is assumed to be an ideal gas, using the Ideal Gas Law given by (Fluent Theory Guide, 2019):

$$\rho = \frac{p_{op} + p}{\frac{R_g}{M_w T_{local}}}, \tag{5}$$

where ρ, p_{op}, p, R_g, and M_w are the fluid density, operating pressure, local static pressure relative to the operating pressure, the universal gas constant, and the molecular weight, respectively. The temperature, T_{local}, is the local gas temperature. The viscosity of air was modelled by the three coefficients using Sutherland's law, given by:

$$\mu = \mu_0\left(\frac{T_{local}}{T_0}\right)^{3/2}\frac{T_0 + S}{T_{local} + S}, \tag{6}$$

where μ, T_0, and μ_0 are the fluid dynamic viscosity, temperature, and the reference viscosity, respectively. The reference viscosity is that of air at a reference temperature, and S is the Sutherland constant (Sutherland, 1893). The properties of the air are given in Table 2.

A no-slip condition was defined on the wall boundaries and the pressure-outlet boundary condition was applied to the outlet. Moreover, a general non-reflecting boundary condition was defined at the outlet to avoid reflection of the acoustic waves at this boundary. The pressure inlet boundary condition was applied to the inlet, which was used to model the sinusoidal acoustic pressure given by:

$$p_{in}(t) = p_0 + (A_p \times \sin(2\pi f t)), \tag{7}$$

where p_{in}, p_0, A_p, and f are the inlet pressure, initial pressure, pressure

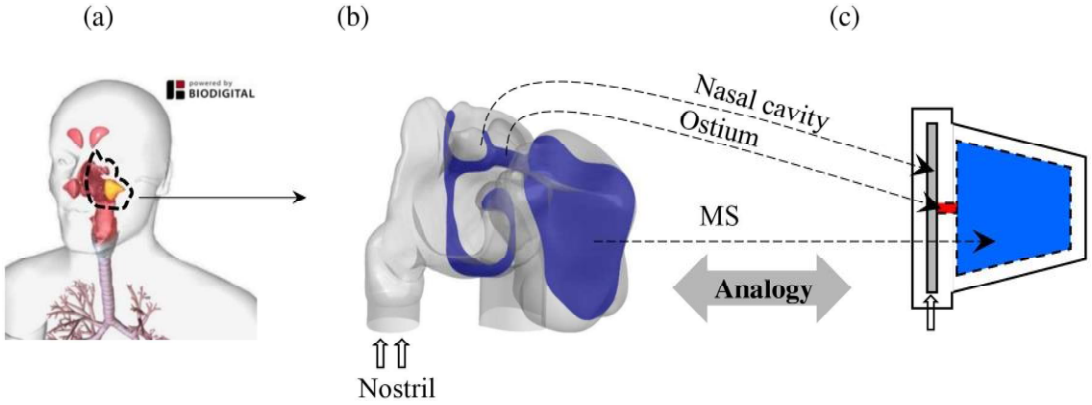

Figure 1. Schematic of (a) the computational domain (reprinted with permission from Springer Nature: Springer Nature, BIOMECHANICS AND MODELING IN MECHANOBIOLOGY, The impact of geometrical parameters on acoustically driven drug delivery to maxillary sinuses, Oveis Pourmehran et al, COPYRIGHT (2019)); (b) a CT-image-based reconstruction of a realistic nose-sinus model, where the MS was extracted from a realistic NC-MS STL file adapted from Kumar et al. (2016) and the NC was extracted from a CAD model of human upper airways adapted from Inthavong et al. (2008); (c) X-Z plane of the simplified NC-MS model as an analogy of the realistic model.

Table 1
Details of the case studies for the idealized model.

Cases	Frequency [Hz]	Sound pressure amplitude [Pa]	Inlet mean flow velocity [m/s]	Re
1-6	300, 350, 400, 455, 500, 550	15	0	0
7-13	455	1, 2, 4, 8, 16, 32, 64	0	0
14-18	455	15	0, 0.16, 0.21, 0.27, 0.54	0, 60, 80, 100, 200

Table 2
Properties of the fluid (air).

Parameter	Symbol	Value	Units
Density	ρ	ideal gas	kg/m^3
Sound speed	c	344	m/s
Dynamic Viscosity	μ	Sutherland' law	kg/m.s
Reference viscosity	μ_0	1.7894×10^{-5}	kg/m.s
Molecular Weight	M	28.966	g/mol
Sutherland constant	S	110.56	K
Reference temperature	T_0	273.11	K
Global gas constant	R_g	8.3145	J/mol.K
Operating pressure	p_{op}	101325	Pa

wave amplitude, and the frequency of interest, respectively.

3.2. Particle phase

To understand the effect of the aero-acoustic parameters on the efficiency of ADD to the MS, a Lagrangian particle tracking approach, using a discrete phase model (DPM), was employed to simulate the particle trajectories. Using this approach, by integrating the equation of force balance on every particle, the particles' trajectories can be tracked. The force balance equation, which equates the particle inertia with the forces acting on the particle, is defined by

$$\vec{F}_p = m_p \frac{d\vec{u}_p}{dt}, \tag{8}$$

where $\vec{F}_p$, m_p, and $\vec{u}_p$ are the total force acting on a particle, particle mass, and the velocity of the particle, respectively. The total force acting on a small particle in an acoustically-driven fluid flow comprises different components given by (Pourmehran et al., 2016):

$$\vec{F}_p = \vec{F}_{\text{Basset}} + \vec{F}_T + \vec{F}_{\text{Saffman}} + \vec{F}_B + \vec{F}_{\text{p.gradient}} + \vec{F}_v + \vec{F}_m + \vec{F}_{\text{Faxen}} + \vec{F}_{\text{rad}} + \vec{F}_g + \vec{F}_D, \tag{9}$$

In this study, most of these forces are neglected as follows: the Basset force, $\vec{F}_{\text{Basset}}$, is neglected given the relatively small density of air, $\rho = 1.225\ kg/m^3$, in comparison with the density of the particle, $\rho_p = 2558\ kg/m^3$ (Bassett, 1888). The thermophoretic force (Loyalka, 1992), $\vec{F}_T$, is a consequence of an unequal exchange of momentum between the fluid and particles caused by the temperature gradient, which is neglected in this study (Calmet et al., 2019). The Saffman's lift, $\vec{F}_{\text{Saffman}}$, and Brownian force, $\vec{F}_B$, act mostly on submicron particles (Ounis et al., 1991; Schwarzkopf et al., 2011), which can be neglected since micron-size particles with a diameter of $2.8\,\mu m$ are used in this study, hence, the diffusion of particles, which depends on the Brownian motion of particles is neglected in this study. The particle diameter of $2.8\,\mu m$ was selected based on the previous study reported by Moghadam et al. (2018). The pressure-gradient, $\vec{F}_{\text{p.gradient}}$, and virtual mass forces, $\vec{F}_v$, can be ignored because they are dominant for a condition where the particle density is smaller than the fluid density (Kolev, 2011; Maul, 2019), which is not the case for this study. The Magnus force is the lift developed due to the rotation of particles. The pressure difference between the two sides of the particle caused by the velocity difference resulting from the particle rotation forms the Magnus force, $\vec{F}_m$, (Crowe et al., 2011). In this study, the Magnus force is negligible compared with the drag force, since $F_m/F_D \cong 6 \times 10^{-8}\omega_d$, where ω_d is the angular velocity of the particle. The Faxen force, $\vec{F}_{\text{Faxen}}$, is considerable when the size of the fluid domain and the particle are in the same order (Chen & Ye, 2000), so this force is neglected for this study because the fluid domain size is four orders of magnitude larger than the particle size.

The acoustic radiation force, $\vec{F}_{\text{rad}}$, is the time-averaged force exerted on a particle in an acoustic field, produced by the nonlinear components of the acoustic pressure (Karlsen, 2018). This force is neglected in this study, not only due to its unimportant role at low-frequencies (<1000 Hz), but also because this study focuses on air-exchange between the MS and NC. For a very low flow velocity, the gravitational force acting on a small particle is significant (Kleinstreuer & Zhang, 2003), which occurs in the MS where the particle and flow velocities are remarkably low. Considering the above-mentioned assumption, the gravitational force (a combination of buoyancy and gravity), $\vec{F}_g$, and drag force, $\vec{F}_D$, are important in this study. In conclusion, the force balance equation for a spherical particle, which is used in this study, reduces to:

$$m_p \frac{d\vec{u}_p}{dt} = \vec{F}_g + \vec{F}_D = m_p \frac{\vec{g}(\rho_p - \rho)}{\rho_p} + m_p \frac{(\vec{u} - \vec{u}_p)}{\tau_r}, \tag{10}$$

where $\vec{g}$ is the gravitational acceleration, $\vec{u}$ is the fluid phase velocity, $\vec{u}_p$ is the particle velocity, ρ_p is the particle density, and τ_r is the particle relaxation time given by:

$$\tau_r = \frac{\rho_p d_p^2}{18\mu} \frac{24}{C_d \text{Re}_p} \tag{11}$$

where d_p and C_d are the particle diameter and drag coefficient, respectively. The drag coefficient for a smooth sphere particle is calculated by the drag coefficient equations developed by Morsi and Alexander (1972), which is correlated to the particle Reynolds number given by $\text{Re}_p = \frac{\rho d_p |u - u_p|}{\mu}$.

3.2.1. Orthokinetic motion

Applying an acoustic wave to an aerosol causes the particles to oscillate at the frequency of the applied acoustic wave velocity; however with a different amplitude and phase (Marshall & Li, 2014). So the particle velocity can be written as:

$$u_p = \eta_p A_u \sin(2\pi f t - \phi_p), \tag{12}$$

where η_p, A_u, and ϕ_p are the particle entrainment coefficient, the maximum particle velocity amplitude, and the phase factor, respectively. The particle entrainment coefficient, η_p, which is the ratio of the particle velocity amplitude to the fluid velocity amplitude, and the phase factor are given by (Marshall & Li, 2014):

$$\eta_p = \frac{1}{\sqrt{1 + (2\pi f \tau_p)^2}}, \tag{13}$$

$$\phi_p = \tan^{-1}(2\pi f \tau_p), \tag{14}$$

where $\tau_p = \rho_p d_p^2 / 18\mu$ is the particle time scale. The term $2\pi f \tau_p$ is known as the acoustic Stokes number, St_{ac}, where, in the limit $f\tau_p \to 0$, the velocity amplitude and phase of the particle reach those of the fluid phase (Achury & Polifke, 2016). For the range of frequencies given in Table 1, the acoustic Stokes number is $0.0182 \le St_{ac} \le 0.0342$, which

results in an entrainment coefficient of $0.978 \leq \eta_p \leq 0.993$ and a phase factor of $0.0187\ \text{rad} \leq \phi_p \leq 0.0342\ \text{rad}$. The ranges of η_p and ϕ_p in this study show that the particles oscillate with an amplitude and phase close to those of the fluid phase. In other words, the particles almost follow the acoustic wave of the fluid.

In the presence of an acoustic field, the orthokinetic particle collisions arise because the phase and amplitude of the particle oscillation depend on the diameter of the particle (Marshall & Li, 2014). Orthokinetic particle collisions are generally quantified by the collision efficiency, f_C, which is a function of the relative acoustic Stokes number, St_{ac12} defined as (Dong et al., 2006):

$$f_C = \left(\frac{St_{ac12}}{St_{ac12} + 0.65}\right)^{3.7}, \tag{15}$$

where St_{ac12} is the relative acoustic Stokes number between two particles with diameters d_{p1} and d_{p2} given by (Marshall & Li, 2014):

$$St_{ac12} = \frac{\rho_p \eta_{12} A_u d_{p2}^2}{18\mu d_{p1}}, \tag{16}$$

where η_{12} is the relative entrainment coefficient between the two particles given by (Marshall & Li, 2014):

$$\eta_{12} = 2\pi f(\tau_{p1} - \tau_{p2})/\sqrt{1 + (2\pi f\tau_{p1})^2}\sqrt{1 + (2\pi f\tau_{p2})^2}, \tag{17}$$

The diameter of the particles in this study is identified as d_p=2.8 μm, hence the relative entrainment coefficient, η_{12}, becomes zero, which results in a zero-collision efficiency. Therefore, orthokinetic collisions do not occur in this study.

4. Solution methodology

ANSYS® Fluent was used to model the NC-MS combination. The details of the model and its validation against experimental data were reported in another article published by the authors (Pourmehran et al., 2020). In that study, the effect of geometrical parameters on the resonance frequency of the simplified NC-MS combination was investigated. The study showed that CFD could predict the resonance frequency in good agreement with the experimental data. However, in this study, we will use the validated CFD model to investigate the effect of acoustic frequency, pressure amplitude, and inlet mean flow rate on drug delivery to the MS. To do so, a particle tracking model has been added to the NC-MS CFD model. A one-way coupling of the fluid-particle phases was performed and is acceptable given the low particle Reynolds number ($Re_p = 0.0086 \ll 1$), a very small volume fraction of the particle phase ($V_p/V_f = 2.92 \times 10^{-7} < 10^{-6}$), a low acoustic Stokes number ($St_{ac} = 0.034 \ll 1$), and the dilute fluid-particle flows with a low Stokes number ($St = 0.031 \ll 1$). The Stokes number, St, is a ratio of the characteristic time of a particle to a characteristic time of the flow, given by

$St = \rho_p d_p^2 U/18\mu D$, where U and D are the mean flow velocity and hydraulic diameter of the inlet, respectively.

In this study, using ANSYS® Fluent, an iterative time-advancement (ITA) algorithm with a SIMPLEC pressure-velocity coupling scheme was used when solving the Navier-Stokes equations. The ITA is employed because NITA (which was used in our previous study, Pourmehran et al. (2020)) is not able to solve the particle trajectory equation. Second-order spatial discretization is used for the pressure, third-order MUSCL is utilized for the density, and QUICK is used for the momentum and energy equations. A second-order implicit solver is used for the transient formulation. To validate this model, the resonance frequency of the simplified model of this study was obtained using an ITA algorithm (which is used in this study) and has been compared with the results obtained using the NITA algorithm (which was used in our previous study (Pourmehran et al., 2020). In addition, the results of the ITA were also compared with the experimental data (Exp), obtained by using an experimental setup similar to that described in Pourmehran et al. (2020). As can be seen in Figure 3, the results of the ITA demonstrate good agreement with the NITA and the experimental data, showing differences of 1.1% and 5.2%, respectively.

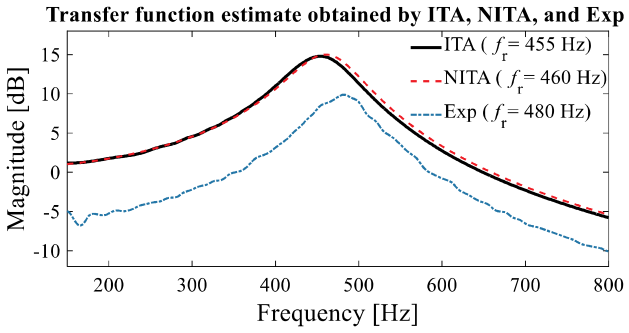

Figure 3. Comparison of the results obtained by an ITA algorithm with the results of a NITA algorithm and the experimental data.

The resonance frequency of the model was estimated using the time-invariant transfer function estimate, which models the linear relationship between the input/inlet (x) and response (y). The input signal (i.e. pressure fluctuations) was recorded at the inlet boundary and the response signal was obtained by calculating the static pressure at the lateral wall of the ostium. The resonance frequency of the system was predicted by calculating the peak value of the transfer function estimate (TF estimate), T_{xy}, in the frequency domain given by

$$T_{xy}(f) = \frac{G_{xy}(f)}{G_{xx}(f)}, \tag{18}$$

where f, G_{xx}, G_{xy} are the frequency of the input acoustic wave, the power spectral densities of the input, and the cross-power spectral density between the input and the response, respectively. To examine the reliability of the static pressure obtained at the inlet and response points, the degree of linearity between these two points was quantified using the magnitude–squared coherence function (Coh), $C_{xy}(f)$, in the frequency domain given by

$$C_{xy}(f) = \frac{|G_{xy}(f)|^2}{G_{xy}(f)G_{yy}(f)}, \tag{19}$$

The magnitude-squared coherence estimate, C_{xy}, gives a value in a range between zero and unity. A value of zero Coh implies that there is no relationship between the inlet and response signals, while a unit value of C_{xy} indicates the static pressure oscillation measured at the inlet boundary is perfectly coherent with the input pressure signal, and the signals from other sources are screened out. A frequency sweep (a linear sine sweep with a frequency range from 150 Hz to 800 Hz for total time, $T_s = 0.2$ s) was used as the input static pressure, and was applied at the inlet boundary using a User Defined Function (UDF) given by

$$p(t) = A_p \sin\left(f_0 t + \frac{f_1 - f_0}{2T_s} t^2\right) \tag{20}$$

where $p(t)$ is the static pressure as a function of time, and A_p is the amplitude of the static pressure. The terms f_0 and f_1 are the starting and final frequencies, respectively. T_s is the time it takes to sweep from f_0 to f_1.

Figure 4 (a) shows the pressure fluctuation versus time. The blue line refers to the frequency sweep applied at the inlet boundary and the red line represents the pressure of the response point at the lateral wall of the MS. A Welch power spectral density estimate was used to illustrate the inlet and response pressure signals in a frequency domain, as demonstrated in Figure 4 (b). The PSD values were obtained using a Hanning window with 2^{10} FFT points and a 75% overlap for a total of 14 averages. The TF estimate of the simplified geometry is shown in

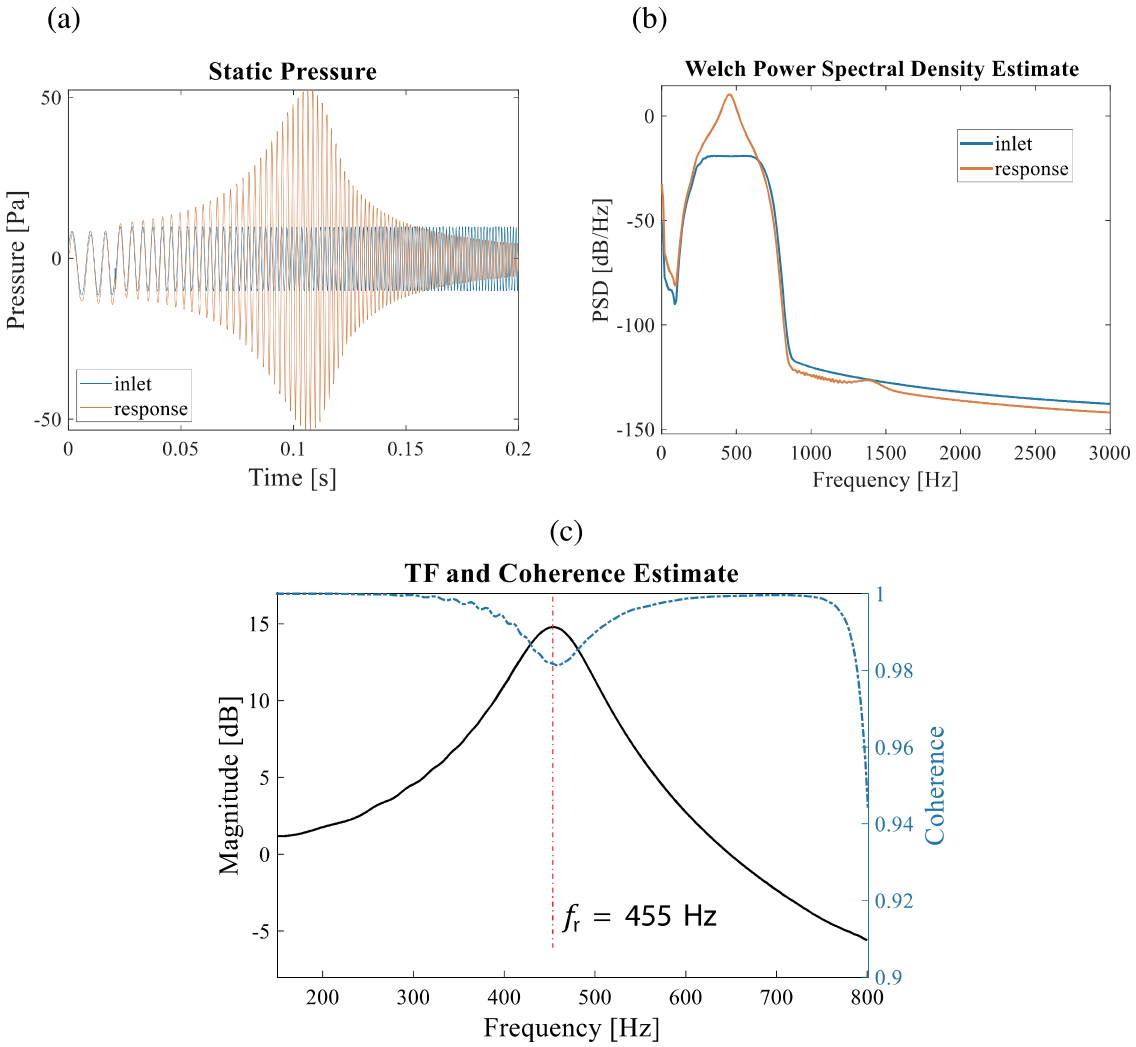

Figure 4. (a) Static pressure at the inlet and response points; (b) Welch power spectral density estimate of the pressure signals at the inlet and response; (c) Transfer function and coherence estimates between the inlet and response.

Figure 4 (c). As can be seen in this figure, the peak value of the TF estimate, which indicates the resonance frequency of the NC-MS combination, occurred at f_r=455 Hz. Figure 4 (c) also shows the magnitude-squared coherence estimate between the inlet and response points for the frequency range from 150 Hz to 800 Hz. It is apparent from this figure that the Coh value is between 0.9 and unity for the selected frequency range, which demonstrates that the pressures detected at the inlet and outlet are highly coherent, thus the TF estimate is reliable. The drop in Coh at the resonance frequency is associated with spectral leakage and nonlinearity and is certainly seen in the resonance peaks.

5. Results and discussion

5.1. Effect of frequency on the efficiency of ADD to the MS

As explained previously, the oscillation of the air plug within the ostium is maximized at the resonance frequency of the NC-MS combination, which results in the highest efficiency of ADD to the MS. To evaluate the ADD efficiency, the mass-flow exchange between the MS and NC at different inlet frequencies was quantified using a particle tracking method. In this method, a known number of particles (80000 inert particles with a diameter d_p = 2.8 μm) were distributed in the NC

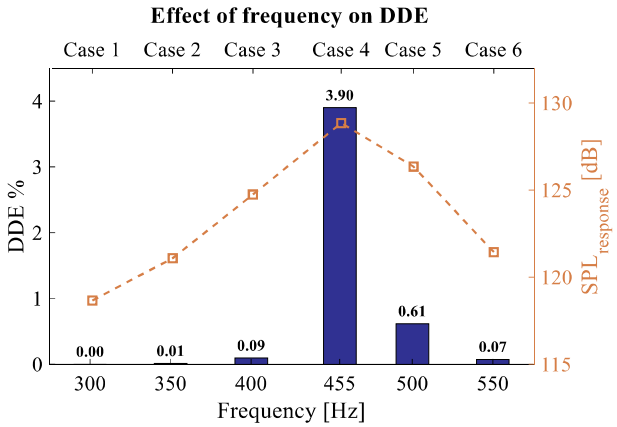

Figure 5. The effect of inlet frequency (Cases 1-6) on the drug delivery efficiency (DDE) to the MS for Cases 1-6 (blue bar chart). The red dashed line demonstrates the sound pressure level at the response point for the simplified NC-MS combination.

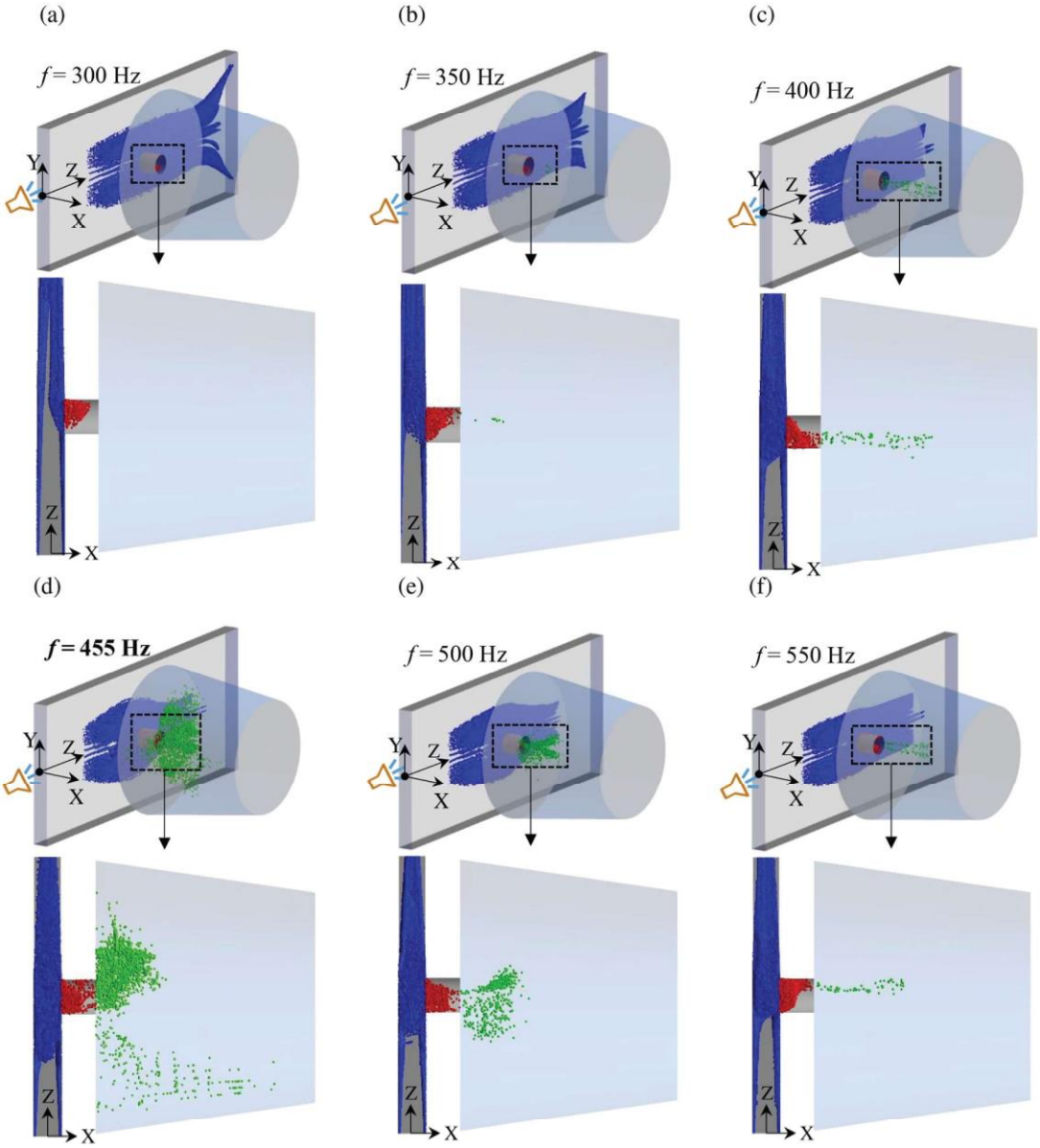

Figure 6. Particle transport patterns for the application of ADD without mean flow for different inlet frequencies (a) f = 300 Hz; (b) f = 350 Hz; (c) f = 400 Hz; (d) f = 455 Hz; (e) f = 500 Hz; (f) f = 550 Hz. The colour of the particles indicates their position as follows: blue refers to the NC, red refers to the ostium, and green refers to the MS domains.

domain. The particles were distributed after 20 periods, when the pressure oscillation is stable. The transport pattern of the particles was simulated for an additional 200 periods.

Given the particle tracking was formulated for one-way fluid-particle coupling, the delivery of the particles to the ostium and MS represents a proxy of the airflow exchange between the ostium and MS. Six different case studies (Cases 1-6) were considered for the investigation of the effect of inlet frequency on the efficiency of ADD to the MS. The amplitude of the inlet pressure was kept constant at A_p = 15 Pa for different inlet frequencies. As discussed in the previous section, the resonance frequency of the selected geometry was found to be f_r=455 Hz, thus it is expected to have the maximum DDE at this frequency.

Figure 5 plots the results obtained from the simulation of particle tracking for Cases 1-6. It indicates that the highest DDE was achieved from the case with an inlet frequency of f = 455 Hz, as expected. For all the cases, the acoustic field at the inlet was applied with an amplitude of 114.5 dB SPL. Figure 5 shows that the DDE for Case 1 (f = 300 Hz) is zero, which reveals that no particles were delivered to the MS after 200 periods (200/300 s). After increasing the inlet frequency to f = 455 Hz (resonance frequency), the DDE increases. However, a clear trend of decreasing of the DDE, from 3.9% to 0.07%, can be seen for the higher frequencies than the resonance frequency (f = 455 Hz). It is inferred that there is a non-linear relationship between the DDE and the inlet frequency, which shows a trend similar to the sound pressure level (SPL) at the response point for different cases. Indeed, the higher the SPL at the response point, the higher the DDE. For example, the values of SPL at the response point for Cases 3 and 5 are obtained as $SPL_{response}$ = 124.7 dB and $SPL_{response}$ = 126.4 dB, which resulted in a DDE of 0.09% and 0.61%, respectively. The $SPL_{response}$ obtained for Case 5 is about 18% ($1 - 10^{\frac{124.7}{20}}/10^{\frac{126.4}{20}}$) more than the $SPL_{response}$ obtained for Case 3,

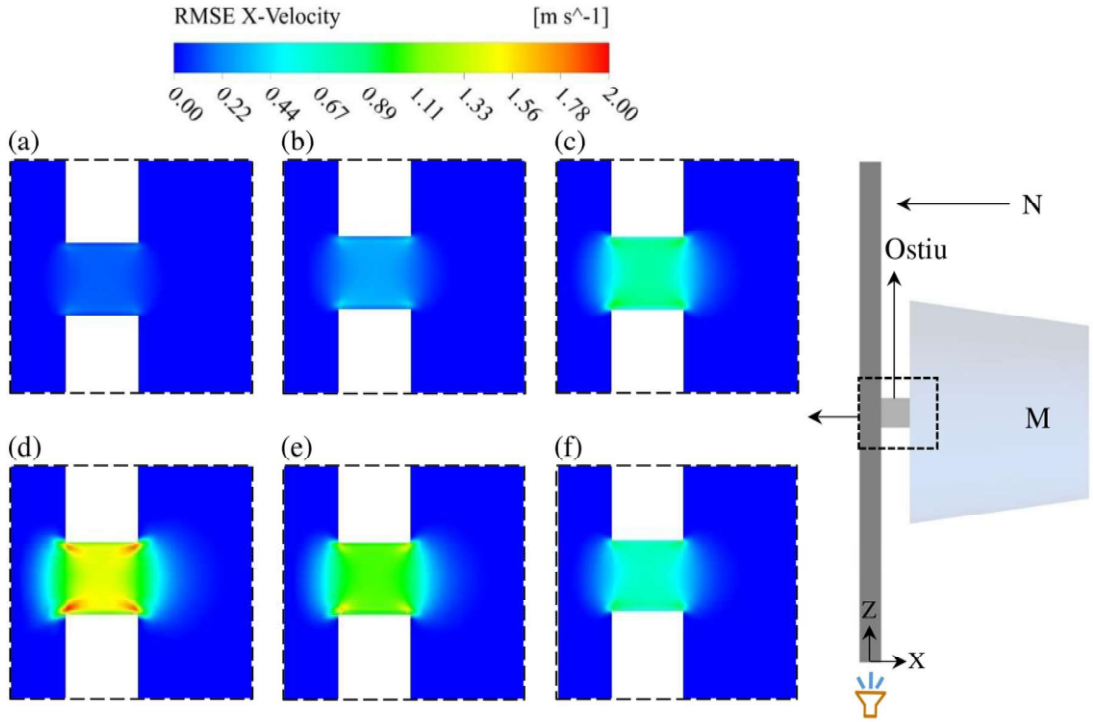

Figure 7. The contour of the RMSE of the X-Velocity around the ostium for different inlet frequencies: $f=300$ Hz; (b) $f=350$ Hz; (d) $f=400$ Hz; (f) $f=500$ Hz; (b) $f=550$ Hz.

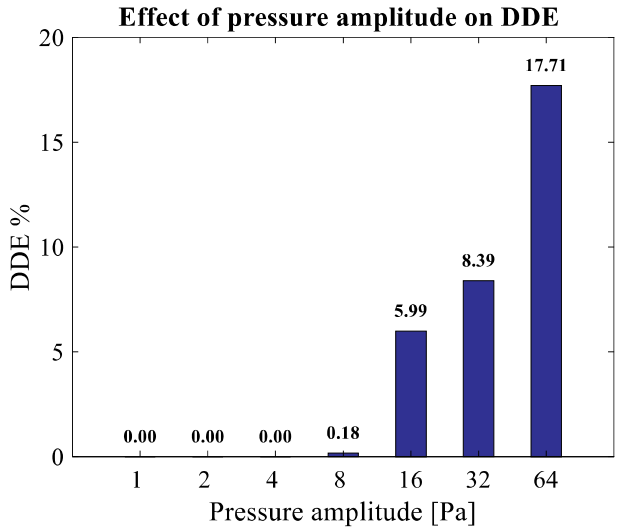

Figure 8. The effect of inlet pressure amplitude (Cases 7-13) on the efficiency of drug delivery to the MS for an inlet pressure amplitude of A_p=15 Pa.

however, the DDE of Case 5 is about 500% more than the DDE of Case 3. Hence, in addition to the inlet frequency, the DDE is significantly sensitive to the magnitude of the SPL at the MS (response point).

Figure 6 (a-f) represents the transport pattern of the particles after 200 periods for different inlet frequencies (Cases 1-6). The particle size has been scaled for better illustration. In Figure 6 (a), it is obvious that no particle is delivered to the MS after 200 periods with an inlet frequency of f = 300 Hz (Case 1), however, a considerable number of particles entered the ostium. Figure 6 (b & c) also shows that the concentration of the particles entering the MS slightly increased with an increase in inlet frequency from 300 Hz to 350 Hz and 400 Hz. Figure 6 (d) demonstrates a significant increase in the number of particles entering the MS at the resonance frequency (f = 455 Hz), followed by a decrease in the concentration of particles entering the MS at frequencies higher than the resonance frequency.

As depicted in Figure 7 (a-f) and using a velocity contour, it can be found that the reason the maximum DDE occurs at the resonance frequency is related to the amplitude of the velocity (X-Velocity in this study) of the airflow in the ostium. Figure 7 (a-f) illustrates the effect of inlet frequency on the root mean square error (RMSE) of the X-Velocity at a plane aligned with the centreline of the ostium. The RMSE is the root mean square (RMS) of the instantaneous velocity subtracted by the time-averaged velocity. Hence, in this study, the RMSE of the X-Velocity is equivalent to the root mean square (RMS) of the fluctuating X-Velocity, which is representative of the amplitude (A_u) of the air plug oscillation in the ostium. According to Figure 7 (a-f), it is evident that the RMSE of the X-Velocity is maximal within and around the corner of the ostium, which demonstrates that the oscillation of the air plug within the ostium resulted from the compressibility of the airflow due to the acoustic field. This figure also shows that the maximum RMSE of the X-Velocity reaches a maximum at the resonance frequency of the NC-MS combination.

5.2. Effect of inlet pressure amplitude on the efficiency of ADD to the MS

In the previous section, it was shown that the amplitude of the air plug oscillation in the ostium reaches a maximum when the NC-MS combination is driven at resonance by an acoustic field applied at the inlet boundary. Therefore, the inlet pressure amplitude is an important parameter in the ADD technique. In this section, the effect of this parameter on the efficiency of drug delivery to the MS is investigated through seven case studies (Cases 7-13 in Table 1). Similar to Cases 1-6, 80000 particles with a diameter of d_p=2.8 μm were distributed in the NC domain after 20 periods. A fixed frequency of f = 445 Hz (the resonance frequency of the idealized NC-MS combination) was applied at the inlet for different pressure amplitudes SPL_{inlet} = 91, 97, 103,

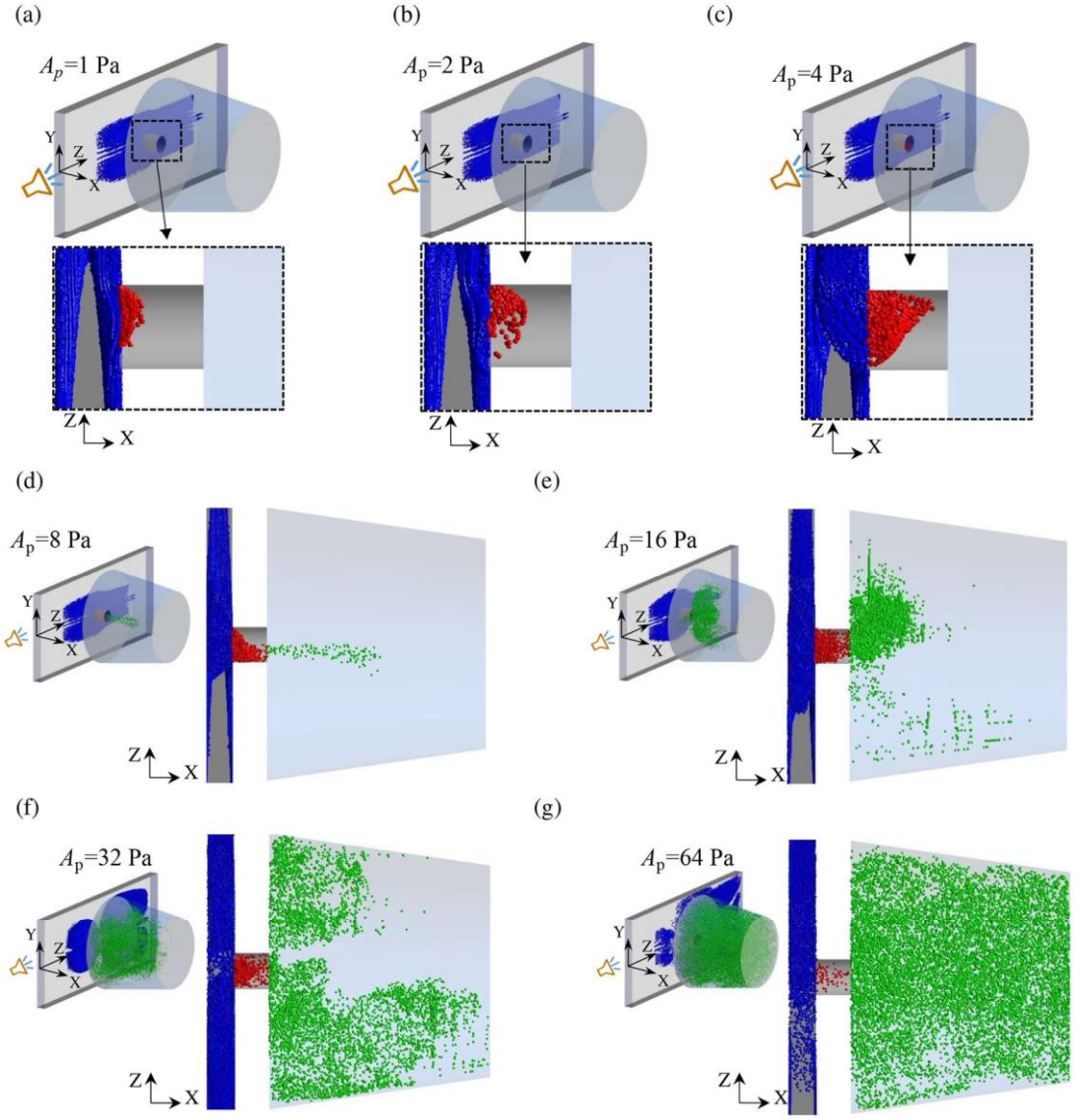

Figure 9. Particle transport pattern for the application of ADD without mean flow for different inlet pressure amplitudes (a) A_p=1 Pa; (b) A_p=2 Pa; (c) A_p=4 Pa; (d) A_p=8 Pa (e) A_p=16 Pa; (f) A_p=32 Pa; (g) A_p=64 Pa. The colour of the particles indicates their position, as follows: blue refers to the NC domain, red refers to the ostium domain, green refers to the MS domain.

109, 115.1, 121.1, 127.1 dB (or A_p=1, 2, 4, 8, 16, 32, 64 Pa). The particle tracking was simulated for 200 periods.

The results obtained from the numerical simulation of particle tracking for different inlet pressure amplitudes are presented in Figure 8. It is apparent from this figure that there is a clear trend of increasing DDE with increasing inlet pressure amplitude, which is in accordance with the findings reported by El Merhie et al. (2016). Although the inlet pressure was driven at the resonance frequency for all cases in Figure 8, it can be seen that for low-pressure-amplitudes at A_p=1, 2, 4 Pa, no particles have entered the MS. However, the results, as shown in Figure 9 (a, b, and c), show the penetration of particles from NC to the ostium when increasing the pressure amplitude from 1 Pa to 4 Pa.

Figure 9 (d-g) also shows a significant increase in the number of particles delivered to the MS when increasing the inlet pressure amplitude from A_p=16 Pa to A_p=64 Pa. It is important to note that, although pressure amplitudes of more than A_p=16 Pa (115.1 dB SPL) cause discomfort and are painful for the human ear (Smith, 1997), the pressure amplitudes of A_p=32 Pa (121.1 dB SPL) and A_p=64 Pa (127.1 dB SPL) were investigated in this section to visualize the effect of this parameter on DDE more effectively. The reason for the increasing trend of DDE versus the inlet pressure amplitude is that it directly affects the amplitude of the oscillation of the air plug (RMSE of X-Velocity) within the ostium. In some cases ($A_p \geq 8$ Pa in this study) the particles are delivered to the MS, where some of them are captured by the very low-velocity vortices in the MS and the remaining particles move back toward the ostium and NC. This phenomenon is repeated in every period. After the 200 periods in this study, a total of 3118 particles captured in those vortices, remained in the MS.

5.3. Effect of inlet mean flow rate on the efficiency of ADD to MS

The effect of the inlet mean flow rate on the efficiency of ADD to the MS was also investigated using the idealized NC-MS model. To do so, the inlet mean flow rate is quantified using five different Reynolds numbers (Re = 0, 60, 80, 100, 200) for the numerical simulation. A

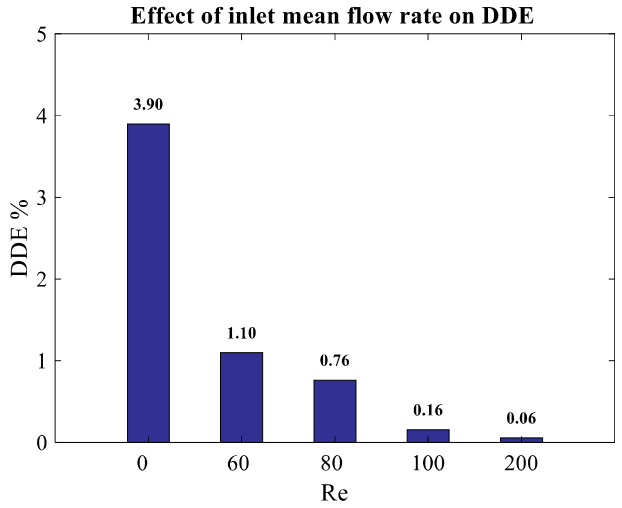

Figure 10. The effect of the inlet mean flow rate (Cases 14-18) on the efficiency of ADD to the MS for a fixed inlet frequency of f = 455 Hz and a pressure amplitude of of A_p=15 Pa.

sinusoidal pressure wave with a frequency of f = 455 Hz, and amplitude of A_p = 15 Pa was superimposed on the flow rate of interest. In the previous section, the particles were distributed in the NC and then the pressure wave was applied at the inlet; in this section, the particles are injected from the nostril (inlet boundary) continuously. However, similar to Cases 1-13, the sinusoidal pressure wave is applied at the inlet for 220 periods and then the efficiency of ADD to the MS is calculated.

Figure 10 shows the effect of the inlet mean flow rate on the efficiency of the drug delivery to MS for Cases 14-18. From this figure, it is clear that the mean flow rate negatively affects the DDE, which is similar to the findings reported by Leclerc et al. (2014). Although it was evident in the previous section that the maximum DDE occurs at the resonance frequency (f_r = 455 Hz), it can be seen in Figure 10 that the DDE can be decreased significantly from DDE = 3.9% to DDE = 0.1% by increasing the inlet Reynolds number from Re = 0 to Re = 200, with an inlet frequency of f = 455 Hz. Indeed, the presence of the mean flow reduces the peak value of the TF estimate at the resonance frequency due to damping (Selamet et al., 2011), which results in a decrease in the SPL at the MS. Thus, in addition to the resonance frequency of the NC-MS combination and optimizing the pressure wave amplitude, it is imperative to reduce the inlet mean flow rate to maximize the efficiency of ADD to the MS.

In the absence of mean flow, where the particles are distributed in the NC with a zero mean velocity, the only driver of the particles is the oscillation of the air plug inside the ostium. Under this condition, the velocity component of the particles in the X-direction (the ostium length direction) is significantly more than that in the Z-direction (the NC direction). However, in the presence of a mean flow, an increase in the inlet mean flow rate enhances the particle velocity in the Z-direction more than that of the X-direction. Therefore, using the mean flow at the inlet, the direction of the velocity vector of the particles turns toward the NC direction, which results in a decrease in the number of particles delivered to the ostium and MS.

5.4. The mechanism underlying the ADD to MS

The results of the computational modelling revealed that some particles transport into the MS and some particles return from the MS to the NC through the ostium. Given there is a much higher number of particles in the NC than in the MS, statistically more particles are delivered to the MS when the time of operation increases. Figure 11 (a) shows the number of particles entering the MS for four periods after 220 periods, with an inlet frequency of f = 455 Hz and pressure amplitude of A_p=15 Pa (Case 4). In this case, 3118 particles had accumulated in the MS during the first 220 periods. The histogram in Figure 11 (a) presents the number of particles entering the MS minus the pre-available particles in the MS. For example, according to Figure 11 (a), at time 224T s (Time – 220T = 4T), 74 particles were accumulated in the MS. This means that across 224T s a total of 3192 (3118+74) particles were accumulated in the MS.

Figure 11 (a) also demonstrates that there is an increasing trend in the number of particles accumulated in the MS for the first half of the period e.g. t = $0 \rightarrow \frac{T}{2}$. However, for the second half of the period, e.g. t = $\frac{T}{2} \rightarrow T$, the number of particles accumulated in the MS shows a

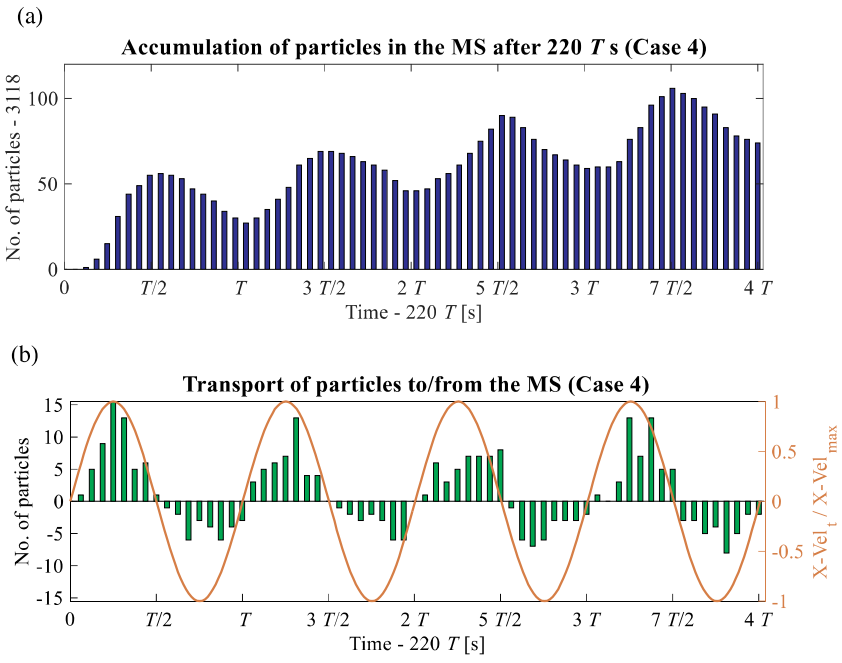

Figure 11. (a) The number of particles accumulated in the MS; (b) the number of particles entering/leaving the MS (the positive value of 'No. of particles' shows the number of particles that have entered the MS and the negative value refers to the number of particles that have left the MS, and the red line in this figure presents the non-dimensional mean X-Velocity at the interface between the ostium and MS for four periods after 220 periods, with an inlet frequency of f = 455 Hz (Case 4, T = 1/455 s).

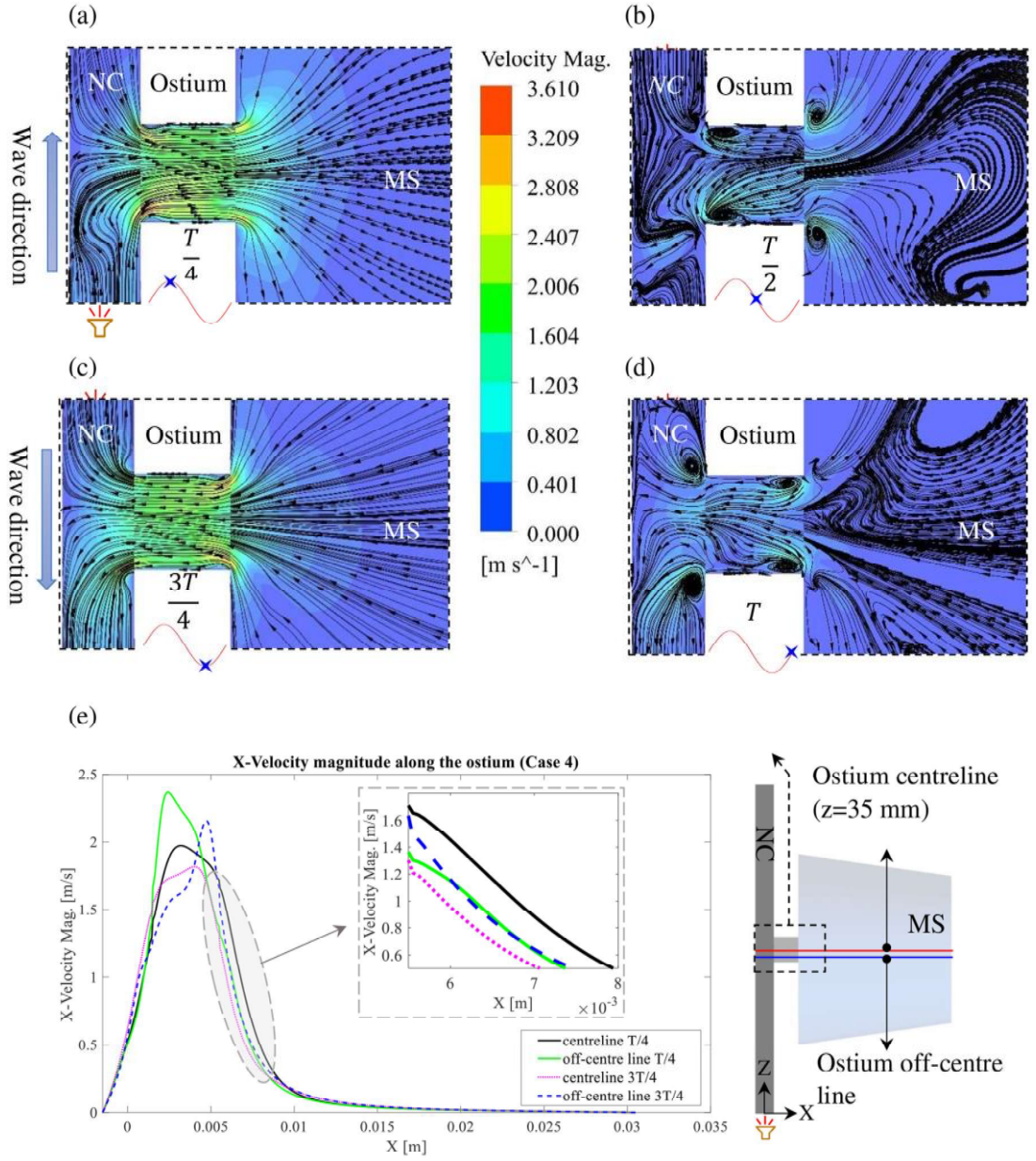

Figure 12. The instantaneous streamlines and contours of the airflow X-Velocity for Case 4 at (a) $t = \frac{T}{4}$ s; (b) $t = \frac{T}{2}$ s; $t = \frac{3T}{4}$ s; $t = T$ s; (e) the instantaneous X-Velocity magnitude along the ostium centre/off-centre lines.

decreasing trend because, at the second half of the period, the air plug in the ostium moves back from the MS toward the NC, which transports some particles from the MS to the NC.

The reason for such an overall increasing trend is explored in Figure 11 (b). This figure represents the particle transport pattern at the interface of the ostium and the MS, versus time. It provides the summary statistics for the number of particles entering/leaving the MS in four consecutive periods, after the first 220 periods. The positive values of the 'No. of particles' indicate the number of particles entering the MS, and the negative values refer to the number of particles leaving the MS towards the ostium. As shown in Figure 11 (b), the number of particles entering the MS increases at the first quarter of the period and then shows a clear trend of decreasing at the second quarter of the period. However, at the third and fourth quarters of the period, some particles move back to the ostium from the MS.

The red line in Figure 11 (b) demonstrates the mean X-Velocity at the interface of the ostium and MS. From this figure, it is obvious that the particle transport between the ostium and the MS is likely to follow a sinusoidal pattern similar to the mean X-Velocity at the ostium-MS interface. However, the mean amplitude of the second half-period associated with the number of particles leaving the MS is lower than that of the first half-period where the particles enter the MS due the lower particle concentration in the MS than in the NC. The difference between the number of particles in the first half-period (the particles entering the MS) and the number of particles in the second half-period (the particles leaving the MS) results in an accumulation of particles in the MS after one period. This phenomenon repeats for every period, leading to an increasing accumulation of particles in the MS over time (Figure 11 (a)).

Figure 12(a-d) shows the airflow features within and around the

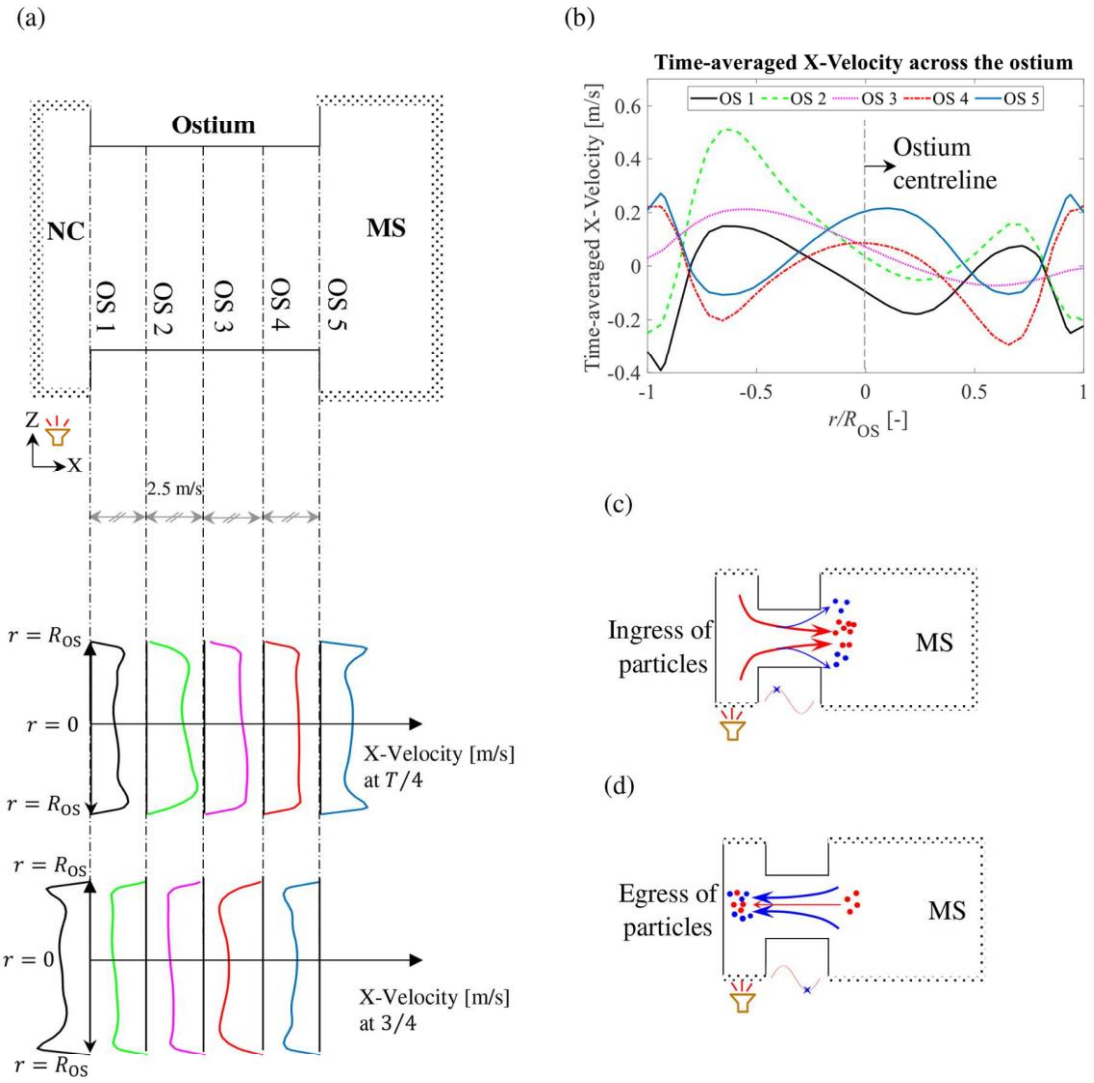

Figure 13. (a) instantaneous X-Velocity across the ostium at the first and third quarters of a period; (b) time-averaged X-Velocity for different cross-centrelines after 220 periods for an inlet frequency of f = 455 Hz and an amplitude of A_p=15 Pa; (c) an overview of particles entering the MS and; (d) leaving the MS.

ostium, which demonstrate the underlying mechanism of the particle transportation from the NC to the MS during the application of ADD. This figure represents the instantaneous airflow streamlines at four different times ($t = \frac{T}{4}$ s, $\frac{T}{2}$ s, $\frac{3T}{4}$s, T s) for Case 4. The figures are depicted on an iso-surface in the X-Z plane, coinciding on the ostium centreline. The 2D arrows on the streamlines show the direction of the airflow and the background contours demonstrate the velocity magnitude in the direction of the 2D arrows. As can be seen in Figure 12 (a & c), the airflow streamlines are almost uniform at $t = \frac{T}{4}$ s and $t = \frac{3T}{4}$ s, where the magnitudes of pressure are maximal and minimal, respectively. At these times, the maximum particle transport between the ostium and MS occurs. Figure 12 (b) & 11 (d) show that minor vortices are generated at the corners of the ostium at the inflection points of the pressure wave ($t = \frac{T}{2}$ s and $t = T$ s), where the direction of the X-Velocity rotates 180 degrees.

Figure 12 (e) demonstrates the X-Velocity magnitude along two lines from the left wall of the NC to the right wall of the MS. One line coincides with the ostium centreline and the other line is parallel to the ostium axis but 1 mm farther from the ostium centreline, which is called the ostium off-centre line. This figure reports the instantaneous results at $t = \frac{T}{4}$ s and $t = \frac{3T}{4}$ s. From Figure 12 (e), it is obvious that the magnitude of the airflow velocity on the ostium centreline at $t_1 = \frac{T}{4}$ s is higher than that at $t_2 = \frac{3T}{4}$ s. In contrast, the airflow velocity magnitude on the ostium off-centre line at t_1 is lower than that at t_2. The term t_1 refers to a time when the air plug in the ostium moves towards the MS with its highest mean velocity amplitude, and t_2 refers to a time when the air plug in the ostium returns to the NC with its highest mean velocity amplitude. Thus, it is inferred that the particles almost enter the MS from the ostium centre area and leave the MS through the ostium off-centre area. Moreover, the portion of particles that have entered the MS from the ostium centre area at t_1, leaves the MS with a lower velocity magnitude at t_2. Therefore, in the backward half-period (from $t = \frac{T}{2}$ s to $t = T$ s), some particles move back to the ostium from the MS, while some particles do not reach the interface of the ostium and the MS due to the reduced velocity, hence, they remain in the MS.

In Figure 13 (a) the instantaneous X-Velocity across the ostium on different lines parallel to the Z-axis is plotted, which shows the velocity distribution across the ostium. Figure 13 (b) presents the time-averaged X-Velocity on the lines, as was used for Figure 13 (a), which gives more details for understanding the airflow and particle transport pattern in

the ostium and the MS. In this figure, the positive X-velocities indicate the airflow entering the MS and the negative X-velocities refer to the airflow leaving the MS. As shown in Figure 13 (b), it is obvious that the airflow enters the ostium almost from the NC through the ostium off-centre areas (the solid black line). However, it is worth noting that significant amounts of the airflow enters the MS through the ostium centre area, which is also shown by the solid blue line in Figure 13 (a). Figure 13 (c) and (d) depict an overview of the ingress of the particles to the MS and egress of the particles from the MS, respectively. Indeed, the main mechanism of drug delivery to the MS using this technique is that the first half-period of the oscillation of the air plug in the ostium carries more particles towards the MS than the second half-period egresses particles from the MS.

6. Conclusion

In this study, direct computational aero-acoustics was used to determine the effect of aero-acoustic parameters, including the frequency and amplitude of the inlet acoustic wave, as well as the inlet mean flow rate, on the efficiency of ADD to the MS. A Lagrangian discrete phase model with one-way fluid-particle coupling was used for the simulation of particle tracking in the presence of an external acoustic field, as applied to an idealized NC-MS model.

The most obvious finding to emerge from this study is that the efficiency of ADD to the MS is affected by the frequency of the inlet acoustic wave. If an acoustic wave, driven at the resonance frequency of the NC-MS combination, is applied to the inlet (nostril), maximum drug delivery efficiency is obtained. The results of this investigation also revealed that the efficiency of the drug delivery to the MS has a direct relationship with the amplitude of the inlet acoustic wave, even at the resonance frequency. It was shown that an increase in the inlet mean flow rate results in a decrease in the efficiency of ADD to the MS, which is similar to the finding reported by Leclerc et al. (2014). The maximum efficiency of ADD to the MS is achieved when the flow rate at the inlet is zero because the mean flow reduces the peak value of the transfer function estimate at the resonance frequency due to damping (Selamet et al., 2011), which results in a reduction of the amplitude of the oscillation of the air plug in the ostium.

The efficiency of ADD to the MS can be improved by decreasing the size of the particles. Indeed, the acoustic Stokes number decreases with a decrease in the particle diameter, which increases the amplitude (entrainment coefficient) of particle motion in the acoustic field. Moreover, an orthokinetic collision may decrease the efficiency of the ADD. Given that, in practice, the particles used in ADD are droplets, the orthokinetic collisions may result in a coalescence, which increases the particle diameter; hence, the efficiency of ADD to the MS may decrease. To avoid an orthokinetic collision, the particles should be of uniform size.

The evidence from this study suggests that to maximize the efficiency of ADD to the MS, it is better to distribute the drug particles in the NC and then apply an acoustic field with a frequency equal to the resonance frequency of the NC-MS combination in the absence of the inlet mean flow. This study also offers new insights into the details of the flow features and mechanisms underlying ADD to the MS. It was found that an ingress/egress of particles to/from the MS occurs in every wave period. The ingress movement phase carries a greater number of particles into the MS than the egress movement phase (due to the higher particle concentration in the NC than in the MS), which is the main reason for particle accumulation in the MS.

Declaration of Competing Interest

The authors declare that they have no conflicts of interest.

Acknowledgments

Financial support for the project has been provided by the Australian Government Research Training Program (RTP), and the Beacon of Enlightenment PhD Scholarship provided by the University of Adelaide. The authors would like to acknowledge the support of the School of Mechanical Engineering, Phoenix High-Performance Computing (HPC), and the Workshop at the University of Adelaide.

References

Achury, J., Polifke, W., 2016. Theoretical investigation of the particle response to an acoustic field. Journal International Journal of Spray Combustion Dynamics 8 (4), 262–270.
Alster, M., 1972. Improved calculation of resonant frequencies of Helmholtz resonators. Journal of Sound and Vibration 24 (1), 63–85.
Bassett, A.B., 1888. A Treatise on Hydrodynamics. Volume one, Dover.
Calmet, H., Inthavong, K., Eguzkitza, B., Lehmkuhl, O., Houzeaux, G., & Vazquez, M. J. P. o. (2019). Nasal sprayed particle deposition in a human nasal cavity under different inhalation conditions. 14(9).
Chen, S.B., Ye, X., 2000. Faxen's laws of a composite sphere under creeping flow conditions. Journal of Colloid and Interface Science 221 (1), 50–57.
Crowe, C.T., Schwarzkopf, J.D., Sommerfeld, M., Tsuji, Y., 2011. Multiphase flows with droplets and particles. CRC press.
Dong, S., Lipkens, B., Cameron, T., 2006. The effects of orthokinetic collision, acoustic wake, and gravity on acoustic agglomeration of polydisperse aerosols. Journal of Aerosol Science 37 (4), 540–553.
Durand, M., Le Guellec, S., Pourchez, J., Dubois, F., Aubert, G., Chantrel, G., ... Reychler, G., 2012. Sonic aerosol therapy to target maxillary sinuses. European Annals of Otorhinolaryngology, Head and Neck Diseases 129 (5), 244–250.
Durand, M., Pourchez, J., Aubert, G., Le Guellec, S., Navarro, L., Forest, V., ... Cottier, M., 2011. Impact of acoustic airflow nebulization on intrasinus drug deposition of a human plastinated nasal cast: new insights into the mechanisms involved. International Journal of Pharmaceutics, 421 (1), 63–71.
El Merhie, A., Navarro, L., Delavenne, X., Leclerc, L., Pourchez, J., 2016. A new strategy to improve drug delivery to the maxillary sinuses: The frequency sweep acoustic airflow. Pharmaceutical Research 33 (5), 1074–1084.
Fluent Theory Guide, 2019. Ansys® Fluent,.,*Release 2019 R2, Help System*. ANSYS, Inc.
Hood, C.M., Schroter, R.C., Doorly, D.J., Blenke, E.J., Tolley, N.S., 2009. Computational modeling of flow and gas exchange in models of the human maxillary sinus. Journal of Applied Physiology 107 (4), 1195–1203.
Howard, C. Q., Cazzolato, B. S., & Hansen, C. H. J. N. C. E. J. (2000). Exhaust stack silencer design using finite element analysis. 48(4), 113-120.
Hyo, N., Takano, H., Hyo, Y., 1989. Particle deposition efficiency of therapeutic aerosols in the human maxillary sinus. Rhinology 27 (1), 17–26.
Inthavong, K., Wen, J., Tian, Z., Tu, J., 2008. Numerical study of fibre deposition in a human nasal cavity. Journal of Aerosol Science 39 (3), 253–265.
Karlsen, J.T., 2018. Theory of nonlinear acoustic forces acting on fluids and particles in microsystems. PhD thesis. Technical University of Denmark, Denmark.
Kauf, H., 1968. Eindringvermögen von aerosolen in nebenräume. Archiv für klinische und experimentelle Ohren-, Nasen-und Kehlkopfheilkunde 190 (1), 95–108.
Kleinstreuer, C., Zhang, Z., 2003. Targeted drug aeroso deposition analysis for a four-generation lung airway model with hemispherical tumors. Journal of Biomechanical Engineering, 125 (2), 197–206.
Kolev, N.I., 2011. In: Kolev, N.I. (Ed.), Springer, Berlin, Heidelberg, pp. 31–85.
Kumar, H., Jain, R., Douglas, R.G., Tawhai, M.H., 2016. Airflow in the human nasal passage and sinuses of chronic rhinosinusitis subjects. PloS One 11 (6), e0156379. https://doi.org/10.1371/journal.pone.0156379.
Leclerc, L., Pourchez, J., Aubert, G., Leguellec, S., Vecellio, L., Cottier, M., Durand, M., 2014. Impact of airborne particle size, acoustic airflow and breathing pattern on delivery of nebulized antibiotic into the maxillary sinuses using a realistic human nasal replica. Pharmaceutical Research 31 (9), 2335–2343.
Loyalka, S., 1992. Thermophoretic force on a single particle—I. Numerical solution of the linearized Boltzmann equation. Journal of Aerosol Science 23 (3), 291–300.
Maniscalco, M., Sofia, M., Weitzberg, E., Lundberg, J., 2006. Sounding airflow enhances aerosol delivery into the paranasal sinuses. European Journal of Clinical Investigation 36 (7), 509–513.
Maniscalco, M., Weitzberg, E., Sundberg, J., Sofia, M., Lundberg, J., 2003. Assessment of nasal and sinus nitric oxide output using single-breath humming exhalations. European Respiratory Journal 22 (2), 323–329.
Marshall, J.S., Li, S., 2014. Adhesive particle flow. Cambridge University Press.
Maul, G.A., 2019. Pressure Gradient Force. In: Finkl, C.W., Makowski, C. (Eds.), Encyclopedia of Coastal Science. Springer International Publishing, Cham, pp. 1390–1392.
Moghadam, S.J., Navarro, L., Leclerc, L., Hodin, S., Pourchez, J., 2018. Toward smart Nebulization: Engineering acoustic airflow to penetrate maxillary sinuses in chronic rhinosinusitis. International Journal of Pharmaceutics 546 (1-2), 188–193.
Morsi, S., Alexander, A., 1972. An investigation of particle trajectories in two-phase flow systems. Journal of Fluid Mechanics 55 (2), 193–208.
Navarro, L., Leclerc, L., Pourchez, J., 2019. Does Acoustic Overlay of Music Improve Aerosol Penetration into Maxillary Sinuses? Online Journal of Otolaryngology and Rhinology 1 (4), 1–3.

Ounis, H., Ahmadi, G., McLaughlin, J.B., 1991. Brownian diffusion of submicrometer particles in the viscous sublayer. Journal of Colloid and Interface Science 143 (1), 266–277.

Pourmehran, O., Arjomandi, M., Cazzolato, B., Ghanadi, F., Tian, Z., 2020. The impact of geometrical parameters on acoustically driven drug delivery to maxillary sinuses. Biomechanics and Modeling in Mechanobiology 19 (2), 557–575.

Pourmehran, O., Gorji, T.B., Gorji-Bandpy, M., 2016. Magnetic drug targeting through a realistic model of human tracheobronchial airways using computational fluid and particle dynamics. Biomechanics and Modeling in Mechanobiology 15 (5), 1355–1374.

Sato, Y., Hyo, N., Sato, M., Takano, H., Okuda, S., 1981. Intra-nasal distribution of aerosols with or without vibration. Zeitschrift fur Erkrankungen der Atmungsorgane 157 (3), 276–280.

Schwarzkopf, J.D., Sommerfeld, M., Crowe, C.T., Tsuji, Y., 2011. Multiphase flows with droplets and particles, 2nd ed. CRC press.

Selamet, E., Selamet, A., Iqbal, A., Kim, H., 2011. Effect of flow on Helmholtz resonator acoustics: A three-dimensional computational study vs. Experiments. Paper presented at the SAE 2011 Noise and Vibration Conference and Exhibition, USA.

Smith, S.W., 1997. Audio processing/human hearing. The scientist and engineer's guide to digital signal processing. California Technical Publishing, USA.

Sutherland, W., 1893. The viscosity of gases and molecular force. The London, Edinburgh, and Dublin Philosophical Magazine and Journal of Science 36 (223), 507–531.

Von Helmholtz, H., Ellis, A.J., 1875. On the Sensations of Tone as a Physiological Basis for the Theory of Music. Longmans, Green and Company, London.

Weitzberg, E., Lundberg, J.O., 2002. Humming greatly increases nasal nitric oxide. American Journal of Respiratory and Critical Care Medicine 166 (2), 144–145.

Xi, J., Si, X.A., Peters, S., Nevorski, D., Wen, T., Lehman, M., 2017. Understanding the mechanisms underlying pulsating aerosol delivery to the maxillary sinus: In vitro tests and computational simulations. International Journal of Pharmaceutics 520 (1), 254–266.

Statement of Authorship

Title of Paper	Effect of Particle Diameter and Density on Acoustic Drug Delivery to Maxillary Sinus – A Sensitivity Study
Publication status	☑ Published ☐ Accepted for Publication ☐ Submitted for Publication ☐ Unpublished and Unsubmitted work written in manuscript style
Publication Details	Pourmehran, O., Arjomandi, M., Cazzolato, B., & Tian, Z. (2020). "Effect of particle diameter and density on acoustic drug delivery to maxillary sinus – A sensitivity study". 22nd Australasian Fluid Mechanics Conference (AFMC2020), Brisbane, Australia. Oral presentation.

Principal Author

Name of Principal Author (Candidate)	Oveis Pourmehran
Contribution to the Paper	Ideas and Concepts • Conducted a comprehensive literature review to find the gaps in the knowledge • Developed the ideas and concepts based on the gaps Experiments and Modelling • Developed simplified and NC-MS models in ANSYS® DesignModeler and SpaceClaim • Developed the CFD models using ANSYS® Fluent to simulate the acoustic wave propagation and particle tracking and particle tracking • Validated CFD model against experimental data Interpretation of Results • Extracted raw data from simulation • Post-processed the simulation results using ANSYS® CFD-Post • Developed a MATLAB code to produce figures • Interpreted the simulation results Manuscript • Developed the first full draft of the manuscript • Applied comments given by co-authors • Revised the manuscript after review and produced a rejoinder • Acted as the corresponding author
Overall percentage (%)	80%
Certification:	This paper reports on original research I conducted during the period of my Higher Degree by Research candidature and is not subject to any obligations or contractual agreements with a third party that would constrain its inclusion in this thesis. I am the primary author of this paper.
Signature	Date: 28/04/2021

Co-Author Contributions

By signing the Statement of Authorship, each author certifies that:

X. the candidate's stated contribution to the publication is accurate (as detailed above);
XI. permission is granted for the candidate in include the publication in the thesis; and
XII. the sum of all co-author contributions is equal to 100% less the candidate's stated contribution.

Name of Co-Author	Maziar Arjomandi		
Contribution to the Paper	Supervised the development of the research, participated in developing ideas, helped in interpretation of results and evaluation of the manuscript.		
Signature		Date	28/04/2021

Name of Co-Author	Benjamin Cazzolato		
Contribution to the Paper	Supervised the research and contributed in academic discussion and manuscript review.		
Signature		Date	28/04/2021

Name of Co-Author	Zhao Tian		
Contribution to the Paper	Supervised the research and contributed in academic discussion and manuscript review.		
Signature		Date	29/04/2021

22nd Australasian Fluid Mechanics Conference AFMC2020
Brisbane, Australia, 7-10 December 2020
https://doi.org/10.14264/28fff1a

Effect of Particle Diameter and Density on Acoustic Drug Delivery to Maxillary Sinus – a Sensitivity Study

O. Pourmehran[1], M. Arjomandi[1], B. Cazzolato[1] and Z. Tian[1]

[1]School of Mechanical Engineering

The University of Adelaide, Adelaide SA 5005, Australia

Abstract

Acoustic drug delivery to human maxillary sinus is a novel technique in the field of targeted drug delivery. This paper investigates the effect of drug particles' diameter and density on the efficiency of drug delivery to maxillary sinus through the direct computational aero-acoustics. A computational fluid dynamic model (CFD) using the discrete phase model has been developed and employed to simulate the transport pattern of the drug particles. For sensitivity study, a simplified model of nose-sinus comprising a nasal cavity, ostium and maxillary sinus has been utilised. It has been concluded that, in an acoustic field, decreasing the particle mass increases the particle entrainment coefficient due to the enhancement of the amplitude (entrainment coefficient) of the particle motion. The results also show that an increase in particles' diameter and density decreases the acoustics stokes number, which negatively affects the drug delivery efficiency.

Keywords

Acoustic drug delivery; Helmholtz resonator; Maxillary sinus; Computational Fluid Dynamics (CFD)

Introduction

Sinusitis is one of the most common diseases associated with rhinology, which affects up to 15% of the population throughout the world [1]. Since the nasal cavity (NC) is exposed to the infections carried by the inhaled aerosols, the maxillary sinus (MS) is highly prone to infection. The only opening to the MS is a slit-like channel of 3-9mm in diameter called ostium. The narrowness of ostium prevents easy access to the MS resulting in a challenge for efficient drug delivery to MS. Most drugs administered through the nostril by a conventional nebulisation system, fail to reach the MS efficiently [2] because the MS is located in a non-ventilated area due to the complexity of human nose geometry. Acoustically-driven drug delivery (ADD) technique offers an alternative solution for increasing the drug delivery efficiency because the pressure-induced flow generated by the acoustic field enhances the air exchange between the NC and MS. The underlying mechanism of the ADD is based on the Helmholtz resonator theory, in which the MS and ostium represent the cavity and neck of a Helmholtz resonator. Based on the Helmholtz resonator principle, in the presence of an external acoustic field, the air plug inside the ostium vibrates at the frequency of the applied acoustic field. The vibration of the air in the ostium causes a pressure difference between the NC and MS, which contributes to the transport of the drug particles from NC to MS. Hence, the highest drug delivery efficiency is achieved when the air plug in the ostium vibrates with the largest amplitude, which occurs at the resonance frequency of the NC-MS combination.

The ADD technique was firstly proposed by Guillerm et al. [3] in 1959 and later in several studies the feasibility of the ADD was investigated using experimental and modelling works. experimental and numerical studies [4, 5]. For a long time, a sinusoidal sound signal with a frequency of 50 Hz and 100 Hz was used by researchers and clinicians as the principle of the acoustically-driven nebulization process [6]. As an example, Weitzberg and Lundberg [7] in an experimental study showed that a humming exhalation could enhance the exchange of air between the NC and MS by 15-fold in comparison with quiet exhalation. Later on, Maniscalco et al. [8] demonstrated that the concentration of exhaled NO is significantly sensitive to the frequency of both the humming and the diameter of the maxillary ostium. Durand et al. [9] investigated the effect of an acoustic signal of 100 Hz on the efficiency of drug delivery to MS, experimentally. They reported that an increase of drug deposition on the sinus wall was achieved by a factor of 1.6 to 3 in comparison with non-acoustic drug delivery. Leclerc et al. [4] investigated the impact of airborne particle size on the efficiency of ADD to MS using an input acoustic frequency of 100 Hz, experimentally. They found that the fraction of particles deposited on the maxillary sinus wall increases when submicron drug particles are used. They reported a 20-fold increase in drug delivery efficiency by use of the particle size of 550 nm in comparison with the particle size of 9.9 μm[4]. In more recent studies, the researchers have utilized the resonance frequency of NC-MS as the inlet frequency exploiting the Helmholtz resonator frequency equation instead of the fixed frequencies of 50 Hz and 100 Hz. Moghadam et al. [5] used a sweep frequency for enhancing drug delivery efficiency. Xi et al. [10] used the Helmholtz resonator frequency equation and examined the effect of inlet frequency on the drug delivery efficiency. They reported that the maximum efficiency of drug delivery was achieved at the resonance frequency of NC-MS and its harmonics. In a recent study, Pourmehran et al. [1] proposed a novel experimental and numerical methods to estimate the resonance frequency of the NC-MS combination. They demonstrated that the Helmholtz resonator formula overestimates the resonance frequency of NC-MS combination by 20%-40%. In a later study [11], they employed this method for the estimation of resonance frequency and showed that the maximum efficiency of drug delivery to MS is achieved at the resonance frequency of NC-MS combination but not with the use of Helmholtz resonator formula. They also briefly discussed the orthokinetic motion of particles and the effect of particle diameter on ADD efficiency theoretically, however, with no case-specific results. In this study, a more accurate technique for the estimation of resonance frequency proposed as described in Pourmehran et al. [1], was applied and the effects of particle diameter and density on the particle Stokes number, entrainment coefficient, and the efficiency of ADD to MS are investigated in more details considering different case studies.

Numerical Modeling

In the present study, direct computational aero-acoustics were employed to simulate acoustically-driven drug delivery to maxillary sinuses. To enable a systematic study [12], a simplified NC-MS geometry (Figure 1) was used given that the resonance frequency of the NC-MS combination is not sensitive to the NC and MS shapes [1]. The three-dimensional (3D) equations of energy, continuity and momentum are employed

as the governing equations of Newtonian and compressible acoustically-driven flow in an unsteady state. The fluid was dry air, and the ideal gas law was employed to calculate the density of air. Also, Sutherland's law with three coefficients was used to resolve the air viscosity.

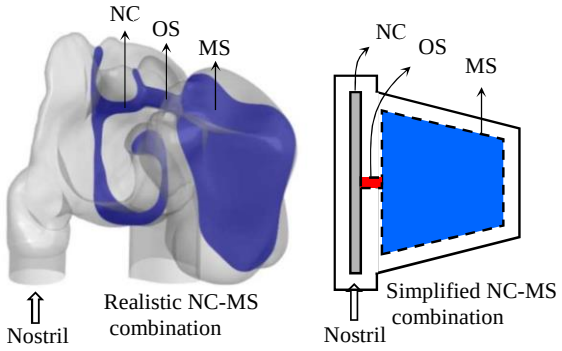

Figure 1. The cross-section of the simplified NC-MS geometry as an analogy of the realistic one-side NC-MS. Reprinted from European Journal of Pharmaceutical Sciences, 151, O. Pourmehran et al, Acoustically-driven drug delivery to maxillary sinuses: Aero-acoustic analysis, 105398, Copyright (2020), with permission from Elsevier

To simulate the particle trajectories, a discrete phase model (DPM) exploiting the Lagrangian particle tracking approach was used. Based on the Lagrangian approach, the trajectories of the particles are tracked through the integration of the force balance equation on each particle. In the presence of an acoustically-driven airflow, the total force which acts on an inert small particle is a combination of several different forces such as Basset, thermophoretic, Saffman, Brownian, pressure-gradient, virtual mass, Magnus, Faxen, gradient and drag forces. All forces except the gradient and drag forces are neglected in this study. A comprehensive discussion on this topic can be found in [11].

Considering the gradient and drag forces, the equation of force balance for a spherical particle, which used in the present study, is given by [11]

$$m_{\mathrm{p}}\frac{d\vec{u}_{\mathrm{p}}}{dt}=\vec{F}_{\mathrm{g}}+\vec{F}_{\mathrm{D}}=m_{\mathrm{p}}\frac{\vec{g}(\rho_{\mathrm{p}}-\rho)}{\rho_{\mathrm{p}}}+m_{\mathrm{p}}\frac{(\vec{u}-\vec{u}_{\mathrm{p}})}{\tau_{\mathrm{r}}}, \quad (1)$$

where $\vec{g}$, $\vec{u}$, $\vec{u}_{\mathrm{p}}$, and ρ_{p} are the gravity acceleration, fluid flow velocity, particle velocity, particle density, respectively. τ_{r} is the particle relaxation time defined by:

$$\tau_{\mathrm{r}}=\frac{\rho_{\mathrm{p}}d_{\mathrm{p}}^2}{18\mu}\frac{24}{C_{\mathrm{d}}\mathrm{Re}_{\mathrm{p}}} \quad (2)$$

where d_{p} is the diameter of particle and C_{d} is the drag coefficient, which is calculated through the equation of drag coefficient derived by Morsi and Alexander [13]. The drag coefficient equation is correlated to particle Reynolds number, given by $\mathrm{Re}_{\mathrm{p}}=\frac{\rho d_{\mathrm{p}}|u-u_{\mathrm{p}}|}{\mu}$.

ANSYS® Fluent was used to model the ADD to the MS in a simplified NC-MS combination. Given that the volume fraction of the particle phase falls in an order of magnitude of less than -6 ($V_{\mathrm{p}}/V_{\mathrm{f}}<10^{-6}$), and due to the low particle Reynolds number ($\mathrm{Re}_{\mathrm{p}} \ll 1$), a one-way coupling of the particle-fluid phases was used for particle tracking through DPM. A pressure-based solver with SIMPLEC scheme was used for solving the Navier-Stokes equations through an iterative time-advancement (ITA) algorithm. Second-order, third-order MUSCL spatial discretization methods were used for the pressure and density, respectively. Also, QUICK spatial discretization was used for the momentum and energy equations. A pressure-inlet boundary condition was applied to the inlet through a user-defined function (UDF) to simulate the sinusoidal acoustic wave given by

$$p_{in}(t)=p_0+\left(A_{\mathrm{p}}\times\sin(2\pi ft)\right), \quad (3)$$

where p_{in} is the inlet pressure, t is the time, p_0 is the initial pressure, A_p is the amplitude of the pressure wave, and f is the inlet frequency. A pressure-outlet boundary condition was applied to the outlet. To prevent reflection of the sound waves, a non-reflecting condition was also applied to the outlet boundary. A no-slip boundary condition was also defined on the walls.

Validation Study

The numerical simulation of this study has been validated against experimental data conducted by the authors at the University of Adelaide. A simplified NC-MS model was constructed using a Zortrax 3D printer device, with a resolution of 0.2 mm. Using an identical experimental setup and the procedure explained in Ref. [1] the resonance frequency of the NC-MS model was obtained. For this purpose, a load speaker was used to generate and apply a white noise signal, covering a range of frequencies from 150 Hz to 800 Hz, to the inlet. A MATLAB code was employed to estimate the transfer function (TF) between the inlet and response pressure waves. To quantify the degree of linearity between two microphones at the inlet and at the response points, a magnitude-squared coherence function (Coh) was utilised. Both the TF and Coh were estimated through a Hanning window with 2^{10} FFT points and a 75% overlap for a total of 14 averages. The Coh falls in the range of [0,1], in which the zero value of Coh shows a non-coherence condition and a unity value of Coh indicated the highest level of coherence between the inlet and response signals.

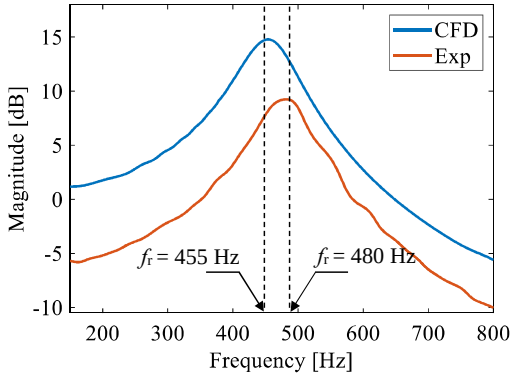

Figure 2. Comparison of the transfer function estimate obtained by CFD and experiment (Exp)

In the frequency range utilised in this study, the Coh exceeded 0.9, which indicates a high level of coherence showing an acceptable accuracy level. The experimental tests were repeated five times to ensure the predictability and repeatability of the results. The TF estimate and Coh function were also obtained via numerical modelling and the results were compared with the experimental data as shown in Figure 2. As can be seen in this figure, the numerical modelling is in good agreement with the experiment, showing a difference of 5.2%, which is due to the discretization and truncation errors of the numerical modelling. This figure also shows that the resonance frequency obtained

by numerical modelling is $f_r = 445$ Hz, which is used as the inlet frequency in this study.

Results and Discussion

Small Particle Behaviour in an Acoustic Field

In general, small particles in an aerosol oscillate if an acoustic field is applied to the aerosol. The particles oscillate with a frequency identical to the frequency of the applied acoustic field but at a different phase and amplitude [14]. Hence, the velocity of a particle can be expressed by $u_\mathrm{p} = \eta_\mathrm{p} A_\mathrm{u} \sin(2\pi f t - \phi_\mathrm{p})$,

where u_p is the velocity of the particle, η_p is the particle entrainment coefficient, A_u is the maximum amplitude of the velocity of the particle, and ϕ_p is phase factor. The particle entrainment coefficient, η_p, is the ratio of the amplitude of the velocity of the particle to the amplitude of the velocity of airflow, which are given by [14] $\eta_\mathrm{p} = 1 + (2\pi f \tau_\mathrm{p})^{2^{-0.5}}$ and $\phi_\mathrm{p} = \tan^{-1}(2\pi f \tau_\mathrm{p})$, where τ_p is the particle time scale given by $\tau_p = (\rho_p\, d_p^2)\,/\,18\mu$. Herein, the acoustic Stokes number is defined by $St_{ac} = 2\pi f \tau_\mathrm{p}$, in which the amplitude of the velocity and phase of the particle approaches the airflow velocity amplitude and phase in the limit of $f\tau_\mathrm{p} \to 0$ [15].

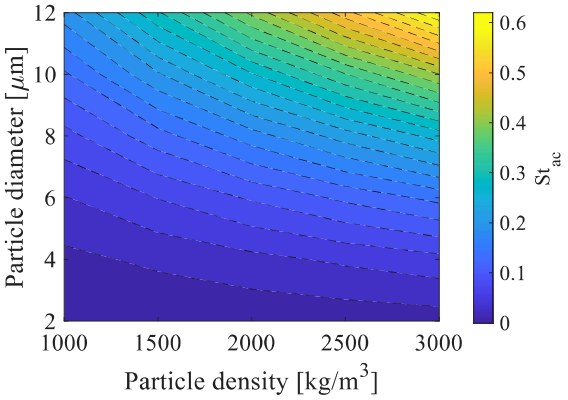

Figure 3. The effect of particle diameter and density on acoustic Stokes number at the resonance frequency (f_r = 455 Hz)

Figure 3 shows the effects of particle diameter and density on acoustic Stokes number at the frequency of $f_r = 455$ Hz. The dynamic viscosity and temperature assumed to be constant. From this figure, it is obvious that both the particle diameter and density have a direct relationship with the acoustic Stokes number. It can be seen from Figure 3 that the effect of particle diameter on the acoustic Stokes number depends on the particle density. For an illustration, for particles with a density of $\rho_p = 1000$ kg/m^3, an increase in particle diameter from 2µm to 12µm, , increases the acoustic Stokes number from 0.006 to 0.203, however, for particles with a density of $\rho_p = 3000$ kg/m^3, the acoustic Stokes number increases from 0.017 to 0.610.

Effect of particle diameter and density on ADD

To evaluate the effect of particle mass on the efficiency of ADD to MS, the airflow exchange between the NC and MS was quantified using a particle tracking scheme for different particle diameter and density. Given that the one-way fluid-particle coupling was used for the formulation of the particle tracking, the transport of particles to the MS is a representative of the exchange of the airflow between the NC and MS. To do so, a total of 5000 inert monodisperse particles were released in the NC zone. The particles were released in the domain after 20 periods to ensure that the pressure oscillation is stable. Then, the dynamic behaviour of the particles was simulated for an additional 100 periods. A total of 11 case studies including six different diameters of the particle (e.g. d_p= 2 µm, 4µm, 6 µm, 8 µm, 10 µm, and 12 µm) and five different densities of the particle (e.g. $\rho_p = 1000$ kg/m^3 to $\rho_p = 3000$ kg/m^3 with an interval of 500) were considered to investigate their effects on drug delivery efficiency. An inlet frequency of f = 455 Hz with an amplitude of $A_\mathrm{p} = 15$ Pa was applied to the inlet boundary for all cases.

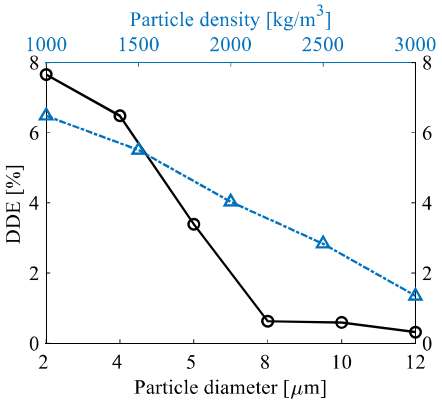

Figure 4. The effect of particle diameter and density on drug delivery efficiency (DDE). The black line shows the effect of particles diameter on DDE for a particle density of ρ_p = 1000 kg/m^3 and the blue line represents the effect of particle density on DDE for a particle diameter of d_p= 4 µm.

In this study, the drug delivery efficiency (DDE) is defined as a percentage of the number of particles delivered to the MS to the total distributed particles in the NC. Figure 4 shows the effect of particle diameter and density on DDE. As can be seen in this figure, both the diameter and density of the particles have an inverse relationship with DDE. It can be concluded that, the lighter the particles are distributed, the higher the DDE is achieved. The decreasing trend of the DDE shown in Figure 4 stems from the effect of particle diameter and density on the acoustic Stokes number. As it was discussed in the previous section, the acoustic Stokes number increases by an increase in the particle diameter and density. On the other hand, an increase in the acoustic Stokes number results in a decrease in particle entrainment coefficient showing a decrease in the amplitude of the particle oscillation. In other words, these particles travel a shorter distance along the ostium in every period, which results in a lower DDE.

In addition to the delivery of the particles to the MS, the deposition of the particles on the walls was also studies. In this regard, the term deposition fraction (DF) was used, which represents the percentage of the number of particles deposited on a wall to the number of particles distributed in the NC initially. Figure 5 (a) represents the effect of particle diameter on the DF at the entire NC-M walls and the NC, ostium, and MS walls. Although the DDE decreases with an increase in particle diameter (Figure 4), the total DF increases (Figure 5 (a)) because the surface area of the bigger particles is larger than the small particles, hence the bigger particles are more likely to be deposited onto walls. Figure 5 (b) demonstrates that changing the particle density does not affect overal DF. This figure also shows that increasing particle density increases the DF on NC wall but decreases DF on ostium wall because fewer particles are delivered to the MS through ostium. Figure 6 shows a snapshot of the particles' transport and deposition pattern when d_p= 4 µm, $\rho_p = 1000$ kg/m^3. From this figure,

it is obvious that most of the particle deposition occurs at the edges of the ostium connected to the NC and MS.

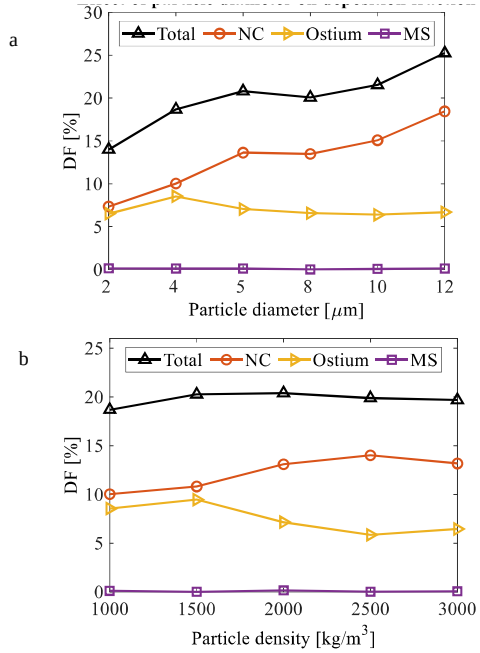

Figure 5. (a) The effect of particle diameter on the deposition fraction (DF) for particles with a density of $\rho_p = 1000$ kg/m^3 ; (b) the effect of particle density on DF for particles with a diameter of d_p= 4 µm.

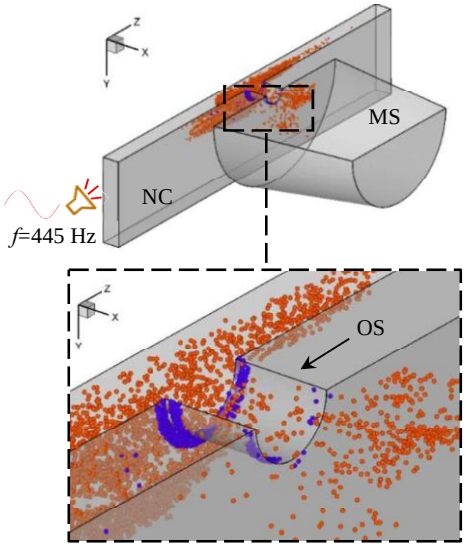

Figure 6. A snapshot of the particle transport and deposition pattern when d_p= 4 µm, $\rho_p = 1000$ kg/m^3,and $f = 455$ Hz at 120th periods. The blue dots show the particles deposited on the walls, and red dots represent the particles' transport pattern

Conclusion

In this study, the effect of particle diameter and density of the efficiency of ADD to the MS was investigated using a CFD model of a simplified NC-MS combination. The model was validated against the experimental data. The results show that, at the resonance frequency of the NC-MS, the acoustic Stokes number decreases, and the drug delivery efficiency increases with decreasing the particle diameter and density. Also, the overall DF on NC-MS walls increases with increasing the particle diameter, however, the variation of the particle density does not have a considerable effect on overall DF.

Acknowledgments

The authors would like to acknowledge the financial support of the University of Adelaide through the Beacon of Enlightenment PhD Scholarship, and the supercomputing resources provided by Phoenix HPC service at the University of Adelaide.

References

1. Pourmehran, O., et al., *The impact of geometrical parameters on acoustically driven drug delivery to maxillary sinuses.* Biomechanics and Modeling in Mechanobiology, 2019.
2. Laube, B.L., *Devices for aerosol delivery to treat sinusitis.* Journal of Aerosol Medicine, 2007. **20**(s1): p. S5-S18.
3. Guillerm, R., et al., *A new method of aerosol penetration into the sinuses.* La Presse Medicale, 1959. **67**(27): p. 1097-1098.
4. Leclerc, L., et al., *Impact of airborne particle size, acoustic airflow and breathing pattern on delivery of nebulized antibiotic into the maxillary sinuses using a realistic human nasal replica.* Pharmaceutical Research, 2014. **31**(9): p. 2335-2343.
5. Moghadam, S.J., et al., *Toward smart Nebulization: Engineering acoustic airflow to penetrate maxillary sinuses in chronic rhinosinusitis.* International journal of pharmaceutics, 2018. **546**(1-2): p. 188-193.
6. Navarro, L., L. Leclerc, and J. Pourchez, *Does Acoustic Overlay of Music Improve Aerosol Penetration into Maxillary Sinuses?* Online Journal of Otolaryngology and Rhinology 2019. **1**(4): p. 1-3.
7. Weitzberg, E. and J.O. Lundberg, *Humming greatly increases nasal nitric oxide.* American Journal of Respiratory and Critical Care Medicine, 2002. **166**(2): p. 144-145.
8. Maniscalco, M., et al., *Assessment of nasal and sinus nitric oxide output using single-breath humming exhalations.* European Respiratory Journal, 2003. **22**(2): p. 323-329.
9. Durand, M., et al., *Sonic aerosol therapy to target maxillary sinuses.* European Annals of Otorhinolaryngology, Head and Neck Diseases, 2012. **129**(5): p. 244-250.
10. Xi, J., et al., *Understanding the mechanisms underlying pulsating aerosol delivery to the maxillary sinus: In vitro tests and computational simulations.* International Journal of Pharmaceutics, 2017. **520**(1): p. 254-266.
11. Pourmehran, O., et al., *Acoustically-driven drug delivery to maxillary sinuses: Aero-acoustic analysis.* European Journal of Pharmaceutical Sciences, 2020: p. 105398.
12. Hood, C.M., et al., *Computational modeling of flow and gas exchange in models of the human maxillary sinus.* Journal of Applied Physiology, 2009. **107**(4): p. 1195-1203.
13. Morsi, S. and A. Alexander, *An investigation of particle trajectories in two-phase flow systems.* Journal of Fluid mechanics, 1972. **55**(2): p. 193-208.
14. Marshall, J.S. and S. Li, *Adhesive particle flow*. 2014: Cambridge University Press.
15. Achury, J. and W. Polifke, *Theoretical investigation of the particle response to an acoustic field.* International Journal of Spray and Combustion Dynamics, 2016. **8**(4): p. 262-270.

Chapter 5

Acoustic drug delivery to the maxillary sinus: *In-vitro* study

In this chapter, using the experimental and computational fluid dynamics (CFD) model, described in Chapter 3, to predict the resonance frequency of the combination of the nasal cavity (NC) and maxillary sinus (MS), as well as considering the important aero-acoustic parameters identified in Chapter 4, the feasibility of acoustic drug delivery (ADD) to a maxillary sinus (MS) were investigated. To do so, an experiment was designed to examine the effect of the aero-acoustic parameters, the input acoustic frequency, amplitude, and particle flowrate on the deposition of aerosols in the MS. A 3D printed model of a realistic nose-sinus geometry was used in the experiments. Sodium fluoride (NaF) 2.5 wt% was used as a drug tracer and was nebulised using a mesh nebuliser. A loudspeaker was used to generate the required acoustic waves. In addition to the experimental configuration, a computational fluid dynamics (CFD) model was developed to predict the particle transport and deposition

in a nose-sinus model, identical to that used in the experiments, under the effect of an input acoustic signal driven at the resonance frequency of the nose-sinus combination. The models developed and the discussions made in this chapter and the related results address the third objective of this work, namely, *"to fabricate a well-designed experimental setup using a 3D printed model of a realistic NC-MS model to examine the efficacy of ADD in drug delivery to the MS*".

The chapter consists of a journal article accepted for publication.

Pourmehran, O., Arjomandi, M., Cazzolato1, B., Tian, Z., Vreugde, S., Javadiyan, S., Psaltis, A., & Wormald, PJ. (2021), "Acoustic drug delivery to maxillary sinuses". *International Journal of Pharmaceutics, 120927 (In Press).*

Statement of Authorship

Title of Paper	Acoustic drug delivery to the maxillary sinus
Publication status	☐ Published ☒ Accepted for Publication ☐ Submitted for Publication ☐ Unpublished and Unsubmitted work written in manuscript style
Publication Details	Pourmehran, O., Arjomandi, M., Cazzolato1, B., Tian, Z., Vreugde, S., Javadiyan, S., Psaltis, A., & Wormald, PJ. (2021), "Acoustic drug delivery to maxillary sinuses". Submitted to International Journal of Pharmaceutics.

Principal Author

Name of Principal Author (Candidate)	Oveis Pourmehran		
Contribution to the Paper	Ideas and Concepts • Conducted a comprehensive literature review to find the gaps in the knowledge • Developed the ideas and concepts based on the gaps Experiments and Modelling • Developed a realistic NC-MS model in ANSYS® SpaceClaim and Austodesk® Inventor • Designed and fabricated an experimental setup for resonance frequency estimation • Designed and fabricated *in-vitro* experimental setup for particle deposition measurement in a 3D printed NC-MS model • Developed a CFD model for estimating the resonance frequency of the NC-MS models as well as to simulate the acoustic wave propagation and particle tracking Interpretation of Results • Extracted raw data from the experiments and simulation • Post-processed the simulation results using ANSYS® CFD-Post • Developed a MATLAB code to conduct signal processing for experimental data and to extract the figures for the acoustics part • Conducted statistical analysis using GraphPad Prism software for the *in-vitro* data • Interpreted the *in-vitro* results • Interpreted the simulation results and compared them with the experimental data Manuscript • Developed the first full draft of the manuscript • Applied comments given by co-authors • Submitted the manuscript • Acted as the corresponding author		
Overall percentage (%)	75%		
Certification:	This paper reports on original research I conducted during the period of my Higher Degree by Research candidature and is not subject to any obligations or contractual agreements with a third party that would constrain its inclusion in this thesis. I am the primary author of this paper.		
Signature		Date	28/04/2021

Co-Author Contributions

By signing the Statement of Authorship, each author certifies that:

XIII. the candidate's stated contribution to the publication is accurate (as detailed above);
XIV. permission is granted for the candidate in include the publication in the thesis; and
XV. the sum of all co-author contributions is equal to 100% less the candidate's stated contribution.

Name of Co-Author	Maziar Arjomandi		
Contribution to the Paper	Supervised the development of the research, participated in developing ideas, helped in interpretation of results and evaluation of the manuscript.		
Signature		Date	28/04/2021

Name of Co-Author	Benjamin Cazzolato		
Contribution to the Paper	Supervised the research and contributed in academic discussion and manuscript review.		
Signature		Date	28/04/2021

Name of Co-Author	Zhao Tian		
Contribution to the Paper	Supervised the research and contributed in academic discussion and manuscript review.		
Signature		Date	29/04/2021

Name of Co-Author	Sarah Vreugde		
Contribution to the Paper	Participated in academic discussion and manuscript review.		
Signature		Date	29/04/2021

Name of Co-Author	Shari Javadiyan		
Contribution to the Paper	Contributed in optimising and fabricating the experimental setup. Participated in academic discussion and manuscript review.		
Signature		Date	29/04/2021

Name of Co-Author	Alkis J Psaltis		
Contribution to the Paper	Participated in academic discussion and manuscript review.		
Signature		Date	29/04/2021

Name of Co-Author	Peter-John Wormald		
Contribution to the Paper	Participated in academic discussion and manuscript review.		
Signature		Date	29/04/2021

Acoustic drug delivery to the maxillary sinus

Oveis Pourmehran[1], Maziar Arjomandi[1], Benjamin Cazzolato[1], Zhao Tian[1], Sarah Vreugde[2], Shari Javadiyan[2], Alkis J Psaltis[2], Peter-John Wormald[2]

[1]School of Mechanical Engineering, The University of Adelaide, Adelaide, SA, Australia

[2]Department of Surgery - Otolaryngology Head and Neck Surgery, The University of Adelaide, Adelaide, SA, Australia

5.1 Abstract

Acoustic drug delivery (ADD) is an innovative method for drug delivery to the nose and paranasal sinuses and can be used to treat chronic rhinosinusitis (CRS). The underlying mechanism of ADD is based on the oscillatory exchange of air between the nasal cavity (NC) and the maxillary sinus (MS) through the ostium, which assists with the transfer of the drug particles from the NC to the sinuses. This study aims to examine the efficacy of ADD for drug delivery to the MS using an acoustic wave applied to nebulised aerosols entering the nostril. Here, the effect of acoustic frequency, amplitude, and nebulisation flowrate on the efficiency of ADD to the MS is investigated experimentally. A computational fluid dynamics model was also developed to understand the deposition and transport patterns of the aerosols. The results showed that superimposing an acoustic frequency of 328 Hz, which is the resonance frequency of the selected 3D printed model of the NC-MS combination, on the nebulised aerosols could improve the efficiency of the drug delivery to the MS by 75-fold compared with non-acoustic drug delivery case (p<0.0001). The experimental data also shows that an increase in the amplitude of excitation, increases the concentration of aerosol

[1] Corresponding author. Present address: School of Mechanical Engineering, the University of Adelaide, North Terrace, Adelaide, SA, 5005, Australia.
Email address: oveis.pourmehran@adelaide.edu.au (Oveis Pourmehran)

deposition in the MS significantly; however, it reaches to a plateau at a sound pressure level of 120 dB re 20 µPa.

5.2 Introduction

Chronic rhinosinusitis (CRS) has a prevalence ranging from 4.9% to 10.9% worldwide (Bhattacharyya, 2012; Cho et al., 2010; Liu et al., 2018; Pilan et al., 2012). Among the various paranasal sinuses, the maxillary sinuses (MS) are the most voluminous. They are connected to the nasal cavity (NC) through a very narrow channel called the ostium. In addition to nasal rinsing with buffered saline solutions, topical therapy with anti-inflammatory drugs forms the mainstay of treatment and various delivery methods are used, including, aerosol-based delivery such as metered-dose pump sprays, and nebulisation (Moffa et al., 2019).

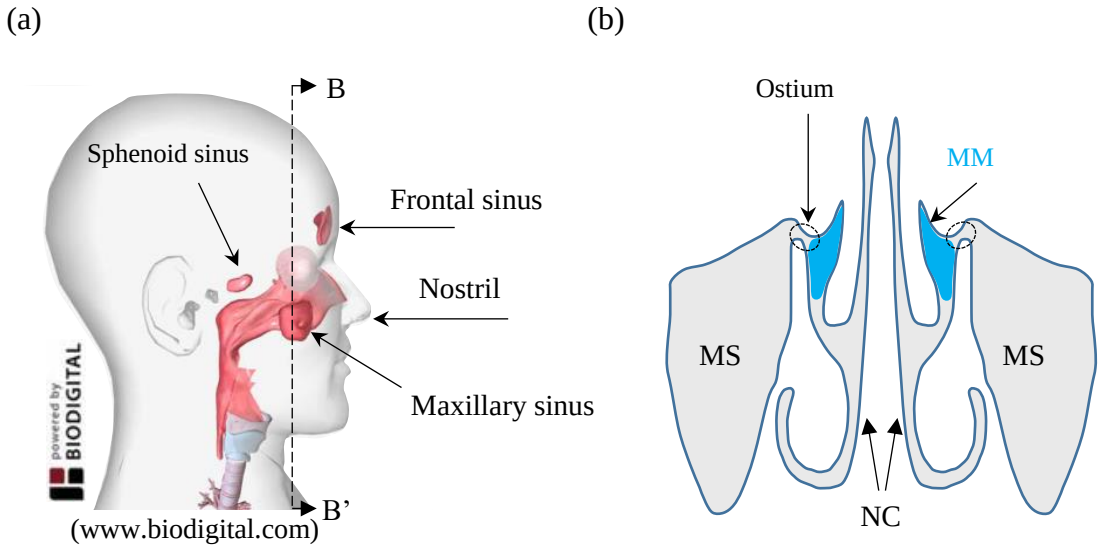

Figure 5.1: A schematic of the paranasal sinuses: (a) sagittal view; (b) section B-B' representing the maxillary sinuses (MS), ostium, middle meatus (MM), and nasal cavity (NC). Reprinted with some manipulations from Xi et al. (2017) with permission from Elsevier.

Metered-dose pump sprays produce particles (droplets) with a median aerodynamic diameter (MAD) of 50-100 µm. Metered-dose pump sprays work based on instilling fine particles into the nostril through activating a hand-operated pump mechanism

(Alagusundaram et al., 2010). The positioning of a metered-dose pump spray and the actuation force influence the dose and particle size of the formulation (Basu et al., 2020). Whilst, the spray pump has been demonstrated to be an efficient method for the delivery of corticosteroids for the treatment of seasonal allergic rhinitis, the majority of the particles produced by sprays are deposited on the nasal valve and cannot reach the posterior regions of NC and poorly-ventilated areas, such as sinuses (Berger et al., 2007; Möller et al., 2014). Therefore, spraying the drug is not an effective method for sinus drug delivery (Suman et al., 1999).

Nebulisers, which are mainly used as a post-surgical treatment, produce finer particles than nasal sprays, in a range of 1-30 μm, which can transport drugs beyond the nasal valve, to reach the ostium and sinuses, (Hilton et al., 2008; Wofford et al., 2015). Although the nebulised drug particles can reach the middle meatus (MM), a very small proportion of the drugs during the nebulisation process enters the MS through the ostium (Wofford et al., 2015). One end of the ostium is connected the MM region of the NC (under the middle turbinate) and the other end of the ostium is connected to the MS. The diameter of the unoperated and operated ostia typically are <5 mm and 10-20 mm, respectively (Cankurtaran et al., 2007; Moghadam et al., 2018; Sharma et al., 2014; Tarhan et al., 2005). Due to the small size of the ostium and barely-accessible location of the MS, it is challenging to deliver the nebulised particles effectively into the MS (Hyo et al., 1989; Möller et al., 2014) (see Figure 5.1).

In the last few years, adding acoustics to a nebuliser demonstrated higher drug deposition in the sinuses when compared with a conventional nebuliser without acoustics (Möller et al., 2010). The use of acoustics in nebulised drug delivery to the MS was first proposed by Kauf (1968), known as acoustic drug delivery (ADD). Given that the sinuses are non-ventilated areas, the oscillating airflow resulting from the acoustic field produces a

pressure gradient between the NC and MS leading to increase the gas exchange between the sinuses and the NC (Suman, 2013).

The efficacy of ADD to the MS has been reported in the literature (Durand et al., 2011; Leclerc et al., 2014; Maniscalco et al., 2013; Maniscalco et al., 2006). In an experimental study Weitzberg et al. (2002) measured the nitric oxide (NO) egressed from the nostril under the effect of humming exhalation. They showed that humming exhalation increased the concentration of exhaled NO up to 15-fold when compared with quiet exhalation, which was confirmed by Maniscalco et al. (2003). Weitzberg et al. (2002) also found that the concentration of exhaled NO varies at different frequencies of humming. The respiratory system releases nitric oxide (NO) in exhaled air, which is largely produced by the paranasal sinuses (Lundberg et al., 1995). Hence, an increase in the exhaled NO under the effect of humming exhalation (acoustic wave) is a representative of an increase in air-exchange between the NC and MS, which can result in enhancing the drug delivery to the MS. Maniscalco et al. (2006) reported that the superposition of acoustic signals with frequencies of 45 Hz, 120 HZ, and 200 Hz (sound pressure level was not reported in their study) on nebulised aerosols entering the nostril enhanced drug deposition on the MS wall by 3-fold, 3.5-fold, and 4.4-fold, respectively. Using an in-vitro study, Durand et al. (2011) showed that a 100 Hz acoustic wave with a sound pressure level of 107 dB re 20μ (measured at the outlet) applied to the nostril could increase aerosol deposition in the MS 3-fold. Leclerc et al. (2014) also showed that the deposition of aerosols with MAD of 2.8 μm in the MS was increased 2- to 3-fold under the effect of a 100 Hz acoustic wave (the sound pressure level was not reported in that study) when compared with the non-acoustic condition.

In a recent study by Hosseini et al. (2019) the effect of the anatomy of the nasal airway on drug delivery to the NC was investigated using the 3D printed models of nasal airways of

2-, 5- and 50-year old human subjects. They used a pulsating airflow with a frequency of 44.5 Hz and amplitude of 24 mbar superimposed to the aerosol stream entering the nostril. They reported that the drug delivery to the MS in the adult subject under application of pulsating airflow was increased 4-fold when compared with uniform airflow (non-pulsating). They demonstrated that the anterior deposition in toddler/child NC is greater than that of adults, which leads to 3-11% decrease in MS deposition and 25% decrease in lung deposition showing the effect of age on MS drug delivery. Hosseini et al. (2019) also showed that the paranasal delivery increases significantly when a bidirectional breathing administration technique is used under pulsating airflow. Using the breathing administration technique under the effect of 45 Hz pulsating nebulisation, Farnoud et al. (2020) investigated the effect of inclination of nosepiece with respect to the horizontal axis. They showed that the pulsating airflow increased the overall particle deposition in the sinuses by 1.5-fold and 2.5-fold for the cases with a nosepiece inclination of 90° and 45°, respectively, when compared with a uniform airflow (non-pulsating) demonstrating the effect of aerosol injection pattern at the nostril. Using a mask, double-head nozzle, and single-head nozzle at the nostril, (Dong et al., 2020) investigated the effect of different aerosol injection pattern on drug delivery to the MS under the effect of pulsating airflow superimposed to the aerosol stream (the frequency and amplitude of pulsation were not reported in the publication). They found that the method of drug administration influence on the efficiency of drug delivery to the sinuses and reported that using a single-head nozzle the deposition of drug in the MS increased by 2-fold when compared with double-size nozzle. They also showed that no MS deposition occurred when a face mask was used.

Initially, acoustic frequencies of 50 Hz and 100 Hz were superimposed onto nebulisation in ADD for sinus drug delivery (Navarro et al., 2019). Historically, these acoustic frequencies were discovered accidentally when researchers found dust deposition in

the sinuses of workers who worked with electrical rotating machines generating sinusoidal waves at frequencies of 50 Hz and 100 Hz (Navarro et al., 2019). However, this phenomenon has been questioned by recent studies, in which it was hypothesised that the underlying rationale of increased aerosol deposition in the sinuses is based on the principle of the Helmholtz resonator (Leclerc et al., 2014; Möller et al., 2014).

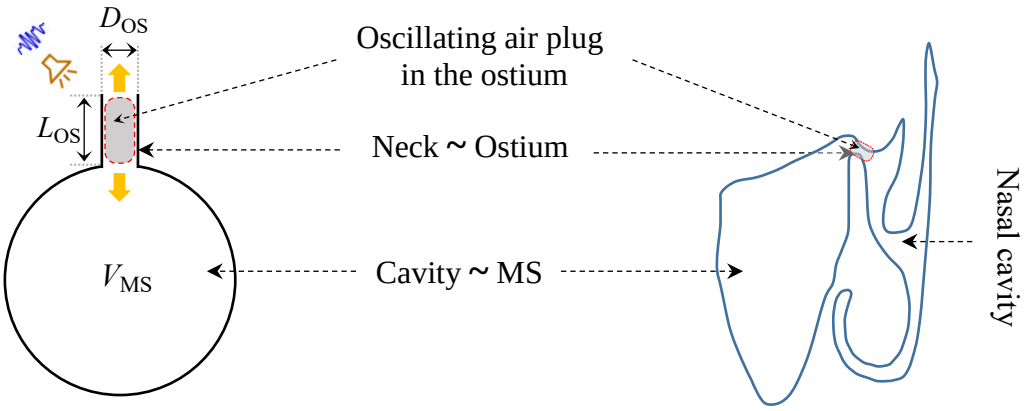

Figure 5.2: (a) Schematic of a Helmholtz resonator; (b) schematic of a cross-section view of an NC-MS combination, reproduced from Xi et al. (2017) with permission from Elsevier. The neck and cavity of the Helmholtz resonator resemble the ostium and MS. V_{MS}: Volume of the cavity (MS), L_{os}: Length of the neck (ostium), D_{os}: Diameter of the neck (ostium)

A Helmholtz resonator is an acoustical device, which is composed of a sphere cavity attached to a narrow tube (known as the neck) (von Helmholtz et al., 1875). When a Helmholtz resonator is in the presence of an external acoustic field, the air plug inside the neck oscillates at a frequency equal to that of the external acoustic field. The amplitude of the air plug oscillation in the neck changes according to the variation of the frequency of the external acoustic field, and it becomes maximum at a specific frequency called "resonance frequency" (Von Helmholtz & Ellis, 1875). At the resonance frequency of a Helmholtz resonator, maximum gas exchange between the cavity and the surrounding media occurs (Möller et al., 2014; Pourmehran, Cazzolato, et al., 2020b). For a Helmholtz resonator with a spherical cavity and a cylindrical neck (see Figure 5.2), the resonance frequency can be estimated by (Xi et al., 2017)

$$f_r = \frac{c}{2\pi}\sqrt{\frac{S_0}{V_{\mathrm{MS}}L_{\mathrm{eq}}}}, \tag{5-1}$$

where c is the sound speed, S_0 is the cross-section area of the neck ($S_0 = \pi D_{\mathrm{os}}^2/4$), V_{MS} is the volume of the cavity, and L_{eq} is the equivalent length of the neck, which can be obtained by L_{eq}=L_{os}+0.6D_{os}. L_{os} is the length of the neck and D_{os} is the diameter of the neck. More accurate expressions, depending on the shape of the cavity and neck, can be derived (Alster, 1972; Howard et al., 2000). A nose-sinus complex is similar to a Helmholtz resonator, where the sinus and ostium behave like the cavity and neck of the Helmholtz resonator, respectively. Hence, drawing on the principle of the Helmholtz resonator, if an external acoustic field is applied to the nostril at a frequency equal to the resonance frequency of the nose-sinus combination, the air exchange between the NC and the sinus should be maximised. The gas exchange between the NC and sinuses is the basic requirement for the transport of aerosols from the NC to the sinuses.

In the ADD technique, the larger the oscillation amplitude of the air plug in the ostium, the greater the number of particles that are delivered to the MS (Pourmehran, Cazzolato, et al., 2020b). Hence, it is imperative to apply an acoustic field with a frequency equal to the resonance frequency of the NC-MS, in which the amplitude of the air plug inside the ostium is maximal. Limited studies have used the classic Helmholtz resonator equation to predict the resonance frequency of the NC-MS to be applied to the nostril for the application of ADD in drug delivery to the MS (Leclerc et al., 2015; Xi et al., 2017).

Leclerc et al. (2015) used the classic equation of Helmholtz resonator (where L_{eq}=L_{os}) to estimate the resonance frequency of a realistic NC-MS model. They reported that at the resonance frequency of the NC-MS combination, the aerosol deposition in the MS increased 4-fold. Xi et al. (2017) investigated the deposition of aerosols with MAD of 3 μm in the MS

using Finite Element Method and experimental tests. Exploiting Equation (5-1), Xi et al. (2017) estimated the resonance frequency of a realistic NC-MS model and reported an increase of 6- to10-fold in aerosol deposition in the MS when compared to a case without acoustics. Pourmehran, Cazzolato, et al. (2020b) showed that the Helmholtz resonator equation overpredicts the resonance frequency of NC-MS by more than 30%, when compared with the experimental data. This discrepancy is due to the fact that the Helmholtz resonator equation was derived for a spherical cavity attached to a cylindrical neck, which is much different from a realistic NC-MS combination. Accordingly, the resonance frequency of the realistic nose-sinus complex estimated in the previous studies might be inaccurate. Hence, for previous studies it was not guaranteed that the air plug in the ostium was activating efficiently under the effect of the fixed acoustic frequency obtained by the Helmholtz resonator equation. So, the highest efficiency of drug delivery could not be achieved.

In addition to the frequency of the inlet acoustic wave, aero-acoustic parameters, such as the inlet acoustic amplitude and breathing pattern (airflow rate), are vital components that play an important role in the ADD technique. Moreover, the size of the nebulised particles affects the efficiency of ADD. using an in-vitro study, demonstrated a weak deposition of 9.9 μm particles but a significant deposition of 2.8 μm particles in the MS under the effect of a 100 Hz acoustic wave. Recently, Pourmehran, Arjomandi, Cazzolato, and Tian (2020) examined the effect of particle diameter and density on the efficiency of ADD in a simplified NC-MS model using computational fluid-particle dynamics. Considering the acoustic Stokes number and particle entrainment coefficient, they demonstrated an increase in particle diameter and density decreases the efficiency of ADD to the MS which is in the line with the findings of Xi et al. (2017). Although the use of small nebulised particles (i.e. 2.8 μm) results in higher ADD efficiency, when the particle diameters are lower than 10 microns, the particles are easily transported to the lung, which is not the intended region for drug delivery to the

MS (Kulkarni et al., 2012). Finally, the effect of the nebulisation flowrate (the particle flowrate) coupled with a constant airflow rate has not yet been investigated in the literature. In this study, using nebulised aerosols with a median diameter of 12 μm, the effect of input acoustic frequency, amplitude, and particle flowrate on the efficiency of ADD to the MS is investigated. A realistic geometry of one-side of an NC-MS combination was used as a nasal replica.

5.3 Materials and Methods

5.3.1 Nasal replica

An NC-MS combination was manufactured with epoxy-based resin (Zortrax Resin BASIC) using a Zortrax Inkspire 3D printer with an accuracy of 0.05mm on the horizontal (X-Y) plane and 0.025mm along the vertical (Z) axis (along printing layer) at the University of Adelaide. The X-Y plane was perpendicular to the inlet of the nostril. The MS was extracted from a realistic NC-MS STL file (for a healthy person) adapted from Kumar et al. (2016) and the NC was extracted from a CAD model of human (healthy 25-year-old Asian male) upper airway adapted from Inthavong et al. (2008). To better understand the potential of the MS behaving as a Helmholtz resonator we decided to estimate the resonance frequency of the NC-MS and to investigate the ADD efficiency for drug delivery to the MS isolated from other sinuses and hence, all the sinuses except the MS were excluded from the model (Figure 5.3). The volume of the sinus was approximately 15 mL and the length and diameter of the ostium were approximately $L_{os} = 5.5$ mm and $D_{os} = 4.2$ mm, respectively. To access the inside of the MS as well as to allow installation of a microphone for acoustic measurement, the NC-MS model was fabricated in three separate parts, P1, P2 and P3, as depicted in Figure 5.3 (b). For measuring the resonance frequency, the P3 was replaced by a microphone to detect the sound

at the response point. A tube with an inner diameter of 8 mm and a length of 9 cm was also attached to the nasopharynx (the nasopharynx has already been extended 1 cm in the original model) to stabilise the outlet flow for preventing the possible reverse flow from the outlet boundary into the NC-MS model induced by the surrounding airflow inside the fume hood where the experiments were conducted.

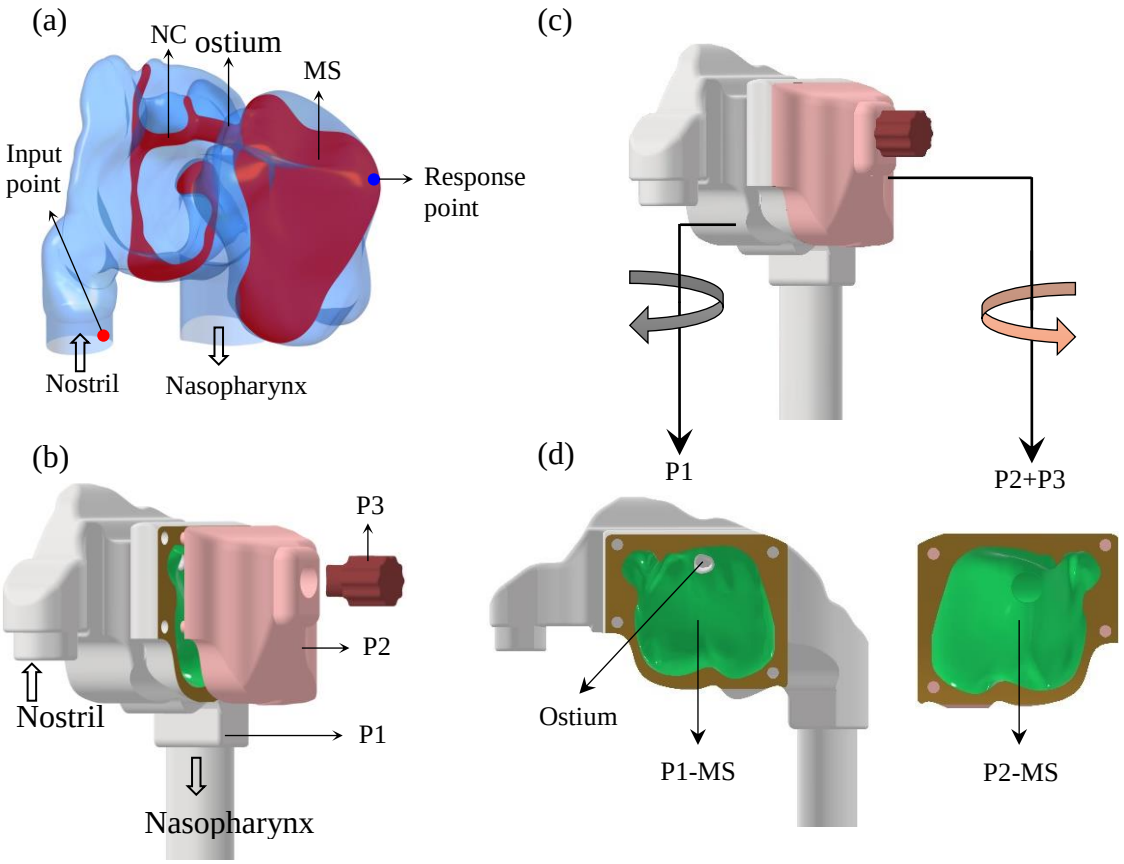

Figure 5.3 (a) Reconstructed model of a realistic nose-sinus geometry; the MS was extracted from a realistic NC-MS STL file adapted from Kumar et al. (2016) and the NC was extracted from a CAD model of human upper airways adapted from Inthavong et al. (2008); (b) the dissembled 3D model of NC-MS representing different parts of 3D printed model; (c) assembled model of NC-MS used in experiments; (d) inside view of the NC-MS model. P1: part 1 comprising the NC, ostium, nostril, nasopharynx, and a portion of MS. P2: part 2 which is a part of MS. P3: part 3 which blocks the holes of the MS wall (on P2). P3 is replaced with microphone for measuring the resonance frequency. P1-MS: the inner surface of the MS that is attached to P1. P2-MS: the inner surface of the MS that is attached to P2.

5.3.2 Experimental setup

Two different in-house experimental setups were used in this (in-vitro) study. The first experimental setup was used to estimate the resonance frequency of the NC-MS combination. In these experiments, an acoustic actuator (a loudspeaker) was used to generate a white broadband noise and applied to the nostril. Two $1/4''$ microphones (Bruel and Kjaer®, Type 4958), Mic 1 and Mic 2, were installed on the NC-MS model: Mic 1 was installed at the nostril which is termed as the input point and Mic 2 was installed at the lateral wall of the MS termed as the response point by replacing with part P3 (see Figure 5.3 (a, b) and Figure 5.4 (b)). The sound pressures at the input and response points were measured using the microphones and a Bruel and Kjaer Photon® signal analyser was used to estimate the transfer function (TF) and coherence.

The second experimental setup was designed and used for the investigation of the drug delivery process and the impact of the variation in nebulisation parameters. A loudspeaker was connected to the nasal tip through a transparent flexible tube. The nasal tip was designed using Autodesk Inventor software and then manufactured by a Zortrax M200 printer (with an accuracy of 0.2mm for the X-Y plane and 0.09mm along the Z-axis). The nasal tip consists of two inlets and one outlet openings (see Figure 5.5 (c)). One of the inlets of the tip was connected to an acoustic signal generator (via the tube) and the other inlet was attached to the nebuliser head. The outlet of the tip was connected to the nostril on the 3D printed model. A vibrating mesh nebulizer manufactured by TEKCELEO® was used to inject the liquid droplets into the NC-MS combination through the nostril. In this study, a droplet generated by the nebuliser is termed as particle. The median diameter of the nebulized particles was 12 µm, which is compliant with US Food and Drug Administration (FDA Guidance for industry 2002; Nasal Spray and Inhalation Solution, Suspension, and Spray Drug Products -

Chemistry, Manufacturing, and Controls Documentation) to reduce the penetration of particles into the lung (Farzal et al., 2019; Kulkarni et al., 2012).

(a)

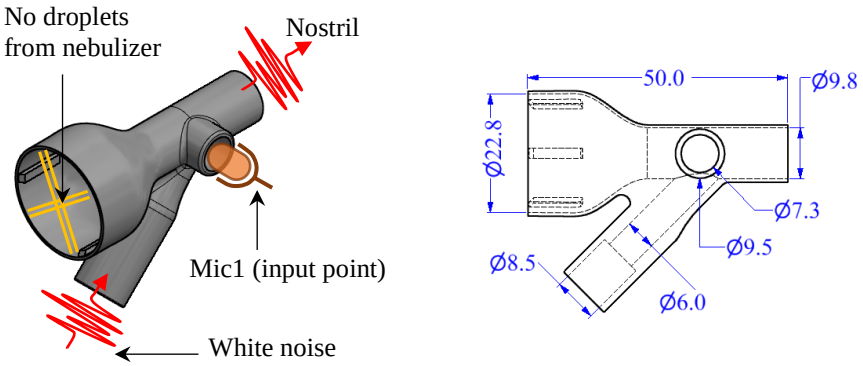

(b)

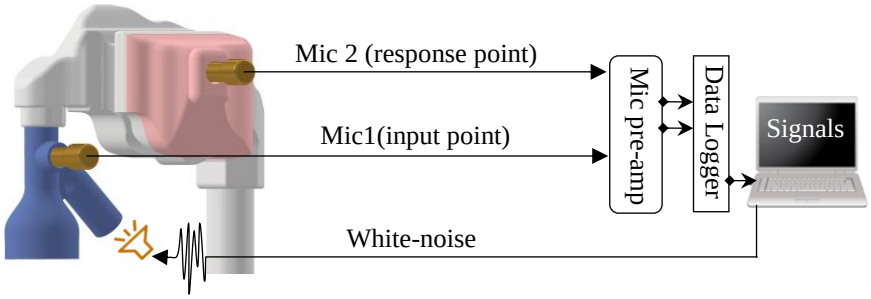

Figure 5.4. (a) 3D view and schematic diagram of the nasal tip used in the first experiments for the estimation of the resonance frequency of the NC-MS combination. The dimensions are presented in mm; (b) schematic of the first experimental setup used for measuring the resonance frequency of the NC-MS model. Mic pre-amp: Microphone preamplifier

As recommended in the literature (Moghadam et al., 2018) and international standards (European standard procedure, NF EN 13544-1), 2.5 wt% sodium fluoride (NaF) was used as the drug tracer test solution. For each experimental test, 4 mL of 2.5 wt% NaF was nebulised and injected into the NC-MS combination through the nostril. Once the nebulization experiment was complete, the inlet and outlet of the NC-MS model were sealed and maintained stationary for 20 min to allow the suspended particles to deposit on the inner wall of the MS. To measure the deposition of nebulised droplets (i.e., NaF solution) in the MS, the inner surface of MS was washed with distilled water to collect the deposited F^- ions. Then the concentration of F^- ions was measured by an Ion-Selective Electrode (ISE) meter, using a fluoride electrode (BANTE Instrument) with an accuracy of 0.001 ppm. Given that the ion-

selective electrodes measure the activity of the analyte, to stable the measurement the ionic strength of the solution should be enhanced to a relatively high level, which was achieved by TISAB-2 buffer. TISAB-2 was prepared by adding 2.7 ml of Acetic acid (98-99%), 17.6 g of Sodium Acetate (anhydrous), and 8 g of Sodium chloride to 200 ml of DI water, then the mixture was transferred to a 250 ml flask and filled with distilled water and shaken well. The following protocol was used to measure the deposition of NaF: To be able to wash the inside of the MS with distilled water and collect the deposited NaF solution, part P2 was detached from part P1 (see Figure 5.3 (d)). To wash the inner wall of P1 (i.e., P1-MS), a silicon pin was used to seal the ostium opening hermetically to prevent leakage of the liquid through the ostium. A volume of 2.5 mL of distilled water was used for washing the surface P1-MS, and 2 mL of distilled water was utilised for washing the inner wall of surface P2-MS. The washing process was carried out using a pipette. Eventually, the total amount of liquid was collected, and then 0.5 mL of TISAB-2 (total ionic strength adjustment buffer) was added to it (i.e., onetime buffer addition). A blank sample was taken before starting the experiments for each parameter (such as acoustic frequency, amplitude, and nebulisation flow rate). After the completion of each experiment, and to prepare the test section for the next experiment, the 3D printed model of the NC-MS combination was washed out with distilled water to clean out any Fluoride contamination from the inner walls then the model was dried with hot air.

After the completion of each experiment and to prepare the test section for the next experiment, the 3D printed model of the NC-MS combination was washed out with distilled water to clean out any Fluoride contamination from the inner walls then the model was dried with hot air.

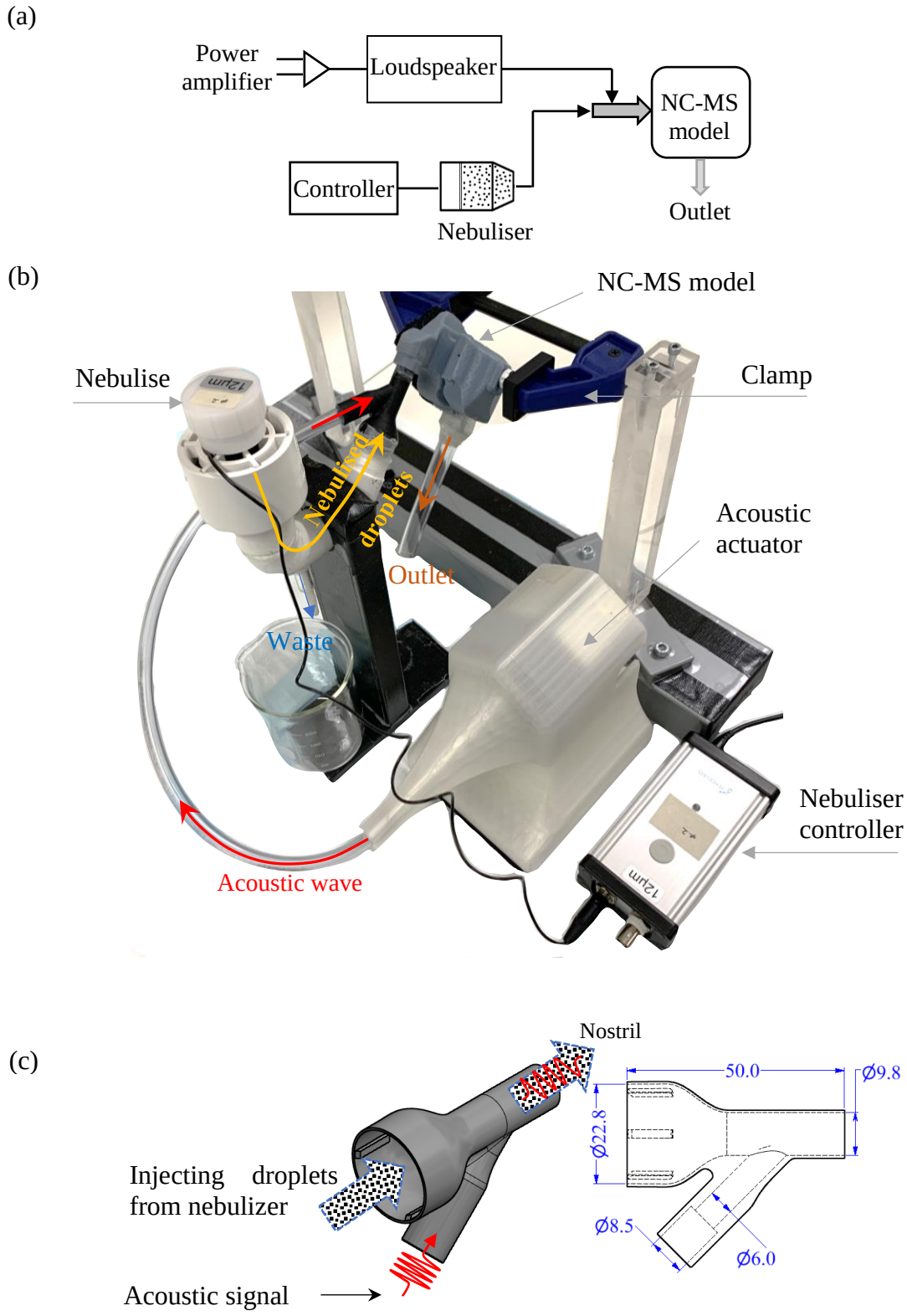

Figure 5.5. (a) Schematic diagram of the second experimental setup; (b) an overview of the second experimental setup used for ADD conducted in a fume hood; (c) 3D view and schematic diagram of nasal tip excluding the microphone holder, which was used for measuring the acoustic pressure in the first experimental setup for estimating the resonance frequency. The dimensions are presented in mm.

As tabulated in Table 5.1, a total of 18 different case studies were considered to investigate the effect of input acoustic frequency (10 cases), acoustic amplitude (4 cases), and particle flow rate (4 cases) on the efficiency of ADD for the MS. The ADD efficacy in this paper is quantified by measuring the concentration of the Fluoride ions deposited on the MS wall and comparing them with that obtained via non-acoustic drug delivery (non-ADD). For all the parameters, the experiments were repeated four times to ensure the results were reliable. The results were presented as the "mean value $\pm$ standard deviation".

Table 5.1. Details of the case studies for the experimental tests

Cases	**Input Frequency [Hz]**	**Input SPL [re 20 µPa]**	**particle flow rate [mL/min]**
1-10	100, 200, 250, 300, 328, 356, 403, 450, 537, 585	126	0.267
11-14	328	113.4, 116.9, 120.6, 126	0.267
15-18	328	126	0.059, 0.098, 0.138, 0.267

5.3.3 Numerical modelling

In addition to the experiments, computational fluid dynamics (CFD) modelling was used to investigate the particle deposition and transportation patterns under an acoustic wave at the resonance frequency of the NC-MS combination. ANSYS® FLUENT 2020 R1 was used to simulate the particle dynamics in a realistic NC-MS model. The geometry of the realistic NC-MS model, used in CFD modelling, was identical to that of the experiments; however, to reduce the computational cost the nasopharynx was restricted to 1 cm (Inthavong et al., 2008; Kumar et al., 2016). Due to the presence of an acoustic field, the fluid medium in this study was selected as compressible dry air and the density of the air was calculated using the ideal gas law. Sutherland's third law (Sutherland, 1893) was used for calculating viscosity. The compressible transient nonlinear Navier-Stokes equations were solved using a pressure-based solver to resolve the airflow field in the presence of an acoustic field. The boundary condition

of the walls was set to be acoustically reflective and adiabatic. Zero-gauge pressure was selected for the outlet boundary condition, as well as the initial condition. For the prediction of resonance frequency of the NC-MS combination, a general non-reflecting boundary condition (NRBC) was applied to the inlet and outlet boundaries. To resolve the momentum and energy equations, density, and pressure, the QUICK, third-order MUSCL, and second-order spatial discretization methods were utilised, respectively. Finally, the transient formulation was resolved using the second-order implicit method.

To predict the resonance frequency of the proposed model (without the nasopharynx extension) using CFD, an acoustic sweep in a range of frequencies from 150 Hz to 800 Hz was applied to the inlet as a pressure-inlet boundary condition given by (Pourmehran, Cazzolato, et al., 2020b):

$$p(t) = A\sin(f_0 t + \frac{t^2(f_1 - f_0)}{2T_s}), \tag{5-2}$$

where $p(t)$ is the time-dependent pressure, and A is the amplitude of the incident pressure. f_0, f_1, and T_s are the starting angular frequency, final angular frequency, and the required time for the acoustic wave to sweep from f_0 to f_1. A total of 1,280,000 polyhedral elements were generated using the polyhedral elements with two prism layers near the wall boundaries. The polyhedral elements were used for mesh generation because of its advantages, such as a shorter run-time, a higher accuracy in determining wall shear stress, and a better convergence (Spiegel et al., 2011). Moreover, a time-step of $\Delta t = 1\mu s$ was used for the simulation of the flow and particle phases, which meets the acoustic courant number required for direct computational aero-acoustic analysis. Figure 5.6 Shows the mesh generated for the proposed realistic NC-MS model. To evaluate the accuracy of the CFD model, the predicted resonance frequency of the NC-MS combination, excluding the nasopharynx extension, was compared with the resonance frequency obtained through the first experimental setup.

A time-independent transfer function estimate (TF estimate) was used to predict the resonance frequency of the NC-MS model. The TF estimate models a linear relationship between the input (*i*) and response (*j*) acoustic waves. The input time-series acoustic wave was obtained by recording the pressure fluctuation at the inlet boundary (input point) and the response time-series acoustic wave was detected via recording the pressure fluctuation at the response point (see Figure 5.3 (a)). The peak value of the TF estimate in the frequency domain represents the resonance frequency of the NC-MS model, which is calculated by

$$T_{ij}(f) = \frac{G_{ij}(f)}{G_{ii}(f)} \tag{5-3}$$

where f is the acoustic frequency at the input point, G_{ij} is the cross-power spectral density between the input and the response, and G_{ii} is the power spectral density of the input acoustic wave. The reliability of the pressure fluctuations, recorded at the input and response points, were examined through a magnitude–squared coherence function (Coh) given by:

$$C_{ij}(f) = \frac{\left|G_{ij}(f)\right|^2}{G_{ii}(f)G_{ij}(f)} \tag{5-4}$$

where $C_{ij}(f)$ is the Coh estimate, which quantifies the degree of linearity between the input and response acoustic waves and gives a value between 0-1. A zero value of Coh indicates that there is no relationship between the input and response acoustic wave; however, a unit value of Coh implies that the pressure fluctuation recorded at the input point is perfectly coherent with the acoustic wave applied to the inlet boundary and the signals from other sources are screened out (Pourmehran, Cazzolato, et al., 2020b).

For modelling the two-phase flow and to capture the impact of flow on nebulised particles, a Lagrangian particle tracking approach, which employs a discrete phase model

(DPM), was used for the particle tracking simulation. In this approach, the trajectories of the particles can be tracked by integrating the equation of force balance on every particle. In this study, the force balance equation, which equates the particle inertia with the forces acting on the particle, is composed of gravitational and drag forces (Pourmehran, Cazzolato, et al., 2020b). The acoustic radiation force has been neglected in this study since its effect on particle movement is significant in ultrasonic medium, while the acoustic field used in this study is in a low-frequency range (<1000 Hz). The effect of all forces exerting on a particle in an acoustic field has been discussed in Pourmehran, Cazzolato, et al. (2020b), which provides more details on the significance of forces acting on a moving particle in an acoustic field.

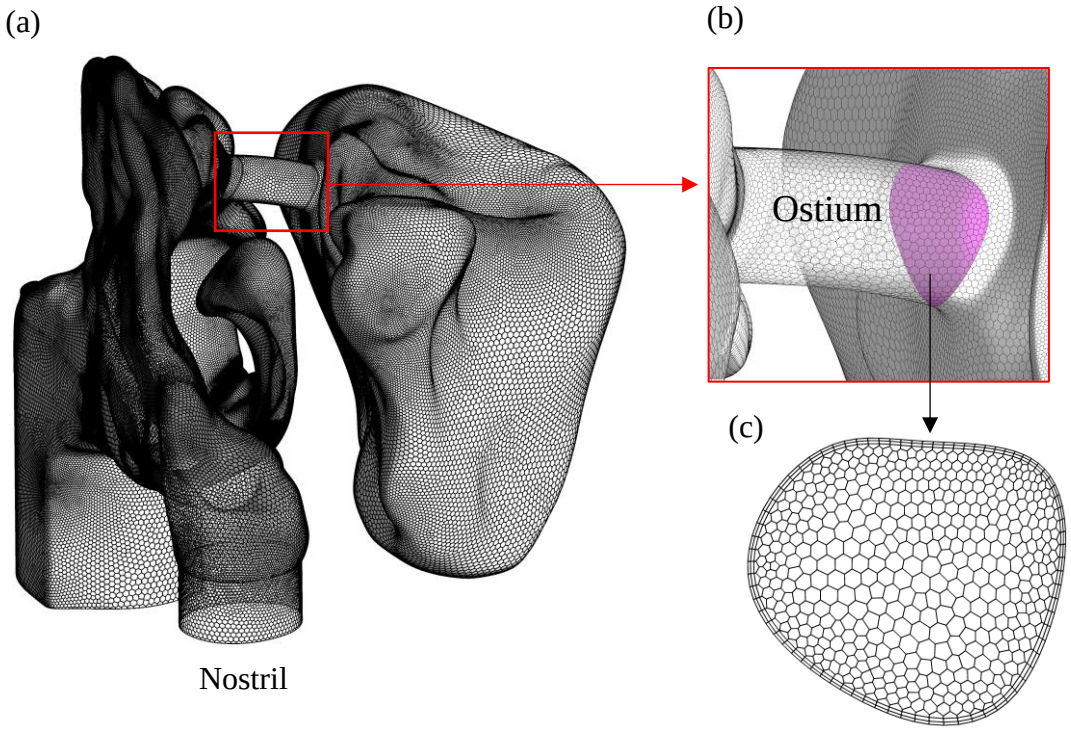

Figure 5.6. (a) an overview of the polyhedral mesh generated for the realistic NC-MS model used in CFD simulation, (b) a close-up view of the ostium and MS; (c) polyhedral mesh at the interface of the ostium and MS.

5.4 Results and discussion

5.4.1 Acoustic analysis

The resonance frequency of the NC-MS combination was estimated using the first experimental setup. The experimental data indicated that the resonance frequency of the NC-MS model of this study is f_r=328 Hz. Figure 5.7 (a) shows the transfer function (TF) and coherence (Coh) estimates between the nostril (input) and MS (response). It should be noted that the resonance frequency of the MS occurs at the peak value of the TF estimate. As can be seen in Figure 5.7 (a), the TF estimates show three peak values. The first peak value at f = 50 Hz is associated with electrical noise, the second peak value at f_r = 328 Hz is the resonance frequency of the NC-MS, and the third peak value is due to the resonance of the NC (Pourmehran, Arjomandi, Cazzolato, Ghanadi, et al., 2020). Figure 5.7 (b) represents the pressure amplitude (dB re 20 µPa) measured at the nostril and MS. As can be seen in this figure, the difference between the sound pressure level (SPL) at the nostril and the MS is maximised at f = 328 Hz, which confirms that the resonance frequency of the NC-MS combination occurs at the second peak value of the TF estimate. The resonance frequency of the NC-MS combination was also estimated using the Helmholtz resonator equation (Equation (5-1)). Considering the MS volume of 15 mL ostium length of $L_{os} = 5.5$ mm, and ostium diameter of $D_{os} = 4.2$ mm, the resonance frequency of the NS-MC combination was estimated as f_r=585 Hz. The difference in the resonance frequency estimated by Equation (5-1) and the experimental data originates from the difference between the geometry of the realistic NC-MS combination and a Helmholtz resonator. The middle meatus affects the resonance frequency of the NC-MS combination while Equation (5-1) does not account for the presence of middle meatus (Pourmehran, Cazzolato, et al., 2020a).

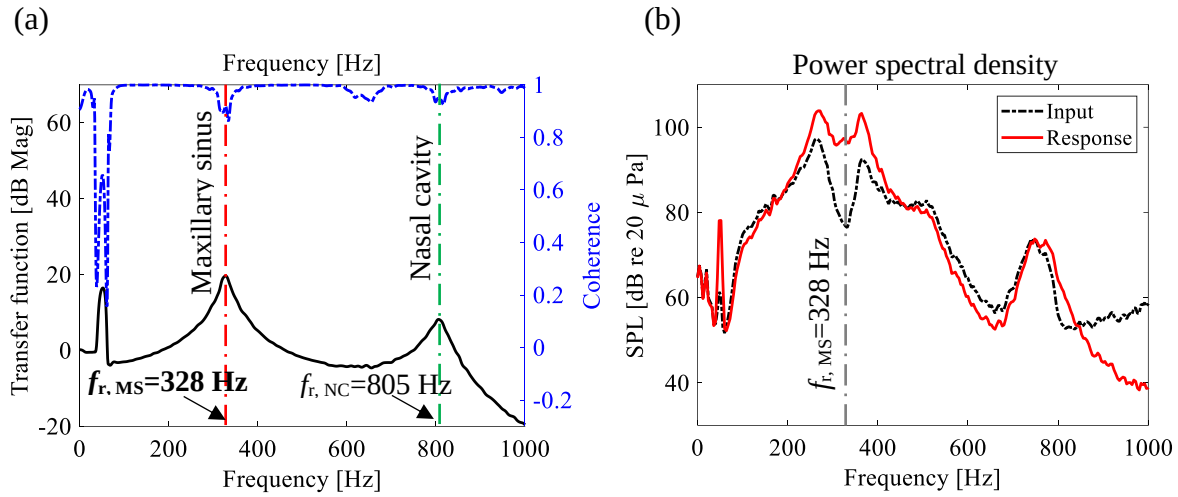

Figure 5.7. a) Transfer function and coherence estimates between the sound pressure at the nostril and the MS; b) Sound pressure level (SPL) between the input and response points versus frequency. The anatomical location of the input and response points are represented in Figure 5.3 (a).

In the first series of experiments, the aerosol deposition on the MS wall was measured under the effect of an acoustic signal, characterised by a fixed frequency applied at the inlet to the nostril (see Figure 5.5 (c)). For each experimental test, the input acoustic signal was characterised by a specific frequency applied at the inlet to the nostril to agitate the nebulised aerosol (NaF) entering the nostril; then the concentration of NaF deposited on the MS wall was measured at high accuracy. In terms of the input frequency, in addition to the resonance frequency of the NC-MS combination estimated in the first experimental setup, (328 Hz), and Helmholtz resonator equation, (585 Hz), four frequencies (100 Hz, 200 Hz, 250 Hz, 300 Hz) that are lower than the resonance frequency and four frequencies (356 Hz, 403 Hz, 450 Hz, 537 Hz) that are higher than the resonance frequency were selected for application to the nostril as additional case studies. The first four frequencies were selected to cover a broad range of TF estimate at frequencies lower than the resonance frequency. The second four frequencies (356-537Hz) were chosen to match the amplitude of the transfer function to the first four frequencies. The rationale behind the selection of those two groups of off-resonance frequencies is to realise the relationship between the TF estimate and ADD efficiency in

addition to understanding the effect of acoustic frequency on the efficiency of ADD. In total, 10 different sinusoidal acoustic signals, with a fixed sound pressure level of almost 126 dB re 20µPa, were applied to the nostril and then the SPL at the input and response points were measured.

Figure 5.8 shows the effect of the input frequency on the SPL at the response point for a fixed input SPL. The SPL in the MS increases when the inlet frequency reaches the resonance frequency. At the resonance frequency, the maximum SPL in the MS occurs, which implies that the pressure fluctuation in the MS is at its maximum at the resonance frequency of the NC-MS combination. Given that the MS is connected to the ostium, the oscillation of the air in the MS is directly interconnected to the oscillation of air plug in the ostium. Accordingly, the amplitude of the oscillation of the air plug in the ostium becomes maximal at the resonance frequency in which the highest air exchange between the NC and MS takes place through the ostium. So, it is expected to achieve the highest efficiency of the ADD at the resonance frequency of the NC-MS combination, which is investigated in the following section.

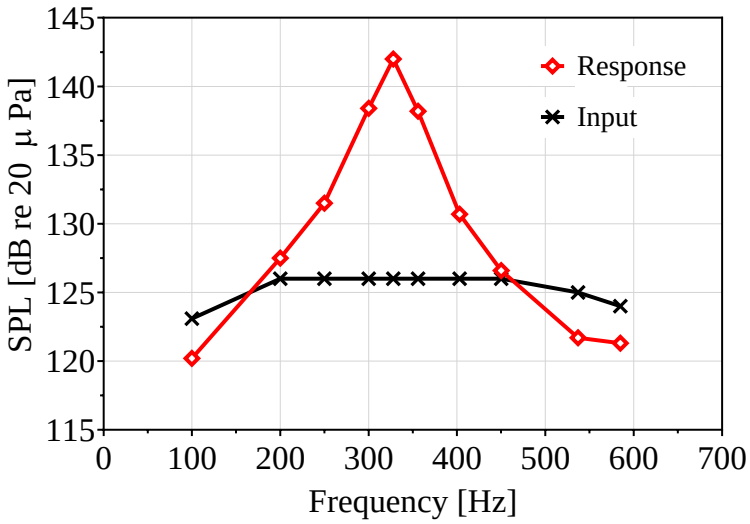

Figure 5.8. The effect of input acoustic frequency on the sound pressure level (SPL) in the MS (response) and at the nostril (input)

The resonance frequency of the proposed NC-MS model used for CFD simulation was obtained f_r=352 Hz as illustrated in Figure 5.9 (a). According to this figure, the results of CFD showed good agreement with the resonance frequency calculated in the experiments (f_r=392 Hz), with a discrepancy of 10%. Figure 5.9 (b) presents the magnitude-squared coherence estimate between the input and response points for both the experimental and CFD results. This figure shows that the value of Coh is close to unity for CFD modelling demonstrating the reliability of the pressure field obtained in CFD modelling. Herein, to reduce the computational cost (by reducing the number of mesh) the nasopharynx was extended only 1 cm rather than 10 cm. However, for drug delivery modelling, the nasopharynx was extended 10 cm to prevent the reverse flow.

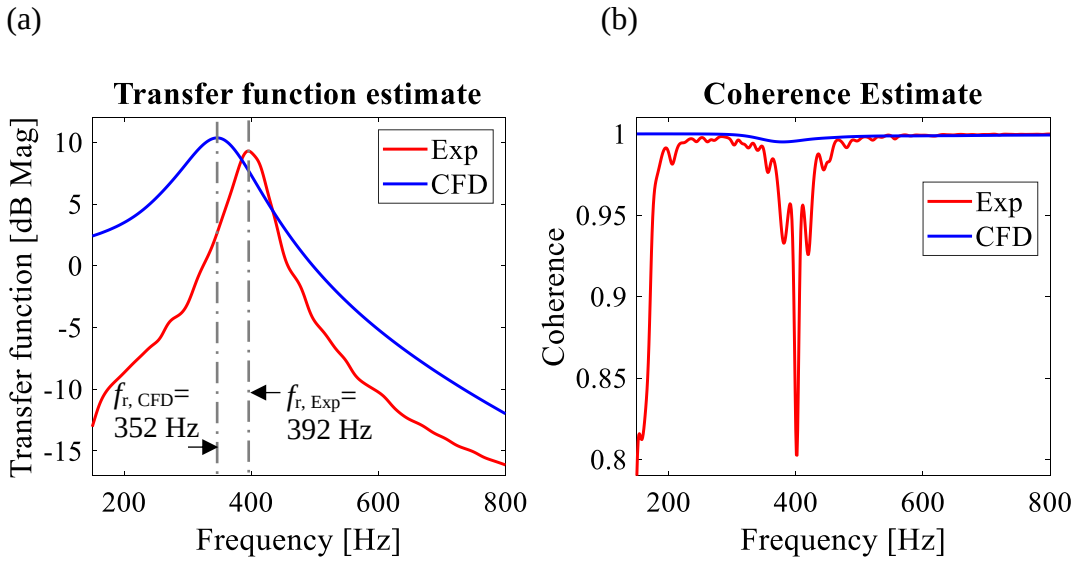

Figure 5.9. a) Transfer function estimate; and (b) coherence estimate between the input and response points obtained by computational fluid dynamics (CFD) and experimental test (Exp). To reduce the computational cost the nasopharynx was extended only 1 cm rather than 10 cm

5.4.2 Effect of acoustic frequency on ADD efficacy

Figure 5.10 shows the effect of input frequency on the concentration of aerosol (NaF) deposited on the MS wall, which reflects the advantages of the ADD technique, when

compared with non-ADD. As can be observed in Figure 5.10, the highest deposition of NaF on the MS wall occurs when the input acoustic frequency is characterised by 328 Hz (the resonance frequency estimated experimentally). The deposition of NaF on the MS wall is high at the frequencies of 250 Hz, 300 Hz, and 356 Hz, and is low at the frequency of 450 Hz, compared with the non-ADD case. However, the effect of superposition of the acoustic wave at the frequencies of 100 Hz, 200 Hz, 403 Hz, 537 Hz, and 585 Hz (the resonance frequency obtained by the Helmholtz resonator equation) is negligible compared with the absence of a superimposed acoustic wave. When the statistical significance test was applied to the deposition results, it was found that ADD with an input frequency of 328 Hz and amplitude of 126 dB re 20µPa increased the concentration of NaF deposited on the MS wall 75-fold compared with non-acoustic nebulisation.

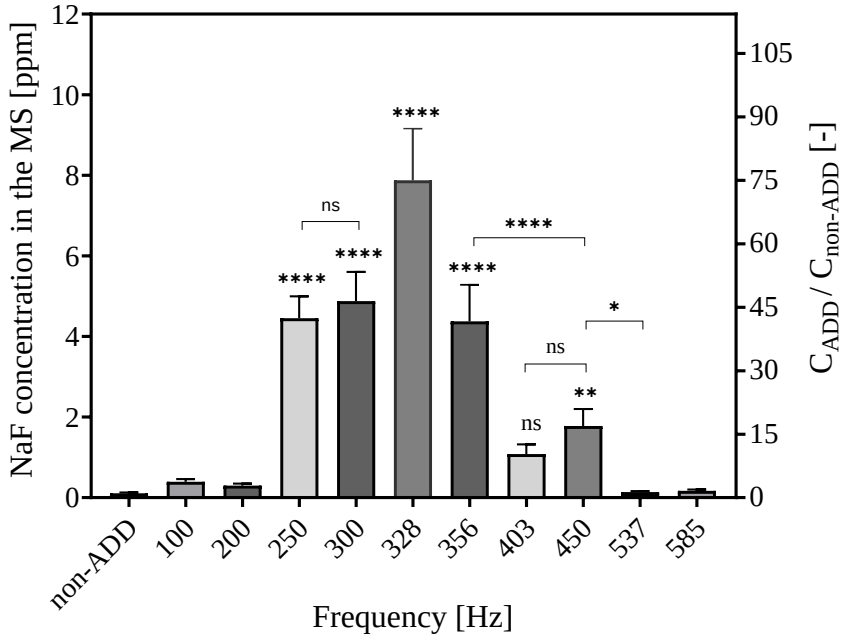

Figure 5.10. The effect of input frequency on aerosol deposition in the MS when the input acoustic amplitude is 126 dB, and the particle flowrate is Qp =0.267 mL/min. Control experiments correspond to the non-ADD case with particle flowrate of 0.267 mL/min. ns (not significant) $p > 0.4$, *$p < 0.03$, **$p = 0.0089$, and ****$p < 0.0001$ by one-way ANOVA with Tukey post hoc test. The right vertical axis represents the ration of the NaF concentration in the MS with acoustics (C_{ADD}) to the NaF concentration in the MS without acoustics ($C_{non-ADD}$)

It might be expected that the deposition of NaF on the MS wall is enhanced when the SPL in the MS increases, and does not change when the SPL in the MS is constant at different frequencies. However, by comparing Figure 5.8 and Figure 5.10, it was found that this expectation was not true for all input frequencies. It was only true for cases with input frequencies of 300 Hz and 356 Hz, with an amplitude of 126 dB re 20μPa, in which the SPL in the MS was obtained at 138.4 dB re 20μPa and 138.2 dB re 20μPa, respectively. These two SPL values are almost equal since the accuracy of the microphones was 0.2 dB re 20μPa. When these two frequencies, 300 Hz and 356 Hz, were superimposed on the nebulised aerosols entering the nostril, the concentration of NaF collected from the MS wall was obtained as 4.9 ppm and 4.4 ppm, which are statistically equal when compared with non-ADD (≈ 0.1 ppm).

For the cases with input frequencies of 250 Hz and 403 Hz, with an amplitude of 126 dB, the concentration of deposited NaF are significantly different (4.5 ppm and 1.1 ppm, respectively), although the corresponding SPL in the MS are almost equal for both cases (131.5 dB re 20μPa and 130.7 dB re 20μPa, respectively). The difference in the deposition of NaF is likely to stem from the difference in the particle displacement given by

$$\delta = \frac{v}{2\pi f} \tag{5-5}$$

where δ, v, and f are the particle displacement in an acoustic field, particle velocity, and the acoustic frequency, respectively. If two acoustic signals with different frequencies have the same SPL, then they should have the same particle velocity (at least this is the case for free field sound propagation). Therefore, according to Equation (5-5) the particle displacement at 250 Hz will be 1.6-fold as much as 403 Hz for the same particle velocity. Moreover, during the experimental tests for the cases with input frequencies of 200 Hz and 403 Hz, some particles were thrown into the tube that connects the speaker to the nasal tip. This observation

reveals that a portion of the nebulised particles were deposited on the nasal tip, which resulted in a decrease in the number of particles passing through the NC and ostium opening. This might imply that the nasal tip was at resonance at the frequencies of 200 Hz and its harmonics, which resulted in aerosol deposition on the inner wall of nasal tip. Hence, the deposition of the NaF under the effect of the acoustic frequencies of 200 Hz and 403 Hz decreased significantly compared with 450 Hz and 250 Hz (see Figure 5.10), even though their corresponding SPLs in the MS were identical (see Figure 5.8).

5.4.3 Effect of acoustic amplitude on ADD efficacy

The amplitude of the acoustic wave, superimposed on the nebulised particles, has a direct relationship with the amplitude of the sound pressure in the MS, which controls the amplitude of the oscillation of the air plug in the ostium. Figure 5.11 (a) shows the SPL at the nostril versus the SPL in the MS, at a fixed frequency of 328 Hz (resonance frequency). From this figure, it is obvious that the SPL in the MS increases with a linear trend when the input SPL increases. Figure 5.11 (b) presents the effect of input SPL on the concentration of NaF deposited in the MS. It is clear from this figure that increasing the input SPL enhances the deposition of NaF in the MS. It is clear from this Figure that increasing the input SPL enhances the deposition of NaF in the MS. Figure 5.11 (b) shows that increasing the input acoustic amplitude increases the aerosol deposition in the MS. However, increasing the amplitude from 120dB upwards did not have a significant effect on the aerosol deposition, which might imply that at certain acoustic amplitude a saturation point for the aerosol deposition is reached. This figure also reveals that at the input SPL of 113.4 dB re 20µPa and lower, the deposition of NaF in the MS is not significant when compared with non-ADD (input SPL=0).

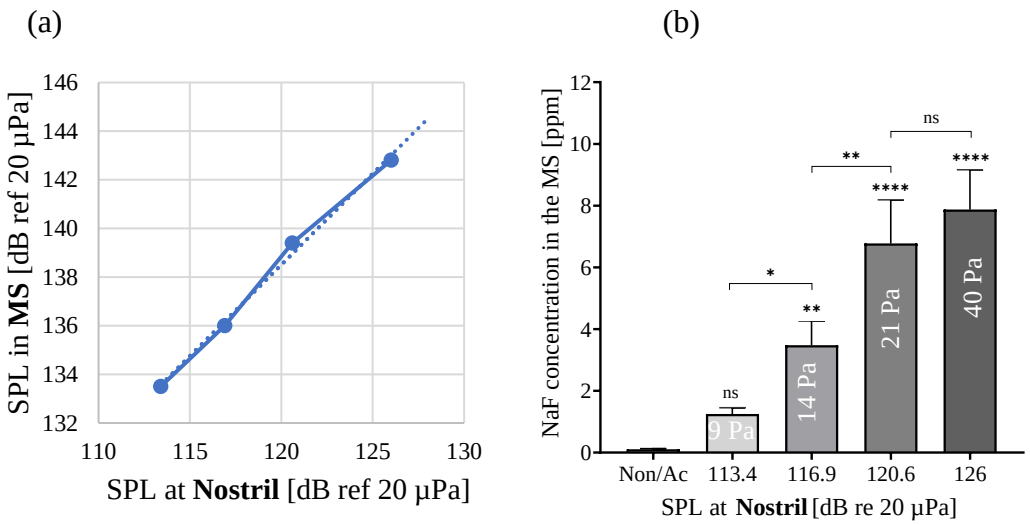

Figure 5.11. (a) SPL at the nostril versus SPL in the MS at a frequency of 328 Hz; (b) effect of the input acoustic amplitude on the aerosol deposition in MS when the input frequency is 328 Hz and particle flowrat is 0.267 mL/min. Control experiments correspond to the non-ADD case with particle flowrate of 0.267 mL/min. ns > 0.4, *p < 0.05, **p < 0.001, and ****p < 0.0001 by one-way ANOVA with Tukey *post hoc* test.

5.4.4 Effect of particle flowrate on ADD efficacy

In this study, a mesh nebuliser was used to nebulise the 2.5%wt NaF. Unlike the compressor nebuliser, the mesh nebuliser does not blow out the nebulised particles using compressed air but instead throws the nebulised particles through a vibrating meshed surface. The frequency of the vibration of the meshed surface indicates the nebulisation flowrate (Q_p), which increases with an increase in the vibration frequency. In this study, the nebulisation flowrate refers to the flowrate of nebulised particles entering the nostril, so we call it the particle flowrate. By using an Arduino board connected to the nebuliser controller, four different particle flowrates, including Q_p=0.059 mL/min, Q_p=0.098 mL/min, Q_p=0.138 mL/min, and Q_p=0.267 mL/min were used. To measure the flowrate of the particles entering the nostril, the nebuliser tank was filled with 100 mL of 2.5%wt NaF and the time required for nebulisation of it was recorded for different frequencies of the vibration of the meshed surface of the nebuliser. A large number of nebulised particles deposited in the nebuliser head, which were collected in a reservoir as the waste and then the volume of it was measure by a

pipette. In all experiments, the waste of the nebulisation of 100 mL of NaF was 96±0.2 mL demonstrating that almost 4 mL of nebulised particles could enter the nostril. Hence, the particle flowrate could be simply estimated by dividing the time required for the nebulisation of 100 mL of 2.5%wt NaF by 4 (mL).

Figure 5.12 shows the effect of the particle flowrate on the deposition of NaF on the MS wall under the effect of an acoustic frequency of 328 Hz and SPL of 126 dB re 20µPa, superimposed on the inlet nebulised particles. All the experiments were conducted for a condition that 4 mL of nebulised particles enter the nostril. The control case in Figure 5.12 corresponds to the NaF deposition with the highest nebulisation flowrate (Q_p=0.267). It is obvious from this figure that the concentration of NaF deposited on the MS wall with a particle flowrate of 0.059 mL/min is about twice that of the control case (a particle flowrate of 0.267 mL/min). However, the time required for 4 mL of the drug tracer to enter the nostril under the effect of a particle flowrate of 0.059 mL/min is 4.5 times longer than that of 0.267 mL/min (68 minutes versus 15 minutes). On the other hand, there is no significant difference between the deposition of NaF under the effect of particle flowrates of 0.098 mL/min and 0.138 mL/min when compared with the control case. Their corresponding nebulisation times are 2.7 times and 2 times longer than that of the control case, respectively. Therefore, a particle flowrate of 0.267 mL/min can be regarded as an optimised value for ADD to the MS. It should be noted that, the results are valid for the NC-MS model used in this study. A series of different realistic nose models should be analysed experimentally to generalise the particle flowrate.

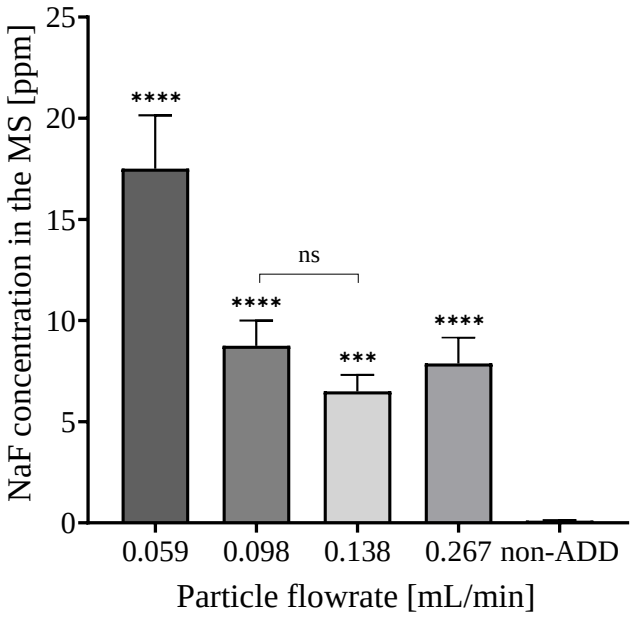

Figure 5.12. The effect of particle flowrate on aerosol deposition. Control experiments correspond to the particle flowrate of 0.267 mL/min. ns > 0.24, ****P < 0.0001 by one-way ANOVA with Tukey *post hoc* test. 4 mL of 2.5% wt NaF was nebulised for all cases.

5.4.5 Droplet formation around the ostium in the MS

In some of the experiments with acoustic inputs, some droplets were observed in the MS but around the edge of the interface of the of the ostium and MS (see Table 5.2). The droplets were observed when the P2 part of the MS was detached from P1, whilst undertaking the washing process. The size of droplets varied in different cases and no droplets were observed for most cases by naked eyes. Figure 5.13 shows the formation of droplets around the ostium edge for a case with an input acoustic frequency of 328 Hz (resonance frequency), input SPL of 126 dB, and particle flowrate of 0.267 mL/min, in which the concentration of the NaF deposited on the MS wall was increased 75-fold when compared with the non-acoustic case.

Table 5.2: Droplet size observed around the MS opening in different experimental cases

Input frequency (Hz)	Input amplitude (dB re 20µPa)	Particle flowrate (mL/min)	Droplet size observed around the MS opening
100	124	0.267	Not visible
200	126	0.267	Not visible
250	126	0.267	Small
300	126	0.267	Small
328	126	0.267	Large
356	126	0.267	Small
403	126	0.267	Not visible
450	126	0.267	Not visible
537	126	0.267	Not visible
585	125	0.267	Not visible
328	113.4	0.267	Not visible
328	116.9	0.267	Not visible
328	120.6	0.267	Average
328	126	0.138	Average
328	126	0.098	Large
328	126	0.059	Large

The reason for the formation of droplets is due to the high area concentration of particles on the trailing edge of the ostium. At the interface of the ostium and MS, the air velocity reduces (Pourmehran, Cazzolato, et al., 2020b) and hence the particles leave the flow and land on the surface. This means we need to make sure that the flow is fast enough to carry the particles into the MS. This also implies that the smaller the particles, the longer they remain in the flow and be carried into the MS. To understand more about the details of ADD to the MS, as well as the formation of droplets in the MS, a CFD model was developed. In the CFD modelling, particles were distributed randomly in the NC around the ostiomeatal complex (OMC), under the effect of an inlet frequency of 352 Hz (the resonance frequency of the NC-MS estimated by CFD) and an input SPL of 126 dB re 20µPa.

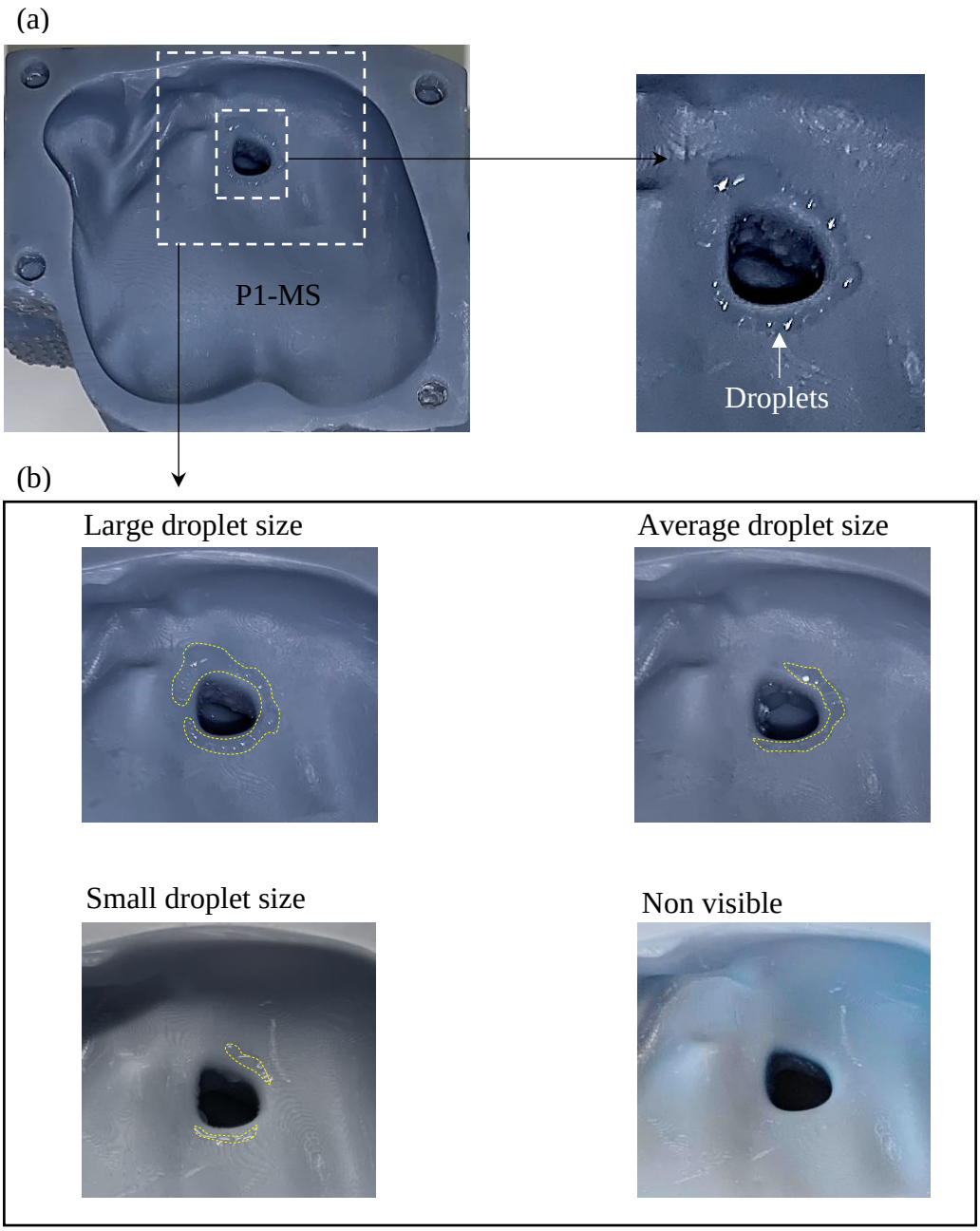

Figure 5.13. (a) A photo of droplets (large-size) deposited around the ostium edge in the MS after applying acoustic drug delivery before washing the MS wall for an input acoustic frequency of f=328 Hz, the amplitude of 126 dB re 20µPa, and particle flowrate of Q_p = 0.267 mL/min; (b) the snapshot of different droplet sizes around the MS opening.

Figure 5.14 (a) shows the distribution of the particles (black colour) before applying the acoustic wave. Figure 5.14 (b-c) represents the particle transportation and deposition pattern after 70 cycles. It is clear from these figures that many particles (approximately 9% of initially-distributed particles) were transported from the NC to the MS after 0.2 s. From Figure 5.14 (b-c) it can be seen that some particles were deposited on the MS wall around the ostium edge (red dots). It can be inferred that the deposition of liquid particles on the ostium wall (blue dots in Figure 5.14 (c)) and on the corner of ostium and MS (red dots Figure 5.14 (c)) increases over time and eventually generate droplets in these areas, which are similar to droplets that were observed in the experiments (Figure 5.13). According to the results of the CFD modelling, not only do some particles deposit (form the droplets) around the ostium edge, but many particles are also delivered into the MS, which will eventually deposit on its wall.

According to Figure 5.14, the reason for the absence of particles in the anterior and posterior regions of the NC, which is in contrast with Siu et al. (2019), is that the particles were initially released in the middle part of the NC with zero velocity to reduce the computational cost. The focus of CFD modelling in this study was to visualise the effect of the acoustic wave on particle movements in the NC-MS combination as well as to investigate the particle deposition in the ostium and MS; hence the mean flow rate was ignored (zero inlet airflow velocity was assumed) and particles were distributed in the NC with zero velocity and then the effect of the acoustic wave on them was investigated.

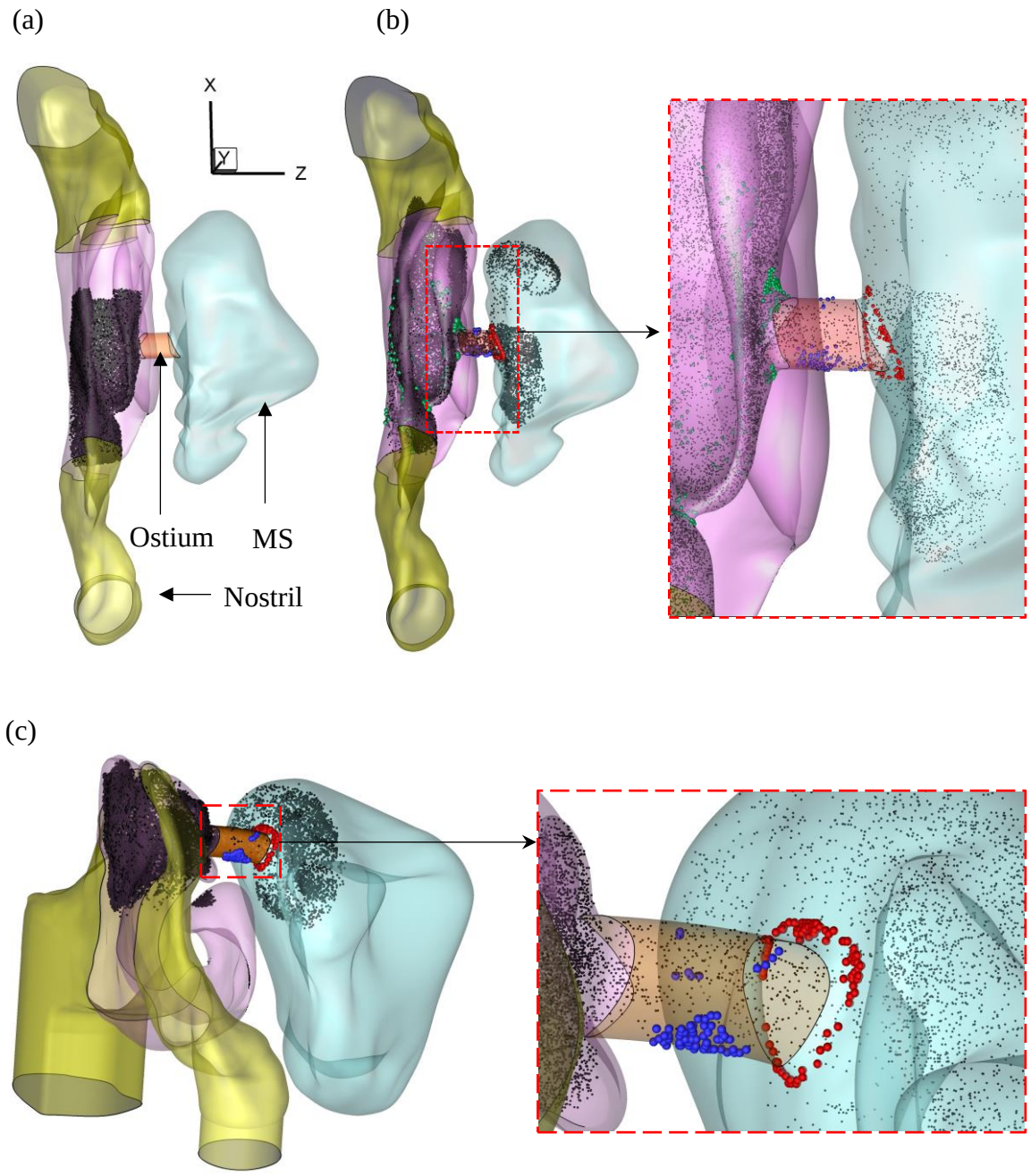

Figure 5.14. (a) CFD simulation of particles distribution in the NC before applying input acoustic wave; (b) Top view and (c) frontal view of particles deposition and transport pattern in NC-MS model after 70 cycles under the effect of input frequency of f = 352 Hz, amplitude of 126 dB re 20µPa. The black dots show the particles suspended in the computational domain, the red, blue, and green dots show the particles deposited on the MS, ostium, and NC walls, respectively. The blue and red dots are scaled up to better visualised the deposited particle in 70 cycles. The deposition of particles in the NC (green dot) has been ignored to display in Figure 5.14 (c) to focus on the deposition of particles in the ostium and MS.

5.5 Conclusion

The main goal of the current study was to determine the vital components that play an important role in ADD for the MS. The effect of different parameters, including the input acoustic frequency, amplitude, and particle flowrate on the deposition of aerosols in the MS, using the ADD technique, was investigated. The exact resonance frequency of the NC-MS model was measured experimentally. An experimental setup was used to conduct the drug delivery simulation and a CFD model was also developed to simulate particle tracking in a realistic model of NC-MS. 2.5 wt% NaF was used as a drug tracer, nebulised with a mesh nebuliser. One of the more significant findings to emerge from this study is that applying an acoustic wave to the nostril at the resonance frequency of the NC-MS combination can significantly increase the deposition of aerosols in the MS. For the NC-MS model used in this study, superimposing an input frequency of 328 Hz and amplitude of 126 dB re 20µPa on nebulised aerosol (12 µm) entering the nostril with a particle flowrate of 0.267 mL/min increased the concentration of NaF deposited in the MS 75-fold. The experimental data showed that increasing the input acoustic amplitude increased the aerosol deposition in the MS. However, increasing the amplitude from 120 dB re 20µPa upwards did not have a significant effect on the aerosol deposition, which might imply that at certain acoustic amplitude a saturation point for the aerosol deposition is reached. This study also found that although decreasing the flowrate of particles entering the nostril increases the aerosol deposition in the MS, the time-duration of nebulisation of a fixed volume of drug solution increases significantly, making treatment tedious. Hence, it is important to find an optimised particle flowrate, which was found to be 0.267 mL/min for this study.

The findings in this study are subject to the following limitations: the experiments used a one-sided nose-sinus model excluding the frontal, ethmoid, and sphenoid sinuses; neglected

mucociliary transport; and incorporated the use of NaF as the drug tracer. In CFD modelling, the humidity of the air was neglected, one-way coupling of fluid and particle was used, and randomly distributed particles were seeded in the NC after 20 acoustic cycles, which is a simplification of the particle flowrate during actual ADD. Nevertheless, neglecting the particle initial velocity could circumvent the complexity of the aerodynamics in the NC and focus on the influences from the acoustic waves.

5.6 Acknowledgements

The authors gratefully acknowledged the financial support of the Beacon of Enlightenment PhD Scholarship provided by the University of Adelaide. This paper and the research behind it would not have been possible without the exceptional support of the Acoustics Workshop and Phoenix High-Performance Computing (HPC) at the University of Adelaide, and the Ear, Nose, & Throat (ENT) group at Basil Hetzel Institute for Translational Research. We also thank Prof Jérémie Pourchez and Dr Lara Leclerc from Université de Lyon, France for their constructive comments in establishing the experimental setup for ADD. The authors are grateful to A/Prof Kiao Inthavong (RMIT University, Australia) and Dr Haribalan Kumar (Aukland University, New Zealand) for the provision of STL files related to the nose geometry.

5.7 References

Alagusundaram, M., Chengaiah, B., Gnanaprakash, K., Ramkanth, S., Chetty, C. M., & Dhachinamoorthi, D. (2010). Nasal drug delivery system-an overview. *American Journal of Pharmacological Sciences, 1*(4), 454-465.

Alster, M. (1972). Improved calculation of resonant frequencies of Helmholtz resonators. *Journal of Sound and Vibration, 24*(1), 63-85.

Basu, S., Holbrook, L. T., Kudlaty, K., Fasanmade, O., Wu, J., Burke, A., Langworthy, B. W., Farzal, Z., Mamdani, M., & Bennett, W. D. (2020). Numerical evaluation of spray position for improved nasal drug delivery. *Scientific Reports, 10*(1), 1-18.

Berger, W. E., Godfrey, J. W., & Slater, A. L. (2007). Intranasal corticosteroids: The development of a drug delivery device for fluticasone furoate as a potential step toward improved compliance. *Expert Opinion on Drug Delivery, 4*(6), 689-701.

Bhattacharyya, N. (2012). Functional limitations and workdays lost associated with chronic rhinosinusitis and allergic rhinitis. *American Journal of Rhinology & Allergy, 26*(2), 120-122.

Cankurtaran, M., Çelik, H., Coşkun, M., Hizal, E., & Cakmak, O. (2007). Acoustic rhinometry in healthy humans: Accuracy of area estimates and ability to quantify certain anatomic structures in the nasal cavity. *Annals of Otology, Rhinology & Laryngology, 116*(12), 906-916.

Cho, Y. S., Choi, S. H., Park, K. H., Park, H. J., Kim, J. W., Moon, I. J., Rhee, C. S., Kim, K. S., Sun, D. I., Lee, S. H., Koo, J. W., Koh, Y. W., Lee, K. H., Lee, S. W., Oh, K. W., Pyo, E. Y., Lee, A., Kim, Y. T., & Lee, C. H. (2010). Prevalence of otolaryngologic diseases in South Korea: Data from the Korea national health and nutrition examination survey 2008. *Clinical and Experimental Otorhinolaryngology, 3*(4), 183-193.

Dong, D., Cai, F., Huang, S., Zhu, X., Geng, J., Liu, J., Lv, L., Zhang, Y., & Zhao, Y. (2020). Assessment of three types of intranasal nebulization devices in three-dimensional printed models and volunteers: a pilot study. *International Forum of Allergy & Rhinology, 10*(12), 1300-1308.

Durand, M., Pourchez, J., Aubert, G., Le Guellec, S., Navarro, L., Forest, V., Rusch, P., & Cottier, M. (2011). Impact of acoustic airflow nebulization on intrasinus drug deposition of a human plastinated nasal cast: New insights into the mechanisms involved. *International Journal of Pharmaceutics, 421*(1), 63-71.

Farnoud, A., Baumann, I., Rashidi, M. M., Schmid, O., & Gutheil, E. (2020). Simulation of patient-specific bidirectional pulsating nasal aerosol dispersion and deposition with clockwise 45° and 90° nosepieces. *Computers in Biology and Medicine, 123*, 1-15.

Farzal, Z., Basu, S., Burke, A., Fasanmade, O. O., Lopez, E. M., Bennett, W. D., Ebert Jr, C. S., Zanation, A. M., Senior, B. A., & Kimbell, J. S. (2019). Comparative study of simulated nebulized and spray particle deposition in chronic rhinosinusitis patients. *International Forum of Allergy & Rhinology, 9*(7), 746-758.

Hilton, C., Wiedmann, T., Martin, M. S., Humphrey, B., Schleiffarth, R., & Rimell, F. (2008). Differential deposition of aerosols in the maxillary sinus of human cadavers by particle size. *American Journal of Rhinology & Allergy, 22*(4), 395-398.

Hosseini, S., & Golshahi, L. (2019). An in vitro evaluation of importance of airway anatomy in sub-regional nasal and paranasal drug delivery with nebulizers using three different anatomical nasal airway replicas of 2-, 5- and 50-Year old human subjects. *International Journal of Pharmaceutics, 563*, 426-436.

Howard, C. Q., Cazzolato, B. S., & Hansen, C. H. (2000). Exhaust stack silencer design using finite element analysis. *Noise Control Engineering Journal, 48*(4), 113-120.

Hyo, N., Takano, H., & Hyo, Y. (1989). Particle deposition efficiency of therapeutic aerosols in the human maxillary sinus. *Rhinology, 27*(1), 17-26.

Inthavong, K., Wen, J., Tian, Z., & Tu, J. (2008). Numerical study of fibre deposition in a human nasal cavity. *Journal of Aerosol Science, 39*(3), 253-265.

Kauf, H. (1968). Eindringvermögen von aerosolen in nebenräume. *Archiv für klinische und experimentelle Ohren-, Nasen-und Kehlkopfheilkunde, 190*(1), 95-108.

Kulkarni, V., & Shaw, C. (2012). Formulation and characterization of nasal sprays: An examination of nasal spray formulation parameters and excipients and their influence on key in vitro tests. *Inhalation*, 10-15.

Kumar, H., Jain, R., Douglas, R. G., & Tawhai, M. H. (2016). Airflow in the human nasal passage and sinuses of chronic rhinosinusitis subjects. *PloS One, 11*(6), 1-14.

Leclerc, L., El-Merhie, A., Navarro, L., Prévôt, N., Durand, M., & Pourchez, J. (2015). Impact of acoustic airflow on intrasinus drug deposition: New insights into the vibrating mode and the optimal acoustic frequency to enhance the delivery of nebulized antibiotic. *International Journal of Pharmaceutics, 494*(1), 227-234.

Leclerc, L., Pourchez, J., Aubert, G., Leguellec, S., Vecellio, L., Cottier, M., & Durand, M. (2014). Impact of airborne particle size, acoustic airflow and breathing pattern on delivery of nebulized antibiotic into the maxillary sinuses using a realistic human nasal replica. *Pharmaceutical Research, 31*(9), 2335-2343.

Liu, T., Cooper, T., Earnshaw, J., & Cervin, A. (2018). Disease burden and productivity cost of chronic rhinosinusitis patients referred to a tertiary centre in Australia. *Australian Journal of Otolaryngology, 1*(1), 1-9.

Lundberg, J., Farkas-Szallasi, T., Weitzberg, E., Rinder, J., Lidholm, J., Änggård, A., Hökfelt, T., Lundberg, J., & Alving, K. (1995). High nitric oxide production in human paranasal sinuses. *Nature Medicine, 1*(4), 370-373.

Maniscalco, M., Pelaia, G., & Sofia, M. (2013). Exhaled nasal nitric oxide during humming: Potential clinical tool in sinonasal disease? *Biomarkers in Medicine, 7*(2), 261-266.

Maniscalco, M., Sofia, M., Weitzberg, E., & Lundberg, J. (2006). Sounding airflow enhances aerosol delivery into the paranasal sinuses. *European Journal of Clinical Investigation, 36*(7), 509-513.

Maniscalco, M., Weitzberg, E., Sundberg, J., Sofia, M., & Lundberg, J. (2003). Assessment of nasal and sinus nitric oxide output using single-breath humming exhalations. *European Respiratory Journal, 22*(2), 323-329.

Moffa, A., Costantino, A., Rinaldi, V., Sabatino, L., Trecca, E. M. C., Baptista, P., Campisi, P., Cassano, M., & Casale, M. (2019). Nasal delivery devices: A comparative study on cadaver model. *BioMed Research International, 2019*, 1-6.

Moghadam, S. J., Navarro, L., Leclerc, L., Hodin, S., & Pourchez, J. (2018). Toward smart nebulization: Engineering acoustic airflow to penetrate maxillary sinuses in chronic rhinosinusitis. *International Journal of Pharmaceutics, 546*(1-2), 188-193.

Möller, W., Schuschnig, U., Bartenstein, P., Meyer, G., Häussinger, K., Schmid, O., & Becker, S. (2014). Drug delivery to paranasal sinuses using pulsating aerosols. *Journal of Aerosol Medicine and Pulmonary Drug Delivery, 27*(4), 255-263.

Möller, W., Schuschnig, U., Khadem Saba, G., Meyer, G., Junge-Hülsing, B., Keller, M., & Häussinger, K. (2010). Pulsating aerosols for drug delivery to the sinuses in healthy volunteers. *Otolaryngology—Head and Neck Surgery, 142*(3), 382-388.

Navarro, L., Leclerc, L., & Pourchez, J. (2019). Does acoustic overlay of music improve aerosol penetration into maxillary sinuses? *Online Journal of Otolaryngology and Rhinology, 1*(4), 1-3.

Pilan, R. R., Pinna, F. d. R., Bezerra, T. F., Mori, R. L., Padua, F. G., Bento, R. F., Perez-Novo, C., Bachert, C., & Voegels, R. L. (2012). Prevalence of chronic rhinosinusitis in Sao Paulo. *Rhinology, 50*(2), 129-138.

Pourmehran, O., Arjomandi, M., Cazzolato, B., Ghanadi, F., & Tian, Z. (2020). The impact of geometrical parameters on acoustically driven drug delivery to maxillary sinuses. *Biomechanics and Modeling in Mechanobiology, 19*(2), 557-575.

Pourmehran, O., Arjomandi, M., Cazzolato, B., & Tian, Z. (2020). *Effect of particle diameter and density on acoustic drug delivery to maxillary sinus – a sensitivity study*. Paper presented at the 22nd Australasian Fluid Mechanics Conference (AFMC2020), Brisbane, Australia.

Pourmehran, O., Cazzolato, B., Tian, Z., & Arjomandi, M. (2020a). *Acoustic behaviour of the human maxillary sinus: The importance of the middle meatus and the ostium on resonance frequency behaviour*. Paper presented at the 18th International Conference Of Numerical Analysis And Applied Mathematics, Rhodes, Greece.

Pourmehran, O., Cazzolato, B., Tian, Z., & Arjomandi, M. (2020b). Acoustically-driven drug delivery to maxillary sinuses: Aero-acoustic analysis. *European Journal of Pharmaceutical Sciences, 151*, 1-14.

Sharma, S. K., Jehan, M., & Kumar, A. (2014). Measurements of maxillary sinus volume and dimensions by computed tomography scan for gender determination. *Journal of the Anatomical Society of India, 63*(1), 36-42.

Siu, J., Johnston, J. J., Pontre, B., Inthavong, K., & Douglas, R. G. (2019). Magnetic resonance imaging evaluation of the distribution of spray and irrigation devices within the sinonasal cavities. *International forum of allergy & rhinology, 9*(9), 958-970.

Spiegel, M., Redel, T., Zhang, Y. J., Struffert, T., Hornegger, J., Grossman, R. G., Doerfler, A., & Karmonik, C. (2011). Tetrahedral vs. polyhedral mesh size evaluation on flow velocity and wall shear stress for cerebral hemodynamic simulation. *Computer Methods in Biomechanics Biomedical Engineering, 14*(01), 9-22.

Suman, J. D. (2013). Current understanding of nasal morphology and physiology as a drug delivery target. *Drug Delivery and Translational Research, 3*(1), 4-15.

Suman, J. D., Laube, B. L., & Dalby, R. (1999). Comparison of nasal deposition and clearance of aerosol generated by a nebulizer and an aqueous spray pump. *Pharmaceutical Research, 16*(10), 1648-1652.

Sutherland, W. (1893). LII. The viscosity of gases and molecular force. *The London, Edinburgh, and Dublin Philosophical Magazine and Journal of Science, 36*(223), 507-531.

Tarhan, E., Coskun, M., Cakmak, O., Celik, H., & Cankurtaran, M. (2005). Acoustic rhinometry in humans: Accuracy of nasal passage area estimates, and ability to quantify paranasal sinus volume and ostium size. *Journal of Applied Physiology, 99*(2), 616-623.

von Helmholtz, H., & Ellis, A. J. (1875). *On the Sensations of Tone as a Physiological Basis for the Theory of Music*. London: Longmans, Green and Company.

Weitzberg, E., & Lundberg, J. O. (2002). Humming greatly increases nasal nitric oxide. *American Journal of Respiratory and Critical Care Medicine, 166*(2), 144-145.

Wofford, M., Kimbell, J., Frank, D., Dhandha, V., McKinney, K., Fleischman, G., Ebert, C., Zanation, A., & Senior, B. (2015). A computational study of functional endoscopic sinus surgery and maxillary sinus drug delivery. *Rhinology, 53*(1), 41-48.

Xi, J., Si, X., Peters, S., Nevorski, D., Wen, T., & Lehman, M. (2017). Understanding the mechanisms underlying pulsating aerosol delivery to the maxillary sinus: In vitro tests and computational simulations. *International Journal of Pharmaceutics, 520*(1), 254-266.

Chapter 6

Effect of inlet flow parameters and nozzle diameter on drug delivery to the maxillary sinus

In the previous section, it was found that using a well-designed acoustic wave, the drug deposition in the MS increased by >45-fold. It was shown that the particle deposition in the MS changes with the mass flow rate of particles entering the nostril, even though an optimal acoustic wave was used. This implies that the efficiency of acoustic drug delivery (ADD) not only depends on the aero-acoustic parameters but also depends on the concentration of particles passing the middle meatus (MM). Hence, an increase in the concentration of particles passing the MM can increase the ADD efficiency. In this chapter, the effect of flow parameters such as turbulence and swirl and the diameter of the nozzle for injecting particles on the performance of drug delivery to the maxillary sinus (MS) is studied. The MS is

perpendicularly connected to the NC through the ostium, which is connected to the main route of the nasal cavity. The aerosolised drug delivery to the olfactory region is limited due to the convoluted anatomy of the NC in the MS, where the airflow rate and particle transport are negligible. Previous studies have shown that the ventilation in the MM is much lower than the ventilation of the main nasal passage and inferior meatus, which contributes to low drug delivery to the MS. Ari et al. (2015) showed experimentally that different inhalation mask shapes affect the performance of drug delivery to the lung. It can be implied that the inlet airflow parameters and distribution of the particles at the nostril can influence the deposition and transport of the particles in different regions of the NC. In this chapter, the effect of inlet flow parameters such as turbulent and swirling flows, as well as the effect of the nozzle diameter, on the airflow behaviour and drug (particle) delivery to the MS were investigated. CFD models using a hybrid RANS-LES model and laminar solver were developed and cross-validated with the available experimental data. A Eulerian-Lagrangian approach was used for the prediction of particle trajectories. The models developed and the discussions made in this chapter address the fourth objective of this work: *"to develop a computational fluid dynamics (CFD) model to investigate the effect of the inlet flow parameters and the nozzle diameter on the particle transport/deposition in a realistic NC-MS combination"*.

The chapter consists of a journal article submitted for publication.

Statement of Authorship

Title of Paper	Effect of the inlet flow profile and nozzle diameter on drug delivery to the maxillary sinus
Publication status	☐ Published ☐ Accepted for Publication ☒ Submitted for Publication ☐ Unpublished and Unsubmitted work written in manuscript style
Publication Details	Pourmehran, O., Arjomandi, M., Cazzolato, B., & Tian, Z. (2021). "Effect of the inlet flow profile and nozzle diameter on drug delivery to maxillary sinus". Submitted to Biomechanics and Modeling in Mechanobiology.

Principal Author

Name of Principal Author (Candidate)	Oveis Pourmehran
Contribution to the Paper	Ideas and Concepts • Conducted a comprehensive literature review to find the gaps in the knowledge • Developed the ideas and concepts based on the gaps Experiments and Modelling • Developed both the NC and NC-MS models in ANSYS® SpaceClaim • Developed a CFD model to simulate the fluid flow and particle tracking • Validated the simulated model with the available experimental data in the literature Interpretation of Results • Extracted raw data from simulation • Post-processed the simulation results using ANSYS® CFD-Post • Developed a MATLAB code to analyse the results and to extract the figures • Interpreted the simulation results Manuscript • Developed the first full draft of the manuscript • Applied comments given by co-authors • Submitted the manuscript • Acted as the corresponding author
Overall percentage (%)	80%
Certification:	This paper reports on original research I conducted during the period of my Higher Degree by Research candidature and is not subject to any obligations or contractual agreements with a third party that would constrain its inclusion in this thesis. I am the primary author of this paper.
Signature	Date: 28/04/2021

Co-Author Contributions

By signing the Statement of Authorship, each author certifies that:

XVI. the candidate's stated contribution to the publication is accurate (as detailed above);
XVII. permission is granted for the candidate in include the publication in the thesis; and
XVIII. the sum of all co-author contributions is equal to 100% less the candidate's stated contribution.

Name of Co-Author	Benjamin Cazzolato		
Contribution to the Paper	Supervised the research and contributed in academic discussion and manuscript review.		
Signature		Date	28/04/2021

Name of Co-Author	Zhao Tian		
Contribution to the Paper	Supervised the research and contributed in academic discussion and manuscript review.		
Signature		Date	29/04/2021

Name of Co-Author	Maziar Arjomandi		
Contribution to the Paper	Supervised the development of the research, participated in developing ideas, helped in interpretation of results and evaluation of the manuscript.		
Signature		Date	28/04/2021

Effect of the inlet flow profile and nozzle diameter on drug delivery to the maxillary sinus

Oveis Pourmehran[1], Benjamin Cazzolato[1], Zhao Tian[1], Maziar Arjomandi[1]

School of Mechanical Engineering, The University of Adelaide, Adelaide, SA, Australia

6.1 Abstract

In this paper, the effect of inlet flow turbulence and swirling, and nozzle diameter on flow features and particle transport/deposition patterns in a realistic combination of the nasal cavity (NC) and maxillary sinus (MS) were examined. A computational fluid dynamics (CFD) model was developed in ANSYS® Fluent using a hybrid Reynolds averaged Navier–Stokes–large eddy simulation (RANS-LES) algorithm. For the validation of the CFD model, the pressure distribution in the NC was compared against the available experimental data in the literature. An Eulerian-Lagrangian approach was employed for the prediction of the particle trajectories using a discrete phase model. Different inlet flow conditions were investigated, with turbulence intensities of 0.15 and 0.3, and swirl numbers of 0.6 and 0.9 applied to the inlet flow at a flow rate of 7 L/min. Monodispersed particles with a diameter of 5 µm were released into the nostril for various nozzle diameters. The results demonstrate that the nasal valve plays a key role in nasal resistance, which damps the turbulence and swirl intensities of the inlet flow. Moreover, it was found that the effect of turbulence at the inlet of the NC on drug delivery to the MS is negligible. It was also demonstrated that increasing the flow swirl at the inlet improves the total particle deposition due to the generation of the centrifugal force,

[1] Corresponding author. Present address: School of Mechanical Engineering, the University of Adelaide, North Terrace, Adelaide, SA, 5005, Australia.
Email address: oveis.pourmehran@adelaide.edu.au (Oveis Pourmehran)

which acts on the particles in the nostril and vestibule. The results also suggest that the drug delivery efficiency to the MS can be increased by using a swirling flow with a moderate swirl number of 0.6. It was found that decreasing the nozzle diameter can increase drug delivery to the proximity of the ostium in the middle meatus, which subsequently increases the drug delivery to the MS.

Keywords: Computational fluid dynamics; Drug delivery; Maxillary sinus; RANS-LES

Nomenclature

C_d	drag coefficient [-]	S_n	swirl number [-]
C_f	fullness coefficient ($D_\mathrm{N}/D_\mathrm{in}$) [-]	$\tau_{ij,\mathrm{LES}}$	Reynolds stress tensor
C_p	concentration of particles [%]	$\tau_{ij,\mathrm{RANS}}$	subgrid-scale stress tensor
d_ae	equivalent aerodynamic diameter [m]	τ_p	particle relaxation time [s]
d_p	particle diameter [m]	$\mathrm{TI_{in}}$	inlet turbulence intensity [-]
D_in	diameter of inlet (nostril) [m]	$\mathrm{TI_{max}}$	max turbulence intensity [-]
D_N	nozzle diameter [m]	U	mean fluid velocity [m/s]
Δ	maximum length of hexahedral cell [m]	u	fluid velocity [m/s]
η_i	local deposition efficiency per unit of area [%/m]	u_a	axial velocity[m/s]
η_T	total deposition efficiency [%]	u_p	particle velocity [m/s]
f	frequency of breathing [Hz]	u_t	tangential velocity [m/s]
F_C	centrifugal force [N]	W	Womersley number [-]
F_g	gravitational force [N]	y^+	normalised wall distance [-]
F_D	drag force [N]		
f_s	shielding function		
g	gravitational acceleration [m/s^2]	**Abbreviations**	
IP	inertial parameter [μm^2 cm^2/s]		
k	turbulent kinetic energy [m^2/s^2]	ADD	acoustic drug delivery
L	characteristic length [m]	CAD	computer-aided design
m_p	particle mass [kg]	CFD	computational fluid dynamics
μ	dynamic viscosity of fluid [kg/m.s]	LES	large eddy simulation
$N_\mathrm{p}^\mathrm{dep}$	number of deposited particles [-]	MM	middle meatus
N_p	number of particles [-]	MS	maxillary sinus
N_p^r	number of particles released at the inlet [-]	NC	nasal cavity
N_p^*	particles' retention criterion [s]	RANS	Reynolds-Averaged Navier–Stokes
ρ_f	density of fluid [kg/m^3]		
ρ_p	density of particle [kg/m^3]	SBES	Stress-Blended Eddy Simulation
ω	specific dissipation rate [1/s]		
R	radius of inlet (nostril) [m]	SST	Shear Stress Transport
S_m	source term	STL	stereolithography
St	Stokes number [-]	WALE	Wall-Adapting Local Eddy-Viscosity

6.2 Introduction

The nasal cavity is an important organ in the human body with critical functions such as humidification and heating the inhaled air, and filtration of the pollutants from the inhaled air (Drettner et al., 1977; Keck et al., 2000). The surface of the nasal cavity is mostly lined with mucosa. The mucosa is highly vascularized, such that the amount of the blood flow to the surface of the NC is higher than that of the blood flow to the brain (Mygind et al., 1978). The mucosal surface of the NC, which is highly vascularized, provides an attractive route for the treatment of sinus-related diseases, such as chronic rhinosinusitis (CRS)(Bell et al., 2012; Rissler et al., 2012; Wichers et al., 2006).

The human NC is constructed by convoluted airways. The maxillary sinus (MS) is located on the lateral side of the NC, where it is difficult to access (see Figure 6.1 (b)). The only opening that can accommodate the delivery of medication to the MS is the ostium which is located in the middle meatus (MM). The locations of MS contribute to some of the challenges for achieving efficient drug delivery to those regions because most inhaled medications either deposit in the anterior region or pass through the inferior meatus and the main passage of the NC, which are far from the target site, the middle meatus and the MS (see Figure 6.1 (b)) (Bahadur et al., 2012; Xi et al., 2015).

For drug delivery to the MS, two components should be considered: the delivery of the drug to the MM where the ostium is located, and the delivery of the drug particles from the MM to the MS (see Figure 6.1 (b)). The latter component has already been investigated in previous studies, which showed that nasal sprays and standard nebulisers (either jet or mesh nebulisers) are not able to efficiently deliver aerosolised medications into the MS (Berger et al., 2007; Hilton et al., 2008; Möller et al., 2014; Wofford et al., 2015). Instead, an active drug delivery technique is required to drive the drug particles from the MM to the MS. Studies

have shown that the most efficient, non-invasive, and low-cost method is acoustic drug delivery (ADD) (Navarro et al., 2019).

In ADD, an acoustic wave is superimposed to the aerosol entering the NC through the nostril. The acoustic wave leads to the oscillation of the airflow in the NC, which causes a pressure difference between the NC and MS resulting in enhanced flow exchange between the NC and MS (Leclerc et al., 2015). The momentum exchange between the MS and NC is the primary requirement for the delivery of the drug particles to the MS through the ostium. The performance of ADD for MS highly depends on the aero-acoustic parameters such as input frequency and sound pressure level (SPL) (Durand et al., 2011). Several studies have investigated the aerosol deposition in the MS using ADD with different input frequencies and SPL, which demonstrated a 3- to 4-fold increase in the aerosol deposition in the MS compared with conventional nebulisation without acoustics (Durand et al., 2011; Leclerc et al., 2014; Maniscalco et al., 2013; Maniscalco et al., 2006). In the recent study by the authors (which has not been published at the time of submission of the current paper), using a well-designed acoustic wave, the drug deposition in the MS was increased by 45-fold. They showed that the particle deposition in the MS changes with the mass flow rate of particles entering the nostril even though an optimal acoustic wave was applied to the nostril. This implies that the efficiency of ADD not only depends on the aero-acoustic parameters but also depends on the concentration of particles passing through the MM. Hence, an increase in the concentration of particles passing through the MM can increase the ADD efficiency proportionally, which is related to the former component of drug delivery to the MS, as mentioned above.

Various delivery methods and devices are available for nasal drug delivery such as nasal sprays and nebulisers. Nasal sprays produce particles with diameters in the range of 50μm-100μm, which almost entirely deposit in the anterior region of the nasal cavity. The

main reason for the deposition of most sprayed particles in the nasal valve is related to the high velocity and the large size of the particles (Inthavong, Ge, et al., 2011; Kimbell et al., 2007; Suman et al., 1999). Hence nasal sprays are not capable of delivering the particles to the meatuses and posterior regions of the NC, which limits their application for delivery of medication to the MS (Shi et al., 2006; Shi et al., 2007; Tong et al., 2016; Xi et al., 2008).

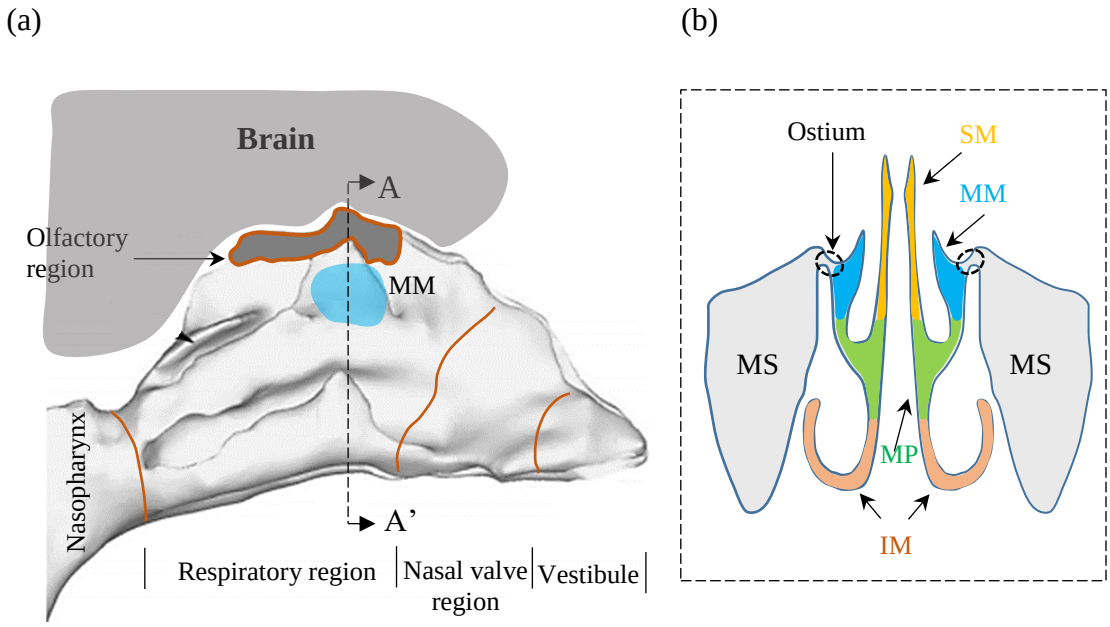

Figure 6.1: (a) An overview of the NC, representing the vestibule, nasal valve region, the respiratory region, olfactory region, middle meatus (MM) and nasopharynx, adapted from Shi et al. (2007) with permission from Elsevier; (b) section A-A' representing the maxillary sinuses (MS), ostium, and superior meatus (SM), middle meatus (MM), main passage, (MP), inferior meatus (IM), adapted from Xi et al. (2017) with permission from Elsevier.

Delivery of medications to the NC using nasal sprays was investigated in several previous studies. Tong et al. (2016) showed that the orientation of the nozzle of the spray plays an important role in NC drug delivery efficiency. Inthavong et al. (2006) used numerical modelling to study the effects of different factors on the deposition patterns of particles injected from nasal sprays. They reported that the geometry of the NC and the features of the nasal spray mainly influence the deposition pattern of the particles. They evaluated the influence of the insertion angle, defined as the angle of the nasal spray with the horizontal

plane, on the deposition efficiency (DE) of the particles. The results depicted that, for particles with diameters of 10 μm to 15 μm, the highest deposition occurred with an insertion angle of 100^{o}; however, the lowest DE occurred with an insertion angle of 70^{o} (Inthavong et al., 2006).

The application of nebulisers, however, has been shown to be an efficient method to overcome the challenges related to the limitation of delivery of particles to the posterior region of the NC and the meatuses (Laube, 2007). Nebulisers produce fine particles in a range of 1-30μm, which enables particle to reach the posterior region (Hilton et al., 2008; Wofford et al., 2015). However, the particle transport in the middle meatus is considerably lower than that of the inferior meatus when a nebuliser is used (Zhao et al., 2004). On the other hand, different studies showed that particle deposition in respiratory airways is impacted by the inhaled flow patterns. Lin et al. (2012) examined the effect of nebuliser types and aerosol face masks on the efficiency of drug delivery to the NC. They reported that the design of an aerosol mask affects the dose of the inhaled aerosolised drug for different types of nebulisers. Using jet and mesh nebulisers, Ari et al. (2015) investigated the impact of airflow rates on particle deposition in the lung. They demonstrated that the drug delivery efficiency using a mesh nebuliser was higher than that using a jet nebuliser. They also found that the efficiency of drug delivery to the lung through the valve mask is higher than that of a standard open aerosol mask. Hence, it can be inferred that the inlet airflow features, and aerosol distribution applied at the nostril, can have an impact on aerosol deposition and transport in different regions of the NC, which is the main motivation of this study.

In this study, the effects of various inlet flow parameters and the diameter of the nozzle (which injects particles) on particle transport and deposition patterns in different parts of the NC are investigated. To do so, various turbulent intensities and swirl numbers were applied at the nostril and their impact on the flow structure in the NC-MS combination, as well as on

the transport/deposition patterns of the particle in the NC-MS combination, was quantified. The effect of the nozzle diameter (the diameter of injection of particles at the inlet) on the aerosol deposition and transport pattern was also studied using computational fluid dynamics (CFD).

6.3 Methods

6.3.1 Nasal cavity geometry

Two different nose geometries were used in this study. The first geometry (G1), which excludes the paranasal sinuses, was used for validation of the CFD model. It was necessary to use G1 since the experimental data for the validation of the CFD model were available for G1 in a recently published article by Van Strien et al. (2021). The second geometry (G2), which includes the MS, was used for conducting the parametric studies. The STL (stereolithography) file of G1 was adapted from Van Strien et al. (2021). The STL file was imported into ANSYS® SpaceClaim to convert the point-cloud to a CAD (computer-aided design) format using the Shrink Wrap technique for improving the quality of the model by smoothening the surfaces. An external facial feature (Figure 6.2(a)) in the shape of a hemisphere (Figure 6.2(b)), was also added to the computational domain to ensure simulation of a realistic condition for inhalation through the nostril (Van Strien et al., 2021). After ensuring the validity of the CFD model through comparison of the G1 inputs with the experimental data, the geometry G2 was used to conduct parametric studies to investigate the effect of the inlet flow parameters and nozzle diameter on the flow features and particle transport in the NC. To measure the particle deposition in different parts of the NC-MS combination, G2 was segmented into 10 zones (see Figure 6.2 (c-d)).

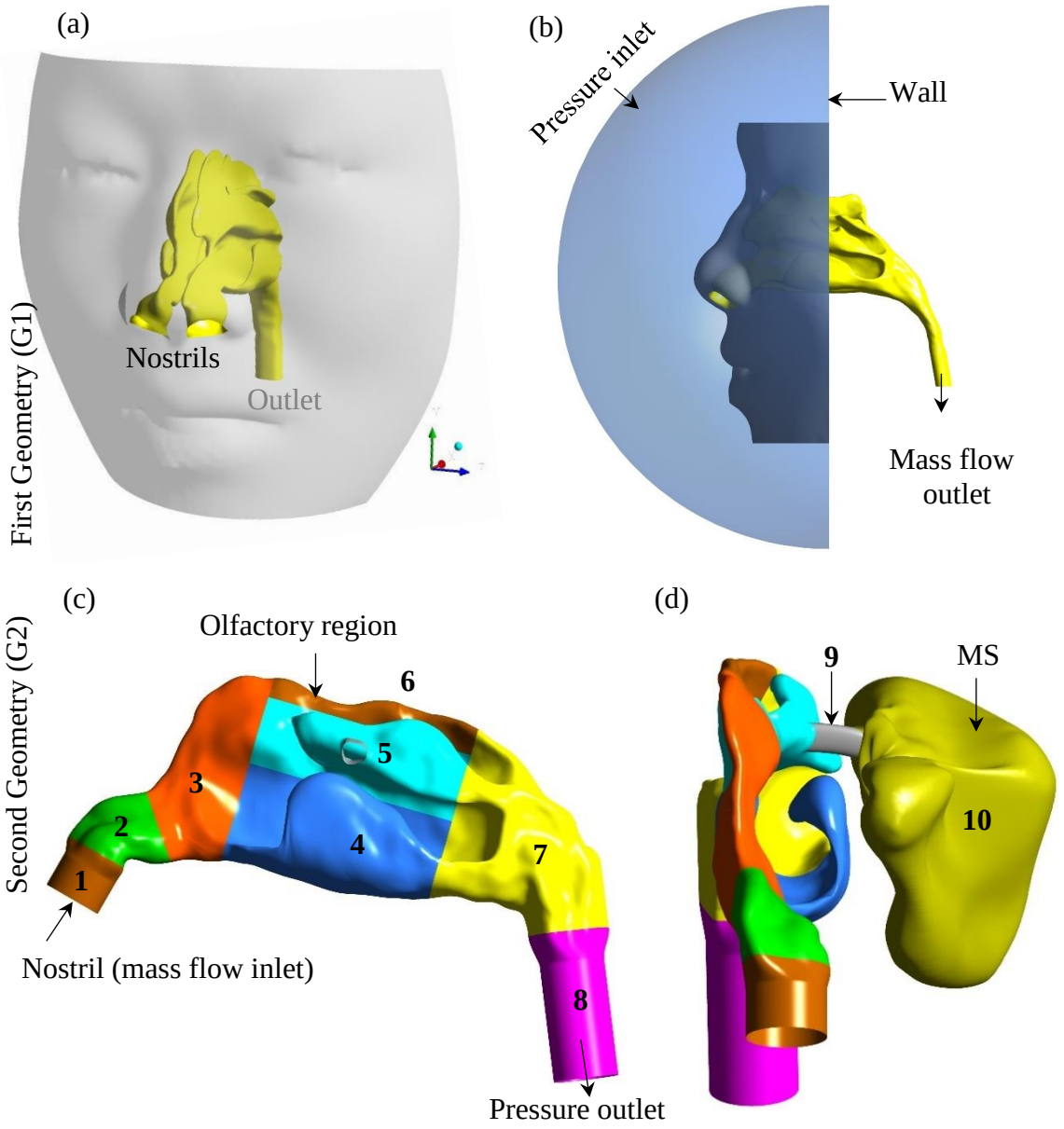

Figure 6.2: (a) Sagittal view, and (b) isometric view, of the first geometry (G1) (the STL model of the geometry was adapted from Van Strien et al. (2021) with permission; (c) sagittal and (d) frontal view of the second geometry (G2). The NC part of G2 was extracted from a CAD model of a realistic human respiratory system adapted from Tian et al. (2008), and the MS part of G2 was generated based on a realistic nose geometry adapted from (Kumar et al., 2016). G2 was segmented into 10 zones. Each zone is defined by a colour and a number between 1-10.

6.3.2 Problem definition and case studies

The main aim of this study is to investigate the effect of inlet flow parameters such as its turbulence intensity and swirl number, and the nozzle diameter in the nostril on the drug

delivery to the MM-Ostium region. MM-Ostium refers to a region in the MM where the ostium connects the MM to the MS as illustrated in Figure 6.3. The reason for considering MM-Ostium region is that when an external acoustic field is applied to the nostril in ADD technique, not only does the air plug inside the ostium fluctuates, but also a portion of the air plug in the middle meatus (i.e., MM-Ostium region). In ADD, the oscillating air plug in the ostium captures the particles from the MM-Ostium region and then deliver them to the MS after several cycles (Pourmehran, Arjomandi, Cazzolato, Ghanadi, et al., 2020). Hence, an increase in the number and residence time of particles in the MM-Ostium region can increase the number of particles delivered to the MS and subsequently increase the ADD performance. It should be noted that in this study, the term particle refers to the droplet generated by a nebuliser.

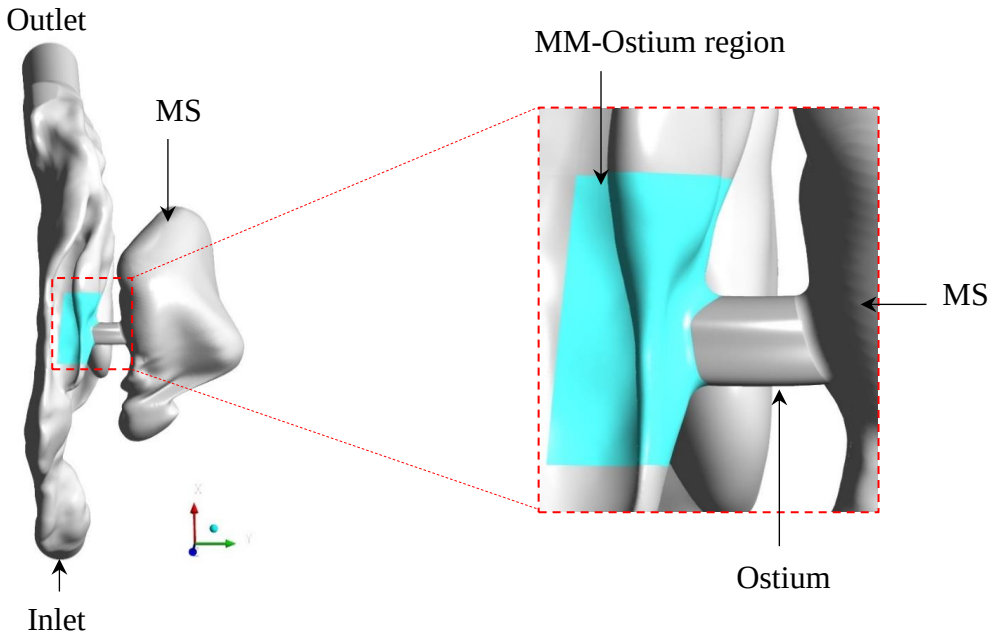

Figure 6.3: The top view of G2 and the MM-Ostium region marked in cyan

To take into account both the instantaneous number of particles and their residence time in the MM-Ostium region, the particles' retention criterion was defined by:

$$N_{\mathrm{p}}^{*} = \int N_{\mathrm{p}} dt \tag{6-1}$$

where N_{p} is the instantaneous number of particles in the target region and t is the time. N_{p}^{*} is the particles' retention criterion calculated by the integration of the number of particles in a target region with respect to the particle time in a specific time frame. The time commences when the particles are released in the inlet.

Two different types of inlet flow were considered in this study: turbulent (2 cases) and laminar (3 cases). For the turbulent cases, two different turbulence intensities of $\mathrm{TI_{in}}$=0.15 and $\mathrm{TI_{in}}$=0.3 were considered. Turbulence intensity is defined as the ratio of the standard deviation of fluctuating flow velocity to the mean flow velocity (Kimura, 2016). The turbulent cases were produced by applying artificial turbulence to the laminar inlet flow with Reynolds number of ($Re = 1023$). The laminar flow cases include a non-swirling inlet flow (S_{n}=0) and two swirling inlet flows (S_{n}=0.6 and S_{n}=0.9). The term S_{n} refers to the swirl number, which quantifies the swirl intensity of the swirling flow defined as the ratio of the tangential momentum flux to the axial momentum flux at the inlet boundary (Hreiz et al., 2011) given by:

$$S_{\mathrm{n}} = \frac{\int r u_{\mathrm{t}} u_a dA}{R \int r u_a^2 dA} \tag{6-2}$$

where r, u_{t}, u_a, and R are the radial coordinate, tangential velocity, axial velocity, and the radius of the inlet boundary, respectively.

The effect of how particles are released in the inlet on the drug delivery to the MM-Ostium region was also studied by considering 5 different fullness coefficients (C_{f}), defined as the ratio of nozzle diameter to the inlet (nostril) diameter given by

$$C_{\mathrm{f}} = \frac{D_{\mathrm{N}}}{D_{\mathrm{in}}} \tag{6-3}$$

where D_{N} is the diameter of the nozzle for injecting the particles at the inlet and D_{in} is the diameter of the inlet boundary. Figure 6.4 illustrates the particle distribution for different C_{f} in the inlet boundary. The particles were injected into the inlet with random position distribution.

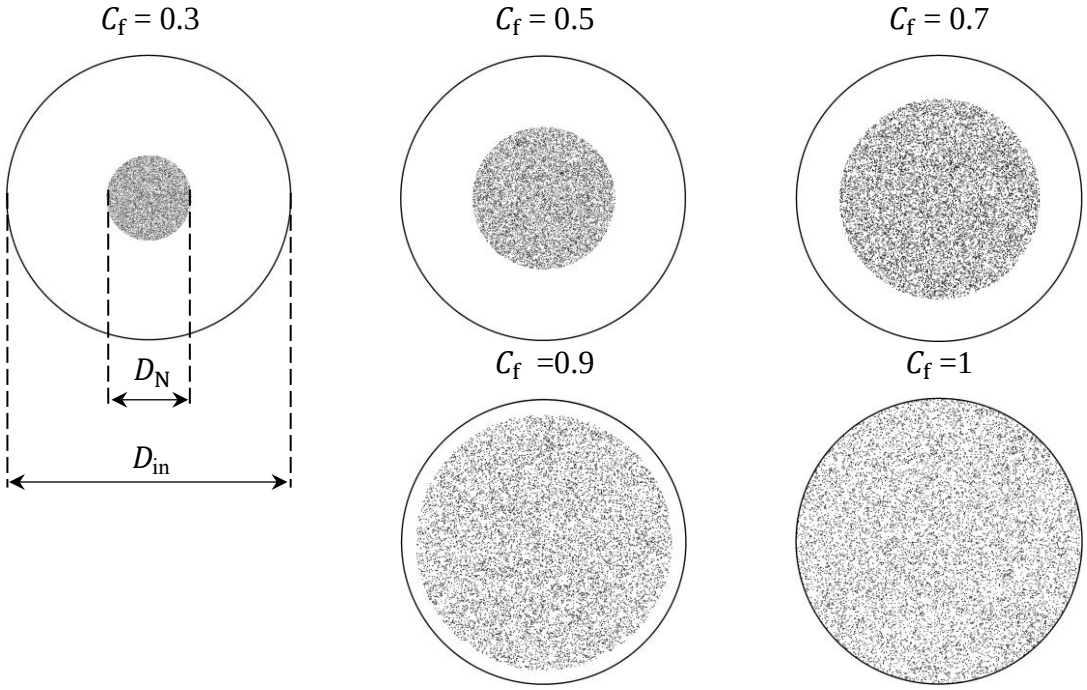

Figure 6.4: A snapshot of monodispersed particle distribution in the inlet for different fullness coefficient (C_{f}). D_{N}: nozzle diameter (the diameter of injection of the particles), D_{in}: inlet diameter

6.3.3 Governing equations and boundary conditions

6.3.3.1 Fluid phase modelling

ANSYS® Fluent 2020 R1 was used to simulate the airflow and particle transport/deposition patterns in a realistic NC-MS model. The working fluid was considered as air, which was

assumed to be Newtonian and incompressible. To investigate the particle deposition and transport pattern, as well as to isolate the outcomes independently from the oscillation variables, a constant inhalation airflow was used instead of a periodic inhalation flow. To ensure the validity of the use of a constant inhalation flow, the impact of cyclic inhalation on the airflow field was evaluated through the Womersley number (W) (Inthavong et al., 2008). W is a non-dimensional number indicating the effect of oscillatory flow on the flow behaviour in an internal flow, such as airflow in the NC and blood flow in the blood vessels (Loudon et al., 1998). The fluid flow behaves similarly to a quasi-steady state when $W < 1$, but the flow behaviour is far from a quasi-steady state when $W > 1$ [46]. The W is defined as:

$$W = \frac{L}{2}\sqrt{\left(\frac{\rho_f f}{\mu}\right)} \tag{6-4}$$

where L is the characteristic length, which is identified as the distance between the two walls of the NC (Inthavong et al., 2008), ρ_f is the fluid density, μ is the dynamic viscosity of the fluid, and f is the frequency of breathing, which is approximately 15 cycles per minute.

In this study, the characteristic length varies between 1 mm to 10 mm for the NC, which results in $0.065 < W < 0.65$. Hence, the assumption of quasi-steady state used in this study is valid for airflow modelling. It is worth mentioning that the quasi-steady state does not refer to a constant flow field over time but it implies that the instantaneous flow rate is characterised by the instantaneous pressure gradient (Loudon et al., 1998). Regarding the effect of periodic flow on particle deposition, (Häußermann et al., 2002) demonstrated that the impact of periodic inhalation-exhalation flow on the deposition of particles in the NC is similar to the particle deposition pattern under a constant inhalation when the flow rate is Q=10 L/min or less (Tian et al., 2008). Given that the flow rate used in the current study is

Q=7 L/min, the assumption of a constant inhalation flow rate is valid for the particle deposition in the NC-MS model (G2).

For cases with turbulent inlet flow, Stress-Blended Eddy Simulation (SBES), which is a Hybrid RANS-LES (RANS: Reynolds-averaged Navier-Stokes, LES: Large Eddy Simulation) turbulence model was used. In the SBES model, LES is used for resolving the flow field beyond the near-wall region, while the RANS model is applied to the near-wall region, which overcomes the need for very small grids in the near-wall region in LES turbulent modelling (Van Strien et al., 2021). The equation of mass conservation in an incompressible flow is given by:

$$\frac{\partial \bar{u}_i}{\partial x_i} = S_{\mathrm{m}} \,, \tag{6-5}$$

where $\bar{u}$ is the flow velocity and S_{m} is a source term originating from the mass added to or subtracted from the fluid due to different phenomena, such as vaporization of the droplets. In this study, S_{m} is zero. The equation describing the conservation for momentum in an incompressible flow is given by:

$$\frac{\partial}{\partial t}\left(\rho_f \bar{u}_i\right) + \frac{\partial}{\partial x_j}\left(\rho_f \bar{u}_i \bar{u}_j\right) = \frac{\partial}{\partial x_j}\left(\rho_f \sigma_{ij}\right) - \frac{\partial \bar{p}}{\partial x_i} + \frac{\partial \tau_{ij}}{\partial x_j} \,, \tag{6-6}$$

where ρ_f, $\bar{u}_i$, p, σ_{ij}, and τ_{ij} are the density of the fluid, vector of the flow velocity, pressure field, stress tensor due to molecular viscosity, and the turbulence stress tensor $\tau_{ij} = \rho_f\left(\overline{u_i u_j} - \bar{u}_i \bar{u}_j\right)$, respectively (Fluent Theory Guide, 2020). The overbar on the velocity and pressure scalars ($\bar{u}_i$ and $\bar{p}$) indicates the Reynolds-averaging and spatial-temporal filtering operations in the RANS and LES models, respectively (Van Strien et al., 2021). In the SBES turbulence model, a blending function is used to blend the turbulence stress tensor, τ_{ij},

between the Reynolds and subgrid-scale stress tensors for the RANS and LES formulations, respectively (Fluent Theory Guide, 2020). The blending function is given by:

$$\tau_{ij} = f_s \tau_{ij,\mathrm{RANS}} + (1 - f_s)\tau_{ij,\mathrm{LES}} \tag{6-7}$$

where f_s is the shielding function with values between zero and unity, $\tau_{ij,\mathrm{RANS}}$ is the Reynolds stress tensor, and $\tau_{ij,\mathrm{LES}}$ is the subgrid-scale stress tensor.

To implement the SBES turbulent model in ANSYS® Fluent, the *k-ω* SST (Shear Stress Transport) model was utilised because the SBES model is embedded in the *k-ω* SST model. Also, a WALE (Wall-Adapting local Eddy-Viscosity) model was used for the subgrid-scale component. A pressure-velocity coupled solver was used for solving the governing equations. A bounded second-order implicit scheme was used for the transient formulation, the second-order scheme was employed for the discretization of the pressure, and the second-order bounded schemes were used for the convective terms. The least-squares cell-based method was utilised for calculating the gradients.

6.3.4 Particle phase modelling

To predict the transport of the particle phase in a fluid, two different approaches can be applied: Euler-Euler and Euler-Lagrange approaches. In the Euler-Lagrange approach, the fluid phase is modelled as a continuum phase, while the particle phase is treated as a discretised phase, which is tracked in the Lagrangian reference frame (Adamczyk et al., 2014). The Euler-Lagrange approach was used in this study since the physical description and the details of the particle transport and deposition patterns can be determined. To predict the particle transport and deposition patterns in the NC-MS combination a discrete phase model (DPM) was used, where the trajectory of the particle phase can be predicted by integrating the force balance on the particle. The force balance equation on a particle is defined by:

$$m_{\mathrm{p}} \frac{d\vec{u}_{\mathrm{p}}}{dt} = \vec{F}_{\mathrm{g}} + \vec{F}_{\mathrm{D}} \,, \tag{6-8}$$

where m_{p}, u_{p}, $\vec{F}_{\mathrm{g}}$, and $\vec{F}_{\mathrm{D}}$ are the particle mass, velocity, gravitational force, and drag force, respectively. Other forces such as the virtual mass, pressure-gradient, Basset, Faxen, Saffman's lift, and Brownian forces were neglected. The virtual mass, Basset, and pressure-gradient forces are considered when the density of the fluid is much greater than the density of the particles (Bassett, 1888; Kolev, 2011; Maul, 2019). In this study, the density of the fluid is much smaller than that of particles ($\rho_f = 1.225$ kg/m^3 vs. ρ_{p}=1000 kg/m^3), hence the virtual mass, Basset, and pressure-gradient forces can be neglected. The Faxen force comes into play when the size of the domains of the particle and fluid are in the same order; while in this study, the size of the particle domain is four orders of magnitude smaller than the size of the fluid domain (Chen et al., 2000). Saffman's lift and Brownian forces are considered when the particles are submicron in size (Ounis et al., 1991; Schwarzkopf et al., 2011), while the monodispersed particles with a diameter of 5 μm used in this study.

The gravitational, $\vec{F}_{\mathrm{g}}$, and drag, $\vec{F}_{\mathrm{D}}$, forces are given by:

$$\vec{F}_{\mathrm{g}} = m_{\mathrm{p}} \frac{\vec{g}\left(\rho_{\mathrm{p}} - \rho_f\right)}{\rho_{\mathrm{p}}} \tag{6-9}$$

$$\vec{F}_{\mathrm{D}} = m_{\mathrm{p}} \frac{\left(\vec{u} - \vec{u}_{\mathrm{p}}\right)}{\tau_{\mathrm{r}}} \tag{6-10}$$

where $\vec{g}$, ρ_{p}, $\vec{u}_{\mathrm{p}}$ and $\vec{u}$ are the gravitational acceleration, density of the particle, velocity of the particle, and the velocity of the fluid, respectively. τ_{p} is the particle relaxation time defined by:

$$\tau_{\mathrm{p}} = \frac{\rho_{\mathrm{p}} d_{\mathrm{p}}^2}{18\mu} \frac{24}{C_{\mathrm{d}} \mathrm{Re}_{\mathrm{p}}} \tag{6-11}$$

where d_{p}, μ, C_{d}, and Re_{p} are the diameter of the particle, the dynamic viscosity of the fluid, the drag coefficient, and the particle Reynolds number, respectively. In this study, it is assumed that the particles are spherical. For a sphere particle with a smooth surface, the drag coefficient can be estimated by Morsi et al. (1972):

$$C_{\mathrm{d}} = a_1 + \frac{a_2}{\mathrm{Re}_{\mathrm{p}}} + \frac{a_3}{\mathrm{Re}_{\mathrm{p}}} \tag{6-12}$$

where the terms a_1, a_2, and a_3 are the constant numbers that were estimated empirically over different ranges of Re_{p} by Morsi et al. (1972).

6.3.5 Boundary conditions

For modelling the airflow in geometry G1, a pressure inlet boundary condition was applied to the inlet (the hemisphere dome, see, Figure 6.2 (b)) with zero gauge-pressure (atmospheric pressure), and a mass flow outlet boundary condition was implemented to the outlet. A no-slip condition was applied to the wall. No particle tracking model was used in G1. For modelling the airflow in geometry G2, the mass flow inlet boundary condition was applied to the inlet and pressure outlet condition that was implemented on the outlet boundary with atmospheric pressure. A uniform velocity profile was used at the inlet due to the negligible effect of the fully developed inlet flow on the particle deposition in the NC (Tian et al., 2008). A no-slip boundary condition was applied to the walls. Regarding the particle phase, the inlet and outlet boundaries were set as “Escape”, and a “Trap” boundary condition was applied to the wall to stimulate the deposition of the particles. 12000 inert particles were released with zero initial velocity in the nostril through the inlet boundary.

6.3.6 Validation of CFD model and mesh independence test

For validation purpose, the pressure at different locations in the NC using the geometry G1 was used. The pressure values were recorded at different points along the NC wall. The location of the points was selected based on the available experimental data and CFD results reported in a recent study by Van Strien et al. (2021). Three different flow rates of Q=10 L/min, Q=15 L/min, and Q=30 L/min were applied to the outlet as a mass flow outlet boundary condition. A laminar solver was used for Q=10 L/min ($Re_{\text{in,right}}$ =823, $Re_{\text{in,left}}$=359) and Q=15 L/min ($Re_{\text{in,right}}$ =1234, $Re_{\text{in,left}}$=585), and the SBES turbulent model was employed for Q=30 L/min ($Re_{\text{in,right}}$ =2529, $Re_{\text{in,left}}$=1271).

Initially, a mesh independence was conducted by comparing the velocity magnitude along a line in a cross-section plane in the nasopharynx region (see Line 1, Figure 6.5 (b)). Using the mosaic technology (introduced by ANSYS® (2020)), a poly-hexcore meshing model was used for generating the meshes. The polyhedral mesh was generated on the surface of the NC while the interior was filled with hexahedron meshes. Polyhedral meshes were used to connect the interior hexahedrons to the inflation with eight prism layers.

For Q=30 L/min the flow is turbulent in the NC, hence, to resolve the large eddies using the LES component of the hybrid RANS-LES turbulence model (the SBES model) a sufficiently fine mesh is required. To meet this requirement, 8 prism layers were generated in the near-wall region. The size of the prism layer connected to the wall was 10% of the interior hexahedral cell length with a growth rate of 1.2. The normalised wall distance (y^+) was less than unity on the NC wall, which satisfies the requirement of the k-ω SST model used in this study. Four different mesh densities of 1.1 million (Mesh 1), 3.3 million (Mesh 2), 5.1 million (Mesh 3), and 8.7 million (Mesh 4) cells at a maximum hexahedral cell length of Δ=0.5 mm, Δ=0.3 mm, Δ=0.25 mm, and Δ=0.2 mm, respectively, were generated to evaluate the mesh

size. Figure 6.5 (d) shows the comparison of the velocity magnitude on Line 1 obtained from different mesh configurations. The meshes with Δ=0.2 mm and Δ=0.25 mm (Mesh 1 and Mesh 2) yield almost the same distribution of the velocity magnitude. Therefore, the mesh model with Δ=0.25 mm was used in this study.

The size of time-step to resolve the eddies containing energy; hence, the Kolmogorov time scale was considered to calculate the time step size using the following equation (Landahl et al., 1989):

$$\tau_n = \sqrt{\frac{\mu}{\rho_f \varepsilon}} \tag{6-13}$$

where τ_n, μ, ρ_f, and ε are the Kolmogorov time scale, fluid viscosity, fluid density, and turbulence kinetic energy per unit mass, respectively. The minimum value for Kolmogorov time scale was $\tau_n = 6 \times 10^{-3}$ s. However, a smaller time step size ($\tau_n = 5 \times 10^{-5}$) was used for the simulations, which can guaranty that the spatial resolution was more than sufficient to resolve the turbulent flow field. The same time step size was also used for the particle tracking simulation.

To ensure that the proposed modelling technique is suitable, the flow behaviour in the G1 was modelled for different mass flow outlet rates: *Q*=10 L/min, *Q*=15 L/min, and *Q*=30 L/min. The pressure values at 16 different locations on the NC wall were determined and compared with the published data. Figure 6.6 (a) illustrates the location of the points on the NC wall including three points on the floor and four points on the lateral walls of both left and right sides of the NC as well as two points in the posterior region of the nasopharynx. Figure 6.6 (b) represents the pressure values at the pre-defined points at different flow rates. It can be observed from this Figure that, the agreement between the results obtained in this

study and the results reported in the literature is reasonably good for both the laminar (Q=10 L/min, Q=15 L/min) and turbulent (Q=30 L/min) flows.

The validation of the particle tracking model (DPM) was examined by comparing the total particle deposition efficiency (η_{T}) in the NC predicted in this study with that reported in the literature. η_{T} is defined by:

$$\eta_{\mathrm{T}} = \frac{N_{\mathrm{p}}^{\mathrm{dep}}}{N_{\mathrm{p}}^{\mathrm{r}}} \times 100\% \,, \tag{6-14}$$

where $N_{\mathrm{p}}^{\mathrm{dep}}$ is the number of particles deposited on the wall and $N_{\mathrm{p}}^{\mathrm{r}}$ is the number of particles released in the nostril initially. Generally, the particle transport/deposition behaviour in a fluid flow is quantified by the dimensionless Stokes number (St), which is the ratio of the particles' momentum response time to the flow-field time scale (Krstić, 2006) given by:

$$St = \frac{\rho_{\mathrm{p}} d_{\mathrm{p}}^2 U}{18 \mu L} \tag{6-15}$$

where U and L are the characteristic velocity and characteristic length, normally taken as the mean flow velocity and the hydraulic diameter the inlet (or a planar surface in the computational domain), respectively. The Stokes number is for understanding the particle transport behaviour in the fluid flow. It indicates whether the particles are in a kinetic equilibrium with the fluid phase (Tian et al., 2005). The application of the St depends highly on the characteristic length of the domain of interest, which changes throughout the different geometries of the NC resulting in a limitation in the calculation of Stokes number in different parts of the NC. To overcome this limitation of the St, the inertial parameter (IP) was used as the criterion for the assessment of the validity of the particle phase model used in this study. The IP is widely used for the assessment of particle deposition in the NC and respiratory airways because the characteristic length and the characteristic velocity associated

with the St is normalised out by using a constant flow rate. The inertial parameter is given by (Inthavong, Tu, et al., 2011a):

$$IP = Q\, d_{\mathrm{ae}}^2 \tag{6-16}$$

where Q is the airflow rate and d_{ae} is the equivalent aerodynamic diameter given by (Yang et al., 2012):

$$d_{\mathrm{ae}} = d_{\mathrm{e}}\sqrt{\frac{\rho_{\mathrm{p}}}{1000\mathrm{X}}} \tag{6-17}$$

where d_{ae} is the aerodynamic diameter is defined as "the diameter of the spherical particle with a density of 1000 kg/m^3 that has the same settling velocity as the particle under study" (Yang et al., 2012). The d_{e} and X are the equivalent volume diameter and the shape factor of the particle, respectively (Yang et al., 2012). For a spherical particle, the d_{e} equals to the particle diameter and X is unity (Yang et al., 2012). In this study, the spherical particles are assumed with a density of $\rho_{\mathrm{p}} = 1000\ \mathrm{kg/m^3}$, hence the equivalent aerodynamic diameter is identical to the particle diameter. The *IP* is a convenient parameter that is normally used for comparing the effect of d_{p} and Q on the deposition efficiency. However, the use of a constant flow rate is a limitation of the inertial parameter given that it does not take into account the complicated shape of the geometry of the NC. Despite this limitation, the inertial parameter is normally used for the demonstration of deposition efficiency of particles, particularly where the determination of characteristic length is limited due to the geometry variation.

The effect of the inertial parameter of the total deposition efficiency in G2 was predicted using the CFD model in this study. The results were compared with the experimental and numerical data reported in the literature (Cheng et al., 2001; Kelly et al., 2004; Pattle, 1961; Shang et al., 2015; Shi et al., 2007; Tian et al., 2008). Figure 6.7 shows that the trend of the deposition efficiency predicted in this study is similar to that of the previous studies, which implies the validity of the particle tracking model of this study. The

variation in deposition efficiency between the current and the previous studies is rooted in the differences between the NC geometry of the current study and the previous studies.

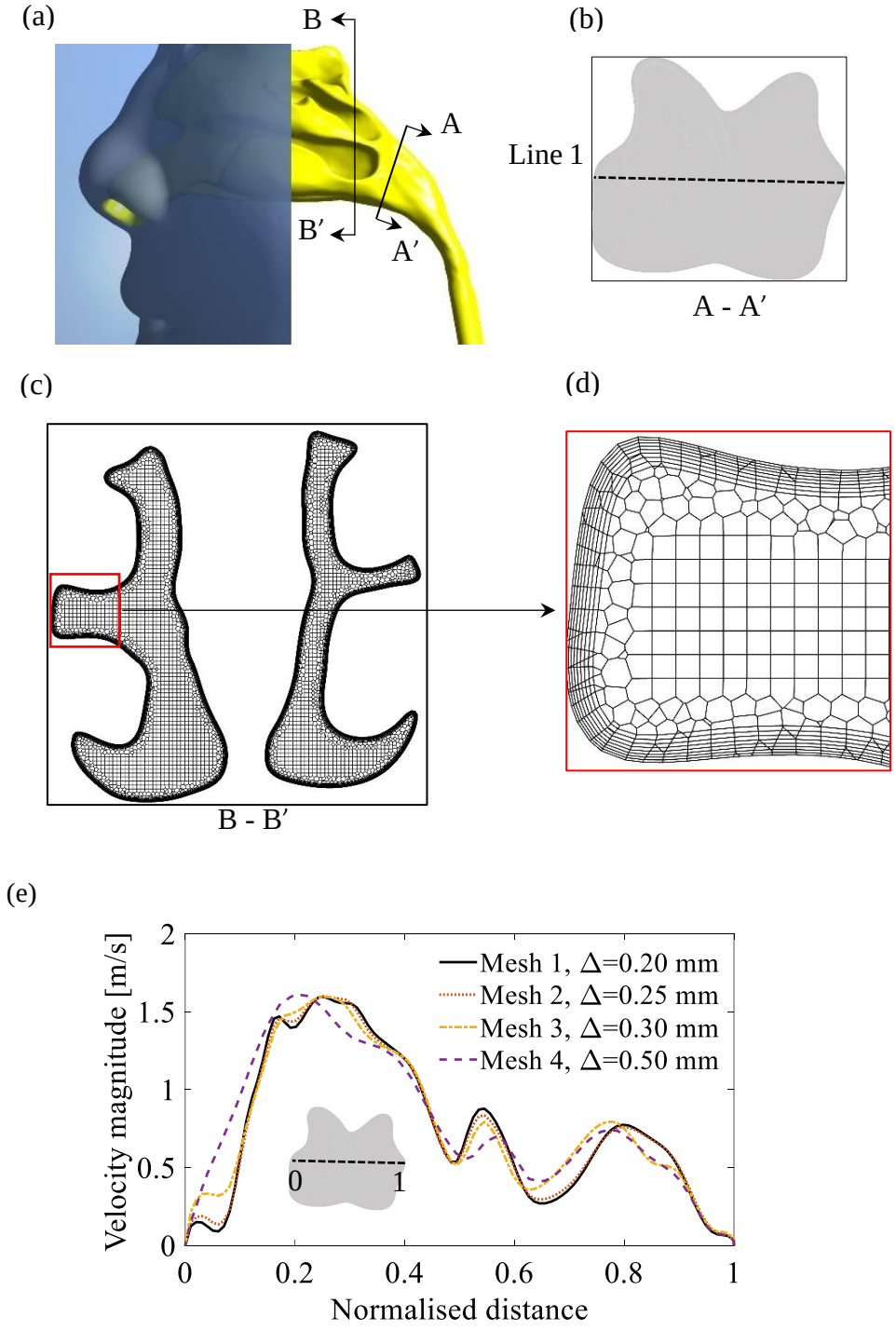

Figure 6.5: (a) Schematic of NC in G1; (b) an overview of the plane A-A' and Line 1; (c) an overview of the meshes on the plane B-B'; (d) zoomed-in view of the mesh on plane B-B' representing the prism layers; (e) mesh independence test based on the velocity magnitude of Line 1 when the flow rate is Q=10 L/min.

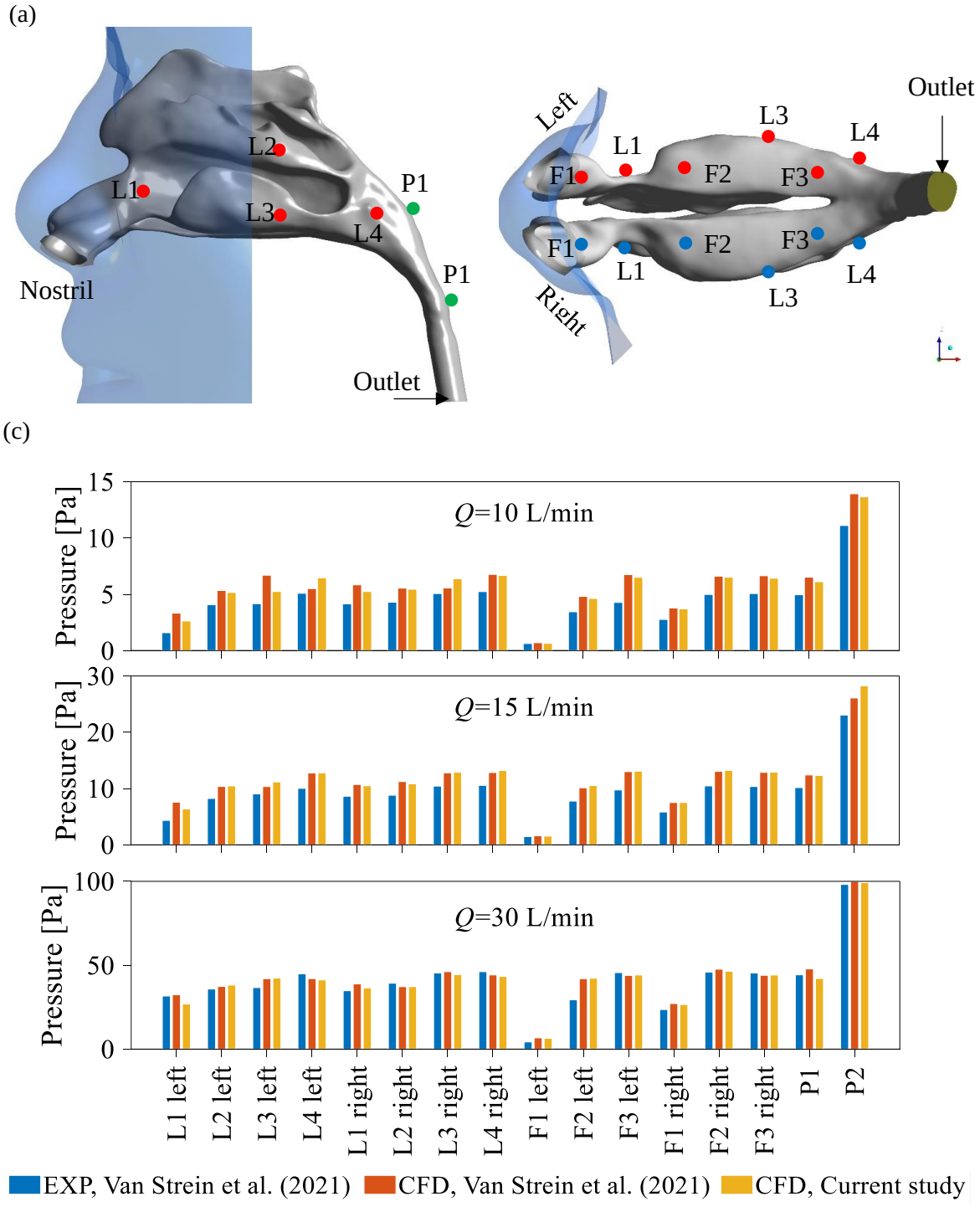

Figure 6.6: (a) An overview of different points defined on the wall of the nasal cavity used for predicting the pressure values (the model was generated through the STL file adapted from Van Strien et al. (2021) with permission); (b) pressure distribution on the wall of the nasal cavity obtained by the current CFD study compared with the experimental data and CFD results reported in (Van Strien et al., 2021) for a flow rate of 10 L/min, 15 L/min, and 15 L/min

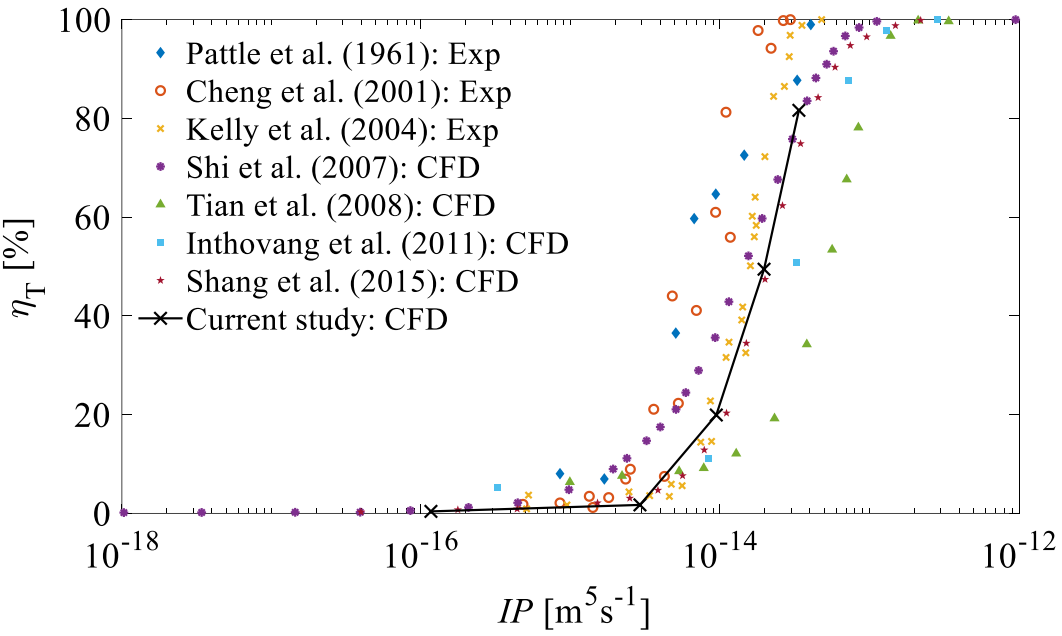

Figure 6.7: A comparison between the CFD results in the current study for total deposition efficiency (η_T) as a function of the inertial parameter (IP) and available data in the literature (Cheng et al., 2001; Inthavong, Tu, et al., 2011b; Kelly et al., 2004; Pattle, 1961; Shang et al., 2015; Shi et al., 2007; Tian et al., 2008)

6.4 Results and discussion

6.4.1 Effect of inlet flow parameters on the flow structure in NC

To investigate the effect of inlet flow parameters on the flow structure, several cross-section planes across the NC were created in critical locations as presented in Figure 6.8 (a). Figure 6.8 (b) shows the comparison of the maximum turbulence intensity (TI_{max}) between the cases with TI_{in}=0.15 and TI_{in}=0.3 on planes P1-P9. The instantaneous contours of turbulence intensity on planes P1-P7 across the NC are presented in Figure 6.8 (c-d). From Figure 6.8 (b), it can be seen that the maximum turbulence intensity decreased remarkably on planes P1 to P4 for both cases. However, from P5-P9 the TI_{max} remains relatively constant. For example, in a case with TI_{in}=0.3, the maximum turbulence intensity is reduced to TI=0.045 in P5. This means that NC operates similar to a settling chamber transforming a turbulent

flow to near laminar flow. By comparing the contours of turbulence intensity on plane P6 between the cases with TI_{in}=0.15 and TI_{in}=0.3, it can be seen that in both cases the turbulence intensities in the ostium and the MM-Ostium region are negligible ($TI \cong 0$). It can be inferred that the implementation of turbulence to the inlet flow has not had a significant effect on the airflow behaviour in the MM-Ostium region (see Figure 6.8 (c-d)).

Figure 6.9 (a-e) presents the instantaneous streamlines and the velocity magnitude contours in plane P6 for different inlet flow parameters. As it is shown in Figure 6.9 (a-c), in the plane P6 the flow structure after introducing turbulence at the inlet is identical to the laminar inlet flow. Based on the streamlines illustrated in Figure 6.9 (d-e), the flow structure in the MM-Ostium region under the effect of swirling inlet flows ($S_n = 0.6$ and $S_n = 0.9$) is also essentially identical to those of non-swirling inlet flows. Therefore, it is inferred that due to the large volume of the NC and the resistance of the nasal valve the flow stabilises and hence the inlet flow preconditioning does not affect the flow features in the MM-Ostium region. When a swirling flow is applied to the inlet, the flow structure in the inferior meatus (marked IM in Figure 6.9) undergoes some change in the number of vortices (i.e. secondary flows) due to the curvature of the anterior region. The anterior region includes the nostril and vestibule. Figure 6.9 (a-e) shows that the swirling flow can influence the flow structure in the NC but mostly in the inferior meatus where the width of the airway is wider than the middle and superior meatuses.

To better understand the role of the nasal valve as an airway resistance Figure 6.10 (a-c) illustrates the streamlines on planes P2-P4 for different inlet flow parameters. The vestibule is located between P2 and P3, and the nasal valve is located between P3 and P4. It is clear from this Figure that there are no significant changes in the flow streamlines in planes P2-P4 under the effect of turbulent inlet flows when compared with the laminar non-swirling

inlet flow. In contrast, the flow structure in planes P2 and P3 changed significantly under the effect of swirling inlet flows. By increasing the swirl intensity of the inlet flow, the number of vortices (i.e. secondary flows) on plane P3 is increased, which demonstrates the impact of swirling flow on the flow structure in the nostril and vestibule regions. However, the influence of all inlet flow parameters on the flow structure in the plane P4 (except the IM region of P4) is negligible compared with plane P3. This implies that the constrictive nasal valve region significantly changes the flow features and reduces the effect of turbulence and swirling flow implemented to the inlet, confirming the airway resistance of the nasal valve. Hence, it might be expected that inlet flow preconditioning does not affect the efficiency of drug delivery to the MS significantly.

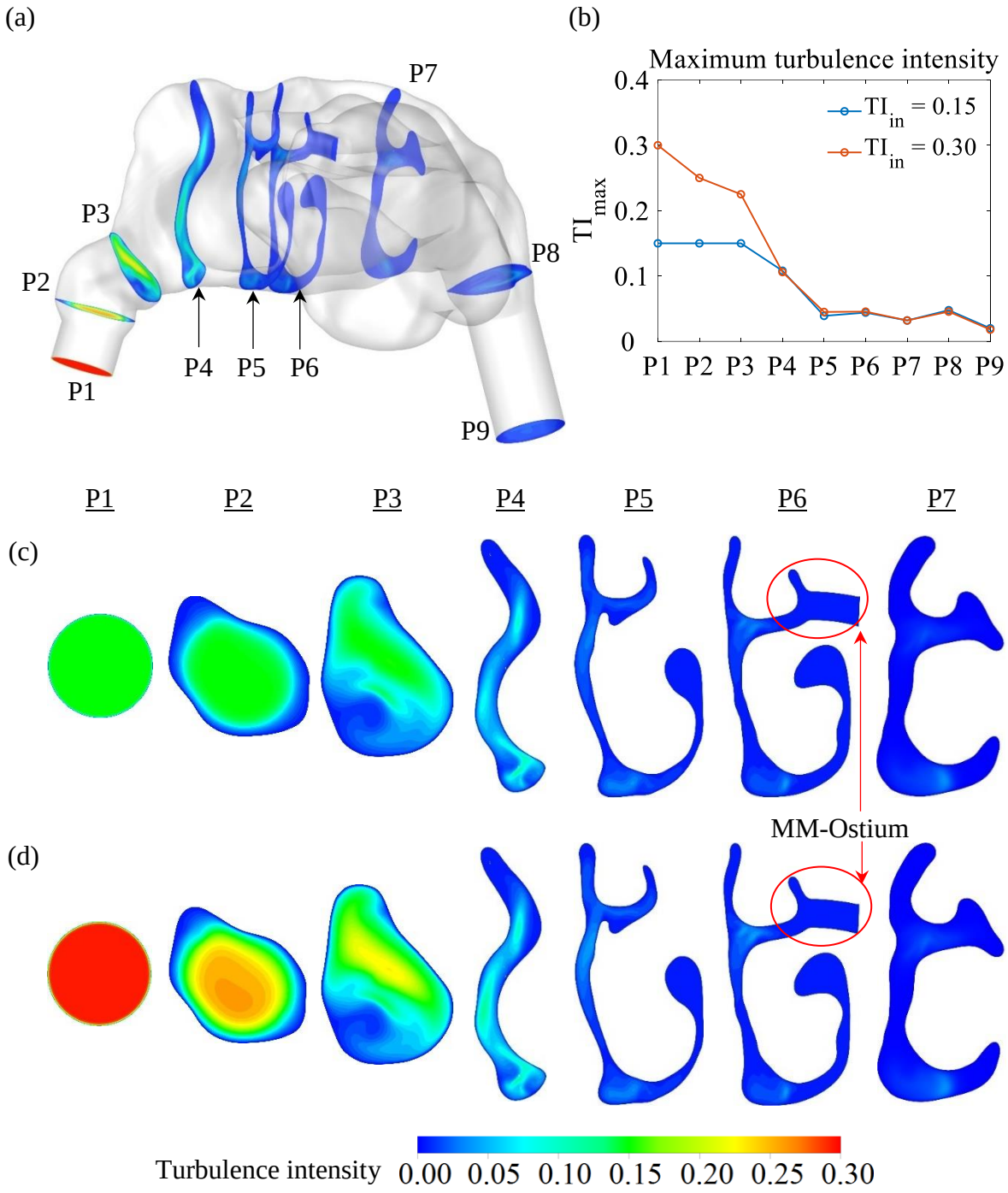

Figure 6.8: (a) Illustration of the location of different cross-section planes in the NC-MS combination G2); (b) maximum turbulence intensity for different cross-sectional planes; (c) instantaneous turbulence intensity (TI) contour demonstrated for different cross-section planes (P1-P7) in the NC-MS combination when the inlet turbulence intensity is TI_{in}=0.15; and (d) TI_{in} =0.3. The inlet mass flow rate was Q=7 L/min.

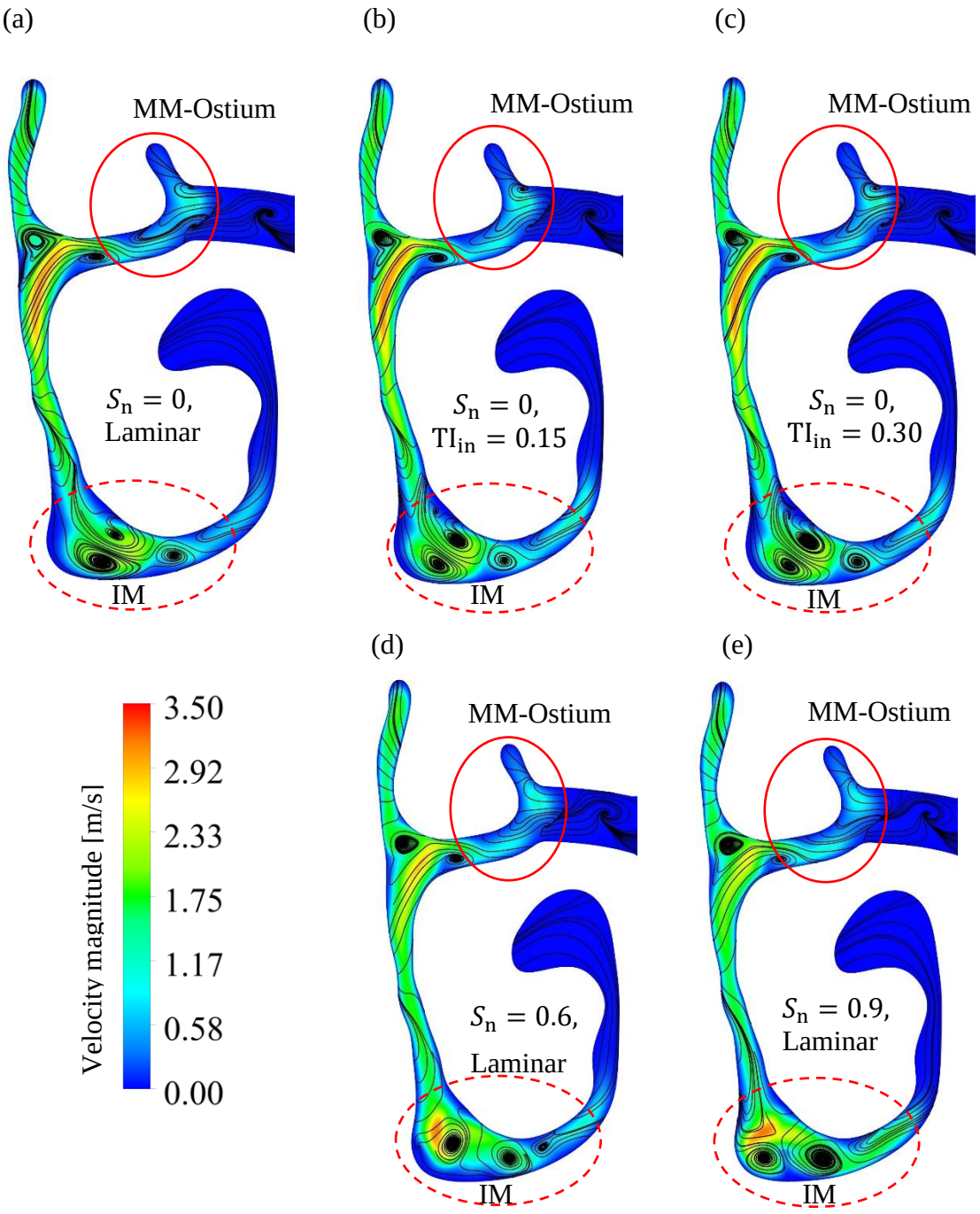

Figure 6.9: Instantaneous flow streamlines and velocity contour on plane P6 under the effect of non-swirling (a) laminar inlet flow; (b) inlet turbulence intensity of $TI_{in} = 0.15$; (c) inlet turbulence intensity of $TI_{in} = 0.3$; and swirling flow with (d) inlet swirl number of $S_n = 0.6$; (e) inlet swirl number of $S_n = 0.9$. Artificial turbulence was applied to the inlet for the turbulent inlet flows.

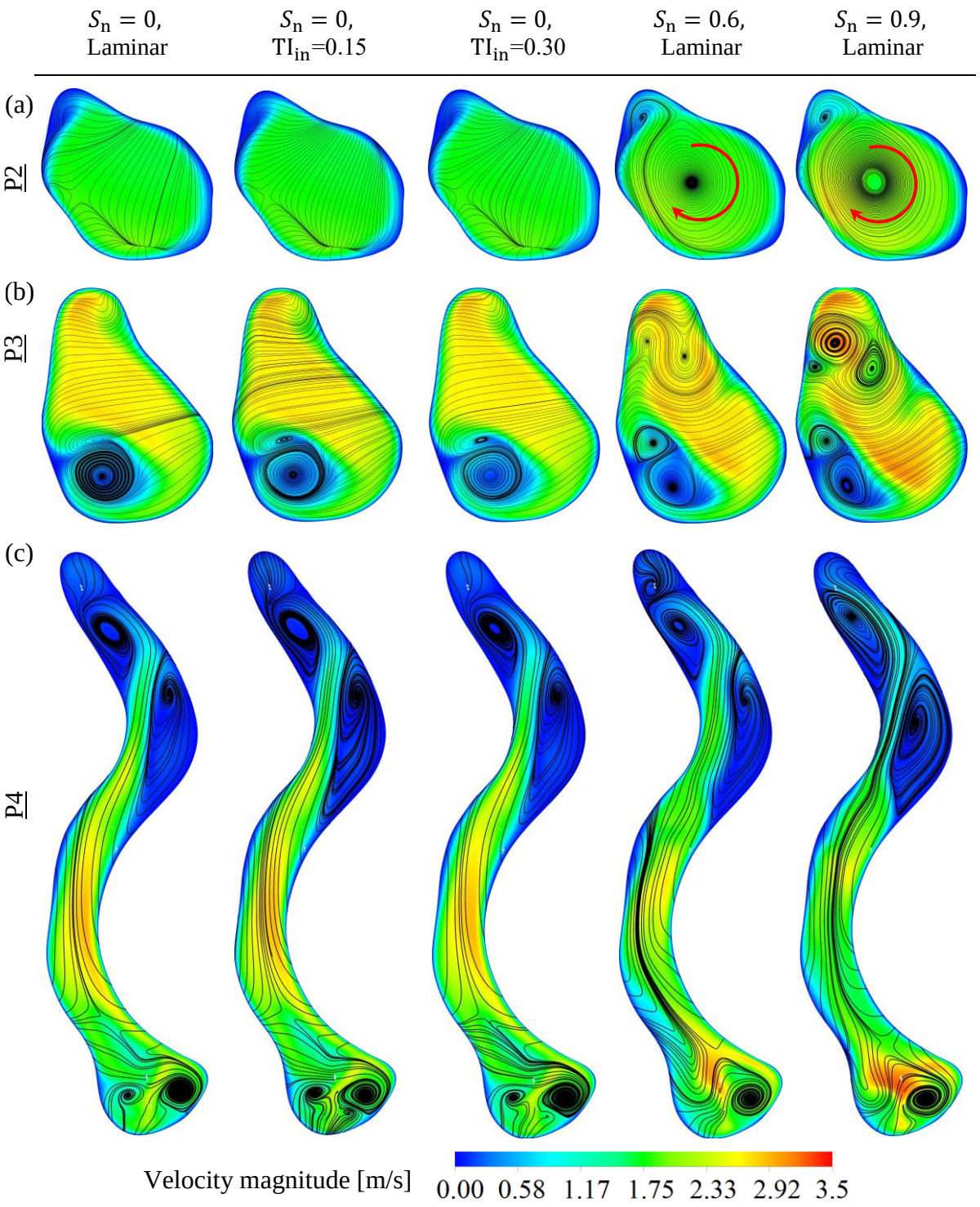

Figure 6.10: Instantaneous flow streamlines and velocity contour on (a) plane P2; (b) plane P3; and (c) plane P4 under the effect of different inlet flow parameters.

6.4.2 Effect of inlet flow parameters on particle transport

Particle tracking simulation provides a detailed understanding of particle transport and deposition. To increase the efficiency of ADD to the MS, the number of particles in the MM-Ostium region should be increased and also the retention of particles in that region should be enhanced. When the ADD technique is applied, the particles are transferred to the MS through the oscillation of the air plug in the ostium. To be more specific, by the oscillating air plug during every cycle, some of the particles in the MM-Ostium region are trapped after several cycles and then transported to the MS (Pourmehran, Arjomandi, Cazzolato, & Tian, 2020). Therefore, to increase the number of particles transported to the MS through ADD, the total number of particles trapped in the oscillating air plug in several consecutive cycles should be increased, which requires longer particle retention in the MM-Ostium. To consider both the number of particles and the retention of particles in the MM-Ostium, the particles' retention criterion (N_{p}^{*}) was estimated using Equation (6-1).

Figure 6.11 (a-b) represents the number of particles in the MM-Ostium region, as a function of particle time, and the related N_{p}^{*} under the effect of turbulent and swirling inlet flows when $C_{\mathrm{f}} = 1$ and $\mathrm{d}_{p} = 5\mu\mathrm{m}$. From Figure 6.11 (b), it can be seen that there are no significant differences in N_{p}^{*} between the cases with turbulent inlet flows and the laminar non-swirling inlet flow in the MM-Ostium region. This behaviour originates from an identical flow behaviour between those cases (see Figure 6.9 and Figure 6.10).

According to Figure 6.11 (a-b), the particle retention criterion for a swirling inlet flow with $S_{\mathrm{n}} = 0.6$ is greater than for a non-swirling inlet flow ($S_{\mathrm{n}} = 0$). Therefore, the efficiency of drug delivery to the MS (through the MM-Ostium using ADD) is expected to increase when a swirling flow (i.e., $S_{\mathrm{n}} = 0.6$) is applied to the inlet. The differences in the N_{p}^{*} in the

cases with swirling and non-swirling flows might take place due to the variations of the flow fields in the nostril and vestibule regions (zones 1 and 2 depicted in Figure 6.2 (e)), which is discussed in the following paragraphs.

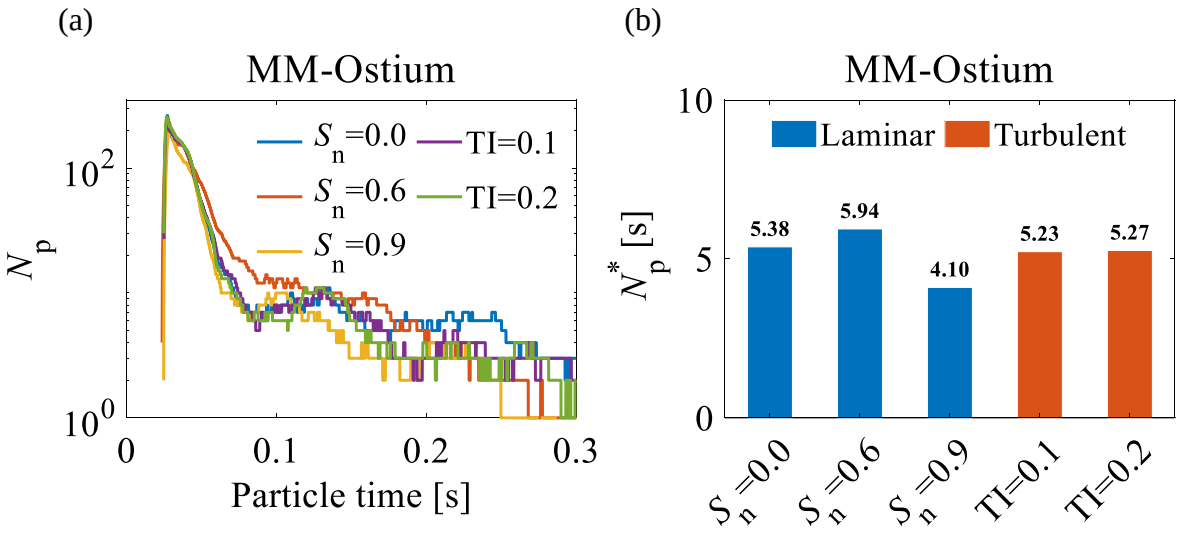

Figure 6.11: (a) The effect of inlet flow parameters on the number of particles (N_p) in the MM-Ostium region in every time-step when C_f =1; (b) particle retention criterion (N_p^*) in the MM-Ostium region under the effect of different inlet flow parameters when $d_p = 5$ µm and $C_f = 1$.

Given the cross-sectional area of the nostril zone (zone 1 depicted in Figure 6.2 (e)) is almost constant, the Stokes number in this region can be calculated using Equation (6-15), which yields $St = 0.0115$. Figure 6.12 presents the Stokes number on planes P1-P9 for different inlet flow parameters. It is clear from this Figure that the Stokes number along the NC is much lower than unity, hence the particles almost follow the fluid streamlines. When a swirling flow is applied to the inlet, the airflow in the nostril swirls around the centreline of the nostril (z-axis), hence, the particles released at the nostril also swirl around the centreline of the nostril. When the particles swirl around an axis, a centrifugal force acts on the particles and drives them toward the wall. The centrifugal force has a direct relationship with the tangential velocity and particle mass.

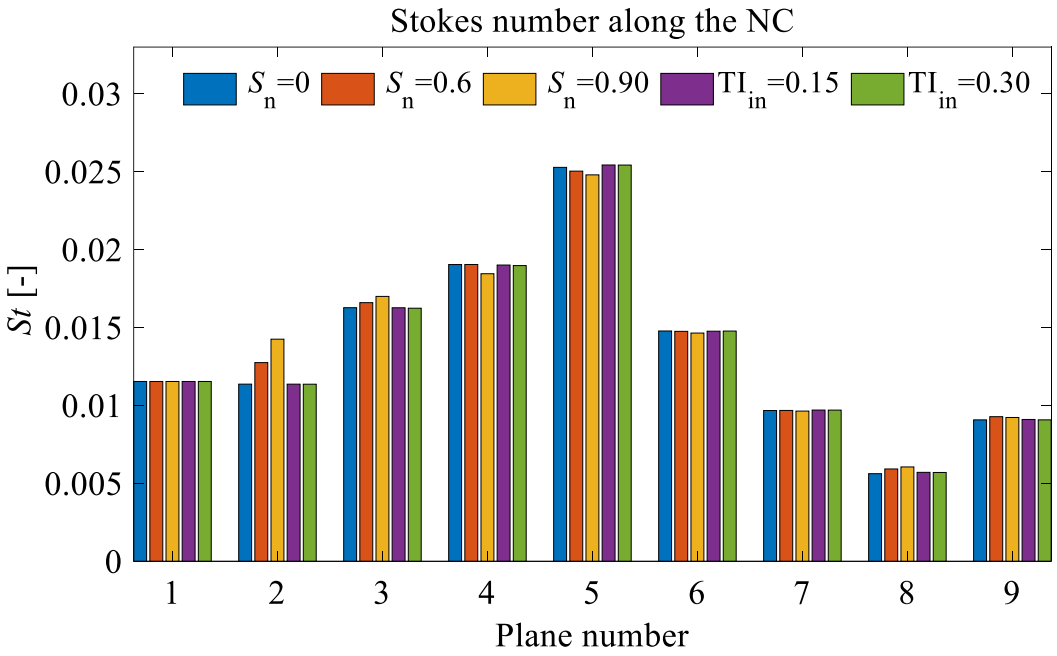

Figure 6.12: Stokes number (*St*) along the nasal cavity on planes P1-P9. The location of P1-P9 are illustrated in Figure 6.8 (a).

The centrifugal force, F_c, can be calculated by:

$$F_c = \frac{m_p u_t^2}{r}\ , \qquad 6\text{-}18$$

where m_p is the particle mass, u_t is the tangential velocity, and r is the radial coordinate. An increase in the swirl intensity of the swirling inlet flow increases the tangential flow velocity, which increases the centrifugal force acting on the particles (see Figure 6.13). Therefore, increasing the swirl number of the inlet flow increases the concentration of particles that are driven towards the wall, which can lead the particles to deposit on the wall. Figure 6.14 (a-b) presents the total and local deposition efficiencies for different inlet flow parameters. This Figure shows that the swirling flow has the effect of increasing the deposition of particles on the wall, where the maximum total deposition efficiency occurs when $S_n = 0.9$. Figure 6.14 (b) reveals that the maximum particle deposition in zones 1 and 2 (nostril and vestibule, respectively) occurs in $S_n = 0.9$, which implies the effect of centrifugal force on the particles in these regions, contributing to an increase in total deposition efficiency.

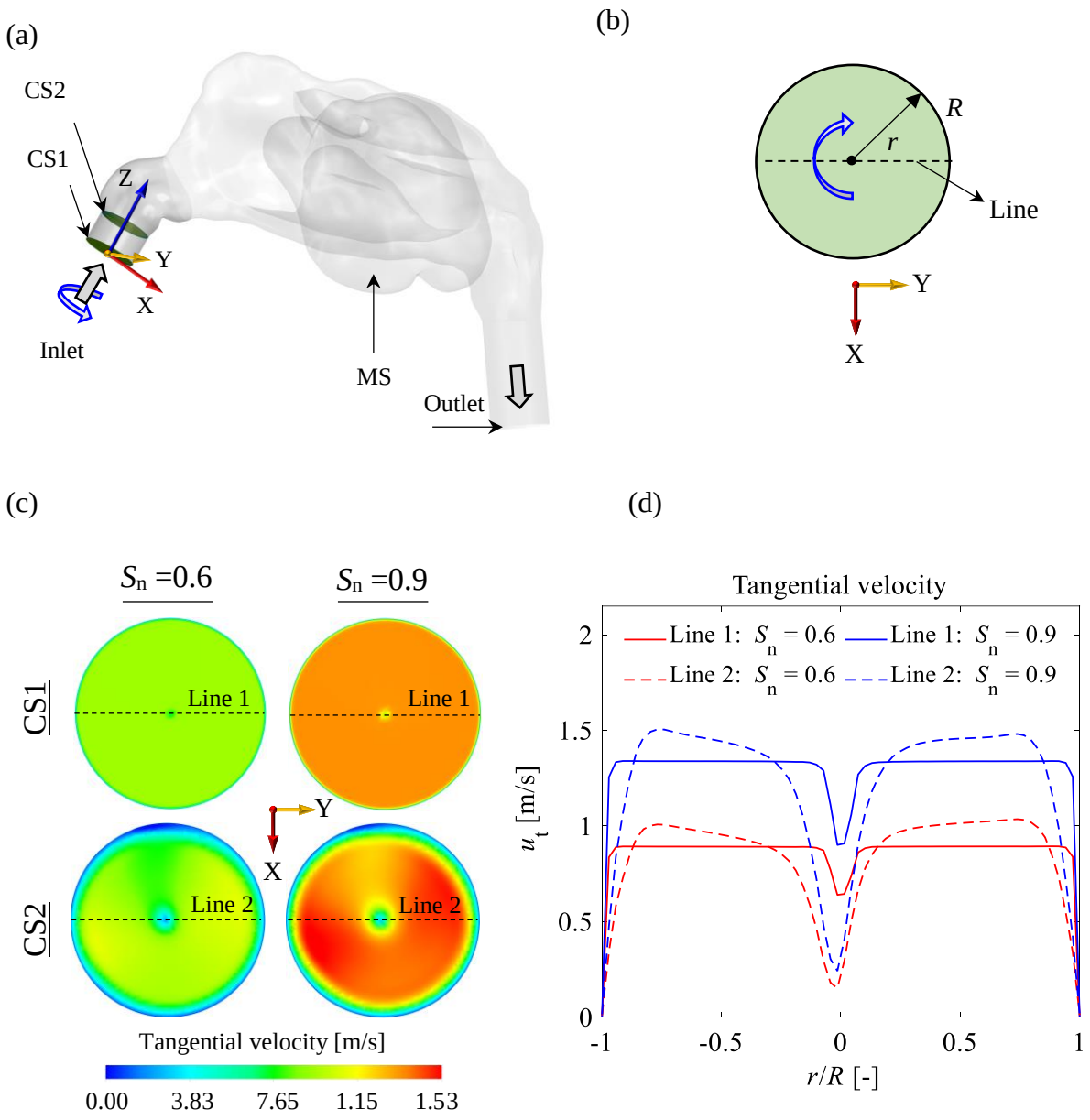

Figure 6.13: (a) An overview of NC-MS geometry (G2) representing two cross-sections (CS1 and CS2) on nostril; (b) a top view of the cross-section representing the rotation of the inlet flow; (c) tangential velocity contours in CS1 and CS2 for different swirl numbers (S_n); (d) tangential velocity profiles on Lines 1 and 2 for different S_n.

The effect of the centrifugal force on the particles can be seen in Figure 6.15 (a). This Figure illustrates the distribution of the particles in plane P2 for different inlet swirl numbers. According to this figure, the application of swirling inlet flow led the particles in the central area of the nostril to move towards the wall due to the centrifugal force. Also, the central area of the nostril, which is empty of particles, becomes wider by increasing the swirl number

from $S_n = 0.6$ to $S_n = 0.9$. This implies that the centrifugal force on the particles was also enhanced when the swirl number increased. The results showed that, despite the approximately similar flow behaviour in the NC-MS geometry on planes P4-P9 (i.e., zones 4-9) for all the inlet flow preconditioning, the particle transport patterns under the effect of swirling inlet flow and non-swirling inlet flow are not identical. This could be due to the effect of flow behaviour on particle transport patterns in the first two zones (i.e., nostril and vestibule).

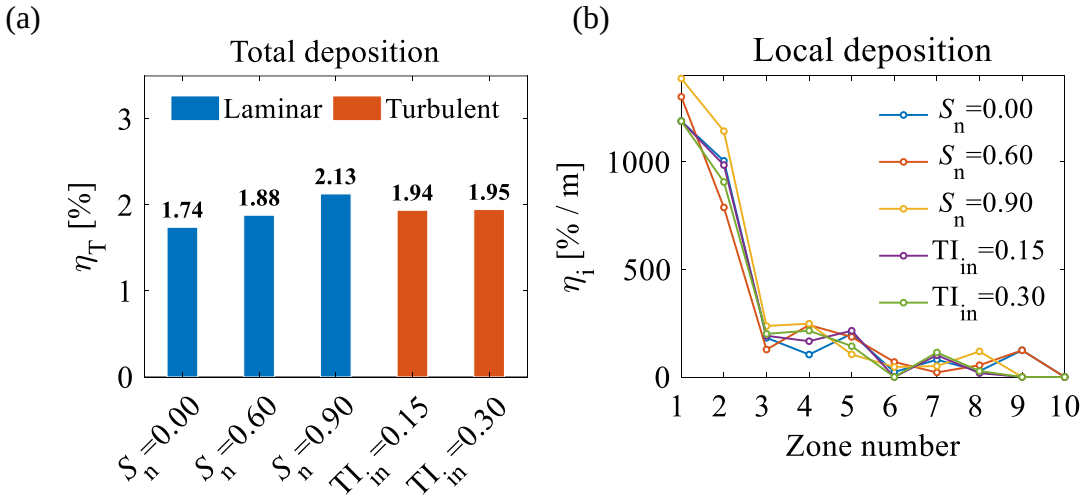

Figure 6.14: The effect of inlet flow parameters on (a) total deposition efficiency (η_T); and (b) local deposition efficiency per unit of area (η_i).

Figure 6.15 (a-b) compares the particle distribution pattern between the non-swirling and swirling inlet flows in planes P2 and P3. The particle distribution patterns in planes P2 and P3 are similar to the flow streamlines in those planes (see Figure 6.10 (a-b)), where the Stokes number is very lower than unity. For swirling inlet flows, the particle distribution patterns in plane P4 (see Figure 6.15 (c)) are not similar to the flow streamlines in plane P4 (see Figure 6.10 (c)), even though the highest Stokes number in the nasal valve (the zone between P3 and P4) is much lower than unity ($St = 0.02$) The reason for the differences between the particle distribution patterns and flow streamlines in plane P4 are rooted in the particle distribution pattern formed in the upstream flow in the vestibule (zone 2). In other

words, the particle distribution patterns that were formed under the effect of swirling flow in the nostril (zone 1) and vestibule regions were partially extended to the nasal valve.

Comparing the particle distribution patterns illustrated in Figure 6.15 (b) and Figure 6.15 (c), it can be seen that the areas in plane P3 that are empty of particles, due to the swirling flow, were extended to plane P4. Figure 6.15 (d) shows that for the cases with swirling inlet flow there is an area in the main passage of plane P5 that is almost devoid of particles, while no swirling flow in that region is observed in the streamlines of that plane (Figure 6.15 (e)). Hence, it can be inferred that the particle transport pattern in the vestibule was extended not only to the nasal valve but also to the areas beyond the nasal valve (zone 3).

In conclusion, the swirling inlet flow undergoes many changes when it passes through the nasal valve where the swirl intensity of the inlet swirling flow is almost damped. The effect of swirling flow on the particles before entering the nasal valve forms a specific particle distribution pattern. The particle distribution pattern in the nostril and vestibule not only does not disappear in the nasal valve but also partly extends to the regions beyond the nasal valve. Accordingly, the differences in N_{p}^{*} between the non-swirling inlet flow and swirling flows presented in Figure 6.11 (a-b) can be explained: the concentration of particles (C_{p}) in the upper part of the plane P3 for $S_{\mathrm{n}} = 0.9$ ($C_{\mathrm{p}} = 7.8\%$) is lower than that of $S_{\mathrm{n}} = 0.6$ ($C_{\mathrm{p}} = 11.6\%$) (see Figure 6.15 (b)). So, they contribute to a lower concentration of particles in the MM-Ostium region for $S_{\mathrm{n}} = 0.9$ given that the particle distribution pattern in plane P3 is partly extended to the regions beyond the nasal valve. Therefore, the particle retention criterion in the MM-Ostium region for $S_{\mathrm{n}} = 0.9$ is lower than for other cases, as presented in Figure 6.11 (a-b).

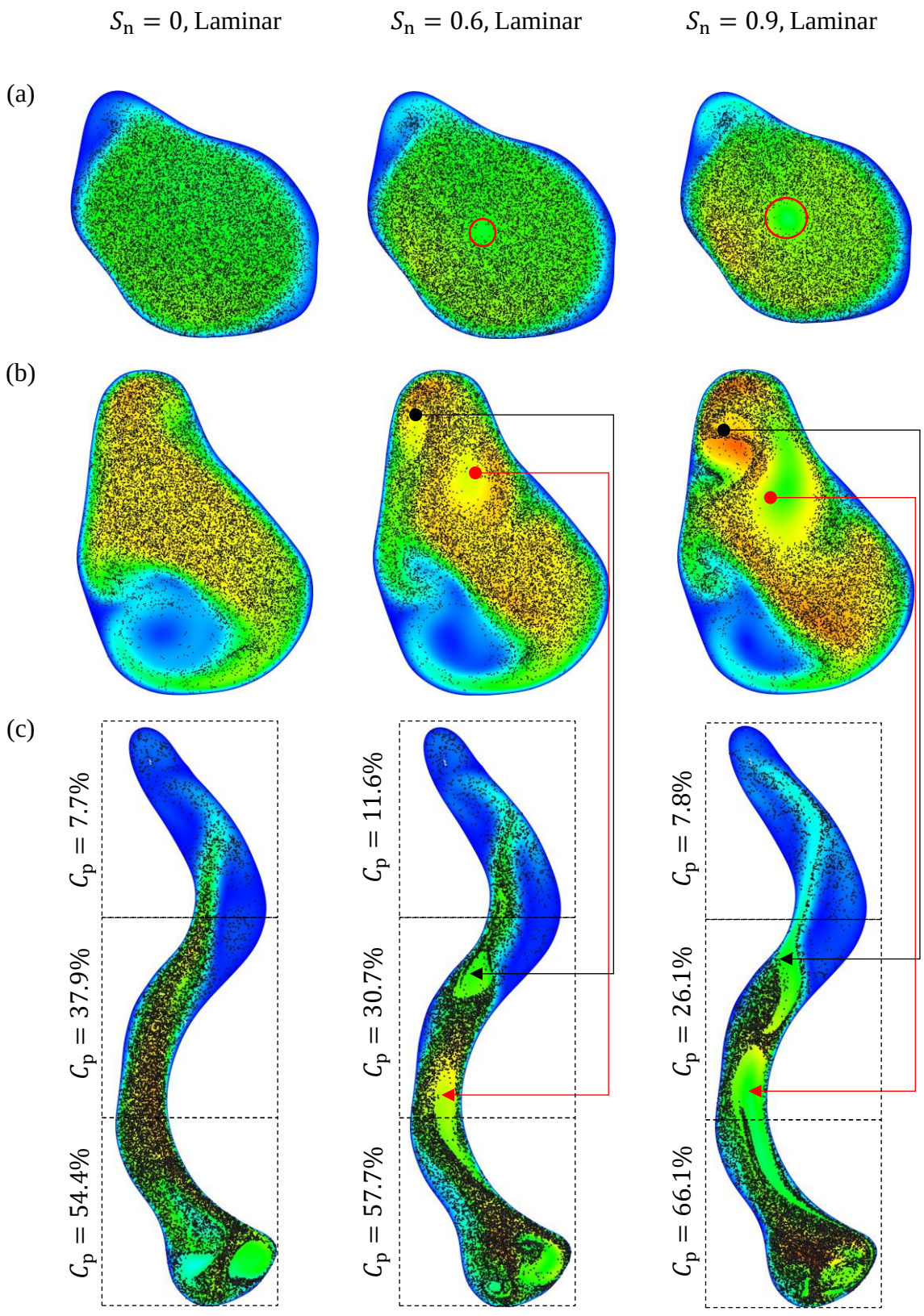
$S_n = 0$, Laminar
$S_n = 0.6$, Laminar
$S_n = 0.9$, Laminar
(a)
(b)
(c)
$C_p = 7.7\%$
$C_p = 37.9\%$
$C_p = 54.4\%$
$C_p = 11.6\%$
$C_p = 30.7\%$
$C_p = 57.7\%$
$C_p = 7.8\%$
$C_p = 26.1\%$
$C_p = 66.1\%$

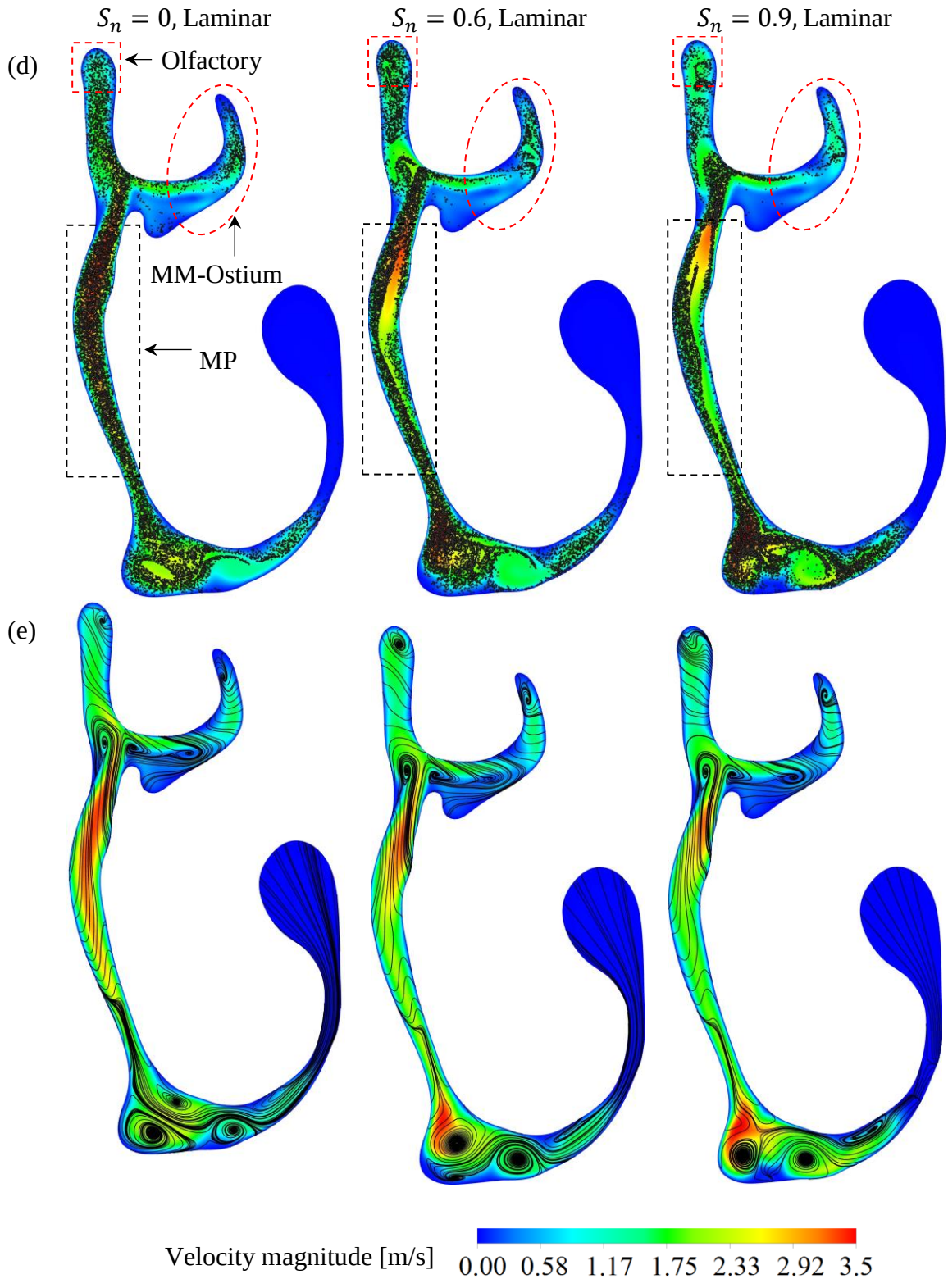

Figure 6.15: Accumulative particle distribution and instantaneous velocity contours under the effect of non-swirling and swirling flows on different planes: (a) P2, (b) P3, (c) P4, and (d) P5; (e) instantaneous flow streamlines and velocity contours on plane 5.

6.4.3 Effect of fullness coefficient on the particle transport pattern

The effect of the fullness coefficient (C_f) on the particle transport/deposition pattern in the NC-MS combination (G2) was investigated under the effect of non-swirling ($S_n = 0$) and swirling ($S_n = 0.6$) inlet flows. Figure 6.16 illustrates an overview of the accumulative particle distribution in plane P3 for different swirling numbers and C_f. According to this figure, when C_f decreases the concentration of particles in the core flow increases. In this study, the core flow is defined as the part of the flow where the velocity magnitude and the velocity gradient are significantly higher and lower than other parts of the flow, respectively. The core flow regions in plane P3 for $S_n = 0$ and $S_n = 0.6$ are illustrated in Figure 6.16.

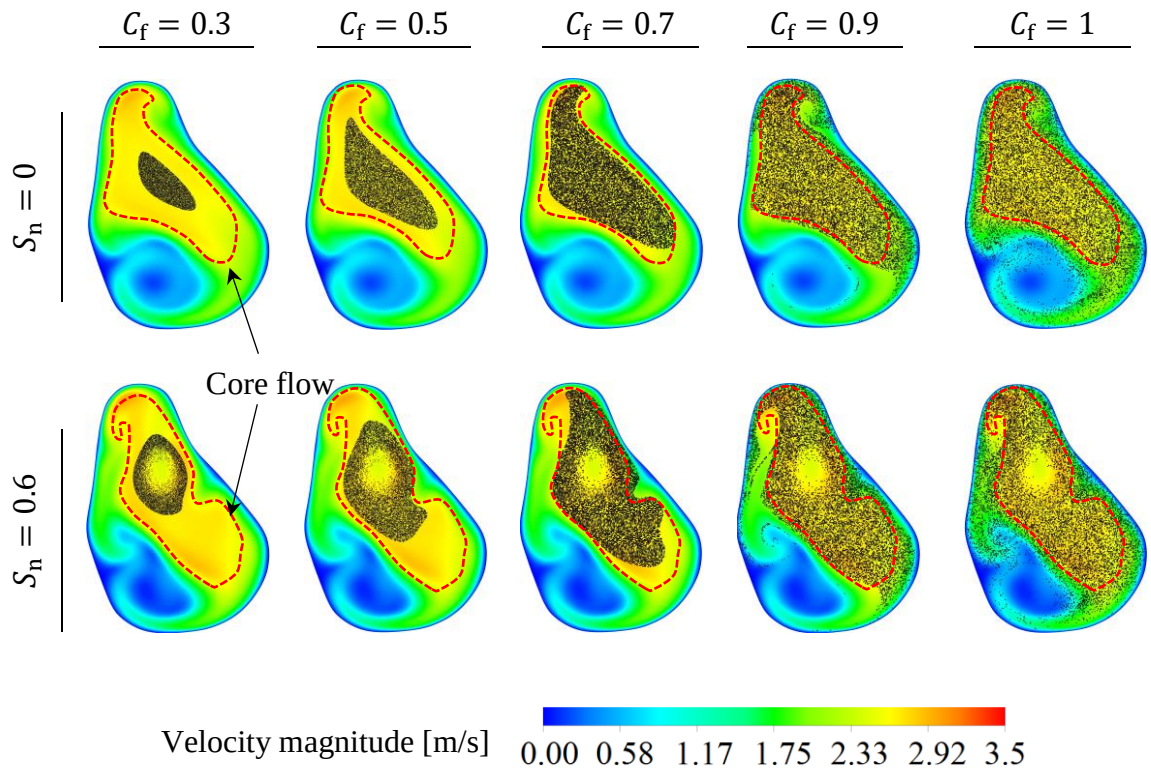

Figure 6.16: Accumulative particle distribution and instantaneous velocity contours in plane P3 for different fullness coefficient (C_f) under the effect of non-swirling and swirling inlet flows.

Given the Stokes number in this study is much lower than unity along the NC region, the particles in the NC can follow the flow. Accordingly, when the concentration of particles in the core flow region increases, the number of particles that can be transported beyond the anterior region increases. When a portion of the particles is distributed out of the core flow region, they need a longer time to be transported to the location beyond the anterior region because the velocity magnitude in that region is much lower than the core flow. To better understand the effect of C_{f} on the particle transport pattern in the NC, Figure 6.17 (a-b) presents an instantaneous particle distribution in the NC for different fullness-coefficient. The particles were coloured, based on the particle velocity magnitude.

Figure 6.17 (a-b) shows that all the injected particles were transported beyond the anterior region for $C_{\mathrm{f}} \leq 0.7$, demonstrating that the particles were almost transported through the core flow region. However, for $C_{\mathrm{f}} = 0.9$ and $C_{\mathrm{f}} = 1$, some particles remained in the anterior region with very low velocity, which shows these particles were not in the core flow in the anterior region (see the colour of particles in the anterior region in Figure 6.17 (a-b)). The particles that are not in the core flow region are likely to deposit on the wall due to the low velocity-magnitude, which contribute to moving the particles towards the wall and eventually depositing there.

Figure 6.18 presents the effect of C_{f} on the total deposition efficiency (η_{T}) and the local deposition efficiency per unit of area (η_i) for different inlet flow parameters. It can be seen from Figure 6.18 (a) that for non-swirling flows, an increase in C_{f} increases the total deposition efficiency from an increased concentration of the particles in the region outside of the core flow. This Figure also shows that the total deposition efficiency in swirling inlet flows is higher than for non-swirling flows. This is due to the centrifugal forces acting on the particles in the core flow, which drive them towards the wall.

In continuous drug delivery, such as drug delivery using nebulisers, the deposition of the particles in the anterior region increases gradually, which can contribute to forming droplets dripping from the nostril as waste. To overcome this problem, a 70% decrease in C_{f} is recommended for the NC-MS geometry of this study. To generalise this result A series of different realistic NC-MS models should be analysed.

Figure 6.19 (a-c) illustrates the number of particles in the MM-Ostium region (as a function of particle time) and the related N_{p}^{*} under the effect of swirling and non-swirling inlet flows for different C_{f} when $\mathrm{d}_{p} = 5$ μm. It can be seen from Figure 6.19 (c) that the effect of C_{f} on N_{p}^{*} for swirling inlet flows is different from non-swirling inlet flows in the MM-Ostium region. This Figure shows that N_{p}^{*} has an inverse relationship with C_{f} when $S_{\mathrm{n}} = 0.6$. However, N_{p}^{*} monotonically increases by increasing C_{f} for non-swirling inlet flow ($S_{\mathrm{n}} = 0$). According to Figure 6.19 (c), the highest N_{p}^{*} for the MM-Ostium region ($N_{\mathrm{p}}^{*} = 8.55$ s) when $C_{\mathrm{f}} = 0.3$ and $\mathrm{S_n} = 0.6$ is approximately 45% greater than a case with $\mathrm{S_n} = 0$, $C_{\mathrm{f}} = 1$ (a common inlet configuration). Therefore, we can infer that when $C_{\mathrm{f}} = 0.3$ and $\mathrm{S_n} = 0.6$, the efficiency of acoustic drug delivery to the MS might be increased by up to 45% when compared with an acoustic drug delivery with a common inlet configuration. It should be noted that these results are valid for the NC-MS geometry (G2) of this study. A series of different realistic NC-MS models should be analysed to generalise the effect of the particles' release diameter and inlet flow parameters on drug delivery efficiency.

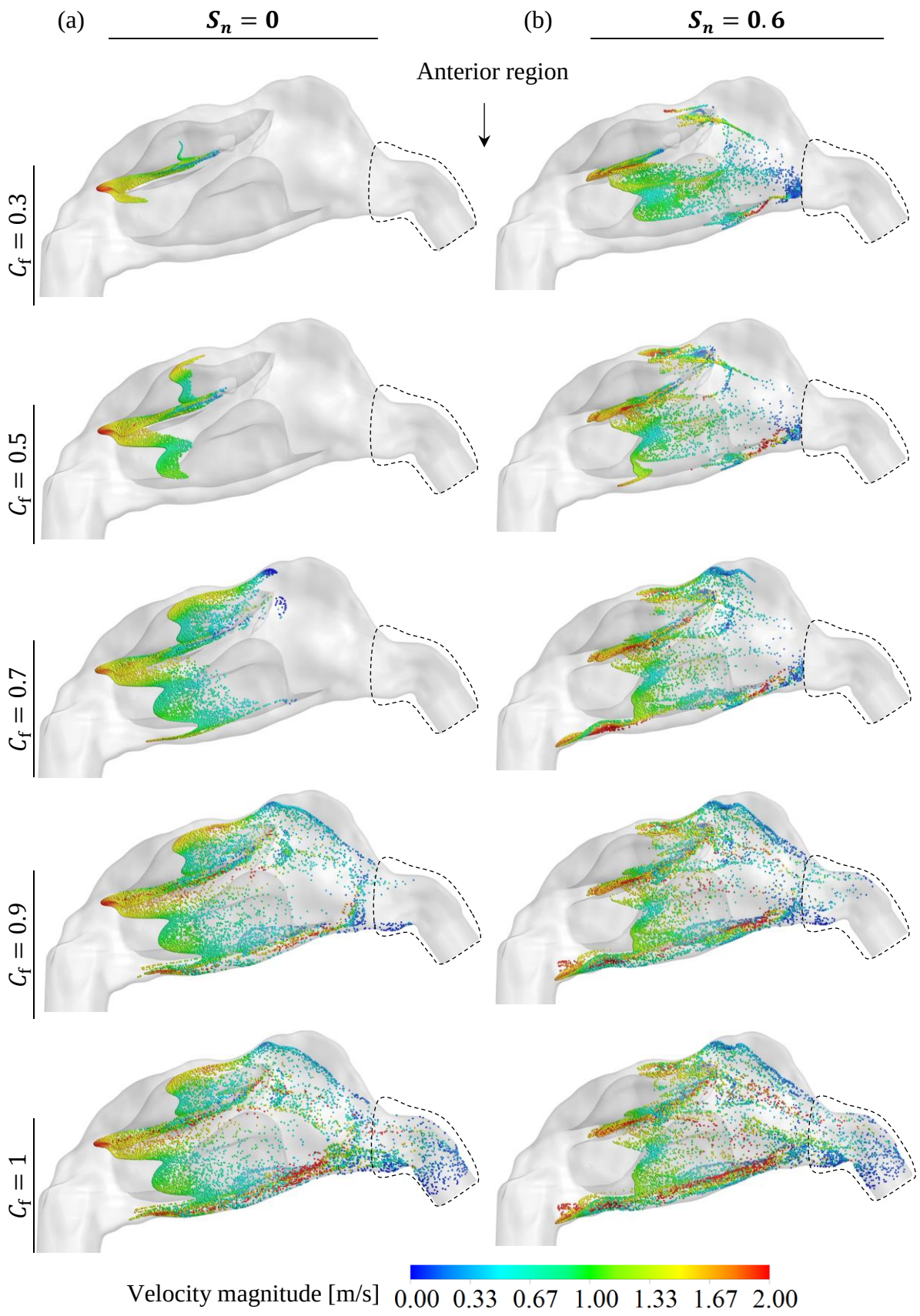

Figure 6.17: Instantaneous particle distributions in the NC for different particles' fullness coefficient (C_f) under the effect of (a) non-swirling inlet flow, and (b) swirling inlet flow.

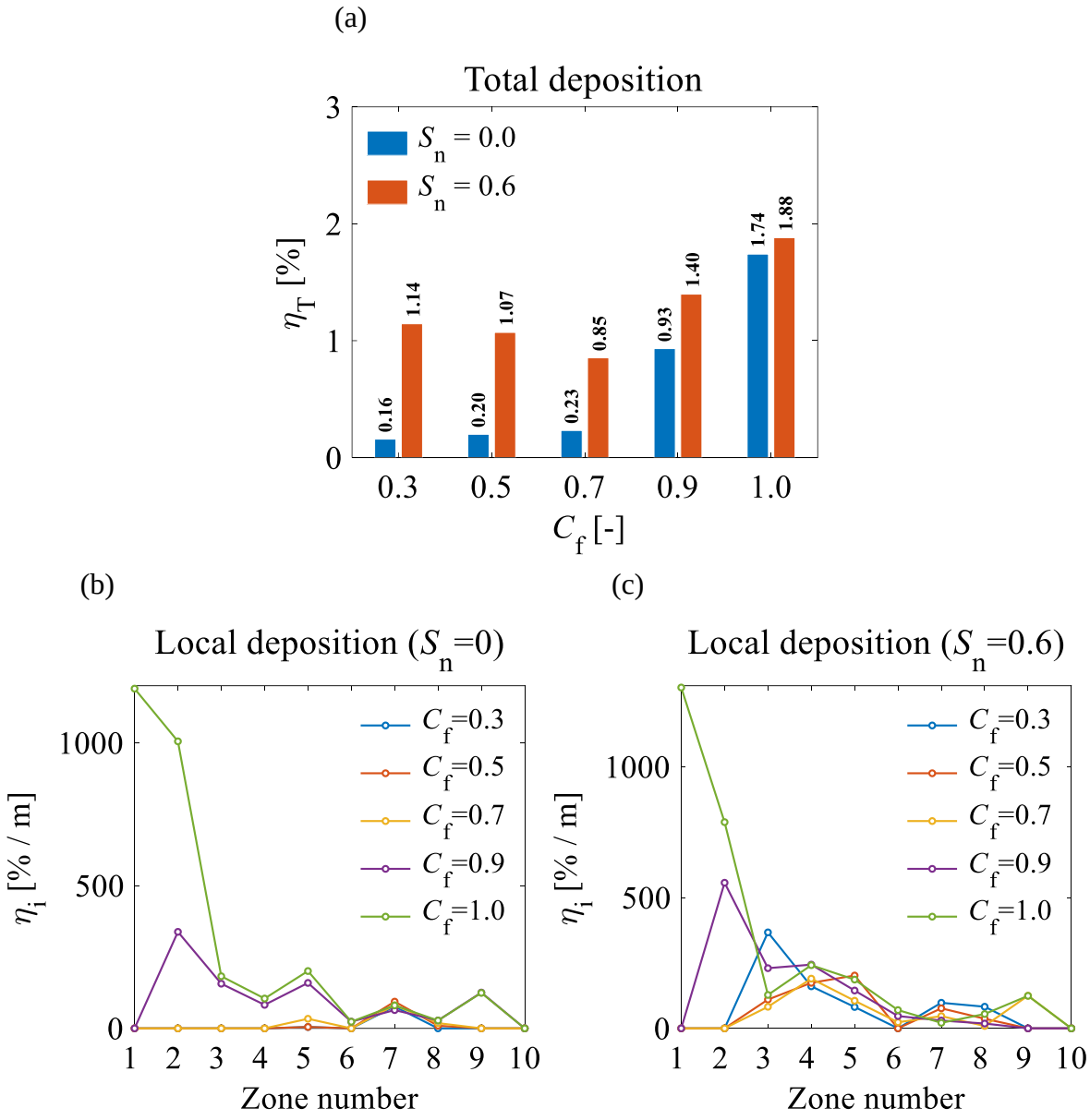

Figure 6.18: (a) The effect of fullness coefficient (C_f) and inlet flow parameters on the total deposition efficiency (η_T); (b) the effect of C_f on local deposition efficiency per unit of area (η_i) for a non-swirling inlet flow ($S_n = 0$); (c) the effect of C_f on η_i for a swirling inlet flow when $S_n = 0.6$. The particle diameter of d_p=5 μm was used for these cases.

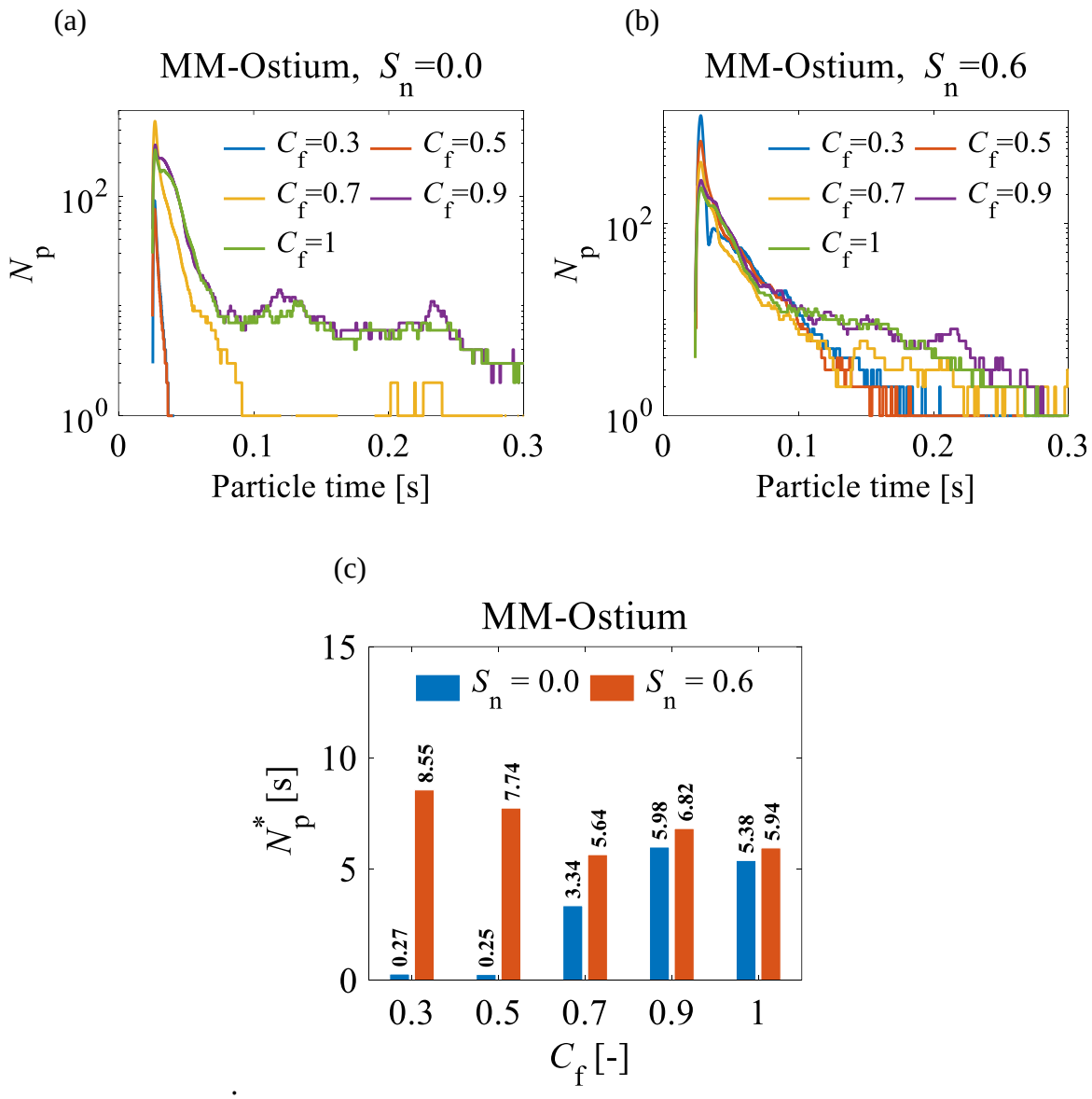

Figure 6.19: The effect of fullness coefficient (C_f) on the number of particles that exist in the MM-Ostium region in every time-step when (a) $S_n = 0$; and (b) $S_n = 0.6$; (c) the effect of C_f on the particles' retention criterion (N_p^*) in the MM-Ostium region for non-swirling and swirling inlet flows.

6.5 Conclusion

The main aim of the present study is to investigate the effect of inlet flow parameters and nozzle diameter (characterised by fullness coefficient) at the inlet on the airflow behaviour and drug (particle) delivery to the maxillary sinus (MS). For parametric studies, two CFD models using hybrid RANS-LES model and laminar solver were developed and validated

against the available experimental data. Exploiting the Eulerian-Lagrangian approach, the particle trajectories were predicted using a discrete phase model (DPM). Given the low particle volume fraction, a one-way coupling method between the fluid and particle phases was used in the particle tracking simulation. Artificial turbulence with intensities of TI_{in}=0.15 and TI_{in}=0.3, as well as two swirl intensities with swirl numbers of S_n =0.6 and S_n =0.9, were applied at the inlet flow with a flow rate of 7 L/min. The effect of these parameters, as well as the effect of fullness coefficients of C_f=0.3, 0.5, 0.7, 0.9, and 1 on the flow behaviour, particle retention criterion (N_p^*), and particle deposition in the MM-Ostium region, were investigated. The results were compared with a laminar non-swirling inlet flow for C_f =1. An increase in particle retention criterion in the MM-Ostium region was calculated to quantify the increase in the drug delivery to the MS region.

One of the more significant findings to emerge from this study is that the turbulence and the swirl applied to the inlet flow were significantly damped when the flow passes through the nasal cavity. This implies that the nasal valve plays the role of airway resistance. The results showed that a turbulent inlet flow has a negligible effect on the particle deposition in the NC and drug delivery to the MM-Ostium regions is negligible. However, the deposition of particles increases with an increase in the swirl intensity of the inlet flow, which comes from the increasing effect of centrifugal force acting on the particles in a swirling flow. This study also found that that the drug delivery (quantified by N_p^*) to the MM-Ostium region increases by using a swirling inlet flow at a moderate swirl number, i.e., S_n =0.6. It was also found that the variation of fullness coefficient affects the drug delivery to the MM-Ostium region significantly. N_p^* in the MM-Ostium region increases with a decrease in the fullness coefficient. The highest N_p^* in the MM-Ostium region in the NC-MS model of this study occurs under the effect of swirling inlet flow (S_n =0.6) with $C_f = 0.3$, which is 45% greater

than N_{p}^{*} for a non-swirling inlet flow (S_{n} =0) with a normal particle release pattern (i.e., C_{f} = 1). The reason for the best performance with S_{n} =0.6 and $C_{\mathrm{f}} = 0.3$ is that it is directed to the left joint after which the centrifugal force pushed the particles to the walls and thus the ostium. In continuous drug delivery, such as drug delivery using nebulisers, the deposition of the particles in the anterior region increases gradually, which can contribute to forming droplets dripping from the nostril as waste. To overcome this problem, a decrease in C_{f} is recommended. It should be noted that the outcome of the current study is subjected to the following limitation: the humidity of the air in the nasal cavity was neglected, the nebulised droplets were considered as inert particles, the nose-sinus geometry was adapted from a healthy subject, and an isothermal condition was assumed. Also, the particles were released at the initial time step while they were monodispersed.

6.6 Acknowledgements

Financial support for the project has been provided by the Australian Government Research Training Program (RTP), and the Beacon of Enlightenment PhD Scholarship provided by the University of Adelaide. The authors would like to acknowledge the support of the School of Mechanical Engineering, Phoenix High-Performance Computing (HPC). The authors are grateful to A/Prof Kiao Inthavong (RMIT University, Australia) and Dr Haribalan Kumar (Aukland University, New Zealand) for the provision of STL files related to the nose geometry.

6.7 References

Adamczyk, W. P., Klimanek, A., Białecki, R. A., Węcel, G., Kozołub, P., & Czakiert, T. (2014). Comparison of the standard Euler–Euler and hybrid Euler–Lagrange approaches for modeling particle transport in a pilot-scale circulating fluidized bed. *Particuology, 15*, 129-137.

ANSYS®. (2020). ANSYS Fluent - CFD Software | ANSYS. In.

Ari, A., de Andrade, A. D., Sheard, M., AlHamad, B., & Fink, J. B. (2015). Performance comparisons of jet and mesh nebulizers using different interfaces in simulated spontaneously breathing adults and children. *Journal of Aerosol Medicine and Pulmonary Drug Delivery, 28*(4), 281-289.

Bahadur, S., & Pathak, K. (2012). Physicochemical and physiological considerations for efficient nose-to-brain targeting. *Expert Opinion on Drug Delivery, 9*(1), 19-31.

Bassett, A. B. (1888). *A Treatise on Hydrodynamics: Volume one*: Dover.

Bell, I. R., & Koithan, M. (2012). A model for homeopathic remedy effects: Low dose nanoparticles, allostatic cross-adaptation, and time-dependent sensitization in a complex adaptive system. *BMC Complementary and Alternative Medicine, 12*(1), 1-21.

Berger, W. E., Godfrey, J. W., & Slater, A. L. (2007). Intranasal corticosteroids: The development of a drug delivery device for fluticasone furoate as a potential step toward improved compliance. *Expert Opinion on Drug Delivery, 4*(6), 689-701.

Chen, S. B., & Ye, X. (2000). Faxen's laws of a composite sphere under creeping flow conditions. *Journal of Colloid and Interface Science, 221*(1), 50-57.

Cheng, Y., Holmes, T., Gao, J., Guilmette, R., Li, S., Surakitbanharn, Y., & Rowlings, C. (2001). Characterization of nasal spray pumps and deposition pattern in a replica of the human nasal airway. *Journal of Aerosol Medicine, 14*(2), 267-280.

Drettner, B., Falck, B., & Simon, H. (1977). Measurements of the air conditioning capacity of the nose during normal and pathological conditions and pharmacological influence. *Acta Oto-laryngologica, 84*(1-6), 266-277.

Durand, M., Pourchez, J., Aubert, G., Le Guellec, S., Navarro, L., Forest, V., Rusch, P., & Cottier, M. (2011). Impact of acoustic airflow nebulization on intrasinus drug deposition of a human plastinated nasal cast: New insights into the mechanisms involved. *International Journal of Pharmaceutics, 421*(1), 63-71.

Fluent Theory Guide. (2020). ANSYS® Fluent, Release 2020 R1, Help System, ANSYS, Inc. In.

Häuβermann, S., Bailey, A., Bailey, M., Etherington, G., & Youngman, M. (2002). The influence of breathing patterns on particle deposition in a nasal replica cast. *Journal of Aerosol Science, 33*, 923-933.

Hilton, C., Wiedmann, T., Martin, M. S., Humphrey, B., Schleiffarth, R., & Rimell, F. (2008). Differential deposition of aerosols in the maxillary sinus of human cadavers by particle size. *American Journal of Rhinology & Allergy, 22*(4), 395-398.

Hreiz, R., Gentric, C., & Midoux, N. (2011). Numerical investigation of swirling flow in cylindrical cyclones. *Chemical Engineering Research and Design, 89*(12), 2521-2539.

Inthavong, K., Ge, Q., Se, C. M., Yang, W., & Tu, J. (2011). Simulation of sprayed particle deposition in a human nasal cavity including a nasal spray device. *Journal of Aerosol Science, 42*(2), 100-113.

Inthavong, K., Tian, Z., Li, H., Tu, J., Yang, W., Xue, C., & Li, C. G. (2006). A numerical study of spray particle deposition in a human nasal cavity. *Aerosol Science and Technology, 40*(11), 1034-1045.

Inthavong, K., Tu, J., & Heschl, C. (2011a). Micron particle deposition in the nasal cavity using the v2–f model. *Computers & Fluids, 51*(1), 184-188.

Inthavong, K., Tu, J., & Heschl, C. (2011b). Micron particle deposition in the nasal cavity using the V2F model. *Computers & Fluids, 51*(1), 184-188.

Inthavong, K., Wen, J., Tian, Z., & Tu, J. (2008). Numerical study of fibre deposition in a human nasal cavity. *Journal of Aerosol Science, 39*(3), 253-265.

Keck, T., Leiacker, R., Heinrich, A., Kühnemann, S., & Rettinger, G. (2000). Humidity and temperature profile in the nasal cavity. *Rhinology, 38*(4), 167-171.

Kelly, J. T., Asgharian, B., Kimbell, J. S., & Wong, B. A. (2004). Particle deposition in human nasal airway replicas manufactured by different methods. Part I: Inertial regime particles. *Aerosol Science and Technology, 38*(11), 1063-1071.

Kimbell, J. S., Segal, R. A., Asgharian, B., Wong, B. A., Schroeter, J. D., Southall, J. P., Dickens, C. J., Brace, G., & Miller, F. J. (2007). Characterization of deposition from nasal spray devices using a computational fluid dynamics model of the human nasal passages. *Journal of Aerosol Medicine, 20*(1), 59-74.

Kimura, K. (2016). Wind loads. In A. Pipinato (Ed.), *Innovative Bridge Design Handbook* (pp. 37-48). Boston: Butterworth-Heinemann.

Kolev, N. I. (2011). Drag, lift, and virtual mass forces. In N. I. Kolev (Ed.), *Multiphase Flow Dynamics 2* (pp. 31-85). Berlin, Heidelberg: Springer.

Krstić, M. (2006). Mixing control for jet flows. In G. D. Roy (Ed.), *Combustion Processes in Propulsion* (pp. 87-96). Burlington: Butterworth-Heinemann.

Kumar, H., Jain, R., Douglas, R. G., & Tawhai, M. H. (2016). Airflow in the human nasal passage and sinuses of chronic rhinosinusitis subjects. *PloS One, 11*(6), 1-14.

Landahl, M. T., Mollo-Christensen, E., & Korman, M. S. (1989). *Turbulence and random processes in fluid mechanics* (2nd ed.). Cambridge: Cambridge University Press.

Laube, B. L. (2007). Devices for aerosol delivery to treat sinusitis. *Journal of Aerosol Medicine, 20*(1), 5-18.

Leclerc, L., El-Merhie, A., Navarro, L., Prévôt, N., Durand, M., & Pourchez, J. (2015). Impact of acoustic airflow on intrasinus drug deposition: New insights into the vibrating mode and the optimal acoustic frequency to enhance the delivery of nebulized antibiotic. *International Journal of Pharmaceutics, 494*(1), 227-234.

Leclerc, L., Pourchez, J., Aubert, G., Leguellec, S., Vecellio, L., Cottier, M., & Durand, M. (2014). Impact of airborne particle size, acoustic airflow and breathing pattern on delivery of nebulized antibiotic into the maxillary sinuses using a realistic human nasal replica. *Pharmaceutical Research, 31*(9), 2335-2343.

Lin, H.-L., Wan, G.-H., Chen, Y.-H., Fink, J. B., Liu, W.-Q., & Liu, K.-Y. (2012). Influence of nebulizer type with different pediatric aerosol masks on drug deposition in a model of a spontaneously breathing small child. *Respiratory Care, 57*(11), 1894-1900.

Loudon, C., & Tordesillas, A. (1998). The use of the dimensionless Womersley number to characterize the unsteady nature of internal flow. *Journal of Theoretical Biology, 191*(1), 63-78.

Maniscalco, M., Pelaia, G., & Sofia, M. (2013). Exhaled nasal nitric oxide during humming: Potential clinical tool in sinonasal disease? *Biomarkers in Medicine, 7*(2), 261-266.

Maniscalco, M., Sofia, M., Weitzberg, E., & Lundberg, J. (2006). Sounding airflow enhances aerosol delivery into the paranasal sinuses. *European Journal of Clinical Investigation, 36*(7), 509-513.

Maul, G. A. (2019). Pressure gradient force. In C. W. Finkl & C. Makowski (Eds.), *Encyclopedia of Coastal Science* (pp. 1390-1392). Cham: Springer International Publishing.

Möller, W., Schuschnig, U., Bartenstein, P., Meyer, G., Häussinger, K., Schmid, O., & Becker, S. (2014). Drug delivery to paranasal sinuses using pulsating aerosols. *Journal of Aerosol Medicine and Pulmonary Drug Delivery, 27*(4), 255-263.

Morsi, S., & Alexander, A. (1972). An investigation of particle trajectories in two-phase flow systems. *Journal of Fluid Mechanics, 55*(2), 193-208.

Mygind, N., & Vesterhauge, S. (1978). Aerosol distribution in the nose. *Rhinology, 16*(2), 79-88.

Navarro, L., Leclerc, L., & Pourchez, J. (2019). Does acoustic overlay of music improve aerosol penetration into maxillary sinuses? *Online Journal of Otolaryngology and Rhinology, 1*(4), 1-3.

Ounis, H., Ahmadi, G., & McLaughlin, J. B. (1991). Brownian diffusion of submicrometer particles in the viscous sublayer. *Journal of Colloid and Interface Science, 143*(1), 266-277.

Pattle, R. (1961). The retention of gases and particles in the human nose. *Inhaled Particles and Vapours, 1*, 302-309.

Pourmehran, O., Arjomandi, M., Cazzolato, B., Ghanadi, F., & Tian, Z. (2020). The impact of geometrical parameters on acoustically driven drug delivery to maxillary sinuses. *Biomechanics and Modeling in Mechanobiology, 19*(2), 557-575.

Pourmehran, O., Arjomandi, M., Cazzolato, B., & Tian, Z. (2020). *Effect of particle diameter and density on acoustic drug delivery to maxillary sinus – a sensitivity study*. Paper presented at the 22nd Australasian Fluid Mechanics Conference (AFMC2020), Brisbane, Australia.

Rissler, J., Swietlicki, E., Bengtsson, A., Boman, C., Pagels, J., Sandström, T., Blomberg, A., & Löndahl, J. (2012). Experimental determination of deposition of diesel exhaust particles in the human respiratory tract. *Journal of Aerosol Science, 48*, 18-33.

Schwarzkopf, J. D., Sommerfeld, M., Crowe, C. T., & Tsuji, Y. (2011). *Multiphase Flows with Droplets and Particles* (2nd ed.): CRC press.

Shang, Y., Inthavong, K., & Tu, J. (2015). Detailed micro-particle deposition patterns in the human nasal cavity influenced by the breathing zone. *Computers & Fluids, 114*, 141-150.

Shi, H., Kleinstreuer, C., & Zhang, Z. (2006). Laminar airflow and nanoparticle or vapor deposition in a human nasal cavity model. *Journal of Biomechanical Engineering, 128*(5), 697-706.

Shi, H., Kleinstreuer, C., & Zhang, Z. (2007). Modeling of inertial particle transport and deposition in human nasal cavities with wall roughness. *Journal of Aerosol Science, 38*(4), 398-419.

Suman, J. D., Laube, B. L., & Dalby, R. (1999). Comparison of nasal deposition and clearance of aerosol generated by a nebulizer and an aqueous spray pump. *Pharmaceutical Research, 16*(10), 1648-1652.

Tian, Z., Inthavong, K., & Tu, J. (2008). Deposition of inhaled wood dust in the nasal cavity. *Inhalation Toxicology, 19*(14), 1155-1165.

Tian, Z., Tu, J., & Yeoh, G. (2005). Numerical simulation and validation of dilute gas-particle flow over a backward-facing step. *Aerosol Science and Technology, 39*(4), 319-332.

Tong, X., Dong, J., Shang, Y., Inthavong, K., & Tu, J. (2016). Effects of nasal drug delivery device and its orientation on sprayed particle deposition in a realistic human nasal cavity. *Computers in Biology and Medicine, 77*, 40-48.

Van Strien, J., Shrestha, K., Gabriel, S., Lappas, P., Fletcher, D. F., Singh, N., & Inthavong, K. (2021). Pressure distribution and flow dynamics in a nasal airway using a scale resolving simulation. *Physics of Fluids, 33*(1), 1-14.

Wichers, L. B., Rowan III, W. H., Nolan, J. P., Ledbetter, A. D., McGee, J. K., Costa, D. L., & Watkinson, W. P. (2006). Particle deposition in spontaneously hypertensive rats exposed via whole-body inhalation: Measured and estimated dose. *Toxicological Sciences, 93*(2), 400-410.

Wofford, M., Kimbell, J., Frank, D., Dhandha, V., McKinney, K., Fleischman, G., Ebert, C., Zanation, A., & Senior, B. (2015). A computational study of functional endoscopic sinus surgery and maxillary sinus drug delivery. *Rhinology, 53*(1), 41-48.

Xi, J., & Longest, P. W. (2008). Numerical predictions of submicrometer aerosol deposition in the nasal cavity using a novel drift flux approach. *International Journal of Heat and Mass Transfer, 51*(23-24), 5562-5577.

Xi, J., Si, X., Peters, S., Nevorski, D., Wen, T., & Lehman, M. (2017). Understanding the mechanisms underlying pulsating aerosol delivery to the maxillary sinus: In vitro tests and computational simulations. *International Journal of Pharmaceutics, 520*(1), 254-266.

Xi, J., Zhang, Z., & Si, X. (2015). Improving intranasal delivery of neurological nanomedicine to the olfactory region using magnetophoretic guidance of microsphere carriers. *International Journal of Nanomedicine, 10*(1), 1211-1222.

Yang, Y., Sze To, G. N., & Chao, C. Y. (2012). Estimation of the aerodynamic sizes of single bacterium-laden expiratory aerosols using stochastic modeling with experimental validation. *Journal of Aerosol Science and Technology, 46*(1), 1-12.

Zhao, K., Scherer, P. W., Hajiloo, S. A., & Dalton, P. (2004). Effect of anatomy on human nasal air flow and odorant transport patterns: Implications for olfaction. *Chemical Senses, 29*(5), 365-379.

Chapter 7

Conclusion and future work

Acoustic drug delivery is a novel, non-invasive technique for delivery of medications to the sinuses, in particular the maxillary sinuses. ADD operates using the pressure differences between the maxillary sinuses and the nasal cavity arising from the oscillation of the air plug in the ostium under the effect of an external acoustic wave applied to the nostril. ADD has been demonstrated to increase the efficiency of drug delivery to the MS compared with conventional non-acoustic drug delivery techniques. There being only a handful scientific research papers in the area of acoustic drug delivery focusing on the feasibility of the ADD in experiments and numerical studies, the underlying mechanism of drug delivery to the MS and recognition of the efficient parameters for increasing ADD efficiency are the key topic of research. In the research presented in this thesis, a series of experiments were conducted, and numerical models were developed to understand the underlying mechanism of ADD. Moreover, several different, related parameters of acoustic drug delivery to the MS were

examined. The following sections present the significance of the study and propose some suggestions for future research.

7.1 Significance of the present work

Since 1950, ADD has been used clinically at two fixed frequencies of 45 Hz or 100 Hz. Several researchers have shown an increase of 2- to 4-fold in the efficiency of drug delivery to the sinuses under the effect of those input frequencies. However, due to the similarity of the NC-MC combination and a Helmholtz resonator, researchers have recently hypothesised that the highest drug delivery to the MS takes place at the resonance frequency of the NC-MC combination. Subsequently, a small number of studies have exploited the fundamental governing equation of a Helmholtz resonator to estimate the resonance frequency of the NC-MS. Applying this resonance frequency to the nostril for assessment, an increase of 3- to 5-fold in drug delivery to the MS was reported when compared with non-ADD. Such an increase in drug delivery efficiency is still insufficient for the treatment of CRS. The main goal of the current study was to develop a deep understanding of the mechanisms underlying acoustic drug delivery to maxillary sinuses in order to increase the efficiency of this delivery technique. In addition to the aero-acoustic analysis, the effects of inlet airflow parameters and nozzle diameter on the flow structure in the NC and drug delivery to the MS were investigated.

The main outcomes and significance of this research can be described as follows:

1. As a starting point for this work, it was necessary to determine the resonance frequency of the NC-MS combination as accurately as possible. To do so, different numerical models, including computational aero-acoustics (CAA) using CFD, finite element analysis (FEA), and the classic Helmholtz resonator equation were developed

to predict the resonance frequency of a simplified NC-MS combination. The resonance frequency obtained by the numerical models were compared with in-house experimental data. It was found that the FEA and the classic Helmholtz resonator equation overestimate the resonance frequency of the NC-MS combination with an unacceptable deviation ($\geq$ 20%) from the experiments, whereas CAA-CFD predicts the resonance frequency with an acceptable deviation, between 0.6% and 8%, from the experiment. Hence, CAA-CFD simulation provides a much more accurate prediction of the resonance frequency of the NC-MS combination compared with more commonly-used methods, and is rooted in the governing underlying equations used in these numerical approaches. CAA-CFD can resolve this aero-acoustic problem better than FEA because it can model the nonlinear phenomena, in particular near the wall and the edge of a solid body, while in FEA, only the linearized Euler equations are resolved.

2. Using the validated CAA-CFD model, the effects of various geometric parameters such as the ostium length/diameter, MS volume/shape, and the NC width on the resonance frequency of 25 simplified NC-MS models were investigated. The results showed that the NC width and the MS shape have negligible effects on the resonance frequency of the NC-MS combination. It was also shown that there is a direct relationship between the resonance frequency of the NC-MS combination and the ostium diameter, while there is an inverse relationship between the resonance frequency and the square root of the ostium length and the MS volume. Hence, it is inferred that acoustic drug delivery to the MS is independent from the shape of the MS and the size of the NC; however, it depends highly on the ostium and MS sizes. Accordingly, given that the size of the ostium and MS in every patient is different,

administration of ADD with a fixed acoustic frequency (e.g., 45 Hz and 100Hz) for every patient cannot guarantee optimal drug delivery to the MS.

3. The effect of the ostium size on the damping ratio of the oscillation of the air plug in the ostium was also investigated experimentally. The results indicated that the damping ratio has an inverse relationship with the diameter of the ostium, and a monotonic relationship with the length of the ostium. This indicates that the amplitude of the input acoustic wave should be adjusted with the damping ratio to achieve improved ADD efficiency. More specifically, given that an increase in the damping ratio reduces the magnitude of the oscillation of the air plug in the ostium, the pressure amplitude of the acoustic source should be increased to counter the effect of the damping.
4. A CAA-CFD model was developed to predict the resonance frequency of a realistic NC-MS combination, as well as to conduct aero-acoustic analysis at the resonance frequency. The CAA-CFD model was validated against the experimental data. The acoustic analysis of the CAA-CFD model revealed that not only does the air plug in the ostium oscillate at the resonance frequency of the NC-MS combination, but also a portion of the air plug in the middle meatus oscillates. This indicates that to increase the efficiency of ADD, not only should the number of particles in the ostium be increased, but also the number of particles in the middle meatus in proximity to the ostium.
5. A validated CFD model was further developed to predict the particle trajectories under the effect of input acoustic wave applied to the inlet in a simplified NC-MS combination. Particle tracking was modelled using a discrete phase model (DPM). Particles were distributed in the simplified NC-MS combination, and then the effects of different aero-acoustic parameters, including the frequency and amplitude of the

acoustic wave applied to the inlet on the efficiency of the ADD to the MS, were investigated. The results of this study indicate that the efficiency of ADD highly depends on the acoustic frequency and amplitude applied to the inlet. It was found that maximum ADD efficiency occurs when an acoustic wave, driven at the resonance frequency of the NC-MS model, is applied to the inlet. The ADD efficiency has a monotonic relationship with the amplitude of the inlet acoustic wave. It was also shown that an increase in the mean flow rate of the inlet airflow decreases the ADD efficiency because the mean flow increases the damping ratio of the oscillation of the air plug in the ostium, which contributes to reducing the amplitude of the oscillation of the air plug in the ostium.

6. A CFD model was developed to understand the effect of particle diameter and density on ADD efficiency using a simplified NC-MS geometry. The evidence from this study suggests that the efficiency of ADD can be enhanced by reducing the particle size from 12 μm to 2 μm. Indeed, a decrease in the diameter of the particles decreases the acoustic Stokes number, which contributes to increasing the amplitude of the motion of the particles in the ostium when an external acoustic wave is applied.

   In practice, the drugs are used as droplets in ADD, so the ADD efficiency may decrease through an orthokinetic collision of droplets. In fact, the droplets can undergo orthokinetic collisions in the presence of an acoustic field. This collusion may lead to a coalescence where the diameter of the particle can increase. An increase in the particle diameter decreases the particle entrainment coefficient, resulting in a decrease in ADD efficiency. To prevent an orthokinetic collision in the presence of an acoustic field, the droplets should be of uniform size.

7. An experiment was designed and fabricated to investigate the effect of aero-acoustic parameters' drug deposition in the MS using a realistic 3D-printed NC-MS model.

Nebulised 2.5 wt% NaF was used as a drug tracer. One of the more significant findings to emerge from this study is that applying an acoustic wave to the nostril at the resonance frequency of the NC-MS combination can significantly increase the deposition of aerosols in the MS. For the NC-MS model used in this study, superimposing an input frequency of 328 Hz and amplitude of 126 dB re 20μPa on nebulised aerosol (12 μm) entering the nostril with a particle flow rate of 0.267 mL/min increased the concentration of NaF deposited in the MS 75-fold. The experimental data showed that increasing the input acoustic amplitude increased the aerosol deposition in the MS. However, increasing the amplitude above 120 dB re 20μPa did not have a significant effect on the aerosol deposition, which might imply that at certain acoustic amplitudes a saturation point for aerosol deposition is reached. The present study confirms previous findings and contributes additional evidence that supports the idea that the maximum efficiency of drug delivery to the MS occurs at the resonance frequency of the NC-MS combination.

8. A CFD model was developed to investigate the effect of inlet flow parameters and the nozzle diameter on the airflow behaviour and drug (particle) delivery to the MM-Ostium region in a realistic NC-MS model. To conduct the parametric studies, two CFD models using a hybrid RANS-LES model and laminar solver were developed and cross-validated with the available experimental data. One of the more significant findings to emerge from this study is that the artificial turbulence and the swirl applied to the inlet flow were significantly damped when the flow passes through the nasal cavity. This implies that the nasal valve plays the role of airway resistance. The results showed that the effect of turbulent inlet flow on the particle deposition in the NC and drug delivery to the MM-Ostium region is negligible. However, the deposition of particles increases with an increase in the swirl intensity of the inlet flow, which

comes from the increasing effect of centrifugal force acting on the particles in a swirling flow. It was also found that the fullness coefficient C_f (i.e., the ratio of nozzle diameter to the inlet diameter) affects the drug delivery to the MM-Ostium region. It was found that an increase in C_f decreases the drug delivery efficacy to the MM-Ostium region. An increase in the particle retention criterion in the MM-Ostium region was calculated to quantify the increase in the drug delivery to the MS region.

7.2 Recommendation for future work

The work presented in this thesis was focused on the development of a fundamental understanding of the underlying mechanism of ADD to determine the most important geometric and aero-acoustic parameters, as well as the inlet flow and particle release preconditions, affecting the efficiency of ADD for drug delivery to the MS. Despite the significant knowledge developed in the field of acoustic drug delivery to the MS, further studies are required to move from concept to commercialisation. Some suggestions for future work are as follows:

1. In this study, a simplified and realistic model of NC-MS was used for the parametric study. However, in practice, other sinuses such as the frontal, ethmoid, and sphenoid sinuses are also infected in some CRS patients. Further work needs to be done to establish whether ADD can be an advantageous approach for drug delivery to those sinuses. To do so, a realistic nose model, including the NC and all paranasal sinuses, is required to undertake parametric studies. The material used in this mode should be identical to the human nose-sinus tissue since the impedance of this model is important in the prediction of the resonance frequency of the nose-sinus combination.

2. The current study showed that the efficiency of ADD depends highly on the acoustic frequency applied to the nostril (inlet) such that when driving at the resonance frequency, the ADD efficiency increases significantly (>50-fold compared with non-ADD). Hence, it is imperative to predict the resonance frequency of the NC-MS combination as accurately as possible, which has been carried out in the current study using experimental and numerical methods. However, there are some limitations to both methods. In the experimental method, a hole was made in the wall of the MS (in a 3D printed model) to install a microphone for detecting the acoustic signals in the MS, which is not feasible in practice. To tackle this problem, further research is needed to develop an experimental method for predicting the resonance frequency of the NC-MS combination without making a hole in the MS wall. The use of a two-microphone method in the prediction of the resonance frequency of the NC-MS combination might be helpful. In the two-microphone method, the incident and reflective acoustic signals can be analysed to predict the resonance frequency of the NC-MS combination rather than the detection of the acoustic signals in the MS.
3. The prediction of the resonance frequency of a realistic NC-MS combination using a CAA-CFD simulation requires significant computational resources and time. An approach to tackle this issue could be the use of machine learning techniques such as Artificial Neural Networks (ANN), which might provide rapid estimation, instead of directly simulating the CAA-CFD models. Further investigation and experimentation into the feasibility of machine learning techniques in the prediction of the resonance frequency of the NC-MS combination are strongly recommended.
4. The effects of orthokinetic collisions of particles on the acoustic Stokes number and ADD efficiency have been investigated in the current study qualitatively. However, future research should concentrate on investigation of orthokinetic collision impacts

on ADD quantitatively, which would enable determination of the optimum size and distribution of the particles.